

Nicolaus Copernicus University in Toruń
Faculty of Physics, Astronomy and Informatics
Department of Quantum Physics

Plasmonic nanostructures supporting frequency conversion in atomic systems

Saeid Izadshenas Jahromi

Dissertation submitted in partial fulfillment
of the requirements for the degree of
Doctor of Physics

Thesis supervised by dr hab. Karolina Słowik
Department of Quantum Physics
Institute of Physics, Nicolaus Copernicus university in Toruń



**NICOLAUS COPERNICUS
UNIVERSITY
IN TORUŃ**

Faculty of Physics, Astronomy
and Informatics

Toruń 2024

Abstract

This thesis presents a comprehensive study on the nonlinear light-matter interactions facilitated by plasmonic nanoantennas and metasurfaces, employing theoretical and numerical modeling as primary research methods. The investigation focuses on various plasmonic nanoantenna and metasurface configurations designed to enhance nonlinear optical processes, such as surface-enhanced Raman scattering, coherent anti-Stokes Raman scattering, light interactions with polar molecules, and multi- and two-photon absorption processes.

Key achievements include the design of plasmonic nanoantennas and metasurfaces that not only amplify these nonlinear processes but also enable the control of resonance frequencies through the application of a gate voltage to a graphene layer in the terahertz band. This capability allows for the tunable enhancement of multi-photon absorption processes, supporting two-, four-, six-, eight-, and ten-photon absorption with a fixed nanoantenna geometry by modulating the gate voltage. Additionally, coupling graphene disks with silver bars facilitates the control of terahertz emission from polar quantum systems. In these processes, the integration of silver and gold nanobars with graphene layers results in two distinct and tunable resonances ranging from the terahertz to the visible regimes. These novel nanoantenna structures can be utilized for their applications in multi-photon fluorescence and optomechanical cavities.

The thesis also explores the design of two metasurfaces with distinct optical response for enhancing Raman scattering. The first metasurface features a metal-insulator-grating configuration, which is tunable and supports multiple resonances that can be adjusted by altering the incident angle, enabling the detection of three Raman shifts in Rhodamine molecules. The second metasurface, with a metal-insulator-metal configuration, overcomes the limitations of the first by offering ultra-broadband resonance and significant electric field enhancement, thereby supporting a wide range of Raman shifts and molecules in both Raman scattering and coherent anti-Stokes Raman scattering processes.

Furthermore, the research proposes a tunable nanoantenna with dual plasmonic modes—bright and dark—that can be tuned by coupling these modes and adjusting the polarization, targeting the near-infrared and visible regimes. The quantum description of the two-photon absorption process reveals different regimes determined by molecular saturation level where orthogonal strategies for signal enhancement should be applied.

In summary, this thesis demonstrates the potential of plasmonic nanoantennas and metasurfaces for substantial enhancement of various nonlinear light-matter interactions through their coupling to atomic systems, advancing the understanding and

control methods of these complex processes.

Streszczenie

Niniejsza rozprawa przedstawia wyniki kompleksowych badań nieliniowych interakcji światła z materią w otoczeniu plazmonicznych nanoanten i metapowierzchni, z wykorzystaniem modelowania numerycznego i teoretycznego jako głównych metod badawczych. Badania koncentrują się na różnych konfiguracjach plazmonicznych nanoanten i metapowierzchni, zaprojektowanych w celu wzmocnienia nieliniowych procesów optycznych, takich jak powierzchniowo wzmocniona spektroskopia Ramana, koherentna spektroskopia Ramana, oddziaływania światła z cząsteczkami polarnymi oraz procesy absorpcji wielofotonowej i dwufotonowej.

Kluczowe wyniki obejmują projektowanie plazmonicznych nanoanten i metasurfaces, które nie tylko wzmacniają te nieliniowe procesy, ale także umożliwiają kontrolę częstotliwości rezonansowych poprzez zastosowanie napięcia bramki do warstwy grafenu w paśmie terahercowym. Ta zdolność pozwala na strojenie wzmocnienia procesów absorpcji wielofotonowej, wspierając absorpcję dwóch, czterech, sześciu, ośmiu i dziesięciu fotonów przy stałej geometrii nanoanteny poprzez modulację napięcia bramki. Dodatkowo, sprzężenie dysków grafenowych z prętami srebrnymi umożliwia kontrolę emisji terahercowej z układów kwantowych z cząsteczkami polarnymi. W tych procesach, integracja prętów srebrnych i złotych z warstwami grafenu prowadzi do dwóch odrębnych i strojalnych rezonansów w zakresie od pasma terahercowego do widzialnego. Te nowatorskie struktury nanoanten mogą znaleźć zastosowanie w fluorescencji wielofotonowej i wnękach optomechanicznych.

Rozprawa zawiera również projekty dwóch metapowierzchni o odmiennych odpowiedziach optycznych w celu wzmocnienia rozpraszania Ramana. Pierwsza metapowierzchnia w konfiguracji metal-izolator-grating charakteryzuje się przestrajalną odpowiedzią optyczną z kilkoma rezonansami, których położenie spektralne może być sterowane przez zmianę kąta padania. Pozwala to na wzmocnienie sygnału detekcji wybranych wartości przesunięć Ramana w cząsteczkach Rhodaminy. Druga metapowierzchnia o konfiguracji metal-izolator-metal oferuje ultra-szerokopasmowy rezonans i znaczne wzmocnienie pola elektrycznego, wspierając tym samym szeroki zakres przesunięć Ramana dla gamy cząsteczek w procesach zarówno rozpraszania Ramana, jak i koherentnego rozpraszania anty-stokesowskiego.

Ponadto, rozprawa opisuje przestrajalną nanoantenę z dwoma modami plazmonicznymi — jasnym i ciemnym — w zakresie bliskiej podczerwieni i widzialnym. Ich właściwości sterowanych poprzez sprzężenie tych modów i dobór polaryzacji. Z opisu kwantowego procesu absorpcji dwufotonowej wynika, że w różnych zakresach nasycenia poziomu wzbudzenia badanych cząsteczek skuteczne są odmienne mechanizmy wzmocnienia sygnału.

Podsumowując, praca ta demonstruje znaczny wpływ nanoanten i metapowierzchni na nieliniowe oddziaływania światła z materią poprzez wykorzystanie plazmonicznych nanoanten i metapowierzchni, poszerzając zrozumienie i zakres metod kontroli tych złożonych procesów.

Dedication

This thesis is dedicated to my family, whose unwavering support and love have been the foundation of my journey. To my mother, whose strength, wisdom, and endless encouragement have seen me through every challenge—this accomplishment is as much yours as it is mine. To my brother, who has always been my confidant and source of inspiration, thank you for believing in me and for being by my side.

I am also deeply grateful to my friends and colleagues, whose friendship and shared experiences have made this journey richer and more meaningful.

Finally, to my supervisor, thank you for your unwavering guidance, patience, and insightful mentorship. Your support has been instrumental in shaping this work into its final form.

Acknowledgements

I would like to extend my heartfelt gratitude to my supervisor, Dr. hab. Karolina Słowik, for her scientific supervision and support throughout my PhD studies. I am also deeply grateful to Dr. hab. Piotr Masłowski for his mentorship in experimental techniques and frequency comb lasers, and to Dr. Tobias Herr for his insights into spectroscopy and sensing.

I am especially indebted to Dr. Petri Karvinen and Prof. Markku Kuittinen for allowing me to join their group for my internship and to work on metasurface fabrication at university of eastern Finland. Additionally, I would like to thank Academia Scientiarum Thoruniensis for providing opportunities for students to share their knowledge and develop their skills through participating in conferences and summer schools.

I wish to thank all collaborators who were directly involved in the studies presented in this thesis, as well as all my colleagues from our research group with whom I had the pleasure to work.

The research presented in this thesis was generously supported by the following grants:

1. National Science Centre, Poland, Project No. 2016/23/G/ST3/04045.
2. National Science Centre, Poland, Grant No. 2018/31/D/ST3/01487.
3. National Centre for Research and Development, QUANTERA II, Project no. QUANTERAII/1/21/E2TPA/2023.
4. Royal Society of Chemistry, travel grant, Grant No. D23-7364220436.



NATIONAL SCIENCE CENTRE
POLAND

Contents

Abstract	i
1 Introduction	1
1.1 Plasmonic metasurfaces	1
1.2 Localized surface plasmon resonances	4
1.2.1 Maxwell's equations and electromagnetic wave interaction	4
1.2.2 The dielectric function of free electron gas	5
1.2.3 Surface plasmon polaritons	6
1.2.4 Localized surface plasmon resonance	9
1.2.5 Influence of geometry and size	14
1.2.6 Influence of materials	16
1.2.7 Plasmonic metasurfaces and their optical properties	17
1.3 Surface plasmon polaritons coupled to atomic system	19
1.3.1 Interaction of plasmon-enhanced light and atomic systems	19
1.3.2 Purcell effect	20
1.3.3 Near-field interaction with atomic systems	22
1.4 Nonlinear optical phenomena	23
1.4.1 Surface enhanced Raman scattering	23
1.4.2 Coherent anti-Stokes Raman scattering	24
1.4.3 Two-photon absorption	25
1.4.4 Polar Molecule	26
1.5 Analytical and numerical techniques	29
1.5.1 Finite Integration Technique	29
1.5.2 Finite Element Method	30
1.5.3 Methods	32
2 Summary of the publications	33
2.1 Published articles comprising the thesis	33
2.2 Other published articles	34
2.3 My work and connections	37

2.4	Author contribution statement	40
3	Conclusions	42
A	Publications	51
A.1	Metasurface for broadband coherent Raman signal enhancement beyond the single-molecule detection threshold	52
A.2	Supporting information for: Metasurface for broadband coherent Raman signal enhancement beyond the single-molecule detection threshold	62
A.3	Hybrid graphene-silver nanoantenna to control THz emission from polar quantum systems	74
A.4	Multiresonant metasurface for Raman spectroscopy beyond single molecule detection level	88
A.5	Multi-Photon Absorption Enhancement by Graphene-Gold Nanostructure	95
A.6	Supplementary Material for Multi-Photon Absorption Enhancement by Graphene-Gold Nanostructure	101
A.7	Molecular saturation determines distinct plasmonic enhancement scenarios for two-photon absorption signal	106

List of Figures

1.1	Schematic diagram of a TM wave incident on a metal-dielectric interface.	7
1.2	Dispersion of SPPs at a dielectric-metal interface. The assumed parameters are $\omega_p = 12 \times 10^{15} s^{-1}$ and $\epsilon_d = 2.25$	9
1.3	Diagram of sphere in electrostatic field $\mathbf{E} = E_0 \mathbf{z}$. The radius is a , and θ is an angle between the position vector \mathbf{r} at point P and the z -axis.	10
1.4	(a) Electric field enhancement distribution for resonant illumination at $\lambda_0 = 360$ nm, (b) absorption cross-section (ACS) and scattering cross-section (RCS), (c) electric field enhancement spectrum of a silver sphere with $a = 20$ nm.	12
1.5	(a) Electric field distribution, (b) absorption cross-section and scattering cross-section, (c) electric field enhancement spectrum of two coupled silver spheres with $a = 20$ nm and $g = 10$ nm.	13
1.6	(a) Linear electric field distribution, (b) absorption cross-section (ACS) and scattering cross-section (RCS), (c) electric field enhancement spectrum of single silver nanorod with $l = 40$ nm and $a = 5$ nm at point (22.5 nm,0,0). (d) Linear electric field distribution, (e) absorption cross-section (ACS) and scattering cross-section (RCS), (f) electric field enhancement spectrum of single silver nanocubic with $l = 40$ nm at point (22.5 nm,0,0). (g) Linear electric field distribution, (h) absorption cross-section (ACS) and scattering cross-section (RCS), (k) electric field enhancement spectrum of single silver nanocone with $l = 40$ nm at point (22.5 nm,0,0).	14
1.7	(a) Electric field enhancement varying by radius in single silver nanosphere, (b) Electric field enhancement varying by refractive index around the silver nanosphere.	15
1.8	Dielectric functions of (a) gold, (b) silver, based Johnson and Christy experimental results, (c) graphene in $T = 300$ K, $\tau = 1$ ps, and $\mu_c = 0.45$ eV.	17

1.9	(a) Schematic of perfect absorber metasurface, (b) transmission, reflectance and absorption spectrum, (c) electric field enhancement spectrum at point (178.5 nm, 0, 0). (d) Schematic of perfect absorber nanoantenna, (e) absorption cross-section (ACS) and scattering cross-section (RCS), (f) electric field enhancement spectrum at point (178.5 nm, 0, 0). The gold disk diameter is 352 nm and the thickness is 20 nm. The periodicity is 600 nm and the spacer thickness is 30 nm. The thickness of gold film is 200 nm.	18
1.10	Diagram of (a) two-level system, (b) coupling of the plasmonic silver nanosphere to a two-level atomic system.	19
1.11	(a) Radiated power ratios of a single silver nanosphere with radius $a = 20$ nm as functions of free-space wavelength of the radiation emitted by a dipole source situated 2.5 nm from the sphere surface; (b) radiated power resonance peak amplitude and (c) radiated power spectra as functions of distance of dipole source from the nanosphere.	21
1.12	Varying electric field enhancement via distance from the surface of a silver nanosphere with the radius $a = 20$ nm.	22
1.13	Energy level diagram of (a) Raman scattering including Stokes and anti-Stokes Raman scattering, (b) coherent anti-Stokes Raman scattering, (c) two-photon absorption process with a following single-photon fluorescence.	24
1.14	Energy scheme (a) and dynamics (b) of a two-level system.	27
1.15	(a) The discretization on orthogonal grid systems. (b) Discretization of the Faraday's law.	30
1.16	The function w (solid blue line) is approximated with w_i (dashed red line), which is a linear combination of linear basis functions Φ_i (solid black line).	31

Chapter 1

Introduction

1.1 Plasmonic metasurfaces

Visible light waves, with energies of several electron Volts (eV) per photon and wavelengths ranging from approximately 400 nm to 800 nm, are particularly interesting for two primary reasons. First, chemical bonds formed by outer electrons of atoms forming molecules or materials typically have energies in the eV range, making this spectral range ideal for studying light-matter interactions. Second, the energy of visible light is higher than that of thermal radiation but lower than the binding energies of inner electrons, resulting in better signal-to-noise ratios for visible light detectors compared to infrared and less damage to matter than ultraviolet radiation. Despite the agreement in energy scales, the interaction strength between light and quantum systems, such as atoms, molecules, or quantum dots, is usually weak. This is due to the strong size mismatch between the quantum systems and electromagnetic wavelengths. A traditional way to enhance these interactions involves resonant cavities, which are now available in a plethora of realizations, from conventional Fabry-Pérot interferometers, to microresonators, to defects in photonic crystal lattices, to name just a few. Metallic nanoparticles, with their ability to spatially confine electromagnetic energy and locally enhance fields through the mechanism described below, can be understood as a specific type of open cavity. Thus, the interaction strength between light and quantum systems can be orders of magnitude stronger in the vicinity of metallic nanoparticles than in free space. This is because of plasmonic excitations – surface waves with evanescent electromagnetic fields that occur at metal-dielectric interfaces[1]. This interaction can be used to enhance energy absorption in quantum systems, facilitate energy transfer from quantum systems to plasmonic systems, and enable continuous energy exchange between the subsystems.

At optical frequencies, metals are not perfect conductors, meaning that the physical properties of metallic nanoparticles can be understood in terms of their electromagnetic eigenmodes. These eigenmodes, known as surface plasmon polaritons (SPPs), are quasi-particles that arise from the interaction between coherent oscillations of the charge density inside the metal (plasmons) and the electromagnetic field[2]. The study of SPPs, now referred to as plasmonics, has spanned over a century of research, exploiting nanoparticles for new avenues in the study of light-matter interactions at optical frequencies. Due to the extraordinary ability of nanoparticles to mediate between propagating radiation and localized electromagnetic fields, a term "nanoantenna" was coined to refer to plasmonic nanoparticles [3].

Two significant discoveries in the 20th century have significantly impacted research on light-matter interaction: the Purcell effect and Raman scattering. The Purcell effect, first described in the context of cavity quantum electrodynamics, highlights the enhancement of a quantum system's spontaneous emission rate due to a resonant cavity, quantified by the Purcell factor[3]. This modification significantly influences light-matter interactions strength.

Interest in light-matter interactions near metallic nanoparticles surged with the discovery of surface-enhanced Raman scattering (SERS) in 1974[4]. These experiments revolutionized the investigation of molecular chemical properties and spurred extensive theoretical and experimental research to understand the interaction between metallic surfaces and quantum systems[5, 6, 7]. While SERS enhances the signal, it is a slow process. Nonlinear Raman scattering, such as coherent anti-Stokes Raman scattering (CARS), offers an alternative approach to enhance the signal more effectively and speed up the process[8]. CARS, based on a four-wave nonlinear optical mixing process, enhances the signal by several orders of magnitude when combined with plasmons. Researchers have demonstrated this enhancement theoretically and experimentally using various plasmonic devices, including gold surface[9], tip enhancement[10], and coupling of plasmonic disks[11]. The other nonlinear optical process is two-photon absorption (TPA). TPA offers high spatial selectivity and improved penetration depth into the absorbing medium[12]. Noble metal nanoantennas with broad resonances are utilized to enhance TPA.

New avenues for research in plasmonics have opened with the discovery of graphene with its unique optoelectronic properties, including extremely low ohmic losses and a tunable optical response. The plasmonic resonances in graphene occur in the terahertz and mid-infrared regimes, making it an ideal material for supporting nonlinear optical processes[13].

An array of nanoantennas that resonantly couple to the electromagnetic fields forms a metasurface, which exhibits unique optical properties not typically observed in nature, such as negative refractive index[14], invisibility cloaking[15], and super

lense[16]. Metasurfaces allow for precise control over spatially varying the optical response, including amplitude, phase, and polarization[17]. The field of metasurfaces is rapidly expanding from the microwave to visible spectrum, enabling the engineering of optical properties across a wide range of disciplines.

To support all these applications, engineering suitable plasmonic nanoantennas and metasurfaces is essential to control the spectral positions and strength of their resonances. High electric field enhancement can be achieved in a single broadband resonance[18], in multiple tunable resonances[19], or in two split resonances [20, 21]. In my work, I explore a variety of plasmonic materials and geometries to design nanoantennas with specific functionalities and tailored spectral properties, when need be - supporting a tunable optical response. This thesis consists of five research articles, of which I was the main author, and an extensive introduction to the physics of nanoantennas and the basics of the quantum theory of light-matter interactions, which are essential to understanding the articles. For this purpose, we introduce Maxwell's equations and the Drude model to simulate noble materials like gold and silver. We then investigate surface plasmons, define atomic systems, and explore applications of coupling atomic systems with surface plasmons, such as SECARS[19, 18], enhanced two-photon absorption, control of Rabi frequency in polar molecules[20] and multiphoton absorption[21].

1.2 Localized surface plasmon resonances

We follow "Plasmonics: Fundamentals and Applications" by Stefan Alexander Maier to explore the optical properties of metals and localized surface plasmons [22].

Maxwell's equations describe the electromagnetic response of bulk materials over a wide frequency range. In this chapter, we introduce Maxwell's equations and their solutions at the interface of metals and dielectrics: surface plasmon polaritons and localized surface plasmons.

1.2.1 Maxwell's equations and electromagnetic wave interaction

To introduce the properties of light-matter interactions, we discuss the fundamentals of the electromagnetic theory. Maxwell's equations describe electromagnetic fields in the presence of currents, charges, and polarizable media. The macroscopic Maxwell's equations in the time domain can be written as follows:

$$\begin{aligned}
 \nabla \cdot \mathbf{D}(\mathbf{r}, t) &= \rho_{\text{ext}}(\mathbf{r}, t), \\
 \nabla \cdot \mathbf{B}(\mathbf{r}, t) &= 0, \\
 \nabla \times \mathbf{E}(\mathbf{r}, t) &= -\frac{\partial \mathbf{B}(\mathbf{r}, t)}{\partial t}, \\
 \nabla \times \mathbf{H}(\mathbf{r}, t) &= \mathbf{J}_{\text{ext}}(\mathbf{r}, t) + \frac{\partial \mathbf{D}(\mathbf{r}, t)}{\partial t}.
 \end{aligned} \tag{1.1}$$

These equations couple four macroscopic fields: the dielectric displacement $\mathbf{D}(\mathbf{r}, t)$, the electric field $\mathbf{E}(\mathbf{r}, t)$, the magnetic field $\mathbf{H}(\mathbf{r}, t)$, and the magnetic induction $\mathbf{B}(\mathbf{r}, t)$. The symbols $\rho_{\text{ext}}(\mathbf{r}, t)$ and $\mathbf{J}_{\text{ext}}(\mathbf{r}, t)$ stand for external charge and current density in the medium where the electromagnetic field propagate. The symbols \mathbf{r} and t indicate the position vector in space and time, respectively. The polarization $\mathbf{P}(\mathbf{r}, t)$ and magnetization $\mathbf{M}(\mathbf{r}, t)$ of the medium link to the Maxwell equations:

$$\begin{aligned}
 \mathbf{D}(\mathbf{r}, t) &= \epsilon_0 \mathbf{E}(\mathbf{r}, t) + \mathbf{P}(\mathbf{r}, t), \\
 \mathbf{H}(\mathbf{r}, t) &= \frac{1}{\mu_0} \mathbf{B}(\mathbf{r}, t) - \mathbf{M}(\mathbf{r}, t),
 \end{aligned} \tag{1.2}$$

where ϵ_0 and μ_0 are the electric permittivity and magnetic permeability of vacuum, respectively.

By considering linear interaction with isotropic media and utilizing Fourier trans-

form $\int dt \exp^{-i\omega t}$ the constitutive relations can be written as:

$$\begin{aligned}\mathbf{D}(\mathbf{r}, \omega) &= \epsilon_0 \epsilon(\omega) \mathbf{E}(\mathbf{r}, \omega), \\ \mathbf{B}(\mathbf{r}, \omega) &= \mu_0 \mu(\omega) \mathbf{H}(\mathbf{r}, \omega),\end{aligned}\tag{1.3}$$

where $\epsilon(\omega)$ is the relative permittivity and $\mu(\omega)$ is relative permeability of the medium. The relative permeability of a nonmagnetic medium is $\mu = 1$.

The dielectric susceptibility $\chi(\omega)$ shows the linear relationship between $\mathbf{P}(\mathbf{r}, \omega)$ and $\mathbf{E}(\mathbf{r}, \omega)$.

$$\mathbf{P}(\mathbf{r}, \omega) = \epsilon_0 \chi(\omega) \mathbf{E}(\mathbf{r}, \omega).\tag{1.4}$$

By combining equations 1.2 and 1.4, the relation of relative permittivity and susceptibility can be found in the form $\epsilon(\omega) = 1 + \chi(\omega)$. The relationship between internal current density $\mathbf{J}(\mathbf{r}, \omega)$ and electric field $\mathbf{E}(\mathbf{r}, \omega)$ is defined as:

$$\mathbf{J}(\mathbf{r}, \omega) = \sigma(\omega) \mathbf{E}(\mathbf{r}, \omega).\tag{1.5}$$

The relative permittivity and conductivity relate to each other as below:

$$\epsilon(\omega) = 1 + \frac{i\sigma(\omega)}{\epsilon_0\omega},\tag{1.6}$$

where i is the imaginary unit. At low frequencies, relative permittivity describes how bound charges respond to a driving field, resulting in an electric polarization, while conductivity describes how free charges contribute to current flow. At optical frequencies, the distinction between bound and free charges becomes less clearly differentiated.

1.2.2 The dielectric function of free electron gas

As we will explain below, the key materials hosting surface plasmon polaritons and, hence, the materials crucial for this dissertation are metals. The optical properties of metals are explained by the plasma model for electrons over a wide frequency range. In the plasma model, details of the crystal lattice potential and electron-electron interactions are neglected, resulting in a description of a quasi-free electron gas. The equation of motion for electron plasma subject to external electric field $\mathbf{E}(t)$ is given by:

$$m\ddot{\mathbf{x}}(t) + m\gamma_e \dot{\mathbf{x}}(t) = -e\mathbf{E}(t),\tag{1.7}$$

where $\gamma_e = 1/\tau$ is a damping rate of the electronic motion, τ is the relaxation time of the free electron gas, m is effective optical mass of an electron, e stands for the elementary charge, and $\mathbf{x}(t)$ is the displacement vector of the electrons in

free electron gas[22]. Here, we consider electromagnetic fields that vary weakly in position; hence, for clarity in this section, we drop the position argument. We assume a harmonic time dependence $\mathbf{E}(t) = \mathbf{E}_0 e^{-i\omega t}$ of the driving field and seek solutions in the form $\mathbf{x}(t) = \mathbf{x}_0 e^{-i\omega t}$. The response becomes:

$$\mathbf{x}(t) = \frac{e}{m(\omega^2 + i\gamma_e\omega)} \mathbf{E}(t). \quad (1.8)$$

The material polarization directly follows the electronic oscillations $\mathbf{P}(t) = -ne\mathbf{x}(t)$, where e and n represent the charge of electrons and number density of free electrons:

$$\mathbf{P}(t) = -\frac{ne^2}{m(\omega^2 + i\gamma_e\omega)} \mathbf{E}(t). \quad (1.9)$$

Using Eq.1.2, the dielectric displacement is written in the form:

$$\mathbf{D}(t) = \epsilon_0 \left(1 - \frac{\omega_p^2}{(\omega^2 + i\gamma_e\omega)}\right) \mathbf{E}(t), \quad (1.10)$$

where $\omega_p^2 = \frac{ne^2}{\epsilon_0 m}$ is the plasma frequency of the free electron gas. The dielectric function of the free electron gas can be identified as:

$$\epsilon(\omega) = 1 - \frac{\omega_p^2}{\omega^2 + i\gamma_e\omega}. \quad (1.11)$$

It is a complex dielectric function $\epsilon(\omega) = \epsilon_1(\omega) + i\epsilon_2(\omega)$. In noble metals in highly polarized environments, the dielectric function is often assumed in a modified form to support bound electrons and other high-frequency process that is not supported in Eq.1.11.

$$\epsilon(\omega) = \epsilon_\infty - \frac{\omega_p^2}{\omega^2 + i\gamma_e\omega}, \quad (1.12)$$

where ϵ_∞ is a high-frequency dielectric constant. The dielectric function of the free electron gas is commonly referred to as the Drude model of the optical response of metals. Fits of the Drude model to experimentally measure dispersive dielectric permittivities of metals have been applied in the articles[19, 20, 18, 21] contributing to this thesis.

1.2.3 Surface plasmon polaritons

We now describe specific solutions to Maxwell's equations that can be found at the interface of metallic and dielectric materials: Surface plasmon polaritons (SPPs) and localized surface plasmon resonances (LSPRs) describe two fundamental phe-

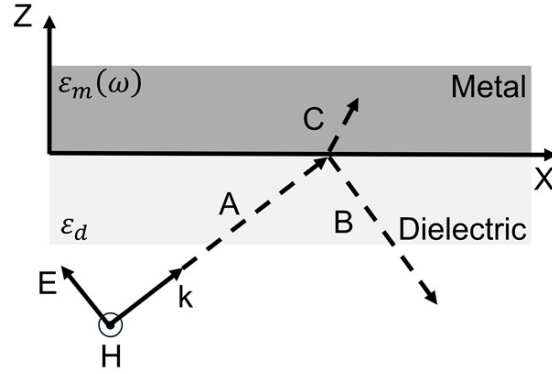


Figure 1.1: Schematic diagram of a TM wave incident on a metal-dielectric interface.

phenomena in the field of plasmonics. SPPs are electromagnetic waves that travel along the metal-dielectric interface. In contrast, LSPRs occur in metallic nanoparticles, where conduction electrons resonate in response to incident light. In this subsection, we briefly introduce the SPPs, while LSPRs, being the focus of my work, are investigated in detail in the following subsection.

Consider an interface between two semi-finite, isotropic and homogeneous media and complex dielectric permittivity $\epsilon(\omega) = \epsilon_r(\omega) + i\epsilon_i(\omega)$, where ϵ_r and ϵ_i represent the real and imaginary parts, respectively. When an electromagnetic wave travels through a polarizable medium, it couples with the induced polarization, forming hybrid modes called surface plasmon polaritons. The associated electromagnetic fields are bound to the surface and decay exponentially in the normal direction.

Let us consider a transverse magnetic mode (TM) of electromagnetic wave at a metal-dielectric interface. We introduce ϵ_d as the dielectric permittivity and ϵ_m as a complex dielectric permittivity of the metal layer. The incident wave propagates at the interface: We define the propagation direction as x , and the direction normal to the interface as z . Then, the associated wavevector can be written as $\mathbf{k} = (k_x, 0, k_z)$. The incoming, reflected, and transmitted waves are shown in Fig.1.1 as A, B, and C, respectively. The fields near the surface are expressed as [22]:

$$\begin{aligned} \mathbf{E} &= [E_x, 0, E_z] \exp^{i(k_x x + k_z z)}, \\ \mathbf{H} &= [0, H_y, 0] \exp^{i(k_x x + k_z z)}. \end{aligned} \quad (1.13)$$

Note that we drop the time dependence of the fields in this section, which is assumed harmonic at the frequency ω . The electric field components can be written as:

$$\begin{aligned} E_x(z) &= \frac{k_z}{\omega \epsilon_0 \epsilon} H_y(z), \\ E_z(z) &= \frac{-k_x}{\omega \epsilon_0 \epsilon} H_y(z). \end{aligned} \quad (1.14)$$

The magnetic and electric fields are investigated in two split areas: Dielectric area ($z < 0$) is medium (1), and metal area ($z > 0$) is medium (2), as denoted by the subscript.

$$\begin{aligned}
 H_{y1} &= A \exp^{-i(k_{x1}x - k_{z1}z)} + B \exp^{-i(k_{z1}z + k_{x1}x)}, \\
 E_{x1} &= \frac{k_{z1}}{\omega \epsilon_0 \epsilon_d} [A \exp^{-i(k_{x1}x + k_{z1}z)} - B \exp^{-i(k_{z1}z + k_{x1}x)}], \\
 E_{z1} &= \frac{-k_{x1}}{\omega \epsilon_0 \epsilon_d} [A \exp^{-i(k_{x1}x + k_{z1}z)} + B \exp^{-i(k_{z1}z + k_{x1}x)}],
 \end{aligned} \tag{1.15}$$

where the symbols A and B are amplitudes of the incident and reflected waves, respectively. The fields in medium (2) are represented as:

$$\begin{aligned}
 H_{y2} &= C \exp^{-i(k_{x2}x - k_{z2}z)}, \\
 E_{x2} &= \frac{k_{z2}}{\omega \epsilon_0 \epsilon_m} C \exp^{-i(k_{x2}x + k_{z2}z)}, \\
 E_{z2} &= \frac{-k_{x2}}{\omega \epsilon_0 \epsilon_m} C \exp^{-i(k_{x2}x + k_{z2}z)},
 \end{aligned} \tag{1.16}$$

where the symbol C is the amplitude of the transmitted wave. Continuity of H_y and E_x at the interface requires $B = C$ as follows:

$$-\frac{k_{z1}}{\epsilon_d} = \frac{k_{z2}}{\epsilon_m}, \tag{1.17}$$

that describe the dispersion relation of surface plasmon polaritons. The wavenumbers depend on surrounding media are formulated as:

$$\begin{aligned}
 k_x^2 + k_{z1}^2 &= \epsilon_d k_0^2, \\
 k_x^2 + k_{z2}^2 &= \epsilon_m k_0^2.
 \end{aligned} \tag{1.18}$$

The dispersion relation of surface plasmon in the metal-dielectric interface is therefore given by:

$$k_x^2 = \frac{\epsilon_d \epsilon_m}{\epsilon_d + \epsilon_m} k_0^2, \tag{1.19}$$

where c is the speed of light in vacuum. The normal component is expressed as:

$$k_{zj}^2 = \frac{\epsilon_j^2}{\epsilon_d + \epsilon_m} k_0^2, \quad j = 1, 2 \tag{1.20}$$

where $\epsilon_j = \epsilon_m, \epsilon_d$. From Eq.1.20, by considering $\text{Im}(\epsilon_m) \ll \text{Re}(\epsilon_m)$, we find solutions of the form of waves propagating along the surface with real k_x and imaginary k_z components, which requires that one of the permittivities must be negative and have absolute value bigger than the other – the condition that is fulfilled at the metal-dielectric interface. In the metal, the permittivity has a negative real part, which yields a material resonance in the dispersion relation when $\epsilon_m + \epsilon_d \approx 0$. In an ideal

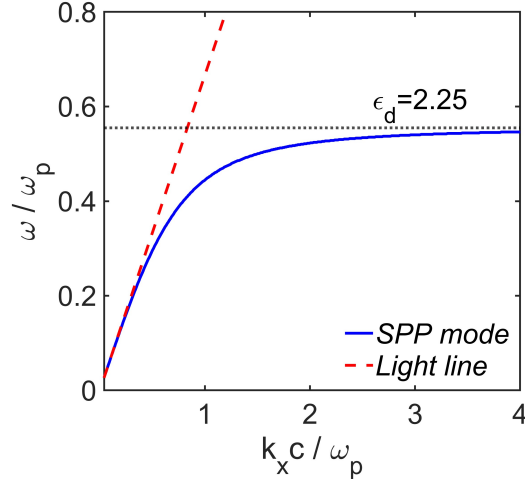


Figure 1.2: Dispersion of SPPs at a dielectric-metal interface. The assumed parameters are $\omega_p = 12 \times 10^{15} \text{ s}^{-1}$ and $\epsilon_d = 2.25$.

lossless metal case, the permittivity in Eq.1.11 is expressed as:

$$\epsilon_m(\omega) = 1 - \frac{\omega_p^2}{\omega^2}. \quad (1.21)$$

The corresponding dispersion curve is illustrated in Fig.1.2. The requirement that k_{zj} be imaginary in order that the electromagnetic field of SPPs decay exponentially into the dielectric-metal media. The SPPs exhibit a dispersion relationship that is positioned to the right side of the dispersion of light in the dielectric medium. This positioning indicates that SPPs are bound to the interface between the dielectric and metal, effectively preventing them from radiating into the surrounding dielectric medium. As a consequence, conventional illumination methods from the adjacent dielectric medium are insufficient to excite SPPs directly.

1.2.4 Localized surface plasmon resonance

Localized surface plasmon resonances (LSPRs) are associated with SPPs confined to surfaces of metallic nanoparticles, typically smaller than the light wavelength. The corresponding confinement of electromagnetic fields leads to their amplification near the nanoparticle surface. In practice, one can excite LSPRs directly with a plane-wave illumination, while special care needs to be required to fulfill the phase-matching condition for exciting SPPs in planar geometries.

To understand the physics behind the LSPRs resonances, we consider a metal nanoparticle of radius a submerged in a static electric field, as depicted in Fig. 1.3. In this case, the polarizability α of the particle can be described as [23, 22]:

$$\alpha = 4\pi a^3 \frac{\epsilon_m - \epsilon_d}{\epsilon_m + 2\epsilon_d}. \quad (1.22)$$

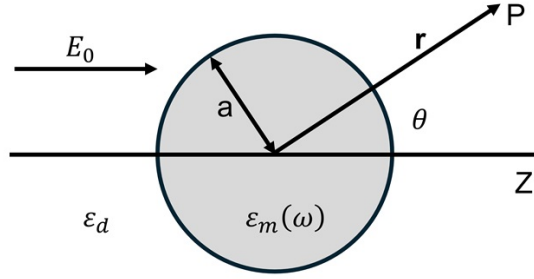


Figure 1.3: Diagram of sphere in electrostatic field $\mathbf{E} = E_0\mathbf{z}$. The radius is a , and θ is an angle between the position vector \mathbf{r} at point P and the z -axis. Figure reproduced following Ref.[1].

The dielectric constants ϵ_m, ϵ_d describe the metallic material of the sphere and the surrounding dielectric, respectively.

By using the Laplace equation to calculate the electric field in azimuthal symmetry and analysis of the boundary conditions at $r \rightarrow \infty$ and $r = a$, the interaction potentials in- and outside the sphere can be formulated as[23, 22]:

$$\begin{aligned}\Phi_{in} &= -\frac{3\epsilon_d}{\epsilon_m + 2\epsilon_d}E_0r \cos(\theta), \\ \Phi_{out} &= -E_0r \cos(\theta) + \frac{\mathbf{p} \cdot \mathbf{r}}{4\pi r^3},\end{aligned}\tag{1.23}$$

where in Φ_{out} , we include the contributions from the applied field and the dipole $\mathbf{p} = \epsilon_0\epsilon_d\alpha\mathbf{E}_0$ induced at the particle center, which we assume polarized along the z axis $\mathbf{E}_0 = E_0\hat{\mathbf{z}}$. The symbol θ is the angle between the position vector \mathbf{r} at point P in Fig. 1.3 and the z -axis.

The field distribution $\mathbf{E} = -\nabla\Phi$ evaluated inside and outside the sphere from Eq.1.23, becomes [22]:

$$\begin{aligned}\mathbf{E}_{in} &= \frac{3\epsilon_d}{\epsilon_m + 2\epsilon_d}\mathbf{E}_0, \\ \mathbf{E}_{out} &= \mathbf{E}_0 + \frac{3\mathbf{n}(\mathbf{n} \cdot \mathbf{p}) - \mathbf{p}}{4\pi\epsilon_0\epsilon_d} \frac{1}{r^3},\end{aligned}\tag{1.24}$$

where \mathbf{n} is the unit vector in the direction of point P. We now consider illumination with a time-harmonic field in the form of a plane wave $\mathbf{E}_0(\mathbf{r}, t) = \mathbf{E}_0(\mathbf{r})e^{-i\omega t} \approx \mathbf{E}_0e^{-i\omega t}$, where we have performed the quasistatic approximation assuming that $\lambda \ll a$, and the field around the particle can be treated as constant. The field induces an oscillating dipole moment $\mathbf{p}(t) = \epsilon_0\epsilon_d\alpha\mathbf{E}_0e^{-i\omega t} \equiv \mathbf{p}e^{-i\omega t}$, being the source of induced electric and magnetic fields. The total fields take the forms $\mathbf{E}(\mathbf{r})e^{-i\omega t}$,

$\mathbf{H}(\mathbf{r})e^{-i\omega t}$ with the distributions[22, 23]:

$$\begin{aligned}\mathbf{H}(\mathbf{r}) &= \frac{ck^2}{4\pi}(\mathbf{n} \times \mathbf{p})\frac{e^{ikr}}{r}\left(1 - \frac{1}{ikr}\right), \\ \mathbf{E}(\mathbf{r}) &= \frac{1}{4\pi\epsilon_0\epsilon_d}\left\{k^2(\mathbf{n} \times \mathbf{p}) \times \mathbf{n}\frac{e^{ikr}}{r} + [3\mathbf{n}(\mathbf{n} \cdot \mathbf{p}) - \mathbf{p}]\left(\frac{1}{r^3} - \frac{ik}{r^2}\right)e^{ikr}\right\}.\end{aligned}\quad (1.25)$$

Here, k is the wavenumber in the surrounding dielectric. In the near zone ($kr \ll 1$), the Eq.(1.25) can be written as:

$$\begin{aligned}\mathbf{H} &= \frac{ick}{4\pi}(\mathbf{n} \times \mathbf{p})\frac{1}{r^2}, \\ \mathbf{E} &= \frac{3\mathbf{n}(\mathbf{n} \cdot \mathbf{p}) - \mathbf{p}}{4\pi\epsilon_0\epsilon_d}\frac{1}{r^3}.\end{aligned}\quad (1.26)$$

By considering the radiation zone with $kr \gg 1$, the dipole fields are represented by the spherical-harmonics:

$$\begin{aligned}\mathbf{H} &= \frac{ck^2}{4\pi}(\mathbf{n} \times \mathbf{p})\frac{e^{ikr}}{r}, \\ \mathbf{E} &= \sqrt{\frac{\mu_0}{\epsilon_0\epsilon_d}}\mathbf{H} \times \mathbf{n}.\end{aligned}\quad (1.27)$$

The near-field zone refers to the region close to the plasmonic nanostructure, typically within a distance less than the wavelength of the incident light, where the electromagnetic field exhibits strong electric field enhancements and rapidly decays with distance. Conversely, the far-field zone is the region at distances much greater than the wavelength of incident light, which is important for signal detection in experiments.

In my research, I have focused on designing nanoparticles with predefined near-field properties, which are key to tailoring light interactions with quantum atomic systems.

The far-field optical response of nanoparticles is usually characterized in terms of the scattering and absorption cross-sections. The scattering cross-section RCS and absorption cross-section ACS are expressed as [24]:

$$\begin{aligned}RCS &= \frac{k^4}{6\pi}|\alpha|^2 = \frac{8\pi}{3}k^4a^6\left|\frac{\epsilon_m - \epsilon_d}{\epsilon_m + 2\epsilon_d}\right|^2, \\ ACS &= k\text{Im}[\alpha] = 4\pi ka^3\text{Im}\left[\frac{\epsilon_m - \epsilon_d}{\epsilon_m + 2\epsilon_d}\right].\end{aligned}\quad (1.28)$$

As demonstrated in Eq.1.28 in small particle $a \ll \lambda$ the efficiency of scattering ($RCS \propto a^6$) is much larger than the efficiency of absorption ($ACS \propto a^3$). In addition, if Eq.1.28 meets the so-called Fröhlich condition $\text{Re}\{\epsilon_m(\omega)\} = -2\epsilon_d$, resonance enhancement occurs in the scattering and absorption cross-sections of the metallic

sphere.

In all the above equations, we consider the small particle that acts as an electric dipole. The absorption and scattering cross-sections are calculated under these circumstances. However, for larger particles, the quasi-static approximation is not justified because of the large phase change of the driving field over the particle volume. Describing their optical response requires a more complex electrodynamic approach, for example, the theory that Mie developed the theory of scattering and absorption in 1908 [25].

Mie theory provides an exact solution for the scattering and absorption of electromagnetic waves by a single spherical particle [25], and it has been later extended to take multiple spherical particles into account[26]. It decomposes the scattered field into a series of spherical harmonics, corresponding to different multipole moments, electric and magnetic, of the particle. Each harmonic represents an oscillating electromagnetic mode, with the total scattered field being the sum of these contributions.

This analytical theory elegantly and comprehensively covers spherical geometries. However, numerical methods are required for arbitrary geometries or larger particles where the phase change over the particle volume is significant. These methods, discussed in section (5), allow for the calculation of scattered field distributions, absorption, and scattering cross-sections for various nanoparticle geometries.

In this work, to ensure a fair comparison, all calculations are performed numerically using commercial software such as CST and COMSOL. The material utilized in this chapter is silver, based on experimental data[27]. Figure. 1.4(a) demonstrates

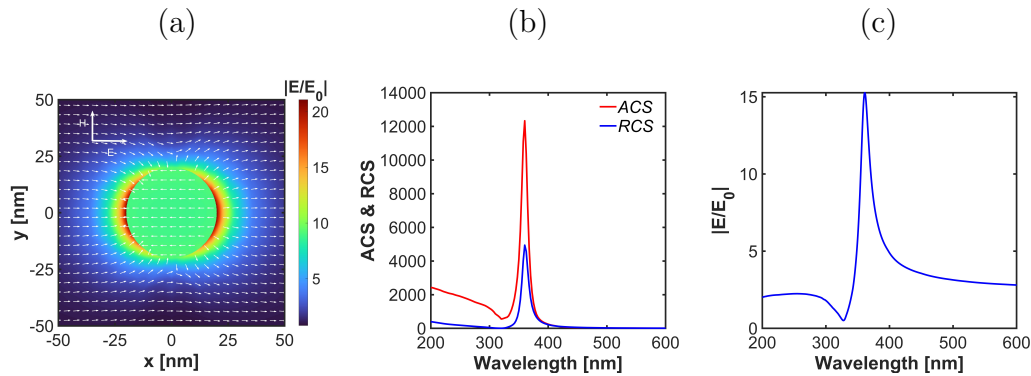


Figure 1.4: (a) Electric field enhancement distribution for resonant illumination at $\lambda_0 = 360$ nm, (b) absorption cross-section (ACS) and scattering cross-section (RCS), (c) electric field enhancement spectrum of a silver sphere with $a = 20$ nm.

electric field distribution with a silver sphere with radius $a = 20$ nm illuminated at the plasmonic resonance. The pattern shows a dipolar distribution around the sphere, which is characteristic of LSPR. The regions of high intensity occur near the surface of the sphere where the oscillating electrons are concentrated. We refer to

this region as a plasmonic hotspot. This hotspot will be the key to enhancing the optical phenomena that occur in molecules positioned at the vicinity of plasmonic nanoparticles, such as Purcell fluorescence enhancement[28], surface-enhanced Raman scattering[7], surface-enhanced coherent anti-Stokes Raman scattering[11, 18] or two-photon absorption[29, 30]. The scattering and absorption cross-sections of a single sphere plotted in Fig. 1.4(b) show resonance in $\lambda_0 = 360$ nm. The particle efficiency (PE) is defined as $PE = \frac{RCS}{RCS+ACS}$. This ratio indicates the proportion of scattering to the total light extinction, understood as the sum of absorption and scattering. A higher value of this ratio implies that the nanostructure mainly scatters light rather than absorbing it. By engineering the material properties, size, and shape of the particle, the particle's efficiency can be enhanced. The PE in a single sphere at the resonance peak is 0.2861. The absorption cross-section is greater than the scattering cross-section because of the small size of the sphere: the field can deeply penetrate the nanosphere's metallic bulk, where the absorption appears. In the next section, we introduce how much the size of particles affects the optical response.

Nanostructures with multiple nanoparticles can exhibit coupling effects between localized plasmons, leading to hybrid modes and altered resonance conditions. This coupling can be tuned by changing the spacing and arrangement of the nanoparticles, providing a way to engineer the optical response for specific applications. Here, we demonstrate the coupling of two silver spheres with $a = 20$ nm, and the gap size between them is $g = 10$ nm.

As demonstrated in Fig. 1.5(a), upon resonant illumination, the electric field in

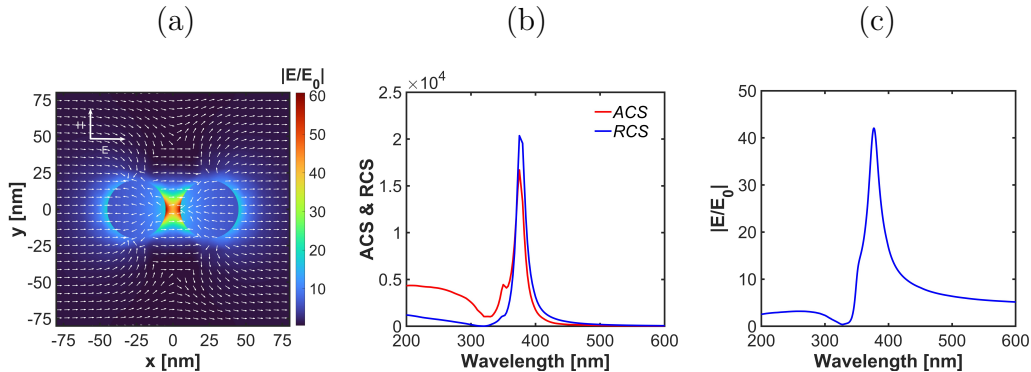


Figure 1.5: (a) Electric field distribution, (b) absorption cross-section and scattering cross-section, (c) electric field enhancement spectrum of two coupled silver spheres with $a = 20$ nm and $g = 10$ nm.

the gap is enhanced up to 60 times, which is three times more than the field around the single sphere. As shown in Fig. 1.5(b), the efficiency of the scattering cross-section is more than the absorption cross-section, and the efficiency of a couple of silver spheres is 0.5494 at the resonance peak, which is enhanced around two times

compared to a single nanosphere with the same size. The electric field enhancement spectrum is shown in Fig. 1.5(c).

1.2.5 Influence of geometry and size

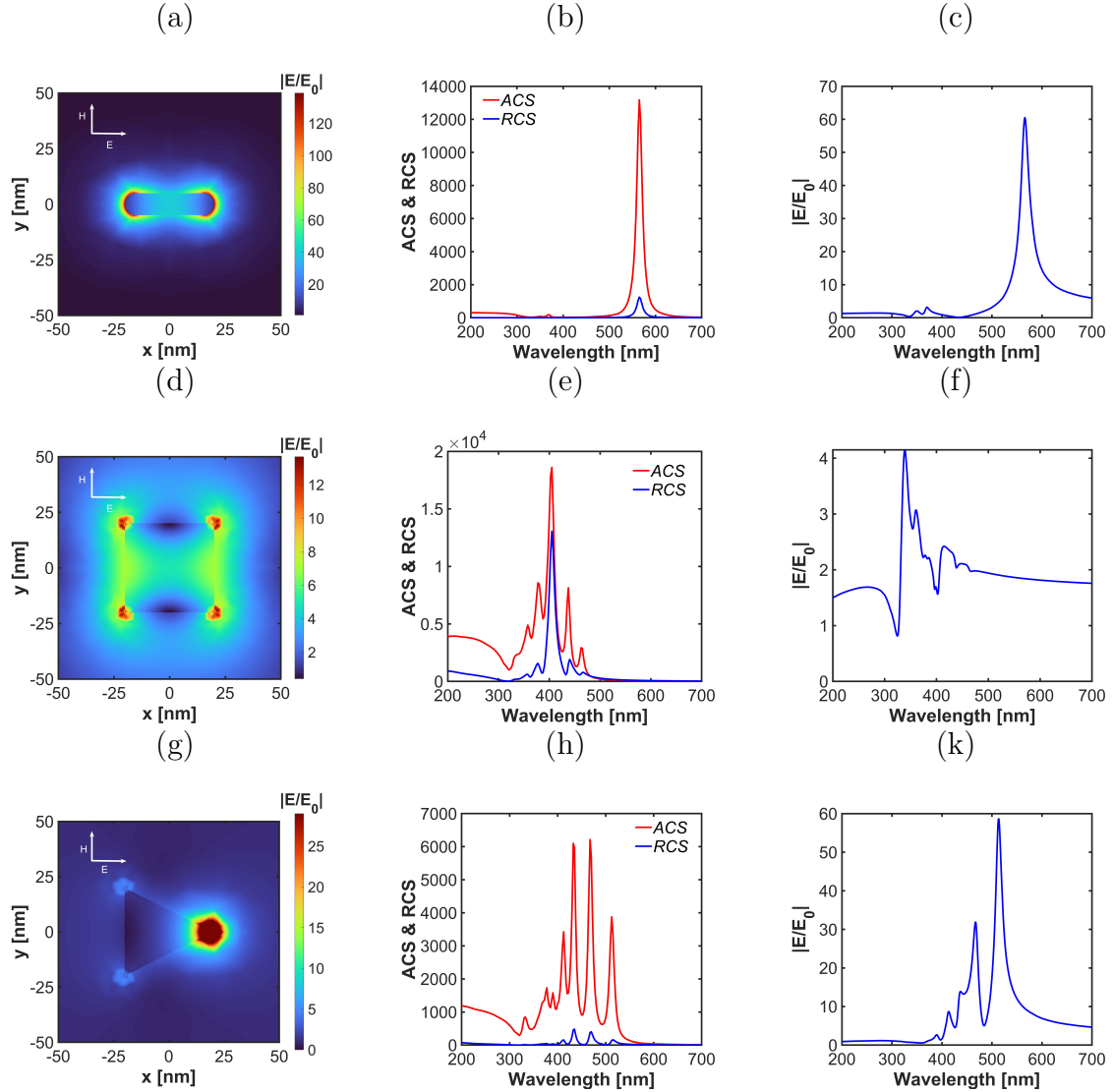


Figure 1.6: (a) Linear electric field distribution, (b) absorption cross-section (ACS) and scattering cross-section (RCS), (c) electric field enhancement spectrum of single silver nanorod with $l = 40$ nm and $a = 5$ nm at point (22.5 nm,0,0). (d) Linear electric field distribution, (e) absorption cross-section (ACS) and scattering cross-section (RCS), (f) electric field enhancement spectrum of single silver nanocubic with $l = 40$ nm at point (22.5 nm,0,0). (g) Linear electric field distribution, (h) absorption cross-section (ACS) and scattering cross-section (RCS), (i) electric field enhancement spectrum of single silver nanocone with $l = 40$ nm at point (22.5 nm,0,0).

As suggested by Eq. (1.22), the geometry of plasmonic nanoparticles significantly influences their optical properties and plasmonic behavior. Different shapes such as

spheres, rods, cubes, and more complex geometries exhibit different plasmonic characteristics due to variations in their surface charge distributions influencing their interactions with the electromagnetic field.

Here, we compare the results obtained for a nanosphere, nanorod, nanocube and nanocone. In all simulations for this part, the electric field polarization is along the x -axis, and the electric field spectrum is calculated at the position $\mathbf{r} = (22.5, 0, 0)$ nm, meaning there is a 2.5 nm space between the particle and the probing point. Field distributions are evaluated on resonance.

LSPR in spherical nanoparticles is largely determined by the uniform curvature of their surface. The resonance condition for spheres is simpler to model, with the dipole mode being dominant. This leads to a single prominent resonance peak, and an isotropic plasmonic response, meaning it does not vary with the direction of the incident light. Nanorods show anisotropic behavior, meaning that their response depends on incident light polarization. The optical response of a silver nanorod is presented in Fig. 1.6(a,b,c). The results for the nanocube and the nanocone are demonstrated in Fig. 1.6(d,e,f) and Fig. 1.6(g,h,k), respectively. They support multiple plasmonic modes with highly localized fields on the edges. So, by precisely tailoring the shape, we can enhance the optical response in different frequency regimes from near-infrared to visible.

The size of plasmonic nanoparticles also plays a crucial role in determining their

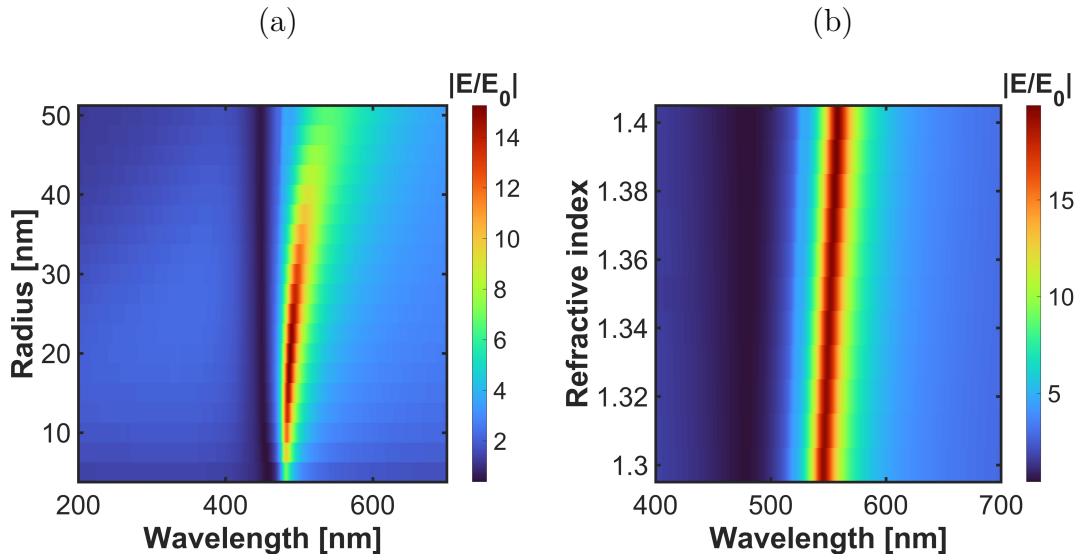


Figure 1.7: (a) Electric field enhancement varying by radius in single silver nanosphere, (b) Electric field enhancement varying by refractive index around the silver nanosphere.

resonance frequency and overall plasmonic properties. We investigate a single silver nanosphere with different radii, as shown in Fig. 1.7(a). As the size of the nanosphere is increased, a redshift appears in the spectral position of the plasmonic

resonance, and the loss increases, resulting in a broader resonance.

1.2.6 Influence of materials

As shown in Eq. 1.22 and Eq. 1.28, polarizability, scattering, and absorption cross-sections of plasmonic nanoparticles depend on the refractive index of the surrounding medium. Fig. 1.7(b) shows the electric field enhancement and resonance of silver nanosphere and how varying refractive indices shift the resonance. By increasing the refractive index of the medium around the nanosphere, a redshift appears in the spectral position of the plasmonic resonance. This feature makes plasmonic nanostructures good candidates for chemical and biosensors.

The other important parameter that affects the polarizability and scattering and absorption cross-section is the complex dielectric function of metal $\epsilon_m(\omega)$. Metals commonly used for fabrication of plasmonic nanostructures are silver, gold, aluminum, copper, and graphene. Silver and gold, being noble metals, support relatively high-quality resonances. In my work, I primarily used gold, silver, and graphene. Gold is one of the most widely used metals in plasmonics because it is chemically inert and highly resistant to oxidation and corrosion. This stability is advantageous for long-term plasmonic applications, especially in biological and medical contexts where biocompatibility is essential [31]. Silver has strongest plasmonic response in the visible and near-infrared regimes. The loss in silver is much smaller than in gold, and it has a narrower optical response compared to other noble metals. Silver oxidizes quickly, making its manufacturing and maintenance more challenging compared to gold [32].

Graphene is a two-dimensional monolayer of carbon with linear electronic dispersion, giving it unique properties such as high electron mobility and zero bandgap. The charge concentration in graphene can be adjusted rapidly through electrostatic gating [33]. Graphene monolayers exhibit strong mechanical properties [34] and high thermal conductivity [35]. The two-dimensional graphene conductivity $\sigma(\omega)$ is modeled with the Kubo formula[36] through its intra- and interband components [37]:

$$\sigma(\omega) = \sigma_{intra}(\omega) + \sigma_{inter}(\omega), \quad (1.29)$$

with the Drude model describing the intraband contribution accounting for the plasmonic response:

$$\sigma_{intra}(\omega) = \frac{2ie^2T}{\pi\hbar(\omega + iT^{-1})} \ln[2 \cosh(\frac{\mu_c}{2T})], \quad (1.30)$$

where \hbar is the reduced Planck constant, T is the electron temperature, and μ_c stands for the chemical potential tunable with the gate voltage. The interband contribution

is described by:

$$\sigma_{inter}(\omega) = \frac{e^2}{4\hbar} \left[G\left(\frac{\omega}{2}\right) - \frac{4\omega}{i\pi} \int_0^\infty \frac{G(\xi) - G\left(\frac{\omega}{2}\right)}{\omega^2 - 4\xi^2} d\xi \right]. \quad (1.31)$$

Here,

$$G(\xi) = \frac{\sinh\left(\frac{\xi}{T}\right)}{\cosh\left(\frac{\mu_c}{T}\right) + \cosh\left(\frac{\xi}{T}\right)}. \quad (1.32)$$

The dielectric function of graphene is given by [38]:

$$\epsilon(\omega) = 1 + \frac{i\sigma(\omega)}{\epsilon_0\omega t_g}, \quad (1.33)$$

where t_g is the graphene thickness, in practice assumed in numerical calculations as 1 nm.

The dielectric functions of gold [27], silver [27] and graphene [37] are shown in Fig.1.8 in visible and mid-infrared regimes. As shown in Fig.1.8(a,b), gold, compared to silver, has more loss and supports plasmons in longer wavelengths. Both support LSPRs in the visible regime. The dielectric function of graphene, shown in Fig.1.8(c), depends on the chemical potential and temperature. With $T = 300$ K, $\tau = 1$ ps, and $\mu_c = 0.45$ eV, graphene is metallic in the mid-infrared regime, where the real part of its dielectric function is negative $\text{Re}\{\epsilon(\omega)\} < 0$, and dielectric in the near-infrared and visible regimes, where $\text{Re}\{\epsilon(\omega)\} > 0$.

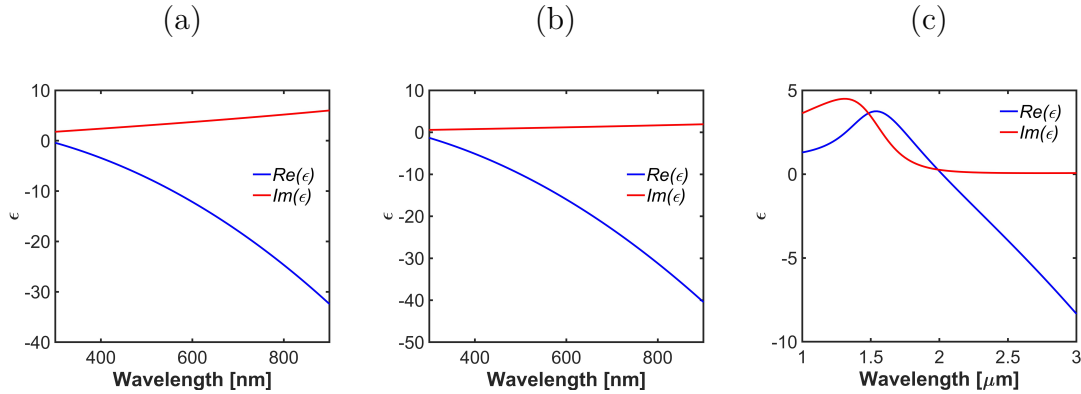


Figure 1.8: Dielectric functions of (a) gold, (b) silver, based Johnson and Christy experimental results[27], (c) graphene[37] for $T = 300$ K, $\tau = 1$ ps, and $\mu_c = 0.45$ eV.

1.2.7 Plasmonic metasurfaces and their optical properties

Plasmonic metasurfaces consist of arrays of plasmonic nanostructures, with unit cells much smaller than the wavelength of incident light. The metasurfaces collectively manipulate light over a large area, enabling control and engineer optical properties, including phase, amplitude and polarization[39]. Unlike individual nanoantennas,

metasurfaces offer broadband resonance, resulting from coupling of multiple resonant elements[40].

Fabricating individual nanoantennas presents greater challenges compared to the metasurfaces, due to the smaller size scale. Consequently, plasmonic metasurfaces offer broader range of functionality compared to individual nanoantennas. In this subsection, I present a perfect-absorber metasurface, as demonstrated by Liu and et al.[41], and compare its optical response with that of an individual nanoantenna. As shown in Fig.1.9, both the individual nanoantenna and metasurface exhibit similar resonance wavelength; however, the electric field enhancement is reduced in the metasurface, while the bandwidth is increased.

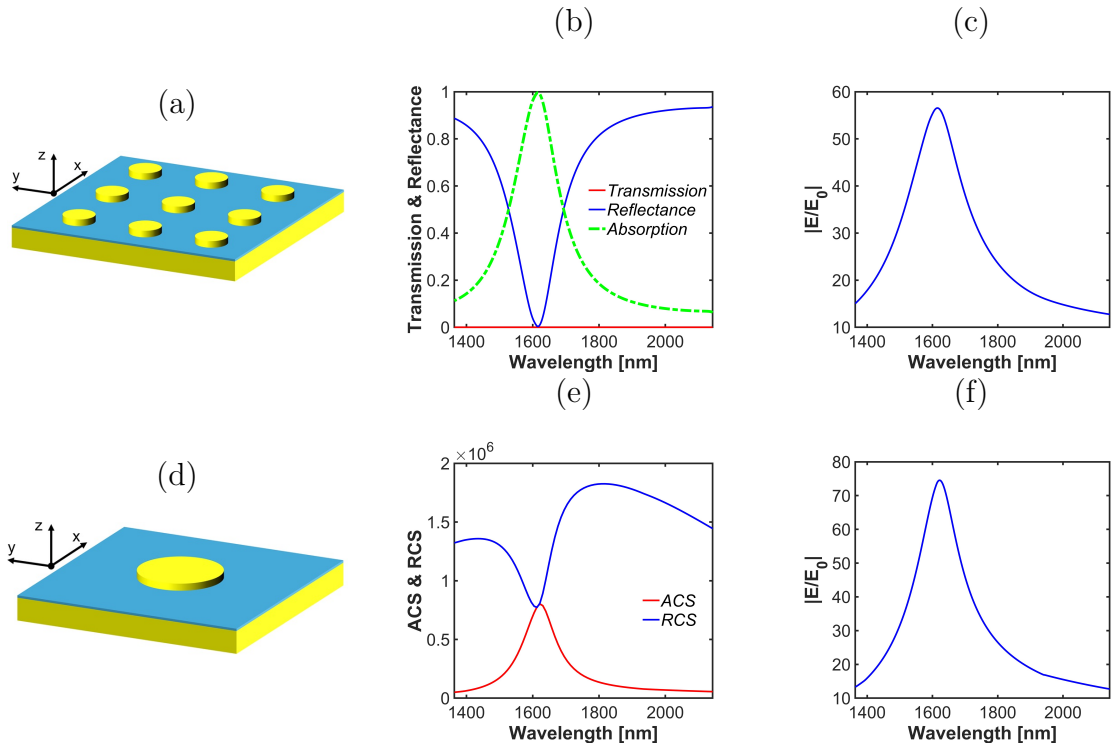


Figure 1.9: (a) Schematic of perfect absorber metasurface, (b) transmission, reflectance and absorption spectrum, (c) electric field enhancement spectrum at point (178.5 nm, 0, 0). (d) Schematic of perfect absorber nanoantenna, (e) absorption cross-section (ACS) and scattering cross-section (RCS), (f) electric field enhancement spectrum at point (178.5 nm, 0, 0). The gold disk diameter is 352 nm and the thickness is 20 nm. The periodicity is 600 nm and the spacer thickness is 30 nm. The thickness of gold film is 200 nm. Studied geometry follows Ref. [41].

1.3 Surface plasmon polaritons coupled to atomic system

From the previous section, we understand how plasmonic nanostructures can be used to control local electromagnetic fields. If atomic systems are positioned in such locally enhanced fields, their interaction strengths with light can be enhanced. In this section, we describe how an atomic system interacts with electromagnetic waves and investigate the effects of these interactions.

1.3.1 Interaction of plasmon-enhanced light and atomic systems

In this subsection, we investigate the interaction of the two-level atomic system and electromagnetic field. An atomic system can represent an atom, molecule, crystal lattice defect, quantum dot, etc., referred to as a quantum emitter in relevant literature. We investigate the basics of the theory of atomic systems to describe the dynamics of coupling of atomic systems with surface plasmons. The interaction

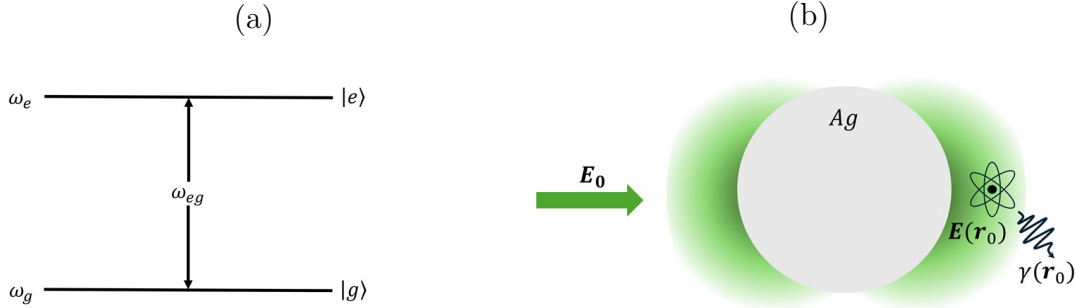


Figure 1.10: Diagram of (a) two-level system, (b) coupling of the plasmonic silver nanosphere to a two-level atomic system.

between the electromagnetic field and a two-level atomic system with the excited and ground states $|e\rangle$, $|g\rangle$ involves the excitation or de-excitation of the atom. These processes can usually be described in the electric dipole approximation, which is justified if the spatial field variations occur at size scales large with respect to the size of the atomic system. This approximation is commonly applied for plasmon-confined fields and was applied in my work. Extensions beyond the electric-dipole approximation have been discussed in literature[42, 43, 44, 45]. The interaction Hamiltonian is[46]

$$H = -\mathbf{E}(\mathbf{r}_0, t) \cdot \hat{\mathbf{d}}. \quad (1.34)$$

Here, \mathbf{r}_0 is the position of the atomic system, and $\hat{\mathbf{d}} = \sum_{i,j \in \{e,g\}} \mathbf{d}_{ij} |i\rangle \langle j|$ is the atomic dipole moment operator, with the transition ($i \neq j$) and permanent ($i = j$) elements

\mathbf{d}_{ij} . In many cases, it is enough to consider the transition elements $\mathbf{d}_{eg} = \mathbf{d}_{ge}^*$, which is assumed from now on in this section. However, in one of the articles that contribute to this thesis[20], we have exploited the permanent dipole elements for field frequency conversion. We now assume a harmonic time dependence of the field with the frequency ω : $\mathbf{E}(\mathbf{r}_0, t) = \mathbf{E}(\mathbf{r}_0) \cos \omega t$. Typically, rotating wave approximation is applied that allows to simplify the interaction Hamiltonian, that takes a time-independent form in the interaction picture:

$$H_{\text{int}} = -\mathbf{E}(\mathbf{r}_0) \cdot (\mathbf{d}_{eg}|e\rangle\langle g| + \mathbf{d}_{ge}|g\rangle\langle e|). \quad (1.35)$$

Note that this Hamiltonian explicitly accounts for the field in the atomic position that can be plasmon-enhanced.

In addition to the energy exchange between the atom and field subsystems, various dissipative processes can occur, such as the spontaneous emission from the atomic system, decoherence from collisions of the atomic systems with the surroundings, coupling of lattice defects with phonons, or decoherence due to optical pumping. These effects are incorporated into the master equation, which describes the evolution of the atomic system:

$$\dot{\rho} = -\frac{i}{\hbar}[H, \rho] + \mathcal{L}(\rho), \quad (1.36)$$

where \mathcal{L} is the Lindblad term that accounts for dissipation [47]. Plasmonic enhancement can influence both the electric field in the Hamiltonian and the spontaneous emission rate in the Lindblad term. The diagram of coupling plasmonic nanosphere to a two-level system is illustrated in Fig.1.10(b). Below, I discuss these two effects.

1.3.2 Purcell effect

The Purcell effect describes how the spontaneous emission rate of an atomic system changes based on the density of photonic states in the surrounding environment. Spontaneous emission occurs when an atomic system interacts with a continuum of electromagnetic modes, usually in the vacuum state, transferring the energy of the excited atomic system to the electromagnetic field, resulting in the exponential decay of the excited state population. The decay is quantitatively described by the spontaneous emission rate, which in the electric-dipole approximation is expressed as[48]:

$$\gamma = \frac{\pi\omega_{eg}}{\hbar\epsilon_0} |\mathbf{d}_{eg}|^2 \varrho(\mathbf{r}_0, \omega_{eg}), \quad (1.37)$$

where ω_{eg} is the frequency of atomic transition, and $\varrho(\mathbf{r}_0, \omega_{eg})$ is the local density of photonic states at position \mathbf{r}_0 at the transition frequency. The above formula can be derived by quantizing the thermal electromagnetic environment and assuming the Markovian approximation, which applies if the interaction with the surroundings is

weak enough. In free space, the density of states takes the form $\varrho = \frac{1}{3\pi^2c^3} \times \omega_{eg}^2$, leading to the well-known Weisskopf-Wigner rate[48]. It is important for the works contributing to this dissertation that the photonic density of states depends on the dispersive properties and geometry of the environment: It is different in free space and in a dielectric, it takes oscillatory position dependence near a mirror[49, 50], and it can be modified with plasmonic nanostructures. The first observation of this phenomenon was made by Purcell in his seminal works in cavities[51], hence, it is known today as Purcell effect.

Remarkably, the electromagnetic density of states and thus, the spontaneous emission rate, can be found by solving the classical Maxwell's equations. To this end, we model the atomic transition as a classical dipole whose power depends on the dispersion properties and geometry of the environment. The spontaneous emission enhancement can then be evaluated as the ratio of total dipole powers near the nanoparticle $P(\mathbf{r}_0, \omega)$ and in free space $P_0(\omega)$, as proposed in Ref.[3]:

$$\gamma = \gamma_0 \frac{P(\mathbf{r}_0, \omega)}{P_0(\omega)}, \quad (1.38)$$

where γ_0 is the spontaneous emission rate in free space. Note that the Purcell enhancement depends on the position of the dipole, representing the atomic system, with respect to the nanoparticle.

The details of the calculation of the dipole power are provided in the section 1.5.3.

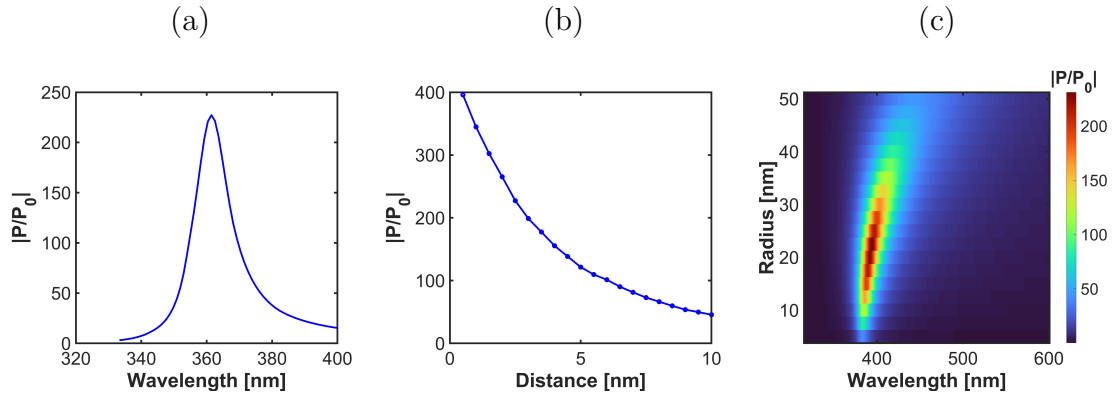


Figure 1.11: (a) Radiated power ratios of a single silver nanosphere with radius $a = 20$ nm as functions of free-space wavelength of the radiation emitted by a dipole source situated 2.5 nm from the sphere surface; (b) radiated power resonance peak amplitude and (c) radiated power spectra as functions of distance of dipole source from the nanosphere.

For demonstration, the Purcell factor of the silver nanosphere is calculated based on Eq.1.38 and shown in Fig.1.11(a) upon illumination with the dipole oriented perpendicularly to the nanosphere surface. The sphere exhibits a resonance peak at 365 nm. In my works, the geometry and material compositions of nanostructures were

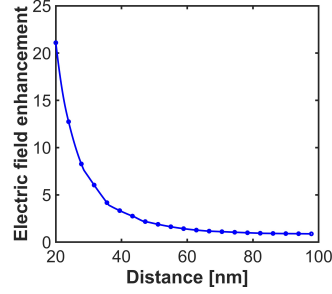


Figure 1.12: Varying electric field enhancement via distance from the surface of a silver nanosphere with the radius $a = 20$ nm.

optimized to tune the plasmonic resonance of nanoparticles to match the transition frequency of the atomic system. The relationship between the Purcell factor of the silver nanosphere and distance is shown in Fig.1.11(b). By varying the nanosphere radius, the Purcell factor can be tuned, as shown in Fig.1.11(c).

1.3.3 Near-field interaction with atomic systems

To discuss the impact of nanoparticles on the atomic systems' dynamics, we recall the light-matter interaction Hamiltonian in Eq. (1.35), where the interaction strength is proportional to the electric field amplitude at the atomic system's position. In the lowest perturbation order, this Hamiltonian describes excitation of an atomic system prepared in its ground state. According to the Fermi's golden rule, the transition rate scales with the square of the transition element of the Hamiltonian[52, 3]. The transition rate enhancement becomes therefore[53]:

$$\frac{\gamma_{exc}}{\gamma_{exc}^0} = \left| \frac{E(\mathbf{r}_0, \omega)}{E_0(\mathbf{r}_0, \omega)} \right|^2, \quad (1.39)$$

where γ_{exc}^0 is the excitation rate in free space, γ_{exc} is the excitation rate near the plasmonic nanostructure. We find that the excitation rate scales quadratically with the field enhancement factor $\left| \frac{E(\mathbf{r}_0, \omega)}{E_0(\mathbf{r}_0, \omega)} \right|$ evaluated at the atomic system's position at the illumination frequency.

LSPRs result in strong near-field enhancement due to their ability to confine electromagnetic fields at the nanoscale. Near the LSPR, the electric field is enhanced in this case by an order of magnitude. Figure.1.12 illustrates the relationship between electric field enhancement and the distance from the surface of the silver nanosphere. A closer distance to the surface of the metallic nanostructure supports stronger interaction. Thus, the distance plays a key role in the coupling strength between the plasmonic nanostructure and the atomic system.

1.4 Nonlinear optical phenomena

Nonlinear optics is at the heart of the study of light-matter interactions. When light interacts with materials possessing nonlinear optical properties, its properties are altered, producing new field components with different phases, frequencies, amplitudes, polarizations, and propagation directions.

Nonlinear optical materials have potential applications in advanced devices such as optical signal processors[54], optical switches[55], frequency generators[56] or optical parametric oscillators[57]. Processes that occur in nonlinear materials include harmonic generation[58], frequency mixing[59], and Raman scattering[7]. Additionally, nonlinear optical materials play a key role in fields like optical data storage[60], optical communication[61], image processing[62], and may be important for the future development of optical computing[63]. These applications highlight the importance of nonlinear optics in advancing optical technologies and expanding the capabilities of optical systems.

In the articles that contribute to this dissertation, I focused on nonlinear light-matter interaction scenarios, in which the presence of atomic systems near nanoparticles unlocks frequency conversion. As a result, a signal is generated in a background-free scheme, that signalizes of the occurrence of the considered process. Below, I introduce the nonlinear phenomena that were investigated.

1.4.1 Surface enhanced Raman scattering

Raman scattering is the phenomenon at the heart of a group of spectroscopic techniques. Discovered in 1928 by C. V. Raman, it is used to determine the vibrational frequencies of molecules. Raman spectroscopy is widely used in physics and chemistry. In the basic scenario of stimulated Raman scattering, incident pump beam of light interacts with the molecule exciting its vibrations, and the difference between an incident photon energy and the vibrational energy is carried away by a photon of a different frequency. In the so-called Stokes process, the emitted light has a lower, and in the anti-Stokes – a higher frequency. The free-space scattering cross-section for this process is relatively weak due to its nonlinear character. The diagram of Raman scattering is illustrated in Fig. 1.13(a), including Stokes and anti-Stokes Raman scattering with red and blue arrows, respectively.

Surface-enhanced Raman scattering (SERS) occurs when the molecule is positioned near a plasmonic nanostructure. In this process, the Raman signal is enhanced due to the highly localized electric field. In the SERS mechanism, the excitation process can occur at a rate improved by the squared field enhancement factor, according to Eq. (1.39). The spontaneous (anti-)Stokes emission process can be enhanced in the

Purcell mechanism, according to Eq. 1.38. The total signal enhancement in SERS is defined as:

$$I_{SERS} = \left| \frac{E(\mathbf{r}_0, \omega_p)}{E_0(\mathbf{r}_0, \omega_p)} \right|^2 \times \frac{P(\mathbf{r}_0, \omega_{S,aS})}{P_0(\mathbf{r}_0, \omega_{S,aS})}, \quad (1.40)$$

where $\omega_{p,S,aS}$ stand for the pump, Stokes and anti-Stokes frequencies. Several nanos-

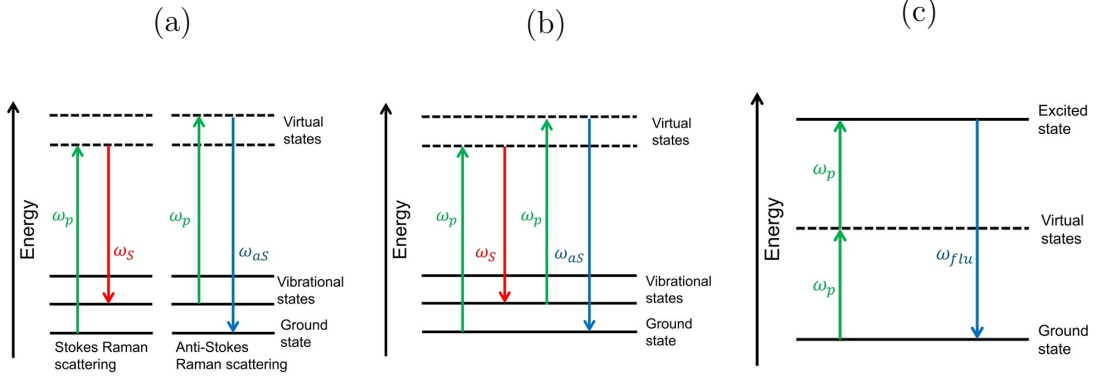


Figure 1.13: Energy level diagram of (a) Raman scattering including Stokes and anti-Stokes Raman scattering, (b) coherent anti-Stokes Raman scattering, (c) two-photon absorption process with a following single-photon fluorescence.

structure geometries have been used to modify the signal enhancement in SERS, including plasmonic nanoparticles [64], nanoshells [65], gap structures [66] and scanning tunnelling microscope tips [67].

1.4.2 Coherent anti-Stokes Raman scattering

Coherent anti-Stokes Raman scattering (CARS) is a nonlinear four-wave mixing process that has a higher sensitivity compared to Raman scattering. CARS is a third-order nonlinear effect where three photons, including two pumps and one Stokes photon, interact coherently through the third-order susceptibility of materials and emit an anti-Stokes photon. The diagram of CARS is illustrated in Fig. 1.13(b). The energy conservation requires that $\omega_{aS} = 2\omega_p - \omega_S$. The CARS signal is low when monitoring the molecule in low concentration[68]. Employing plasmonic nanostructures is a useful method to enhance the signal of CARS[11]. Plasmonic nanoparticles can be used to enhance CARS signal. Yet, it is challenging to design a particle that would support resonances covering the pump, Stokes, and anti-Stokes frequencies. To overcome this challenge, different plasmonic structures supporting broadband response[18] or multiple sharper resonances[19] were employed. The studied geometries include multiple coupled nanoparticles [11], gold surface[9], an atomic-force microscope tip [10], and nanohole-slit arrays[69].

My calculations were performed under the assumption that the excitation and emission enhancements can be treated separately. The transition enhancement in CARS

driven by enhanced pump and Stokes beams can be expressed as a product of enhancement factors from Eq.(1.39)[18]:

$$\frac{\gamma_{exc}}{\gamma_{exc}^0} = \left| \frac{E(\mathbf{r}_0, \omega_p)}{E_0(\mathbf{r}_0, \omega_p)} \right|^4 \left| \frac{E(\mathbf{r}_0, \omega_S)}{E_0(\mathbf{r}_0, \omega_S)} \right|^2, \quad (1.41)$$

where $E(\mathbf{r}_0, \omega_{p,S})$ and $E_0(\mathbf{r}_0, \omega_{p,S})$ are the electric field amplitudes at the pump and Stokes frequency near the plasmonic nanostructure and in free space, respectively. The anti-Stokes emission has its source in the induced dipole moment in the anti-Stokes transition, hence, its enhancement can be modeled as the dipole power ratio according to Eq.(1.38):

$$\frac{\gamma_{emi}}{\gamma_{emi}^0} = \frac{P(\mathbf{r}_0, \omega_{aS})}{P_0(\omega_{aS})}. \quad (1.42)$$

The resulting signal enhancement in surface-enhanced CARS (SECARS) can be written as:

$$I_{SECARS} = \left| \frac{E(\mathbf{r}_0, \omega_p)}{E_0(\mathbf{r}_0, \omega_p)} \right|^4 \times \left| \frac{E(\mathbf{r}_0, \omega_S)}{E_0(\mathbf{r}_0, \omega_S)} \right|^2 \times \frac{P(\mathbf{r}_0, \omega_{aS})}{P_0(\omega_{aS})}. \quad (1.43)$$

In my works, I have shown that nanostructure designs sustaining a broad optical response can show better performance than structures tailored to three individual resonances [19, 18]. Moreover, I have demonstrated that the spectrally broad design can be used to enhance the Raman signal for many molecular species in a relatively broad range of Raman shifts.

1.4.3 Two-photon absorption

Two-photon absorption (TPA) is a nonlinear optical process where two photons simultaneously interact with a molecule, exciting it from the ground state to the first excited state, and then the molecule emits a photon as it returns to the ground state, producing fluorescence. The absorption cross-section for this second-order nonlinear process in the molecules is low, requiring high-intensity lasers to overcome the low absorption cross-section. The energy level diagram of TPA is illustrated in Fig. 1.13(c). Enhancing TPA with plasmonic nanostructures presents a challenge due to the need for two distinct resonance frequencies in the visible and near-infrared regimes. Nanostructures with broadband response were employed to support both excitation and fluorescence of molecules[70].

We apply a quantum-mechanical approach to investigate the dynamics of a TPA system under continuous-wave illumination at frequency ω_p . The Hamiltonian of a two-level system coupled to light through a two-photon interaction can be written as:

$$H = \frac{1}{2} \hbar \omega_{eg} \sigma_z + \hbar \Omega^{(2)} (e^{-2i\omega_p t} \sigma_+ + e^{2i\omega_p t} \sigma_-), \quad (1.44)$$

where $\sigma_- = |e\rangle\langle g|$ and $\sigma_+ = \sigma_-^\dagger$ are Pauli flip operators, $\sigma_z = |e\rangle\langle e| - |g\rangle\langle g|$ is the population inversion operator, ω_{eg} is the transition frequency from the ground state to excited state and $\Omega^{(2)}$ is the two-photon coupling strength with the molecule.

To explore the coupling of plasmonic nanostructure to the TPA process, we have two split processes: excitation and fluorescence. In the excitation process, the electric field enhancement around the position of the molecule is calculated, and the excitation rate is written as:

$$\frac{\gamma_{exc}}{\gamma_{exc}^0} = \frac{|\mathbf{E}(\mathbf{r}, \omega_{ig})|^4}{|\mathbf{E}_0(\mathbf{r}, \omega_{ig})|^4}, \quad (1.45)$$

where γ_{exc} and γ_{exc}^0 are excitation rates near plasmonic nanostructure and in free space, respectively, the electric fields in the position of molecule near the plasmonic nanostructure and in free space are $E(\mathbf{r}, \omega_{ig})$ and $E_0(\mathbf{r}, \omega_{ig})$, respectively. The fluorescence process is modeled by the single-photon spontaneous emission, which is expressed as:

$$\frac{\gamma_{flu}}{\gamma_{flu}^0} = \frac{P(\mathbf{r}_0, \omega_{eg})}{P_0(\mathbf{r}_0, \omega_{eg})}, \quad (1.46)$$

where γ_{flu} and γ_{flu}^0 are the fluorescence rate near the plasmonic nanostructure and in free space, respectively. The total radiated powers near plasmonic nonstructure and in free space are $P(\mathbf{r}_0, \omega_{eg})$ and $P_0(\mathbf{r}_0, \omega_{eg})$, respectively. Assuming independent excitation and emission processes, the signal enhancement in TPA can be expressed as a product of terms in Eqs.(1.45) and (1.46):

$$I_{TPA} = \frac{\gamma_{exc}}{\gamma_{exc}^0} \times \frac{\gamma_{flu}}{\gamma_{flu}^0} = \frac{|\mathbf{E}(\mathbf{r}, \omega_{ig})|^4}{|\mathbf{E}_0(\mathbf{r}, \omega_{ig})|^4} \times \frac{P(\mathbf{r}_0, \omega_{eg})}{P_0(\mathbf{r}_0, \omega_{eg})}. \quad (1.47)$$

In my work, I have designed a dual-mode cross-shaped nanostructure addressing molecular absorption and fluorescence properties for several molecular dyes[71]. The proposed plasmonic nanostructure is composed of four nanobars arranged in a cross shape, featuring two independent plasmonic modes. These modes can be switched by adjusting the polarization angle. Additionally, each resonance can be tuned independently within the near-infrared and visible regimes by altering the lengths of the nanobars. In the same work, I demonstrated that in this process, the independent excitation and emission assumption does not hold, and the optimal enhancement scenario depends on the molecular saturation level.

1.4.4 Polar Molecule

The final nonlinear phenomenon investigated in my works is the generation of radiation at Rabi frequency in polar molecules. The mechanism is briefly explained

below.

The optical properties of atomic systems are determined by spatial symmetries, quantified through multipolar transition moments. When driven by a resonant plane wave, a two-level system experiences a periodic transfer of population between the levels, known as Rabi oscillations [48]. The frequency of these oscillations depends on the amplitude of the driving field and the transition dipole moment of the quantum system. However, this fundamental quantum optical effect is rarely analyzed in polar systems, where broken inversion symmetry induces new effects. For instance, polar systems can have different permanent dipole moments in their ground and excited states, leading to an additional oscillating dipole that radiates at the Rabi frequency [72, 73]. This frequency can be controlled all optically across a broad range, from GHz to THz, often far from the original transition frequency. This example highlights the significant impact of the spatial symmetry breaking and the resulting polar nature of the system on its optical properties.

Here, we describe the mechanisms of low-frequency radiation generation in polar systems. The electric dipole moment of a two-level quantum system is expressed as:

$$\mathbf{d} = \frac{1}{2} (\mathbf{d}_{ee} - \mathbf{d}_{gg}) \sigma_z + \frac{1}{2} (\mathbf{d}_{ee} + \mathbf{d}_{gg}) I + \mathbf{d}_{eg} \sigma^+ + \mathbf{d}_{ge} \sigma^-. \quad (1.48)$$

The dipole moment has off-diagonal, induced elements $\mathbf{d}_{ge} = \mathbf{d}_{eg}^*$, responsible for transitions between the excited $|e\rangle$ and ground $|g\rangle$ states upon illumination with an electromagnetic field, and diagonal, permanent elements $\mathbf{d}_{ee}, \mathbf{d}_{gg}$, which are nonzero for polar systems, i.e., systems that break spatial inversion symmetry. These latter elements, referred to as "permanent dipole moments" (PDMs), are typically neglected in light-matter interaction problems; however, they may lead to interesting physics, including low-frequency radiation emission (Fig.1.14). Figure.1.14(a)

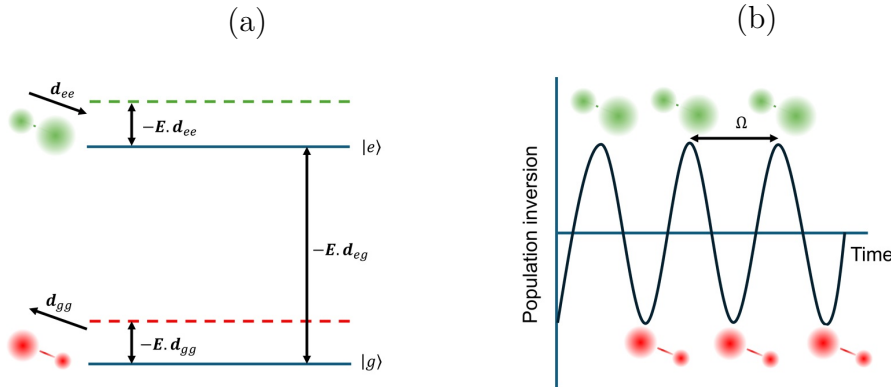


Figure 1.14: Energy scheme (a) and dynamics (b) of a two-level system. Figure prepared following Ref. [20].

demonstrates the energy scheme of a two-level polar system that interacts with electric field \mathbf{E} . The population of the system oscillates between the eigenstates with

Rabi frequency Ω_0 . For systems with PDMs, Rabi population transfer gives rise to an oscillating permanent dipole moment $\mathbf{d}_{ee} - \mathbf{d}_{gg}$, as schematically depicted in Fig.1.14(b). This oscillating dipole, in turn, is the source of radiation at the Rabi frequency.

By methods beyond the scope of this thesis, it can be shown that in polar systems, the Rabi frequency is modified to the form combining the effective interaction strength $\Omega_0 \frac{2}{\kappa} J_1(\kappa)$ [72] and the spontaneous emission rate of two-level system γ_0 :

$$\Omega_{polar} = \sqrt{(\Omega_0 \frac{2}{\kappa} J_1(\kappa))^2 - (\frac{\gamma_0}{4})^2}, \quad (1.49)$$

where $\kappa = \mathbf{E}_0 \frac{(\mathbf{d}_{ee} - \mathbf{d}_{gg})}{\hbar\omega}$, $J_1(\kappa)$ is the Bessel function of the first kind. This is the frequency of oscillations of the permanent dipole at which the radiation is generated in the polar system.

My work was to design a nanoantenna that would allow tuning the frequency (1.49) of the emitted radiation through modification of Ω_0 and γ_0 to plasmon-enhanced values Ω , γ . The field enhancement in the vicinity of plasmonic nanoparticles leads to rescaling of the spontaneous emission rate according to Eq. (1.38), and of the Rabi frequency Ω to the form

$$\Omega = \Omega_0 \frac{E(\mathbf{r}_0, \omega_{eg})}{E_0(\mathbf{r}_0, \omega_{eg})}, \quad (1.50)$$

where $E(\mathbf{r}_0, \omega_{eg})$ and $E_0(\mathbf{r}_0, \omega_{eg})$ denote here the electric field components parallel to the transition dipole moment near the plasmonic nanostructure and in free space. I have used silver nanorods to achieve electric field enhancement at the frequency ω_{eg} in the visible regime. With sufficiently strong illumination, this allows to shift the resulting Rabi frequency Ω_{polar} to the THz regime.

To support generation of Rabi-frequency radiation in this regime, I have employed coupled graphene disks. The disks enhance the emission rate at the Rabi frequency by the Purcell factor $\frac{P(\mathbf{r}_0, \Omega)}{P_0(\Omega)}$, where $P(\mathbf{r}_0, \Omega)$, $P_0(\Omega)$ are radiated power near plasmonic nanostructure and in free space respectively.

1.5 Analytical and numerical techniques

Classical electrodynamic simulations have significantly enhanced our quantitative understanding of plasmonic devices and materials, as well as the excitation and collection optics variables responsible for high enhancements. These insights have guided the design of SERS, SECARS, surface-enhanced TPA, and improved terahertz emission control from polar molecules. Several numerical methods are commonly used to interpret a wide range of nano-optical processes. Popular numerical methods include the finite element method and the finite integration technique. In this section, I briefly introduce these two methods.

1.5.1 Finite Integration Technique

CST STUDIO SUITE is a general-purpose electromagnetic simulation software that uses the Finite Integration Technique (FIT), which was introduced by Weiland in 1976[74]. This numerical method provides a comprehensive spatial discretization framework that can be applied to a wide range of electromagnetic problems, from static field calculations to high-frequency applications in both time and frequency domains. In this section, the fundamental aspect of FIT is explained.

FIT discretizes Maxwell's equations in their integral form rather than the differential form.

$$\begin{aligned}
 \oint_{\partial A} \mathbf{E} \cdot d\mathbf{s} &= - \int_A \frac{\partial \mathbf{B}}{\partial t} \cdot d\mathbf{A}, \\
 \oint_{\partial A} \mathbf{H} \cdot d\mathbf{s} &= \int_A \left(\frac{\partial \mathbf{D}}{\partial t} + \mathbf{J} \right) \cdot d\mathbf{A}, \\
 \oint_{\partial V} \mathbf{D} \cdot d\mathbf{A} &= \int_V \rho dV, \\
 \oint_{\partial V} \mathbf{B} \cdot d\mathbf{A} &= 0,
 \end{aligned} \tag{1.51}$$

where $d\mathbf{A}$ represents the differential vector element of surface area A and $d\mathbf{s}$ represents infinitesimal vector element of the contour ∂A , and V denotes to any volume with closed boundary surface ∂V . To numerically solve these equations, a finite calculation domain must be defined based on the specific application problem. By selecting an appropriate mesh system, this domain is divided into numerous small grid cells.

After gridding the calculation domain, the meshing process is divided into two steps: primary mesh and dual mesh. The primary mesh is visible in the mesh view, while the dual mesh is orthogonally set up internally. Maxwell's equations are discretized on these two orthogonal grid systems, with the degrees of freedom displayed as integral values. The electric grid voltages (e) and magnetic facet fluxes (b) are defined

on the primary grid, while the dielectric facet fluxes (d) and magnetic grid voltages (h) are defined on the dual grid, as shown in Fig.1.15(a). As a result, Maxwell's

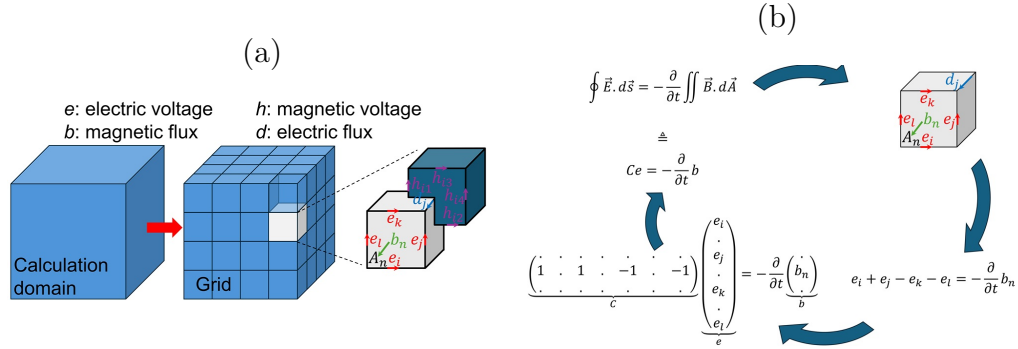


Figure 1.15: (a) The discretization on orthogonal grid systems. (b) Discretization of the Faraday's law.

equations can be formulated for each cell facet individually, as introduced below and schematically depicted in Fig.1.15(b). With C and (\tilde{C}) standing for discrete curl operators in the primary and dual grids, as well as discrete divergence operators S and \tilde{S} , Maxwell's equations can be discretized to the form:

$$\begin{aligned}
 Ce &= -\frac{d}{dt}b, \\
 \tilde{C}h &= \frac{d}{dt}d + j, \\
 \tilde{S}d &= q, \\
 Sb &= 0.
 \end{aligned} \tag{1.52}$$

The equations reformulated for the FIT method are precisely equivalent to the original Maxwell's equations. In my calculations, I relied on the implementation of FIT in CST STUDIO SUITE, introduced by Weiland in 1976[74].

1.5.2 Finite Element Method

The finite element method (FEM) represents a powerful numerical approach widely utilized for addressing boundary value problems, involving partial differential equations (PDEs). The core concept behind the FEM is to discretization of the problem domain into a finite number of smaller, interconnected subdomain referred to as elements. This process, known as discretization, the equations are numerically solved in each element, ultimately enabling an approximation of the solution over the entire problem domain. Mathematically, the principle behind the FEM is that a problem expressed in its weak form can provide an approximate solution to the problem in its strong form.

In the strong form, the field variables are required to maintain continuity across

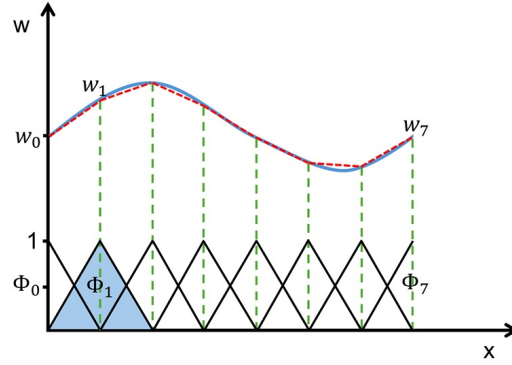


Figure 1.16: The function w (solid blue line) is approximated with w_i (dashed red line), which is a linear combination of linear basis functions Φ_i (solid black line). Figure prepared following Ref. 75.

the domain, with continuous partial derivatives up through the order of PDE. Conversely, the weak form relaxes these continuity requirements, permitting discontinuities, provided they are integral across the domain. Reformulating the PDEs into their weak form allows for the application of linear algebraic methods, facilitating the derivation an approximate solution to the original problem.

In general, a function $w(x)$ can be expressed as a series expansion in terms of basis function Φ_i , such that:

$$\mathbf{w}(\mathbf{x}) = \sum_i w_i \phi_i(\mathbf{x}), \quad (1.53)$$

where w_i represents the coefficients corresponding to each basis function. Within the framework of FEM, the basis functions Φ_i are characterized by being non-zero only within a specific element associated with index i . This decomposition strategy enables the function $w(\mathbf{x})$ to be approximated to arbitrary accuracy with piece-wise linear basis functions and sufficiently small elements. To make clear this principle, I demonstrated one-dimensional problem in Fig.1.16. Here, w represents electric field along the length of a simulation domain.

After expressing the function $w(x)$ as a series of basis functions $\Phi_i(x)$, the next step in the FEM is to create a system of algebraic equations using the weak form of PDE. This process involves integrating the product of basis functions and the differential operators over each element, which leads to the formation of local matrices and load vectors. These local matrices and vectors are then combined into a global system of equations that represents the entire domain of the problem. The local matrix K and the load vector Form a linear system $Kw = F$, where w contains the coefficients of the basis functions. This linear system is then solved using numerical techniques to determine the coefficients w . These coefficients approximate the solution to the original PDE across the entire domain.

1.5.3 Methods

In my work, I utilized two electromagnetic software applications: CST Studio Suite and COMSOL Multiphysics. Both are excellent for electromagnetic simulations, each offering distinct advantages depending on the electromagnetic models. CST Studio Suite is more streamlined for simulating electromagnetic problems, while COMSOL provides the flexibility to incorporate different models and equations into the solver. Consequently, I used both in my thesis.

My simulations involved two models: one using a plane wave to represent laser illumination, and the other using a dipole source to model atomic system transitions. In the plane wave model, I worked with nanoantenna and metasurface structures, which required different boundary conditions. For the nanoantenna, I used a plane wave source with a perfectly matched layer (PML) domain to absorb outgoing waves, calculating the absorption and scattering cross-sections. If the nanoantenna had symmetry, I implemented symmetry planes in the YZ, XZ, and XY directions to reduce simulation time. For the metasurface, I applied periodic boundary conditions in the X and Y directions to extend the unit cell, resulting in the transmittance, reflectance, and absorption spectrum of the metasurface. In both cases, I defined a probe point to calculate the electric field at the position of the atomic system. In the dipole illumination model, with a PML domain surrounding the nanoantenna, I calculated the radiated and absorbed power based on Eqs. 1.54 and 1.55. The system's dyadic Green's function is evaluated at the position of the dipole source. To calculate the power radiated from and absorbed by the nanostructure, we use Poynting's theorem. [23, 20, 18]:

$$P_{\text{rad}}(\omega) = \oint \langle \vec{E}_{\text{sca}}(\vec{r}, \omega) \times \vec{H}_{\text{sca}}(\vec{r}, \omega) \rangle d\vec{A}, \quad (1.54)$$

$$P_{\text{abs}}(\omega) = \int \langle \vec{J}_{\text{ind}}(\vec{r}, \omega) \cdot \vec{E}_{\text{ind}}(\vec{r}, \omega) \rangle dV, \quad (1.55)$$

where similarly to $\vec{E}_{\text{sca}}(\vec{r}, \omega)$, the symbol $\vec{H}_{\text{sca}}(\vec{r}, \omega)$ denotes the scattered part of the magnetic field, and $\vec{J}_{\text{ind}}(\vec{r}, \omega)$ and $\vec{E}_{\text{ind}}(\vec{r}, \omega)$ represent the currents and electric field in the nanostructure volume. The integrals are evaluated, respectively, at the spherical surface of the simulation volume and inside the volume of the nanostructure elements.

Chapter 2

Summary of the publications

2.1 Published articles comprising the thesis

1. **Izadshenas, Saeid**, Piotr Masłowski, Tobias Herr, and Karolina Słowik. "Multiresonant metasurface for Raman spectroscopy beyond single molecule detection level." *EPJ Applied Metamaterials* 9 (2022): 11.
2. **Izadshenas, Saeid**, and Karolina Słowik. "Metasurface for broadband coherent Raman signal enhancement beyond the single-molecule detection threshold." *APL Materials* 11, no. 8 (2023).
3. **Izadshenas, Saeid**, Piotr Gładysz, and Karolina Słowik. "Hybrid graphene-silver nanoantenna to control THz emission from polar quantum systems." *Optics Express* 31, no. 18 (2023): 29037-29050.
4. **Izadshenas Jahromi, Saeid**, and Karolina Słowik. "Multiphoton absorption enhancement by graphene-gold nanostructure." *Optics Letters* 49, no. 14 (2024): 3914-3917.
5. **Izadshenas Jahromi, Saeid**, and Karolina Słowik. "Molecular saturation determines distinct plasmonic enhancement scenarios for two-photon absorption signal." *arXiv*, (2024).

2.2 Other published articles

Below, I list the articles I authored or co-authored that are not a part of this thesis. Below each article data, the article abstract is presented.

A. Published during doctoral studies

1. **Izadshenas, S.**, and K. Słowik. "Metal-Insulator-Metal Plasmonic Metasurface for Optical Nonlinear Sensing: Achieving High Field Enhancement and Broadband Optical Response." In 2023 Seventeenth International Congress on Artificial Materials for Novel Wave Phenomena (Metamaterials), pp. X-142. IEEE, 2023.

This study proposes a metal-insulator-metal plasmonic metasurface for nonlinear sensing applications. The predicted signal enhancement factor for the coherent anti-Stokes Raman scattering (CARS) reaches 11 orders of magnitude compared to the free-space realization. The metasurface is versatile and highly efficient, supporting signal enhancement for a wide range of Raman shifts and various molecular species without the requirement of tuning. Its relative ease of fabrication, broadband performance, and the high electric field enhancement it supports make it a valuable platform for nonlinear optical sensing, including CARS, surface-enhanced Raman scattering (SERS), and two photon absorption scenarios.

2. **Jahromi, S. Izadshenas**, T. Herr, P. Masłowski, and K. Słowik. "Multiresonant nanostructures for surface-enhanced coherent anti-Stokes Raman spectroscopy." In 2021 Fifteenth International Congress on Artificial Materials for Novel Wave Phenomena (Metamaterials), pp. 170-172. IEEE, 2021.

Coherent anti-Stokes Raman scattering (CARS) is a well-known tool in molecular spectroscopy. In this work we combine CARS with surface plasmon enhancement on a periodic metasurface. The proposed metal-insulator-grating nanostructured geometry supports three resonances, as required by the CARS scenario. We briefly discuss the knobs to tune these resonances, so that the spectral distance between them could eventually match the Raman shift of selected molecules. In this report, we focus on one particular tuning possibility that is available after the metasurface fabrication. With each of the resonances providing field

enhancement by more than 2 orders of magnitude, we achieve CARS signal enhancement factors of the order of 10^{18} .

3. **Jahromi, S. Izadshenas.** "Graphene Plasmonic Tunable Multisensors in Terahertz Band." In 2022 Sixteenth International Congress on Artificial Materials for Novel Wave Phenomena (Metamaterials), pp. X-202. IEEE, 2022.

We propose tunable graphene-based multisensors sustaining absorption efficiency exceeding 95% in the terahertz domain. Due to the graphene components, the absorption frequency is tunable with gate voltage. The perfect absorber can operate as a refractive index sensor with a sensitivity around 54.54 m/RIU . More importantly, it can be operated as a temperature sensor with the sensitivity of 13.75 m/K . Due to the high sensing performance, the structure has a great potential for chemical applications.

B. Published before starting the doctoral studies

1. **Izadshenas, S., A. Zakery, and Z. Vafapour.** "Tunable slow light in graphene metamaterial in a broad terahertz range." *Plasmonics* 13 (2018): 63-70.

A graphene-based metamaterial with tunable electromagnetically induced transparency is numerically studied in this paper. The proposed structure consists of a graphene layer composed of H shape between two cut wires, by breaking symmetry can control EIT-like effects and by increasing the asymmetry in the structure has strong coupling between elements. It is important that the peak frequency of transmission window can be dynamically controlled over a broad frequency range by varying the chemical potential of graphene layer. The results show that high refractive index sensitivity and figure of merit can be achieved in asymmetrical structures which is good for sensing applications. We calculated the group delay and the results show we can control the group velocity by varying the S parameter in asymmetrical structure. The characteristics of our system indicate important potential applications in integrated optical circuits such as optical storage, ultrafast plasmonic switches, high performance filters, and slow-light devices.

2. **Jahromy, S. Izadshenas,** and A. Zakery. "Tunable metamaterial structures and slow light effects using plasmon induced transparency." In Conference on Lasers and Electro-Optics/Pacific Rim, p. s1460. Optica Publishing Group, 2017.

We present a dynamically frequency tunable plasmon induced transparency(PIT) in metamaterial devices composed of a graphene nanostructure for the terahertz (1-10 THz) region. The most common way to get a PIT effect is creating the coupling between bright and dark modes. Graphene show unusual behavior that enables new tunable plasmonic metamaterials and applications in terahertz frequency range. The PIT resonant frequency can be dynamically tuned by varying the gate voltage applied to the graphene without re-fabrication the nanostructures. A metamaterial sensor based on these coupling effects yields a sensitivity of 8152 nm/RIU. PIT has been demonstrated to be able to greatly slow down the speed of light. Slow light is important for routing optical information. In the vicinity of the PIT transparent peak it offers a large positive group Index, suggesting slow light. At the transparent peak, the group Index is 278.7. These features show remarkable potential for slow light devices, optical sensing and switching in metamaterials.

2.3 My work and connections

Over the four years of my PhD research, I focused on developing novel plasmonic metasurfaces and nanostructures to enhance nonlinear phenomena in atomic systems subject to external illumination. My work covers coherent anti-Stokes Raman scattering enhancement, controlling terahertz emission in polar molecules, and improving two- and multi-photon absorption. The unifying theme across these studies is exploring the potential of advanced-design nanostructures to contribute to the understanding of light-matter interactions.

1- Raman Scattering Enhancement

My contributions focused on the subject of Raman scattering[18, 19] have significantly advanced the predicted signal enhancement limits in coherent Raman scattering. While previous studies have explored various geometries for CARS enhancement, such as nanovoid gold surfaces[9], gold film-gold particles[76], and gold nanoparticles[77], our approach utilizing a multiresonant metal-insulator-grating metasurface has achieved tunable, high electric field enhancement.

In Ref.[19], we demonstrated Raman scattering enhancement beyond the single-molecule detection level. We designed and optimized a metasurface in metal-insulator-grating configuration to enhance the coherent Raman signal of selected molecules. The tunability of the metasurface allowed us to adjust its size to match the Raman peak of rhodamine. Additionally, our metasurface covers a broad range of Raman shifts due to its wide spectral response. The grating on the bottom of metasurface plays a key role in switching between different Raman shifts by changing the incident angle.

This work improves upon existing proposals by introducing a novel multiresonant metal-insulator-grating metasurface, achieving much stronger signal enhancement – predicted at the level of up to 14 orders of magnitude in optimal conditions. The metasurface not only provides high electric field enhancement but also offers tunability, allowing for the switching between distinct Raman shifts by altering the incident angle. With its broad spectral response, this metasurface is a flexible tool that supports a wide range of molecular species.

Our follow-up study[18] further extended this concept to broadband coherent Raman signal enhancement in metal-insulator-metal (MIM) configuration metasurface. This work addresses the limitations of previous approaches by utilizing MIM configuration to support an ultra-broad spectra response with high electric field enhancement, achieved by coupling nanodisks to the reflective layer. The signal intensity

enhancement was predicted up to 20 orders of magnitude. The proposed metasurface supports a wide range of Raman shifts from 600 to 1600 cm^{-1} and accommodates various molecular species. Moreover, the MIM metasurface was described using an RLC circuit model to predict its optical response semi-analytically, showing excellent agreement between the optical response obtained numerically and within the RLC circuit model.

2- Terahertz emission control in polar molecule

In our work on terahertz emission nanoantennas[20], we investigated the application of hybrid graphene-silver nanoantennas to control terahertz emission from polar quantum systems. This project was a collaboration with Piotr Gładysz. PG modeled the Hamiltonian of polar molecule, while I designed the hybrid graphene-silver nanoantenna. The proposed nanoantenna consists of two independent elements operating in distinct frequency regimes. The silver nanorods atop the nanoantenna tune the emission frequency of polar molecule, shifting it from MHz to the THz regime. Additionally, the coupled graphene disks significantly enhance the emission signal in the THz band, providing tunability to adjust the device's operation frequency according to the illumination conditions.

3- Multi-photon Absorption Enhancement

Our work on multiphoton absorption [21] represents a hybrid graphene-gold nanoantenna designed to support two distinct and independent resonances, spanning from THz - mid-infrared to the near-infrared - visible regimes. This tunable nanoantenna facilitates two-, four-, six-, eight- and ten-photon absorption by adjusting the gate voltage applied to the graphene disk. The gold nanobars on top of the nanoantenna significantly enhance single-photon fluorescence emission, with calculated fluorescence signal enhancements reaching five orders of magnitude in two-photon absorption and more than thirteen orders of magnitude for higher nonlinearities. The proposed nanoantenna shows great potential for supporting various quantum phenomena, including tunable optomechanical interactions and multi-photon processes.

4- TPA cross-shaped nanostructures

Our study on two-photon absorption process led to the design of cross-shaped nanostructures with two distinct and independent resonances in near-infrared and visible regimes. The cross-shaped nanoantenna, composed of four nanorods with different plasmonic modes, enables us to couple bright and dark modes by adjusting the polarization angle, resulting in distinct resonances that enhance the absorp-

tion and fluorescence of molecules. We integrated a silver metal film into the proposed nanoantenna as a reflective layer to enhance the optical response and support stronger light-matter interactions. The proposed nanoantenna meets the essential requirements for achieving stronger two-photon absorption with significant fluorescence signal enhancement. We compared three different dye molecules to illustrate how molecular engineering can enhance signals in two-photon absorption. In this work, we also discussed the quantum description of two-photon absorption, which allowed us to determine optimal strategies for signal enhancement below and within the saturation regime.

In summary, my research centered on the study and development of advanced nanoantennas and metasurfaces for nonlinear light-matter interactions. By utilizing innovative metasurfaces and nanoantennas, I have achieved designs that promise significant signal enhancements in Raman spectroscopy, control over THz emission, and multiphoton and two-photon absorption efficiency. My work in nonlinear light-matter interaction opens new possibilities for stronger and tunable interactions, enhancing signals across various nonlinear optical applications.

2.4 Author contribution statement

I was the main contributor to the research presented in the publications which make up this thesis. For these five articles, the first draft of manuscripts were written by me and most of figures were made by me. I was responsible for submitting the articles to the journals and for editing the manuscripts in the response to other authors' or reviewers' comments; I am the corresponding author of these publications.

Hereby I declare that my contribution to the paper:

Izadshenas, Saeid, Piotr Masłowski, Tobias Herr, and Karolina Słowik.

"Multiresonant metasurface for Raman spectroscopy beyond single molecule detection level." EPJ Applied Metamaterials 9 (2022): 11.

includes the idea of proposed MIG metasurface, making electromagnetic simulations, making figures, writing the first draft. I was the corresponding author of this paper.

Hereby I declare that my contribution to the paper:

Izadshenas, Saeid, and Karolina Słowik. "Metasurface for broadband coherent Raman signal enhancement beyond the single-molecule detection threshold." APL Materials 11, no. 8 (2023).

includes the idea of proposed MIM metasurface, writing the first draft, making electromagnetic simulations, making figures, designing RLC circuit model. I was the corresponding author of this paper.

Hereby I declare that my contribution to the paper:

Izadshenas, Saeid, Piotr Gładysz, and Karolina Słowik. "Hybrid graphene-silver nanoantenna to control THz emission from polar quantum systems." Optics Express 31, no. 18 (2023): 29037-29050.

includes designing the nanoantenna, making electromagnetic simulations, writing the first draft in nanoantenna performance, making most of figures. I was the corresponding author of this paper.

Hereby I declare that my contribution to the paper:

Izadshenas Jahromi, Saeid, and Karolina Słowik. "Multiphoton

absorption enhancement by graphene–gold nanostructure.” *Optics Letters* 49, no. 14 (2024): 3914-3917.

includes writing the first draft, making all figures, making electromagnetic simulations. I was the corresponding author.

Hereby I declare that my contribution to the paper:

Izadshenas Jahromi, Saeid, and Karolina Słowik. ”Molecular saturation determines distinct plasmonic enhancement scenarios for two-photon absorption signal.” *Arxiv*, (2024).

includes writing the first draft and some part of final draft, making electromagnetic simulations, making most of figures. I was the corresponding author of this paper.

Chapter 3

Conclusions

This study has focused on enhancing nonlinear light-matter interactions using plasmonic nanoantennas and metasurfaces. The findings demonstrate how various configurations of plasmonic nanoantennas and metasurfaces can significantly enhance different nonlinear optical processes, including surface-enhanced Raman scattering, coherent anti-Stokes Raman scattering, interactions in polar quantum systems, and multi- and two-photon absorption.

Our analysis revealed that metasurfaces with metal-insulator-metal and metal-insulator-grating (MIG) configurations not only support a wide range of Raman shifts across various molecules but may potentially achieve a total signal enhancement of up to 20 orders of magnitude. Additionally, the MIG metasurface offers tunable optical response by adjusting the incident angle.

By integrating graphene layers with silver and gold nanoantennas, we have demonstrated the ability to convert between two distinct electromagnetic frequency regimes, from terahertz to visible, with a tunable response. The proposed hybrid nanostructure enables the control of terahertz emission in polar quantum systems. Another design of graphene-silver nanoantennas was proposed to enhance multi-photon absorption, supporting both excitation and spontaneous emission in different molecules. These nanoantennas also show potential in enhancing single-molecule detection in optomechanical cavities and multi-photon processes.

The cross-shaped plasmonic nanoantennas presented in this study allow for the demonstration of two tunable resonances in the near-infrared and visible regimes. This capability facilitates a detailed investigation of the two-photon absorption process, enabling not only significant signal enhancement in TPA but also supporting distinct enhancement mechanisms in two saturation regimes.

In summary, this research is focused on investigation and design of various plasmonic

metasurfaces and nanoantennas to explore nonlinear light-matter interactions across multiple applications. These findings not only provide new methods of control but also deepen our understanding of nonlinear optical processes.

Bibliography

- [1] S. A. Maier and H. A. Atwater, “Plasmonics: Localization and guiding of electromagnetic energy in metal/dielectric structures,” *Journal of applied physics*, vol. 98, no. 1, 2005.
- [2] D. K. Gramotnev and S. I. Bozhevolnyi, “Plasmonics beyond the diffraction limit,” *Nature photonics*, vol. 4, no. 2, pp. 83–91, 2010.
- [3] L. Novotny and N. Van Hulst, “Antennas for light,” *Nature photonics*, vol. 5, no. 2, pp. 83–90, 2011.
- [4] M. Fleischmann, P. J. Hendra, and A. J. McQuillan, “Raman spectra of pyridine adsorbed at a silver electrode,” *Chemical physics letters*, vol. 26, no. 2, pp. 163–166, 1974.
- [5] J. Gersten and A. Nitzan, “Electromagnetic theory of enhanced raman scattering by molecules adsorbed on rough surfaces,” *The Journal of Chemical Physics*, vol. 73, no. 7, pp. 3023–3037, 1980.
- [6] A. Wokaun, J. Gordon, and P. Liao, “Radiation damping in surface-enhanced raman scattering,” *Physical Review Letters*, vol. 48, no. 14, p. 957, 1982.
- [7] J. Langer, D. Jimenez de Aberasturi, J. Aizpurua, R. A. Alvarez-Puebla, B. Augu e, J. J. Baumberg, G. C. Bazan, S. E. Bell, A. Boisen, A. G. Brolo, *et al.*, “Present and future of surface-enhanced raman scattering,” *ACS nano*, vol. 14, no. 1, pp. 28–117, 2019.
- [8] A. Downes and A. Elfick, “Raman spectroscopy and related techniques in biomedicine,” *Sensors*, vol. 10, no. 3, pp. 1871–1889, 2010.
- [9] C. Steuwe, C. F. Kaminski, J. J. Baumberg, and S. Mahajan, “Surface enhanced coherent anti-stokes raman scattering on nanostructured gold surfaces,” *Nano letters*, vol. 11, no. 12, pp. 5339–5343, 2011.
- [10] T. Ichimura, N. Hayazawa, M. Hashimoto, Y. Inouye, and S. Kawata, “Tip-enhanced coherent anti-stokes raman scattering for vibrational nanoimaging,” *Physical review letters*, vol. 92, no. 22, p. 220801, 2004.

- [11] Y. Zhang, Y.-R. Zhen, O. Neumann, J. K. Day, P. Nordlander, and N. J. Halas, “Coherent anti-stokes raman scattering with single-molecule sensitivity using a plasmonic fano resonance,” *Nature communications*, vol. 5, no. 1, pp. 1–7, 2014.
- [12] J. M. Hales, D. J. Hagan, E. W. Van Stryland, K. Schafer, A. Morales, K. D. Belfield, P. Pacher, O. Kwon, E. Zojer, and J.-L. Brédas, “Resonant enhancement of two-photon absorption in substituted fluorene molecules,” *The Journal of chemical physics*, vol. 121, no. 7, pp. 3152–3160, 2004.
- [13] J. D. Cox and F. J. Garcia de Abajo, “Nonlinear graphene nanoplasmonics,” *Accounts of Chemical Research*, vol. 52, no. 9, pp. 2536–2547, 2019.
- [14] R. A. Shelby, D. R. Smith, and S. Schultz, “Experimental verification of a negative index of refraction,” *science*, vol. 292, no. 5514, pp. 77–79, 2001.
- [15] D. Schurig, J. J. Mock, B. Justice, S. A. Cummer, J. B. Pendry, A. F. Starr, and D. R. Smith, “Metamaterial electromagnetic cloak at microwave frequencies,” *Science*, vol. 314, no. 5801, pp. 977–980, 2006.
- [16] N. Fang, H. Lee, C. Sun, and X. Zhang, “Sub-diffraction-limited optical imaging with a silver superlens,” *science*, vol. 308, no. 5721, pp. 534–537, 2005.
- [17] D. R. Smith, R. Liu, and T. J. Cui, *Metamaterials: theory, design, and applications*. Springer US, 2010.
- [18] S. Izadshenas and K. Słowik, “Metasurface for broadband coherent raman signal enhancement beyond the single-molecule detection threshold,” *APL Materials*, vol. 11, no. 8, p. 081120, 2023.
- [19] S. Izadshenas, P. Masłowski, T. Herr, and K. Słowik, “Multiresonant metasurface for raman spectroscopy beyond single molecule detection level,” *EPJ Applied Metamaterials*, vol. 9, p. 11, 2022.
- [20] S. Izadshenas, P. Gładysz, and K. Słowik, “Hybrid graphene-silver nanoantenna to control thz emission from polar quantum systems,” *Optics Express*, vol. 31, no. 18, pp. 29037–29050, 2023.
- [21] S. I. Jahromi and K. Słowik, “Multiphoton absorption enhancement by graphene–gold nanostructure,” *Optics Letters*, vol. 49, no. 14, pp. 3914–3917, 2024.
- [22] S. A. Maier *et al.*, *Plasmonics: fundamentals and applications*, vol. 1. Springer, 2007.
- [23] J. D. Jackson, *Classical electrodynamics*. John Wiley & Sons, 2021.

- [24] C. F. Bohren and D. R. Huffman, *Absorption and scattering of light by small particles*. John Wiley & Sons, 2008.
- [25] G. Mie, “Beiträge zur optik trüber medien, speziell kolloidaler metallösungen,” *Annalen der physik*, vol. 330, no. 3, pp. 377–445, 1908.
- [26] D. Mackowski, “The extension of mie theory to multiple spheres,” in *The Mie theory: Basics and applications*, pp. 223–256, Springer, 2012.
- [27] P. B. Johnson and R.-W. Christy, “Optical constants of the noble metals,” *Physical review B*, vol. 6, no. 12, p. 4370, 1972.
- [28] A. F. Koenderink, “Single-photon nanoantennas,” *ACS photonics*, vol. 4, no. 4, pp. 710–722, 2017.
- [29] O. S. Ojambati, R. Chikkaraddy, W. M. Deacon, J. Huang, D. Wright, and J. J. Baumberg, “Efficient generation of two-photon excited phosphorescence from molecules in plasmonic nanocavities,” *Nano Letters*, vol. 20, no. 6, pp. 4653–4658, 2020.
- [30] X. Lu, D. Punj, and M. Orrit, “Two-photon-excited single-molecule fluorescence enhanced by gold nanorod dimers,” *Nano Letters*, vol. 22, no. 10, pp. 4215–4222, 2022.
- [31] X. Hu and X. Gao, “Multilayer coating of gold nanorods for combined stability and biocompatibility,” *Physical Chemistry Chemical Physics*, vol. 13, no. 21, pp. 10028–10035, 2011.
- [32] B. Bhattarai, Y. Zaker, A. Atnagulov, B. Yoon, U. Landman, and T. P. Bigioni, “Chemistry and structure of silver molecular nanoparticles,” *Accounts of chemical research*, vol. 51, no. 12, pp. 3104–3113, 2018.
- [33] Q. Bao and K. P. Loh, “Graphene photonics, plasmonics, and broadband optoelectronic devices,” *ACS nano*, vol. 6, no. 5, pp. 3677–3694, 2012.
- [34] C. Lee, X. Wei, J. W. Kysar, and J. Hone, “Measurement of the elastic properties and intrinsic strength of monolayer graphene,” *science*, vol. 321, no. 5887, pp. 385–388, 2008.
- [35] A. A. Balandin, S. Ghosh, W. Bao, I. Calizo, D. Teweldebrhan, F. Miao, and C. N. Lau, “Superior thermal conductivity of single-layer graphene,” *Nano letters*, vol. 8, no. 3, pp. 902–907, 2008.
- [36] G. W. Hanson, “Dyadic green’s functions and guided surface waves for a surface conductivity model of graphene,” *Journal of Applied Physics*, vol. 103, no. 6, 2008.

- [37] L. A. Falkovsky, “Optical properties of graphene,” in *Journal of Physics: conference series*, vol. 129, p. 012004, IOP Publishing, 2008.
- [38] J. Parmar, S. K. Patel, and V. Katkar, “Graphene-based metasurface solar absorber design with absorption prediction using machine learning,” *Scientific Reports*, vol. 12, no. 1, p. 2609, 2022.
- [39] A. V. Kildishev, A. Boltasseva, and V. M. Shalaev, “Planar photonics with metasurfaces,” *Science*, vol. 339, no. 6125, p. 1232009, 2013.
- [40] Z. Li, E. Palacios, S. Butun, and K. Aydin, “Visible-frequency metasurfaces for broadband anomalous reflection and high-efficiency spectrum splitting,” *Nano letters*, vol. 15, no. 3, pp. 1615–1621, 2015.
- [41] N. Liu, M. Mesch, T. Weiss, M. Hentschel, and H. Giessen, “Infrared perfect absorber and its application as plasmonic sensor,” *Nano letters*, vol. 10, no. 7, pp. 2342–2348, 2010.
- [42] N. Rivera, I. Kaminer, B. Zhen, J. D. Joannopoulos, and M. Soljačić, “Shrinking light to allow forbidden transitions on the atomic scale,” *Science*, vol. 353, no. 6296, pp. 263–269, 2016.
- [43] T. Neuman, R. Esteban, D. Casanova, F. J. García-Vidal, and J. Aizpurua, “Coupling of molecular emitters and plasmonic cavities beyond the point-dipole approximation,” *Nano letters*, vol. 18, no. 4, pp. 2358–2364, 2018.
- [44] E. Rusak, J. Straubel, P. Gładysz, M. Göddel, A. Kędziorski, M. Kühn, F. Weigend, C. Rockstuhl, and K. Słowik, “Enhancement of and interference among higher order multipole transitions in molecules near a plasmonic nanoantenna,” *Nature communications*, vol. 10, no. 1, p. 5775, 2019.
- [45] M. Kosik, O. Burlayenko, C. Rockstuhl, I. Fernandez-Corbaton, and K. Słowik, “Interaction of atomic systems with quantum vacuum beyond electric dipole approximation,” *Scientific reports*, vol. 10, no. 1, p. 5879, 2020.
- [46] C. Cohen-Tannoudji, J. Dupont-Roc, and G. Grynberg, *Atom-Photon Interactions: Basic Processes and Applications*. Wiley, 1998.
- [47] P. Meystre and M. Sargent, *Elements of quantum optics*. Springer Science & Business Media, 2007.
- [48] M. O. Scully and M. S. Zubairy, *Quantum optics*. Cambridge university press, 1997.
- [49] K. Drexhage, H. Kuhn, and F. Schäfer, “Variation of the fluorescence decay

- time of a molecule in front of a mirror,” *Berichte der Bunsengesellschaft für physikalische Chemie*, vol. 72, no. 2, pp. 329–329, 1968.
- [50] K. Drexhage, “Influence of a dielectric interface on fluorescence decay time,” *Journal of luminescence*, vol. 1, pp. 693–701, 1970.
- [51] E. M. Purcell, “Spontaneous emission probabilities at radio frequencies,” in *Confined Electrons and Photons: New Physics and Applications*, pp. 839–839, Springer, 1995.
- [52] R. Shankar, *Principles of quantum mechanics*. Springer Science & Business Media, 2012.
- [53] P. Anger, P. Bharadwaj, and L. Novotny, “Enhancement and quenching of single-molecule fluorescence,” *Physical review letters*, vol. 96, no. 11, p. 113002, 2006.
- [54] G. A. Wurtz, R. Pollard, W. Hendren, G. Wiederrecht, D. Gosztola, V. Podolskiy, and A. V. Zayats, “Designed ultrafast optical nonlinearity in a plasmonic nanorod metamaterial enhanced by nonlocality,” *Nature nanotechnology*, vol. 6, no. 2, pp. 107–111, 2011.
- [55] L. Wu, Z. Xie, L. Lu, J. Zhao, Y. Wang, X. Jiang, Y. Ge, F. Zhang, S. Lu, Z. Guo, *et al.*, “Few-layer tin sulfide: a promising black-phosphorus-analogue 2d material with exceptionally large nonlinear optical response, high stability, and applications in all-optical switching and wavelength conversion,” *Advanced Optical Materials*, vol. 6, no. 2, p. 1700985, 2018.
- [56] A. Fiore, V. Berger, E. Rosencher, P. Bravetti, and J. Nagle, “Phase matching using an isotropic nonlinear optical material,” *Nature*, vol. 391, no. 6666, pp. 463–466, 1998.
- [57] E. Rosencher, A. Fiore, B. Vinter, V. Berger, P. Bois, and J. Nagle, “Quantum engineering of optical nonlinearities,” *Science*, vol. 271, no. 5246, pp. 168–173, 1996.
- [58] S.-n. Zhu, Y.-y. Zhu, and N.-b. Ming, “Quasi-phase-matched third-harmonic generation in a quasi-periodic optical superlattice,” *Science*, vol. 278, no. 5339, pp. 843–846, 1997.
- [59] S. Liu, P. P. Vabishchevich, A. Vaskin, J. L. Reno, G. A. Keeler, M. B. Sinclair, I. Staude, and I. Brener, “An all-dielectric metasurface as a broadband optical frequency mixer,” *Nature communications*, vol. 9, no. 1, p. 2507, 2018.
- [60] M. Gu, X. Li, and Y. Cao, “Optical storage arrays: a perspective for future

- big data storage,” *Light: Science & Applications*, vol. 3, no. 5, pp. e177–e177, 2014.
- [61] D. Cotter, R. Manning, K. Blow, A. Ellis, A. Kelly, D. Nasset, I. Phillips, A. Poustie, and D. Rogers, “Nonlinear optics for high-speed digital information processing,” *Science*, vol. 286, no. 5444, pp. 1523–1528, 1999.
- [62] S. R. Marder, “Organic nonlinear optical materials: where we have been and where we are going,” *Chemical communications*, no. 2, pp. 131–134, 2006.
- [63] A. Miller, K. Welford, and B. Daino, *Nonlinear optical materials and devices for applications in information technology*, vol. 289. Springer Science & Business Media, 2013.
- [64] D. M. Solís, J. M. Taboada, F. Obelleiro, L. M. Liz-Marzán, and F. J. García de Abajo, “Optimization of nanoparticle-based sers substrates through large-scale realistic simulations,” *ACS photonics*, vol. 4, no. 2, pp. 329–337, 2017.
- [65] W. Kiefer, *Surface enhanced Raman spectroscopy: analytical, biophysical and life science applications*. John Wiley & Sons, 2010.
- [66] C. Huck, M. Tzschoppe, R. Semenyshyn, F. Neubrech, and A. Pucci, “Chemical identification of single ultrafine particles using surface-enhanced infrared absorption,” *Physical Review Applied*, vol. 11, no. 1, p. 014036, 2019.
- [67] R. L. Giesecking, J. Lee, N. Tallarida, V. A. Apkarian, and G. C. Schatz, “Bias-dependent chemical enhancement and nonclassical stark effect in tip-enhanced raman spectromicroscopy of co-terminated ag tips,” *The journal of physical chemistry letters*, vol. 9, no. 11, pp. 3074–3080, 2018.
- [68] A. C. Eckbreth and R. J. HALL, “Cars concentration sensitivity with and without nonresonant background suppression,” *Combustion Science and Technology*, 1981.
- [69] Y. Feng, Y. Wang, F. Shao, L. Meng, and M. Sun, “Surface-enhanced coherent anti-stokes raman scattering based on coupled nanohole–slit arrays,” *Physical Chemistry Chemical Physics*, vol. 24, no. 22, pp. 13911–13921, 2022.
- [70] X. Lu, D. Punj, and M. Orrit, “Two-photon-excited single-molecule fluorescence enhanced by gold nanorod dimers,” *Nano Letters*, vol. 22, no. 10, pp. 4215–4222, 2022.
- [71] S. Izadshenas and K. Słowik, “Molecular saturation determines distinct plasmonic enhancement scenarios for two-photon absorption signal,” 2024.
- [72] O. Kibis, G. Y. Slepyan, S. Maksimenko, and A. Hoffmann, “Matter coupling

- to strong electromagnetic fields in two-level quantum systems with broken inversion symmetry,” *Physical review letters*, vol. 102, no. 2, p. 023601, 2009.
- [73] P. Gładysz, P. Wcisło, and K. Słowik, “Propagation of optically tunable coherent radiation in a gas of polar molecules,” *Scientific reports*, vol. 10, no. 1, p. 17615, 2020.
- [74] T. Weiland, “A discretization model for the solution of maxwell’s equations for six-component fields,” *Archiv Elektronik und Uebertragungstechnik*, vol. 31, pp. 116–120, 1977.
- [75] COMSOL Multiphysics, “The finite element method (fem).” <https://www.comsol.com/multiphysics/finite-element-method>, 2024. Accessed: 2024-08-09.
- [76] S. Abedin, K. Roy, X. Jin, H. Xia, S. Brueck, and E. O. Potma, “Surface-enhanced coherent anti-stokes raman scattering of molecules near metal–dielectric nanojunctions,” *The Journal of Physical Chemistry C*, vol. 126, no. 20, pp. 8760–8767, 2022.
- [77] X. Hua, D. V. Voronine, C. W. Ballmann, A. M. Sinyukov, A. V. Sokolov, and M. O. Scully, “Nature of surface-enhanced coherent raman scattering,” *Physical Review A*, vol. 89, no. 4, p. 043841, 2014.

Appendix A

Publications

RESEARCH ARTICLE | AUGUST 29 2023

Metasurface for broadband coherent Raman signal enhancement beyond the single-molecule detection threshold

Saeid Izadshenas   ; Karolina Słowik 



APL Mater. 11, 081120 (2023)
<https://doi.org/10.1063/5.0165585>



31 May 2024 14:18:44



APL Quantum
First Articles Online
No Article Processing Charges for Submissions
Through December 31, 2024
[Read Now](#)



Metasurface for broadband coherent Raman signal enhancement beyond the single-molecule detection threshold

Cite as: APL Mater. 11, 081120 (2023); doi: 10.1063/5.0165585

Submitted: 29 June 2023 • Accepted: 9 August 2023 •

Published Online: 29 August 2023



View Online



Export Citation



CrossMark

Saeid Izadshenas^{a)}  and Karolina Słowik 

AFFILIATIONS

Institute of Physics, Faculty of Physics, Astronomy and Informatics, Nicolaus Copernicus University in Toruń, 87-100 Toruń, Poland

^{a)} Author to whom correspondence should be addressed: sizadshenas@doktorant.umk.pl

ABSTRACT

Broadband enhancement of Raman signals is vital for molecular spectroscopy and sensing applications. However, typically, there is a compromise between the resonance width and the local field enhancement factors. Here, we merge the broadband open plasmonic cavity concepts with the geometry exploiting narrow gaps and a reflecting layer. This results in a metasurface design that maintains substantial electric field confinement in the gap volume accompanied by a broad spectral response. The confined field is enhanced through constructive interference between the plasmonically enhanced illuminating beam and the field reflected at the bottom layer. The resulting field can interact with analyte molecules and support Raman scattering. With an optimized metasurface geometry involving a pair of gold nanodisks and a thin gold film, we demonstrate numerically that our metasurface can simultaneously enhance Raman signals from various molecular species, potentially resulting in unprecedented signal intensities enhanced by up to 20 orders of magnitude, facilitating molecular detection and identification. Our design offers a practical and promising solution for improving the sensitivity of Raman techniques and has significant implications for the field of nonlinear optical spectroscopy. Moreover, our metasurface is compatible with current fabrication technologies, making it suitable for various applications in sensing and imaging.

© 2023 Author(s). All article content, except where otherwise noted, is licensed under a Creative Commons Attribution (CC BY) license (<http://creativecommons.org/licenses/by/4.0/>). <https://doi.org/10.1063/5.0165585>

I. INTRODUCTION

Gap surface plasmon metasurfaces (GSPMs) are a promising technology in the field of photonics and plasmonics due to their simplicity of fabrication and ability to fully control the amplitude, phase, and polarization of reflected light.¹ These metasurfaces are made of a metal film and metal subwavelength elements arranged in a periodic fashion with a subwavelength dielectric spacer in between. GSPMs have numerous potential applications, including beam-steerers,² flat lenses,³ holograms,^{4,5} absorbers,^{6,7} color printing devices,⁸ polarization controllers,^{9,10} surface wave couplers,¹¹ and dynamically reconfigurable metasurfaces.¹² GSPMs can be relatively easily fabricated with a single lithography step and have the ability to function as an absorbing element due to strong near-field coupling between the metallic layers.^{13–17} Layered structures are commonly used in the construction of GSPMs due to their simplicity.¹⁸ In addition to

their fabrication benefits, GSPMs exhibit broadband behavior.¹⁹ For example, a broadband and highly efficient anomalous meta-reflect array was created using trapezoid-shaped nanorods.² The resulting multifunctional GSP-based metalens was able to split and focus orthogonal linear polarizations into different focal spots. GSPMs may also alter their spectral properties when covered with different dielectric materials, making them useful for sensing applications.²⁰ Overall, the feasibility and simplicity of GSPMs, combined with their broadband resonance character, make them a promising emerging technology with numerous potential applications.¹

The ability to amplify weak optical signals makes plasmonics an attractive avenue for advancing nonlinear optical technologies in fields such as laser frequency conversion, generation of ultrashort laser pulses, all-optical signal processing, ultrafast switching, and spectroscopy.^{21–23} Plasmonic enhancement of Raman spectroscopy signals has been predicted and applied in a variety of

realizations.^{24–27} Among numerous Raman techniques, coherent Raman anti-Stokes scattering (CARS) is especially susceptible to plasmonic enhancement due to the underlying high-order non-linearity. Surface-enhanced CARS has been experimentally realized with thin films,²⁸ nanowires,²⁹ gratings,^{30,31} and nanovoid arrays.³² Exploiting GSPMs in this context led to a demonstration of single-molecule signal detection at the gap of plasmonic nanoquadruplers.³³ Employing core-shell structures enabled the time-resolved recording of single-molecule signals.³⁴ Theoretical work on coupled nanohole-slit arrays predicted CARS signal enhancement by an unprecedented 18 orders of magnitude.³⁵ In the supplementary material, Sec. I, we review selected previous literature on various approaches to CARS enhancement with metallic or dielectric nanostructures. This contribution is focused on a broadband GSPM design feasible for fabrication with state-of-the-art technology. The metasurface supports a broadband optical response achieved due to constructive interference of plasmonic modes. These modes sustain significant absorption losses, which are responsible for their large spectral width. In consequence, absorption, usually considered a drawback, is exploited to achieve a crucial advantageous feature: The broadband operation enables the metasurface to simultaneously support Raman signal enhancement of various molecular species, thus waiving the requirement for tunability. The narrow gap employed in the design enables the combination of this broadband response with a substantial electric field enhancement, potentially giving rise to an unprecedented increase in the Raman signal intensity for a zoo of molecules.

II. METASURFACE CHARACTERISTICS

The GSPM is designed in a metal-insulator-metal configuration. Its unit cell consists of a metal film at the bottom for reflection and constructive interference of fields in the enhancement volume, a SiO₂ spacer layer, and two nanodisks on top sustaining broadband plasmonic enhancement and separated by a gap [Figs. 1(a) and 1(b)]. The metasurface is periodic in the x and y directions and subject to x -polarized plane wave illumination from the top along the z direction. The unit-cell geometry is optimized numerically to maximize

the enhancement factor of CARS for a broad range of molecular Raman shifts (see Methods for simulation details). The resulting geometry has the unit cell period $P = 300$ nm, the radius $r = 39$ nm of each nanodisk, the gap $g = 3$ nm between the nanodisks, the thicknesses $h_1 = 28$ nm of the gold nanodisks, $h_2 = 300$ nm of the insulator, and $h_3 = 270$ nm of the gold film. Fabrication of this and similar structures may be possible, e.g., by combining electron beam lithography with the liftoff technique³⁶ or through pattern transfer nanomanufacturing.^{37,38}

Figure 1(c) shows the reflectance and absorption spectra, consisting of two overlapping resonances in the visible domain that together form broad plateaux, which is our operational spectral range. This range Δf_{EF} exceeding 140 THz is marked in Fig. 1(c) with the red dashed-dotted vertical lines. We define Δf_{EF} based on the requirement of a near-field enhancement factor exceeding 100 at the position in the middle of the gap, as also discussed below. Such strong enhancement is achieved due to constructive interference with the bottom gold reflecting layer: See the supplementary material for simulation results with varying spacer thickness (Sec. II) and in the absence of the reflecting layer (Sec. III). Additionally, the width of the plasmonic resonance of the disks is increased when adding the mirror layer. The transmittance is entirely suppressed in the investigated range due to the presence of the metallic film at the bottom of the structure. Note that we have not assumed vanishing transmittance *a priori*. The numerically evaluated absorption and reflectance spectra based on the finite element method (see Methods) are in very good agreement with the fit to the semi-analytical transmission line theory (TLT) results. The latter method is described in detail in the supplementary material, Sec. IV. The absorption by the metal bulk makes the resonances spectrally broad, turning the loss into an advantage. The broadband character of the metasurface's response may be useful in applications for high-resolution displays,³⁹ plasmonic lenses,⁴ spatial phase modulators,^{40,41} and various Raman spectroscopy realizations.⁴² Despite the significant absorption loss, the local electric field enhancement can actually exceed two orders of magnitude, as we demonstrate in Sec. III, which results from the reflection at the mirror formed by the bottom metallic layer and the constructive interference of the reflected and the incoming field. In

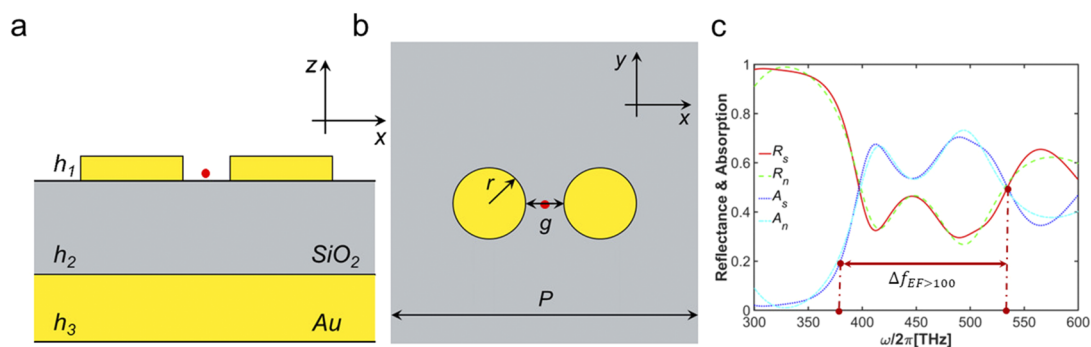


FIG. 1. Side (a) and top (b) views of a unit cell of the investigated metasurface. Periodicity is assumed in the x and y directions. The red dot marks the highest-symmetry point relevant to the following calculations. (c) Reflectance (red solid line) and absorption (blue dotted-dashed line) spectra of the investigated metasurface with fixed geometry parameters given in the main text. The parameters R_s and A_s represent the reflectance and absorption evaluated numerically, while R_n and A_n have been calculated according to the transmission line theory model.

Sec. IV, we discuss how these features can be exploited to achieve an unprecedented enhancement of Raman signals in the coherent anti-Stokes technique.

III. SURFACE ENHANCED COHERENT ANTI-STOKES RAMAN SCATTERING

CARS is a Raman spectroscopy technique for molecular detection and identification that takes advantage of the coherent, background-free signal generated in the sample.⁴³ The technique involves three coherent electromagnetic beams: Co-polarized pump and Stokes beams at frequencies ω_p and ω_s illuminate a molecular sample inducing a sequence of transitions involving the initial ground state $|g\rangle$, the Raman excited state $|R\rangle$, and a pair of virtual states $|v_{1,2}\rangle$, as schematically depicted in Fig. 2(a). Consequently, a dipole moment is induced in the molecule associated with the virtual $|v_2\rangle \rightarrow |g\rangle$ transition. As a result, a coherent signal is generated at the so-called anti-Stokes frequency $\omega_{aS} = 2\omega_p - \omega_s$, following energy conservation. In free-space or traditional-cavity-based implementations, the coherent signal is emitted in the direction determined by momentum conservation. The CARS signal intensity I_{CARS} scales quadratically with the anti-Stokes dipole moment d_{aS} induced by the incoming pump and Stokes beams $E_{x,0}(\mathbf{r}_m, \omega_p)$, $E_{x,0}(\mathbf{r}_m, \omega_s)$ at the molecular position \mathbf{r}_m ,⁴²

$$I_{\text{CARS},0} \sim d_{aS}^2 \sim |\chi_{xxxx}(-\omega_{aS}, \omega_p, -\omega_s, \omega_p) \times E_{x,0}(\mathbf{r}_m, \omega_p)^2 E_{x,0}^*(\mathbf{r}_m, \omega_s)|^2, \quad (1)$$

where the subscript 0 indicates that we refer to free-space implementations and the star denotes the complex conjugation. Without losing generality, we have assumed the polarization of the beams along the x direction, and $\chi_{xxxx}(-\omega_{aS}, \omega_p, -\omega_s, \omega_p)$ is the third-order susceptibility component of molecules at the relevant frequencies.

In the surface-enhanced realization of CARS (SECARS), the signal intensity is improved through several mechanisms, all potentially involving the tailored optical response of plasmonic metasurfaces. We perform our calculations under the weak-excitation assumption, where excitation enhancement and emission enhancement can be treated separately.

1. **Excitation enhancement:** Subwavelength confinement of electromagnetic fields contributes to the signal at the right-hand side of Eq. (1). In consequence, transitions in molecules driven by locally enhanced pump and Stokes fields occur at improved rates. According to Eq. (1), this results in an enhancement of the CARS signal by the factor

$$g_p^2 g_s \equiv \left| \frac{E_{x,\text{MS}}(\mathbf{r}_m, \omega_p)}{E_{x,0}(\omega_p)} \right|^4 \left| \frac{E_{x,\text{MS}}(\mathbf{r}_m, \omega_s)}{E_{x,0}(\omega_s)} \right|^2. \quad (2)$$

Here, the fields at the molecular position in the presence of the metasurface are denoted with the subscript MS and include the incoming and scattered contributions. We have assumed plane-wave illumination, for which the incoming field amplitudes are position-independent. Note that in the presence of the metasurface, the response is not isotropic, and we focus on the x field polarization component that optimizes the performance of the investigated metasurface.

1. The electric near-field enhancement at the highest-symmetry point of the GSPM illuminated with an x -polarized plane wave at normal incidence from the top is shown with the blue curve in Fig. 2(b). This spectrum reflects the double-peak character of the absorption and reflectance from Fig. 1(c), providing strong, over 100-fold field enhancement in a broad spectral range between 378 and 518 THz. This range is wide enough to support different kinds of molecules in a wide range of Raman shifts.
2. **Emission enhancement:** The resulting molecular signal at the anti-Stokes frequency is additionally improved by the radiative Purcell enhancement factor. For a dipolar transition, it can be evaluated as the ratio of electric-dipole emission powers $P(\omega_{aS})$ radiated in the presence and absence of the metasurface,⁴⁴

$$g_{aS} = \frac{P_{\text{rad,MS}}(\mathbf{r}_m, \omega_{aS})}{P_0(\omega_{aS})}. \quad (3)$$

This ratio is plotted as a function of dipole frequency with the orange line in Fig. 2(b). The dipole position has been fixed at

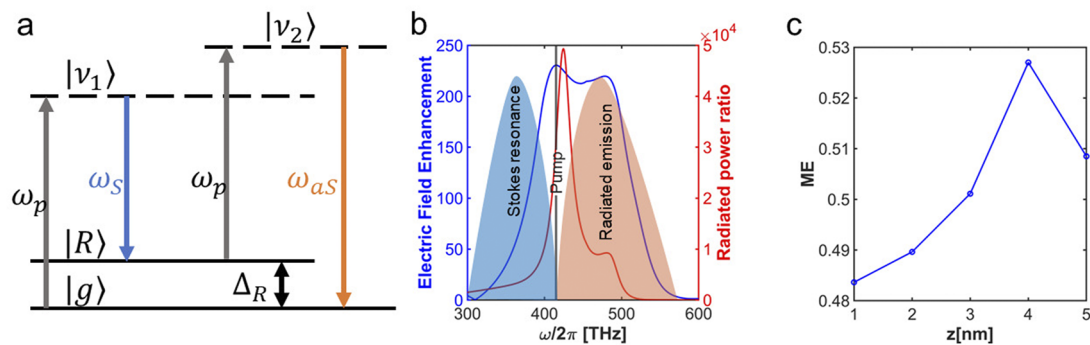


FIG. 2. (a) Molecular energy scheme for CARS: The transitions occur among the ground state $|g\rangle$, the Raman state $|R\rangle$, and a pair of virtual states $|v_{1,2}\rangle$ and are coupled with the pump (black arrows), Stokes (blue arrows), and anti-Stokes (red arrows) beams. (b) Electric field enhancement spectrum (blue curve) and radiated power ratio spectrum (red curve). The shaded regions indicate the spectral ranges in which the Stokes beam is tuned and the anti-Stokes signal is generated. (c) Metasurface efficiency according to Eq. (4) as a function of the molecular position $(0, 0, z)$.

the highest-symmetry point of the metasurface marked with the red dot in Figs. 1(a) and 1(b). For simulation details, see Methods. Naturally, the resonances observed in the power ratio are narrower than those characterizing the field enhancement. The power enhancement exceeding 4 orders of magnitude is achieved again in a broad range of frequencies from 399 to 458 THz.

In parallel to radiative emission, the electromagnetic energy of the molecular dipole can also be absorbed in the metallic bulk of the nanoparticles forming the metasurface. The ratio of radiated and total (radiated + absorbed) powers is quantified with the efficiency

$$\eta(\mathbf{r}_m, \omega) = \frac{P_{\text{rad,MS}}(\mathbf{r}_m, \omega)}{P_{\text{rad,MS}}(\mathbf{r}_m, \omega) + P_{\text{abs,MS}}(\mathbf{r}_m, \omega)}, \quad (4)$$

which is a function of both the position and frequency of the source dipole. Note that this factor is already taken into account in the definition of g_{as} as expressed via the radiated power in Eq. (3). The metasurface efficiency is demonstrated in Fig. 2(c) for the dipole position, which varied along the z axis with respect to the highest-symmetry point of the structure (red dot in Fig. 1) and is relatively stable around the level

of 50%. We provide more results on near-field dependence on geometry parameters in the supplementary material, Sec. II.

Finally, the ratio between the CARS signals obtained in the presence and absence of the metasurface can be expressed as the product of the pump g_p , Stokes g_s , and anti-Stokes g_{as} enhancement factors, defined in Eqs. (2) and (3)

$$G_{\text{SECARS}}(\omega_p, \omega_s, \mathbf{r}_m) = g_{\text{as}}(2\omega_p - \omega_s, \mathbf{r}_m) g_p(\omega_p, \mathbf{r}_m)^2 g_s(\omega_s, \mathbf{r}_m). \quad (5)$$

We have emphasized the spectral dependence of G_{SECARS} on the pump and Stokes frequencies and the molecular position \mathbf{r}_m concerning the nanoparticle geometry. Please note that the limitation to molecules responding to the collinear pump and Stokes polarization could be lifted with a polarization-independent metasurface design, e.g., with an additional disk dimer oriented along the y direction.

IV. SURFACE ENHANCED CARS SIGNAL CHARACTERISTICS

In the usual experimental realizations of CARS, the pump frequency ω_p is fixed while the Stokes frequency ω_s is fine-tuned. On

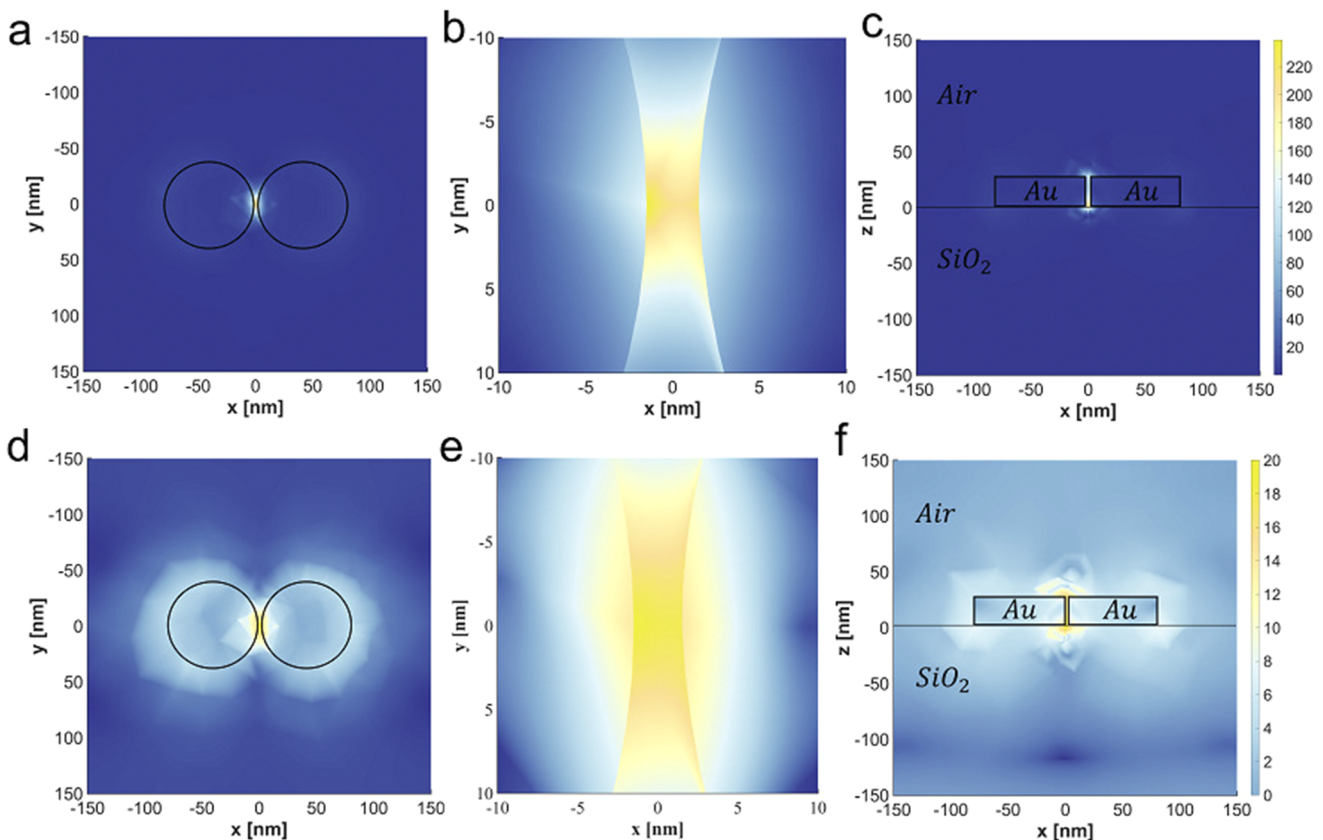


FIG. 3. (a)–(c) Field enhancement distributions around the nanodisks: (a) in the xy plane with $z = 0$, (b) zoom of (a), (c) in the xz plane, with $y = 0$. (d)–(f) Maps of the logarithmic SECARS enhancement factor $\log_{10}[G_{\text{SECARS}}]$ (d) for $z = 0$, (f) for $y = 0$. (e) Zoomed panel (d).

two-photon Raman resonance, $\omega_p - \omega_s = \Delta_R$, the anti-Stokes signal is efficiently generated. Below, we fix the pump frequency at $\omega_p/2\pi = 450$ THz at the center of the plateaux spectral region in Fig. 1(c), which allows flexibility of the Stokes and anti-Stokes beam frequencies that ideally should also fit in the plateaux. We evaluate $G_{\text{SECARS}}(\omega_p, \omega_s, \mathbf{r}_m)$ for a given Stokes frequency $\omega_s = \omega_p - \Delta_R$. The anti-Stokes signal frequency becomes $\omega_{\text{aS}} = \omega_p + \Delta_R$.

First, we consider a fixed $\Delta_R = 35$ THz = 1167 cm^{-1} , corresponding to a resonant Stokes frequency of $\omega_s/2\pi = 415$ THz. The field enhancement distribution around the nanostructure is shown in Figs. 3(a)–3(c) for illumination at the pump frequency. Enhancement factors exceed 200 in the gap region. Similar field profiles are found for other illumination frequencies in the range between 360 and 540 THz, in accordance with the spectrum in Fig. 2(b). We evaluate the SECARS enhancement factor $G_{\text{SECARS}}(\omega_p, \omega_s, \mathbf{r})$ at different positions \mathbf{r} in the unit cell with a fixed $z = 0$ nm [Fig. 3(d)] or $y = 0$ [Fig. 3(f)]. (See also a depiction in greater detail in the supplementary material, Sec. V.) The simulations involve independent calculations of the Stokes and pump enhancement factors with the plane wave and the anti-Stokes enhancement factor in the dipole illumination scheme, as described in Eqs. (2) and (3). The resulting SECARS enhancement maps demonstrate that the strongest signal enhancement is expected for molecular positions at the highest-symmetry point in the gap between the nanodisks. The enhancement

factor predicted at the optimal point reaches an impressive 19 orders of magnitude, slightly exceeding previously obtained literature results.^{31,35} This value is also well above the single-molecule detection threshold for the CARS technique, estimated at 10 orders of magnitude.³³ The volume of space where a single molecule could be detected assuming this threshold corresponds to the yellow regions in Figs. 3(d)–3(f). Figure 3(e) shows a zoom of panel (d) on the highest-enhancement region. Note that the saturation threshold for the off-resonant CARS scenario, which is here considered, and for pulsed illumination has been predicted at the pump intensity $I_p \sim 10^{22} \frac{\text{W}}{\text{m}^2}$ at the Stokes intensity $I_s \sim 10^{15} \frac{\text{W}}{\text{m}^2}$.⁴⁵ These values hugely exceed realistic numbers for plasmonic-based scenarios.

As a result of the broadband character of the near field enhancement spectrum [Fig. 4(a)], the SECARS enhancement factor at a fixed position $G_{\text{SECARS}}(\omega_p, \omega_s, \mathbf{r}_{\text{opt}})$ is robust for the broad range of Raman shifts up to 1700 cm^{-1} [Fig. 4(b)]. The supplementary material, Sec. II, illustrates more curves corresponding to other values of z . The same Figs. 4(a) and 4(b) demonstrate that the near field enhancement factor and the resulting SECARS signal enhancement factor may vary strongly as the molecular position is shifted along the z axis. The maximum electric field enhancement is achieved in the gap directly above the glass surface and, depending on field frequency, drops by a factor of 4–5 at a height of 30 nm (supplementary material, Fig. S2). For the highly nonlinear process of CARS, this

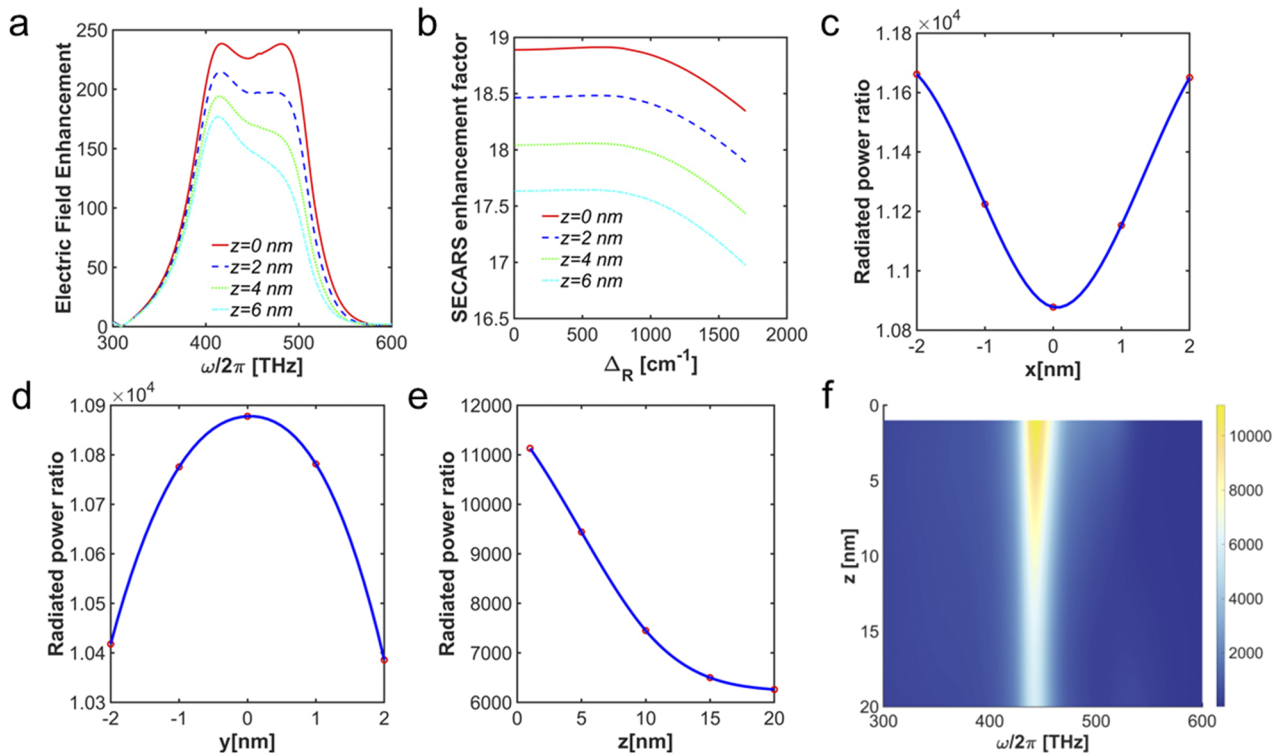


FIG. 4. (a) and (b) Dependence of electric field enhancement spectra $g(\mathbf{r}_m, \omega)$ in the plane-wave illumination scheme (a) and SECARS enhancement spectra $G_{\text{SECARS}}(\mathbf{r}_m, \omega)$ (b) on the molecular position $\mathbf{r}_m = (0, 0, z)$. (c)–(e) Radiated power ratio $\frac{P_{\text{rad,MS}}(\mathbf{r}_m, \omega/2\pi=450 \text{ THz})}{P_0(\omega/2\pi=450 \text{ THz})}$ for the molecular position \mathbf{r}_m varied along the x (c), y (d) or z (e) axes. In (c), $y = 0$ and $z = 2.5$ nm; in (d), $x = 0$ and $z = 2.5$ nm; in (e), $x = y = 0$. (f) As in (e), but for a range of dipole source frequencies.

corresponds to a reduction of the SECARS signal enhancement factor from 19 to 15 orders of magnitude. The most stable response is obtained around $z = \frac{h_L}{2}$ (supplementary material, Fig. S2), i.e., around the middle of the disk height due to a capacitor effect. Above the disks, the performance quickly drops for $z > 30$ nm. The radiated power ratio at the anti-Stokes frequency proves to be much more robust against position shifts in the xy plane but also sensitive to the position in the z direction [Figs. 4(c)–4(e)]. Panel (f) demonstrates that the power enhancement spectrum is suppressed by a factor of 2 as the position changes from $z = 1$ nm to $z = 20$ nm. The averaged SECARS enhancement in the 20×20 nm² area of the xy plane centered at $z = 0$ [Fig. 3(e)] and excluding the area within the metallic disks is $G_{\text{SECARS}}^{\text{av}} = 5 \times 10^{16}$. Similarly, the average enhancement factor in the fragment of the $y = 0$ plane between the disks is $G_{\text{SECARS}}^{\text{av}} = 1.6 \times 10^{17}$.

Among the geometry parameters of the metasurface, the small gap in which the electromagnetic fields are strongly confined is crucial to achieving such a significant SECARS enhancement. In Figs. 5(a) and 5(b), we study the strong modulation of the near field enhancement factor $g(\mathbf{r}_{\text{opt}}, \omega)$ (a) and the SECARS signal enhancement factor G_{SECARS} (b) on the gap size in the range of 2–15 nm. Note the robustness of G_{SECARS} against the Raman shift again [Fig. 5(b)]. The possibility to further enhance the signal with the same geometry is limited, as gaps smaller than 2 nm are challenging to fabricate. Moreover, one should not expect further signal enhancement with even smaller gaps: larger molecules might be unlikely to fit in the gap, tunneling effects might suppress the field enhancement, and finally, surface adsorption might change the molecular chemical and, hence, Raman properties. On the other hand, the predicted CARS enhancement factors already reach the single-molecule detection threshold for gaps as large as 15 nm [see Fig. 5(b)], which should not pose particular technological challenges and can be fabricated by electron beam lithography.^{46–48} Another parameter that strongly influences the field enhancement factor and, therefore, the SECARS signal is the disk radius [Figs. 5(c) and 5(d)]. As the radius increases from 30 to 60 nm, we observe the appearance and splitting of a pair of resonances with an optimized broadband near-field spectrum for radii of around 40 nm [Fig. 5(c)]. The broad response for this radius results in the optimized SECARS enhancement factor [Fig. 5(d)]. The dependence of the enhancement factors on other geometrical

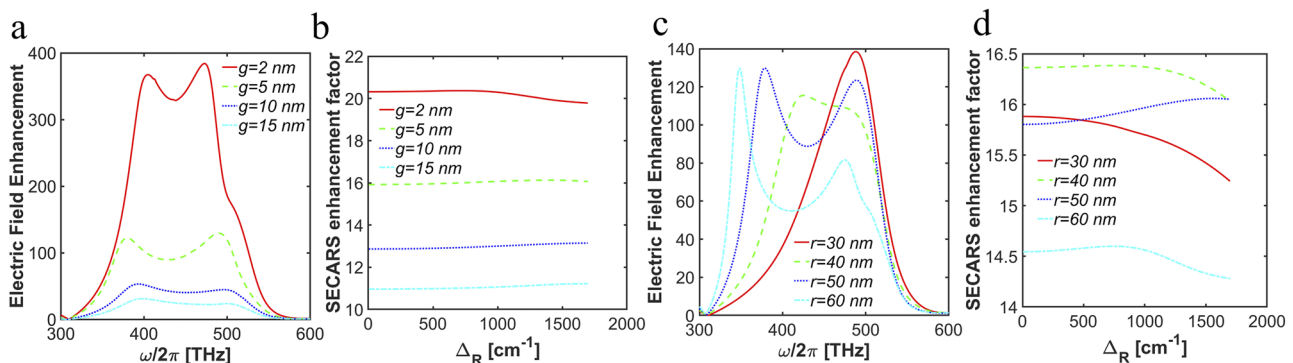


FIG. 5. (a) and (b) Dependence of electric field enhancement spectra $g(\mathbf{r}_{\text{opt}}, \omega)$ (a) and SECARS enhancement spectra $G_{\text{SECARS}}(\mathbf{r}_{\text{opt}}, \omega)$ (b) on the gap size g . (c) and (d) As (a) and (b), but for varied disk radii.

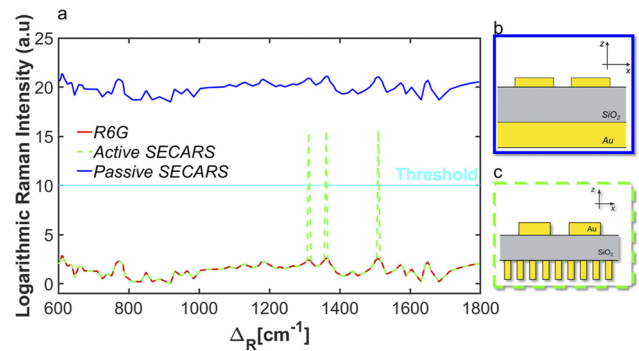


FIG. 6. Red solid line: Raman spectrum of rhodamine 6G from Ref. 49. Green dashed line: Raman spectrum of rhodamine 6G multiplied by the SECARS signal enhancement factor for the active metasurface discussed in Ref. 31. Blue solid line: Raman spectrum of rhodamine 6G multiplied by the SECARS signal enhancement factor for the metasurface proposed in this work. The cyan line represents the single-molecule detection threshold.

parameters of the metasurface is discussed in the supplementary material, Sec. II. In the same section, we characterize the impact of smoothed disk edges.

Finally, we compare the performance of the passive metasurface studied in this work with the previously investigated active design.³¹ The latter was based on the metal-insulator-grating configuration, with the bottom gold layer replaced with a grating. That geometry allowed for optical response in the form of three tunable resonance peaks to quasi-independently control the pump, Stokes, and anti-Stokes modes. Their spectral positions could be adjusted by geometry engineering or the incident angle of the illuminating beams to match selected molecular Raman profiles. The possibility of post-fabrication tuning through the incidence angle yields the “active” characteristic of the metasurface in opposition to the “passive” one, tunable by design. We have demonstrated the tunability of rhodamine 6G with its characteristic Raman peaks at 1314, 1363, and 1512 nm, all enhanced above the single-molecule detection threshold (Fig. 6). In the figure, the red line represents

the Raman spectrum $S_{R6G}(\Delta)$ of rhodamine 6G,⁴⁹ while the green dashed line is the predicted spectrum of a rhodamine molecule optimally positioned and oriented on the optimized active metasurface. This result is calculated as a product of the rhodamine spectrum and the predicted signal enhancement $G_{\text{SECARS}}^{\text{active}}(\Delta)S_{R6G}(\Delta)$. Contrary, the passive metasurface described here does not enforce three resonances for the three field modes. Dropping this demanding condition allowed us to achieve a much stronger amplification over a wide spectral range; now, the entire investigated range of the Raman spectrum of the molecule is enhanced by a factor of the order of 10^{19} with little modulations (blue line in Fig. 6). This fact makes the metasurface universal, i.e., supporting CARS signal enhancement for a variety of molecular species. Since the metasurface enhances the signal strength but weakly distorts the molecular Raman response spectral shape, it may support both molecular detection and identification. Moreover, the structure's potential to enhance nonlinear light-matter interaction processes extends beyond the CARS technique. In the supplementary material, Sec. VI, we analyze the potential of the structure to enhance SERS signals.

V. CONCLUSIONS

In summary, this article's broadband metasurface, combining gap geometry with a reflecting layer, offers a promising solution for Raman spectroscopy applications. The optimized metasurface unit cell has a period of 300 nm, a nanodisk radius of 39 nm, a gap between the nanodisks of 3 nm, and nanodisk, spacer, and gold film thicknesses of 28, 300, and 270 nm, respectively. Due to the broadband optical response, the metasurface is able to simultaneously enhance Raman signals for various molecular species without the need for tunability and holds the potential for an unprecedented increase in signal intensity.

Our study demonstrated excellent agreement between optical responses obtained through numerical simulations and within transmission line theory. Our estimates of the SECARS enhancement factor, based on realistic experimental scenarios, predict significant signal enhancement beyond the single-molecule detection threshold, even in relatively large spatial volumes compared to other plasmonic nanostructures.

Furthermore, the device's broadband operation makes it compatible with various types of molecules, providing opportunities for molecular detection and identification applications at low concentrations, even at the single-molecule level. Our work provides a promising solution for advancing the study of molecular interactions at the nanoscale, with significant implications for the field of nonlinear optics.

SUPPLEMENTARY MATERIAL

In the supplementary material file, we provide an overview of previous literature on various realizations of SECARS. More results for metasurfaces with varied geometry parameters are provided. Additionally, we have included the effects of mirror metal film in the optical responses of the metasurfaces. Transmission line theory is introduced and the fit parameters that reproduce the numerically obtained data are collected. We discuss in greater detail the electric field distribution in the metasurface unit cell. Finally, we delve into the expanding applications of broadband metasurfaces.

ACKNOWLEDGMENTS

The authors are grateful for the financial support of the National Science Center, Poland, Grant No. 2018/31/D/ST3/01487.

AUTHOR DECLARATIONS

Conflict of Interest

The authors have no conflicts to disclose.

Author Contributions

Saeid Izadshenas Jahromi: Conceptualization (equal); Formal analysis (equal); Investigation (equal); Methodology (equal); Software (equal); Validation (equal); Visualization (equal); Writing – original draft (equal); Writing – review & editing (equal). **Karolina Słowik:** Conceptualization (equal); Formal analysis (equal); Project administration (equal); Resources (equal); Supervision (equal); Validation (equal); Writing – original draft (equal); Writing – review & editing (equal).

DATA AVAILABILITY

The data that support the findings of this study are available from the corresponding author upon reasonable request.

APPENDIX: METHODS

The metasurface was modeled using the finite-element method using the COMSOL Multiphysics simulation software. The dispersive properties of gold were modeled using the Johnson and Christie data,⁵⁰ while the spacer layer was modeled as a dielectric with a refractive index of $n = 1.45$.

For the plane-wave illumination scenario, we exploit the periodic boundary condition along the x and y directions. Two ports were placed in the z direction to calculate the absorption, reflectance, and electric field distribution.

For the dipolar illumination scheme, the scattering boundary conditions are assumed to be a spherical domain surrounded by perfectly matched layers, and the source is modeled as an x -oriented monochromatic point-dipole. We determine the time-averaged scattered P_{rad} and absorbed P_{abs} powers according to⁵¹

$$P_{\text{rad}}(\omega) = \iint \langle \mathbf{E}_{\text{sca}}(\mathbf{r}, \omega) \times \mathbf{H}_{\text{sca}}(\mathbf{r}, \omega) \rangle \cdot d\mathbf{A}, \quad (\text{A1})$$

$$P_{\text{abs}}(\omega) = \iiint \langle \mathbf{J}_{\text{ind}}(\mathbf{r}, \omega) \cdot \mathbf{E}_{\text{ind}}(\mathbf{r}, \omega) \rangle \cdot dV, \quad (\text{A2})$$

with the electric and magnetic scattered fields given by $\mathbf{E}_{\text{sca}}(\mathbf{r}, \omega)$ and $\mathbf{H}_{\text{sca}}(\mathbf{r}, \omega)$. The symbol $\mathbf{E}_{\text{ind}}(\mathbf{r}, \omega)$ stands for the electric field induced in the metal, with the corresponding current density $\mathbf{J}_{\text{ind}}(\mathbf{r}, \omega)$. The integrals are, respectively, performed on an oriented sphere surface \mathbf{A} of a large radius of 1209 nm and inside the volume V of the GSPM metasurface.

The transmission line theory approach to model the optical response of the proposed metasurface is described in detail in the

supplementary material, Sec. IV. The numerical fit to the obtained analytical expressions has been performed using the MATLAB built-in fit function. Custom codes are available upon request.

REFERENCES

- 1 F. Ding, Y. Yang, R. A. Deshpande, and S. I. Bozhevolnyi, "A review of gap-surface plasmon metasurfaces: Fundamentals and applications," *Nanophotonics* **7**, 1129–1156 (2018).
- 2 Z. Li, E. Palacios, S. Butun, and K. Aydin, "Visible-frequency metasurfaces for broadband anomalous reflection and high-efficiency spectrum splitting," *Nano Lett.* **15**, 1615–1621 (2015).
- 3 F. Aieta, P. Genevet, M. A. Kats, N. Yu, R. Blanchard, Z. Gaburro, and F. Capasso, "Aberration-free ultrathin flat lenses and axicons at telecom wavelengths based on plasmonic metasurfaces," *Nano Lett.* **12**, 4932–4936 (2012).
- 4 D. Wen, F. Yue, G. Li, G. Zheng, K. Chan, S. Chen, M. Chen, K. F. Li, P. W. H. Wong, K. W. Cheah, E. Yue Bun Pun, S. Zhang, and X. Chen, "Helicity multiplexed broadband metasurface holograms," *Nat. Commun.* **6**, 8241–8247 (2015).
- 5 X. Li, L. Chen, Y. Li, X. Zhang, M. Pu, Z. Zhao, X. Ma, Y. Wang, M. Hong, and X. Luo, "Multicolor 3D meta-holography by broadband plasmonic modulation," *Sci. Adv.* **2**, e1601102 (2016).
- 6 K. Aydin, V. E. Ferry, R. M. Briggs, and H. A. Atwater, "Broadband polarization-independent resonant light absorption using ultrathin plasmonic super absorbers," *Nat. Commun.* **2**, 517 (2011).
- 7 H. Zhu, F. Yi, and E. Cubukcu, "Plasmonic metamaterial absorber for broadband manipulation of mechanical resonances," *Nat. Photonics* **10**, 709–714 (2016).
- 8 A. S. Roberts, A. Pors, O. Albrektsen, and S. I. Bozhevolnyi, "Subwavelength plasmonic color printing protected for ambient use," *Nano Lett.* **14**, 783–787 (2014).
- 9 N. Yu, F. Aieta, P. Genevet, M. A. Kats, Z. Gaburro, and F. Capasso, "A broadband, background-free quarter-wave plate based on plasmonic metasurfaces," *Nano Lett.* **12**, 6328–6333 (2012).
- 10 Y. Yang, W. Wang, P. Moitra, I. I. Kravchenko, D. P. Briggs, and J. Valentine, "Dielectric meta-reflectarray for broadband linear polarization conversion and optical vortex generation," *Nano Lett.* **14**, 1394–1399 (2014).
- 11 F. Ding, R. Deshpande, and S. I. Bozhevolnyi, "Bifunctional gap-plasmon metasurfaces for visible light: Polarization-controlled unidirectional surface plasmon excitation and beam steering at normal incidence," *Light: Sci. Appl.* **7**, 17178 (2018).
- 12 Q. Wang, E. T. F. Rogers, B. Gholipour, C.-M. Wang, G. Yuan, J. Teng, and N. I. Zheludev, "Optically reconfigurable metasurfaces and photonic devices based on phase change materials," *Nat. Photonics* **10**, 60–65 (2016).
- 13 N. Mou, S. Sun, H. Dong, S. Dong, Q. He, L. Zhou, and L. Zhang, "Hybridization-induced broadband terahertz wave absorption with graphene metasurfaces," *Opt. Express* **26**, 11728–11736 (2018).
- 14 A. Nemat, Q. Wang, M. Hong, and J. Teng, "Tunable and reconfigurable metasurfaces and metadevices," *Opto-Electron. Adv.* **1**, 180009 (2018).
- 15 J. Park, J.-H. Kang, X. Liu, S. J. Maddox, K. Tang, P. C. McIntyre, S. R. Bank, and M. L. Brongersma, "Dynamic thermal emission control with InAs-based plasmonic metasurfaces," *Sci. Adv.* **4**, eaat3163 (2018).
- 16 C. Meng, P. C. V. Thrane, F. Ding, J. Gjesing, M. Thomaschewski, C. Wu, C. Dirdal, and S. I. Bozhevolnyi, "Dynamic piezoelectric MEMS-based optical metasurfaces," *Sci. Adv.* **7**, eabg5639 (2021).
- 17 S. Gwo, C.-Y. Wang, H.-Y. Chen, M.-H. Lin, L. Sun, X. Li, W.-L. Chen, Y.-M. Chang, and H. Ahn, "Plasmonic metasurfaces for nonlinear optics and quantitative SERS," *ACS Photonics* **3**, 1371–1384 (2016).
- 18 A. Pors and S. I. Bozhevolnyi, "Plasmonic metasurfaces for efficient phase control in reflection," *Opt. Express* **21**, 27438–27451 (2013).
- 19 S. Wang, P. C. Wu, V.-C. Su, Y.-C. Lai, C. Hung Chu, J.-W. Chen, S.-H. Lu, J. Chen, B. Xu, C.-H. Kuan, T. Li, S. Zhu, and D. P. Tsai, "Broadband achromatic optical metasurface devices," *Nat. Commun.* **8**, 187 (2017).
- 20 N. Liu, T. Weiss, M. Mesch, L. Langguth, U. Eigenthaler, M. Hirscher, C. Sonnichsen, and H. Giessen, "Planar metamaterial analogue of electromagnetically induced transparency for plasmonic sensing," *Nano Lett.* **10**, 1103–1107 (2010).
- 21 E. Kim, F. Wang, W. Wu, Z. Yu, and Y. R. Shen, "Nonlinear optical spectroscopy of photonic metamaterials," *Phys. Rev. B* **78**, 113102 (2008).
- 22 J. Butet, P.-F. Brevet, and O. J. F. Martin, "Optical second harmonic generation in plasmonic nanostructures: From fundamental principles to advanced applications," *ACS Nano* **9**, 10545–10562 (2015).
- 23 M. Kauranen and A. V. Zayats, "Nonlinear plasmonics," *Nat. Photonics* **6**, 737–748 (2012).
- 24 L. Tong, T. Zhu, and Z. Liu, "Approaching the electromagnetic mechanism of surface-enhanced Raman scattering: From self-assembled arrays to individual gold nanoparticles," *Chem. Soc. Rev.* **40**, 1296–1304 (2011).
- 25 S. S. Kharintsev, A. V. Kharitonov, S. K. Saikin, A. M. Alekseev, and S. G. Kazarian, "Nonlinear Raman effects enhanced by surface plasmon excitation in planar refractory nanoantennas," *Nano Lett.* **17**, 5533–5539 (2017).
- 26 K. Milenko, S. S. Fuglerud, A. Aksnes, R. Ellingsen, and D. R. Hjelme, "Optimization of SERS sensing with micro-lensed optical fibers and Au nanofilm," *J. Lightwave Technol.* **38**, 2081–2085 (2020).
- 27 A. M. Shrivastav, U. Cvelbar, and I. Abdulhalim, "A comprehensive review on plasmonic-based biosensors used in viral diagnostics," *Commun. Biol.* **4**, 70 (2021).
- 28 C. Zong, R. Cheng, F. Chen, P. Lin, M. Zhang, Z. Chen, C. Li, C. Yang, and J.-X. Cheng, "Wide-field surface-enhanced coherent anti-Stokes Raman scattering microscopy," *ACS Photonics* **9**, 1042–1049 (2022).
- 29 H. Kim, D. K. Taggart, C. Xiang, R. M. Penner, and E. O. Potma, "Spatial control of coherent anti-Stokes emission with height-modulated gold zig-zag nanowires," *Nano Lett.* **8**, 2373–2377 (2008).
- 30 L. Ouyang, T. Meyer-Zedler, K.-M. See, W.-L. Chen, F.-C. Lin, D. Akimov, S. Ehtesabi, M. Richter, M. Schmitt, Y.-M. Chang, S. Gräfe, J. Popp, and J. S. Huang, "Spatially resolving the enhancement effect in surface-enhanced coherent anti-Stokes Raman scattering by plasmonic Doppler gratings," *ACS Nano* **15**, 809–818 (2020).
- 31 S. Izadshenas, P. Maslowski, T. Herr, and K. Słowik, "Multiresonant metasurface for Raman spectroscopy beyond single molecule detection level," *EPJ Appl. Metamater.* **9**, 11 (2022).
- 32 C. Steuwe, C. F. Kaminski, J. J. Baumberg, and S. Mahajan, "Surface enhanced coherent anti-Stokes Raman scattering on nanostructured gold surfaces," *Nano Lett.* **11**, 5339–5343 (2011).
- 33 Y. Zhang, Y.-R. Zhen, O. Neumann, J. K. Day, P. Nordlander, and N. J. Halas, "Coherent anti-Stokes Raman scattering with single-molecule sensitivity using a plasmonic Fano resonance," *Nat. Commun.* **5**, 4424–4427 (2014).
- 34 S. Yampolsky, D. A. Fishman, S. Dey, E. Hulkko, M. Banik, E. O. Potma, and V. A. Apkarian, "Seeing a single molecule vibrate through time-resolved coherent anti-Stokes Raman scattering," *Nat. Photonics* **8**, 650–656 (2014).
- 35 Y. Feng, Y. Wang, F. Shao, L. Meng, and M. Sun, "Surface-enhanced coherent anti-Stokes Raman scattering based on coupled nanohole-slit arrays," *Phys. Chem. Chem. Phys.* **24**, 13911–13921 (2022).
- 36 K. Q. Le, Q. M. Ngo, and T. K. Nguyen, "Nanostructured metal-insulator-metal metamaterials for refractive index biosensing applications: Design, fabrication, and characterization," *IEEE J. Sel. Top. Quantum Electron.* **23**, 388–393 (2017).
- 37 L. Ye, T. Pearson, Y. Cordeau, O. T. Mefford, and T. M. Crawford, "Triggered self-assembly of magnetic nanoparticles," *Sci. Rep.* **6**, 23145 (2016).
- 38 L. Ye, T. Pearson, C. Dolbashian, P. Pstrak, A. Mohtasebzadeh, B. Fellows, O. T. Mefford, and T. M. Crawford, "Magnetic-field-directed self-assembly of programmable mesoscale shapes," *Adv. Funct. Mater.* **26**, 3983–3989 (2016).
- 39 W. Yang, S. Xiao, Q. Song, Y. Liu, Y. Wu, S. Wang, J. Yu, J. Han, and D.-P. Tsai, "All-dielectric metasurface for high-performance structural color," *Nat. Commun.* **11**, 1864 (2020).
- 40 Y. Yao, R. Shankar, M. A. Kats, Y. Song, J. Kong, M. Loncar, and F. Capasso, "Electrically tunable metasurface perfect absorbers for ultrathin mid-infrared optical modulators," *Nano Lett.* **14**, 6526–6532 (2014).

- ⁴¹G.-Y. Lee, G. Yoon, S.-Y. Lee, H. Yun, J. Cho, K. Lee, H. Kim, J. Rho, and B. Lee, "Complete amplitude and phase control of light using broadband holographic metasurfaces," *Nanoscale* **10**, 4237–4245 (2018).
- ⁴²G. Eesley, *Coherent Raman Spectroscopy* (Pergamon Press, 1981).
- ⁴³R. F. Begley, A. B. Harvey, and R. L. Byer, "Coherent anti-Stokes Raman spectroscopy," *Appl. Phys. Lett.* **25**, 387–390 (1974).
- ⁴⁴A. E. Krasnok, A. P. Slobozhanyuk, C. R. Simovski, S. A. Tretyakov, A. N. Poddubny, A. E. Miroshnichenko, Y. S. Kivshar, and P. A. Belov, "An antenna model for the Purcell effect," *Sci. Rep.* **5**, 12956–13016 (2015).
- ⁴⁵A. K. Patnaik, S. Roy, and J. R. Gord, "Saturation of vibrational coherent anti-Stokes Raman scattering mediated by saturation of the rotational Raman transition," *Phys. Rev. A* **87**, 043801 (2013).
- ⁴⁶G.-C. Li, Q. Zhang, S. A. Maier, and D. Lei, "Plasmonic particle-on-film nanocavities: A versatile platform for plasmon-enhanced spectroscopy and photochemistry," *Nanophotonics* **7**, 1865–1889 (2018).
- ⁴⁷S. Zhang, G.-C. Li, Y. Chen, X. Zhu, S.-D. Liu, D. Y. Lei, and H. Duan, "Pronounced Fano resonance in single gold split nanodisks with 15 nm split gaps for intensive second harmonic generation," *ACS Nano* **10**, 11105–11114 (2016).
- ⁴⁸H. Duan, A. I. Fernández-Domínguez, M. Bosman, S. A. Maier, and J. K. W. Yang, "Classical down to the nanometer scale," *Nano Lett.* **12**, 1683–1689 (2012).
- ⁴⁹E. Kirubha and P. K. Palanisamy, "Green synthesis, characterization of Au–Ag core–shell nanoparticles using gripe water and their applications in nonlinear optics and surface enhanced Raman studies," *Adv. Nat. Sci.: Nanosci. Nanotechnol.* **5**, 045006 (2014).
- ⁵⁰P. B. Johnson and R.-W. Christy, "Optical constants of the noble metals," *Phys. Rev. B* **6**, 4370 (1972).
- ⁵¹K. Stowik, R. Filter, J. Straubel, F. Lederer, and C. Rockstuhl, "Strong coupling of optical nanoantennas and atomic systems," *Phys. Rev. B* **88**, 195414 (2013).

Supporting information for:

Metasurface for broadband coherent Raman signal enhancement beyond the single-molecule detection threshold

S. Izadshenas, K. Słowik

Contents

1	Advances in SECARS: an overview of previous literature	1
2	Tailoring optical response of the metasurface: variation of geometrical parameters	4
3	Enhancing Optical Response through Metal Film Mirrors	4
4	Transmission line theory for gap surface plasmon metasurface	7
5	Field distribution of a pair of coupled dipoles	10
6	Expanding Applications of Broadband Metasurfaces	10

1 Advances in SECARS: an overview of previous literature

Table I collects a selection of references to recent works on CARS enhancement with plasmonic or dielectric nanostructures. We briefly review these contributions below.

In their publication, Abedin et al.¹ showcase their experimental discoveries that utilize gold film and gold nanoparticles to improve CARS for sensing chemical and biomolecular substances. Their research exhibits a maximum electric field enhancement factor of 100 and a signal enhancement of 12 orders of magnitude. The study centers on the Raman shift spanning from 1540 to 1660 cm^{-1} for mercaptomethyl benzonitrile (MMBN) molecules. These findings hold potential for the advancement of more effective CARS methods for sensing chemical and biomolecular substances in diverse scientific and medical domains¹.

Abedin et al.² tackle the issue of stability and reproducibility in SECARS for swift biomolecular sensing by employing high-index dielectric particles as nanoantennas, replacing

Table I: Selection of previous works exploring CARS enhancement using plasmonic or dielectric nanostructures.

SECARS			
Source	Structure	Raman range [cm ⁻¹]	Signal enhance- ment
1	Metal-dielectric nanojunction	1550 – 1650	10 ¹²
2	Silicon nanoantenna	1580 – 1600	10 ⁹
3	Plasmonic Doppler grating	400 – 2400	10 ³
4	Au NPs film	1525 – 1675	10 ⁵
5	MoS ₂	980 – 1060	10 ⁹
6	coupled nanohole-slit arrays	0 – 4000	10 ¹⁸
7	Plasmonic nanoquadrumer	800 – 2000	10 ¹¹
8	Plasmonic nanovoid gold surface	800 – 2000	10 ⁴
9	Gold Zig-Zag Nanowires	-	10 ⁵
10	Plasmonic coreshell NPs	1550 – 1650	-

conventional metallic antennas. The team’s experimental demonstration of enhanced molecular CARS signals observed in proximity to Si nanoantennas is the first of its kind and offers superior thermal stability in contrast to metallic counterparts. The maximum electric field enhancement is 14 in the 1540-1630 cm⁻¹ range, and the maximum signal enhancement is 9 orders of magnitude. Pyridine molecules are the focus of the team’s study. These findings carry significant implications for the advancement of SECARS as a dependable tool for biomolecular sensing in various scientific and medical domains².

The work by Ouyang et al.³ investigates the amplification effects of plasmonic gratings in the input and output beams of nonlinear SECARS. Using a plasmonic Doppler grating (PDG), the authors experimentally analyze the enhancement mechanism and demonstrate that while simultaneous enhancement in the input and output beams is significant for SECARS, the amplification in the pump and anti-Stokes beams plays a more crucial role in the overall enhancement than in the Stokes beam. The PDG platform may also be utilized to examine enhancement mechanisms in other nonlinear light-matter interactions or the impact of plasmonic gratings on fluorescence lifetime. The maximum signal enhancement for Rhodamine 6G in the study is 3 orders of magnitude within the range of 400-2400 cm⁻¹³.

Zong et al.⁴ have developed a wide-field CARS microscope for swift imaging of nanotags in live cells and label-free detection of metabolic molecules. This microscope achieves an imaging speed of 120 fps, capturing hyperspectral stacks of over 1 million Raman spectra simultaneously with a spectral resolution of 10 cm⁻¹. The maximum signal enhancement for metabolic molecules falls within the range of 1525-1675 cm⁻¹, with a value of 5 orders of magnitude. The applications of this development include 3D time-lapse wide-field CARS imaging of nanotags in live cells and label-free detection of adenine released from the *S. aureus* bacteria⁴.

Shutov and colleagues⁵ investigate the potential of two-dimensional (2D) semiconductors, particularly monolayer molybdenum disulfide (MoS₂), in SECARS spectroscopy. They report a substantial chemical enhancement factor of 10⁹ over CARS for pyridine-ethanol solutions containing 2D MoS₂ nanocrystals, attributed to charge transfer states and resonant MoS₂

excitation. The maximum signal enhancement for pyridine molecules is 9 orders of magnitude in the range of 980-1060 cm^{-1} . The study indicates that 2D semiconductors could be a promising alternative to noble metal nanoparticles for SECARS applications⁵.

Feng et al.⁶ challenge the use of metal nanohole arrays for SECARS due to their relatively low signal enhancement. Through theoretical studies based on the finite element method, the authors investigate the effect of nanoslits on SECARS and optical transmission in Au nanohole-slit arrays. They demonstrate that the addition of nanoslits significantly enhances the SECARS signal, resulting in approximately $\sim 10^6$ improvement in signal enhancement compared to nanohole-only structures. Exploiting plasmonic nanohole-slit structures leads to a maximum field enhancement of 18 orders of magnitude in the range of up to 4000 cm^{-1} . The authors also demonstrate the high directionality of the device, which is useful for designing high-sensitivity SECARS platforms. These findings open up new engineering directions for high-performance sensing and spectroscopy devices⁶.

Zhang et al.⁷ propose utilizing plasmonic Fano resonances for achieving single-molecule sensitivity in CARS. The authors demonstrate the enhancement in CARS signal of about 11 orders of magnitude compared to spontaneous Raman scattering, enabling the detection of individual molecules. They use the statistically rigorous bi-analyte method to verify the findings. The approach may have consequences for medical diagnostics, forensics, homeland security, and other fields requiring high-sensitivity molecular detection. The maximum signal enhancement is achieved in the Raman range of 800-2000 cm^{-1} ⁷.

Steuwe and colleagues⁸ have demonstrated a SECARS sensitivity enhancement of $> 10^3$ times over SERS using reproducible nanostructured surfaces. A correlation between plasmon resonances and SECARS intensities is demonstrated and improved by $\sim 10^5$ over standard CARS. The demonstrated imaging of molecular monolayers using SECARS paves the way for reliable single-molecule Raman spectroscopy and fast molecular imaging on plasmonic surfaces. The maximum signal enhancement achieved is 10 orders of magnitude in the range 800-2200 cm^{-1} ⁸.

Kim et al.⁹ have observed CARS emission in lithographically patterned gold nanowires. The anti-Stokes response is polarized in the direction of the transverse surface plasmon resonance of the wire. Control of wire height enables tuning of the plasmon polarizability with stronger anti-Stokes emission correlated to structures that support higher plasmon polarizability. The research suggests that the detection procedure of the vibrational response of surface-tethered molecules should involve a mechanism for separating the molecular response from the strong intrinsic anti-Stokes emission of the metallic substrate. The maximum signal enhancement achieved is 5 orders of magnitude⁹.

Yampolsky and colleagues¹⁰ demonstrate the real-time observation of single-molecule vibrational wave packets through time-resolved SECARS. Coupling molecules to dipolar nanoantennas yields the sensitivity required to detect a single molecule's motion under ambient conditions. The authors observe that the vibrational coherence on a single molecule does not undergo pure dephasing and develops phase fluctuations with characteristic statistics, presenting the time evolution of discretely sampled statistical states¹⁰.

2 Tailoring optical response of the metasurface: variation of geometrical parameters

In Figs. S1 and S2, we briefly present the modulation of the near-field enhancement spectra and the SECARS signal enhancement factor due to modification of the thickness h_1 of the nanodisks, thickness h_2 of the spacer, thickness h_3 of the metallic substrate, periodicity P of the metasurface, and the distance z of the molecular position to the spacer surface. Unless otherwise stated, the geometry parameters of the metasurface unit cell are set at the values presented in Table II, the molecule position is $x = y = 0$, $z = 1$ nm, and the probe frequency $\omega_p/2\pi = 450$ THz is fixed for the calculation of the SECARS enhancement factor.

Table II: Geometry parameters of the discussed GSPM. In Figs. S1 and S2, a selected parameter is varied, while others are fixed accordingly to the values in this table.

Geometry size		
Parameter	Value [nm]	Description
h_1	28	Nanodisk thickness
h_2	300	Spacer thickness
h_3	270	Metal film thickness
r	39	Nanodisk radius
g	3	Gap size
P	300	Periodicity

The geometry of the proposed metasurface involves sharp disk edges, which may be difficult to achieve in practice. To verify the impact of smoother edges at the top of the nanodisks, we have assumed curvature radii of 1 nm and 5 nm. Note that the bottom edges remain sharp. In Fig. S3, we compare the results for electric field enhancement by the structure with sharp and smoothed edges. These simulations were made with a gap of 3 nm. Panels (a) and (b) show the electric field enhancement in the gap between nanodisks at z positions of $z = 0$ nm (nanodisks' bottom) and $z = 26$ nm (near nanodisks' top). We find the expected reduction of field enhancement near the curved edges: as the curvature is increased from 0 to 5 nm, the enhancement decreases at $z = 26$ nm because of the increased nanodisk distance, as shown in Fig. S3(b). However, the field near the bottom of the disks ($z = 0$) is enhanced further than in the sharp edge case [Fig. S3(a)]. This could be explained as follows: by adding curvature to the top nanodisk edges, less charge is accumulated at the top and more charge is shifted towards the bottom of the gap, as suggested by Figs. S3(c-e). The charge accumulated at the bottom leads to a stronger field enhancement in that region.

3 Enhancing Optical Response through Metal Film Mirrors

The influence of a metal film mirror on the optical properties of our structure is discussed below. We compare the electric field enhancement of metasurface with and without mirror film to shed light on the key differentiating factors.

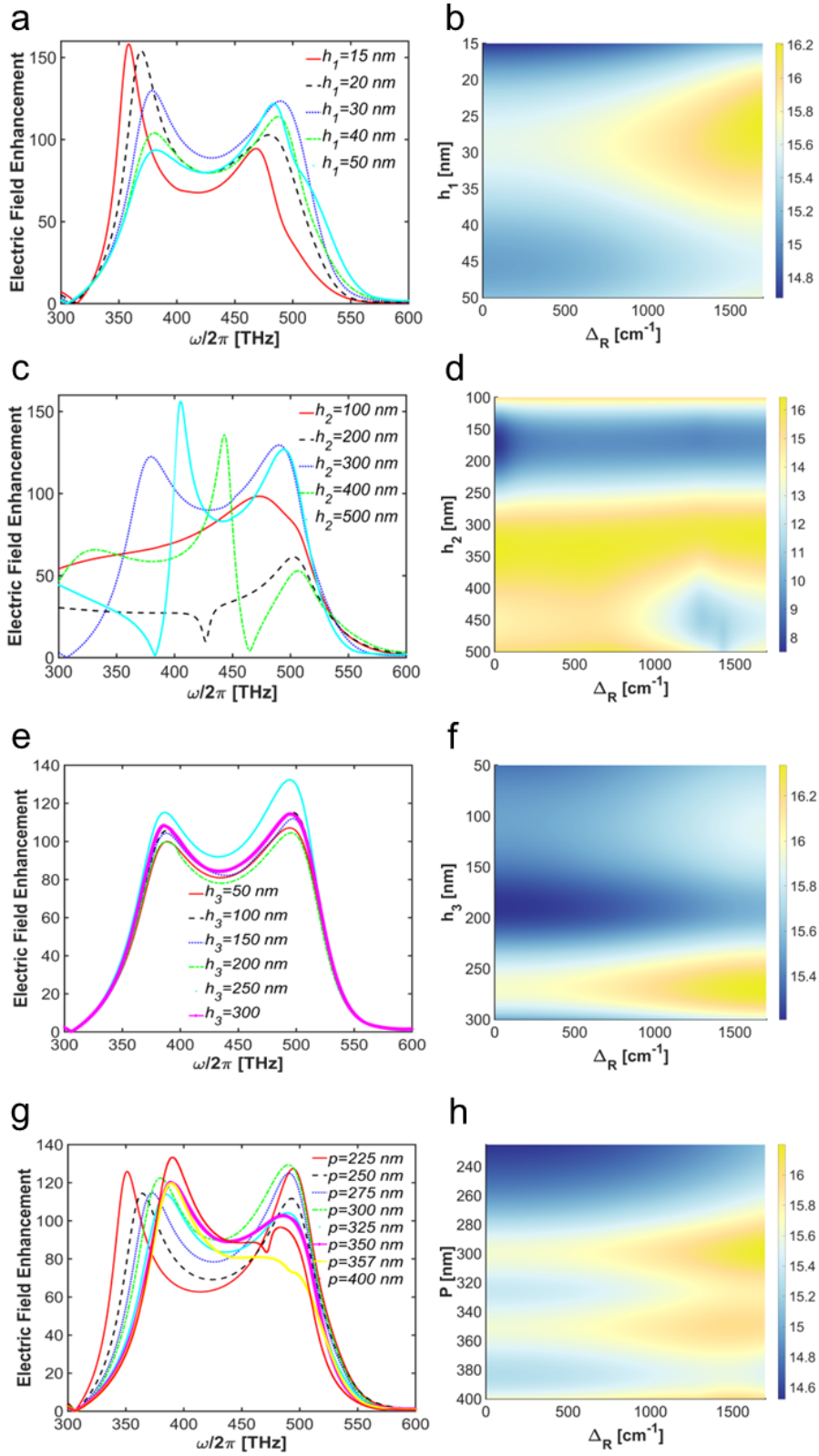


Figure S1: Electric field enhancement spectra (a,c,e,g), and distribution of SECARS enhancement factor (b,d,f,h) for selected values of thickness of the gold nanodisks (a,b), spacer (c,d), thickness of the metal film (e,f) and periodicity (g,h), respectively. The SECARS signal enhancement is shown in the logarithmic scale.

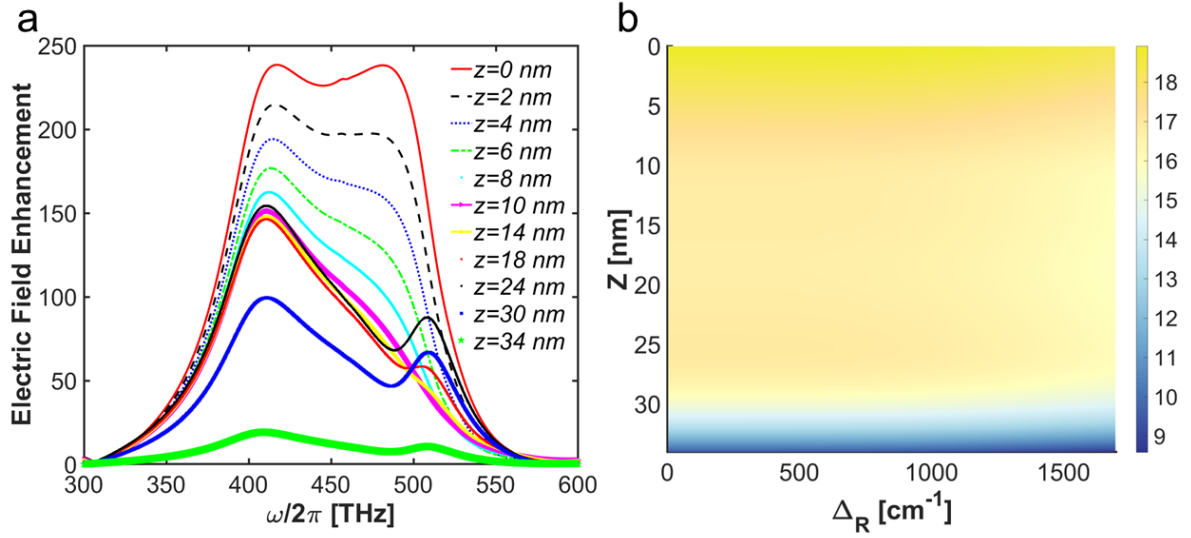


Figure S2: Dependence of the electric field enhancement (a), and distribution of the SECARS enhancement factor (b) on the distance of the molecule position to the surface.

Figure S4 demonstrates the maximum electric field enhancement in the metasurface with and without mirror film. To evaluate the SECARS signal enhancement, we fix the Stokes, pump and anti-Stokes frequencies at $\omega_S/2\pi = 400.10$ THz, $\omega_p/2\pi = 439.49$ THz, $\omega_{aS}/2\pi = 478.88$ THz, which are separated by the dominant Raman shift of rhodamine 6G at 1314 cm^{-1} . These specific values maximize the SECARS signal enhancement for rhodamine 6G by the investigated metasurface. The resulting electric field enhancement factors in the metasurface with mirror film are $EF_S=363.2$, $EF_p=329.95$, $EF_{aS}=376.41$ and in metasurface without mirror film are $EF_S=187.88$, $EF_p=305.7$, $EF_{aS}=194.45$ (see also TableIII). Thus, the field enhancement factors are increased by the presence of a mirror. This enhancement is accompanied by a larger resonance bandwidth thus amplifying the overall optical response. Furthermore, the signal enhancement factor in the metasurface with mirror film exhibits a magnitude 19 times greater than that of the metasurface without mirror film, as evidenced by the data presented in Table III.

We thus have demonstrated how the metallic substrate enhances the SECARS signal and the operational bandwidth of the device.

Table III: Comparative Analysis of SECARS in Rhodamine 6G at 1314 cm^{-1} .

Structure	EF_S	EF_p	EF_{aS}	Signal enhancement factor
Metasurface with mirror film	363.2	329.95	376.41	2.22×10^{20}
Metasurface without mirror film	187.88	305.7	194.45	1.16×10^{19}

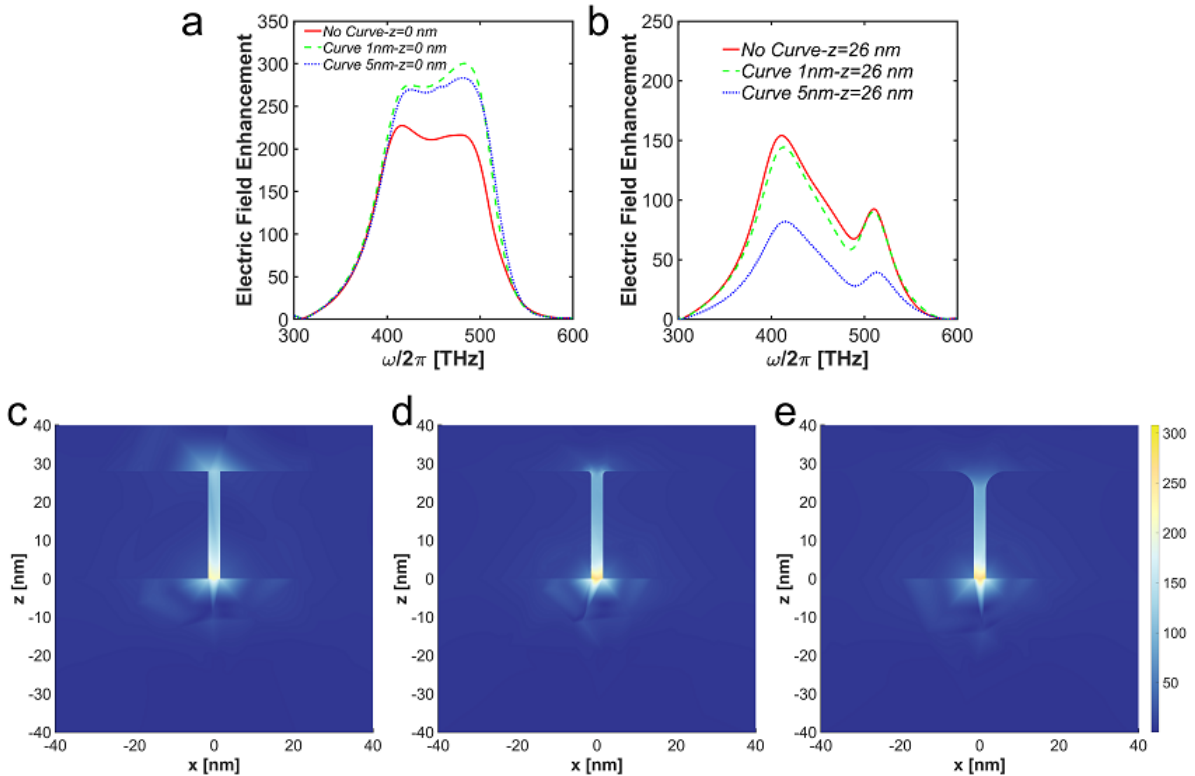


Figure S3: Electric field enhancement spectra (a,b) and field distributions (c-e) for sharp and curved edges on top of the disks. (a) The curvature of the top edges leads to further field enhancement at the bottom, for $z = 0$. (b) As expected, the field enhancement near the top is reduced by the curved edges. The reduction is insignificant for the curvature radius of 1 nm but reaches a factor of 3 for the radius of 5 nm. (c-e) Field enhancement maps for the sharp edges (c), and edges with the curvature of 1 nm (d), and 5 nm (e).

4 Transmission line theory for gap surface plasmon meta-surface

Here we briefly introduce the transmission line theory (TLT)¹¹ and interpret in its terms the obtained optimized response of the GSPM. The transmission line model and ABCD matrix are commonly used approaches to describe the optical properties of metasurfaces. Metasurfaces are typically comprised of layered and patterned materials. In the metal-dielectric-metal configuration considered in our work, the two coupled nanodisks are positioned at the uppermost layer. A metal thin film sits at the bottom layer, with a dielectric spacer sandwiched between the two metal layers. The transmission line model assumes that electromagnetic waves propagate in open space and are transmitted into the periodic structure, disregarding the capacitive or inductive coupling between the metal nanodisks and the thin film layer, and treating each metal layer separately. The electromagnetic waves are incident normally onto the periodic structure, with the electric field polarized along the x -axis. An

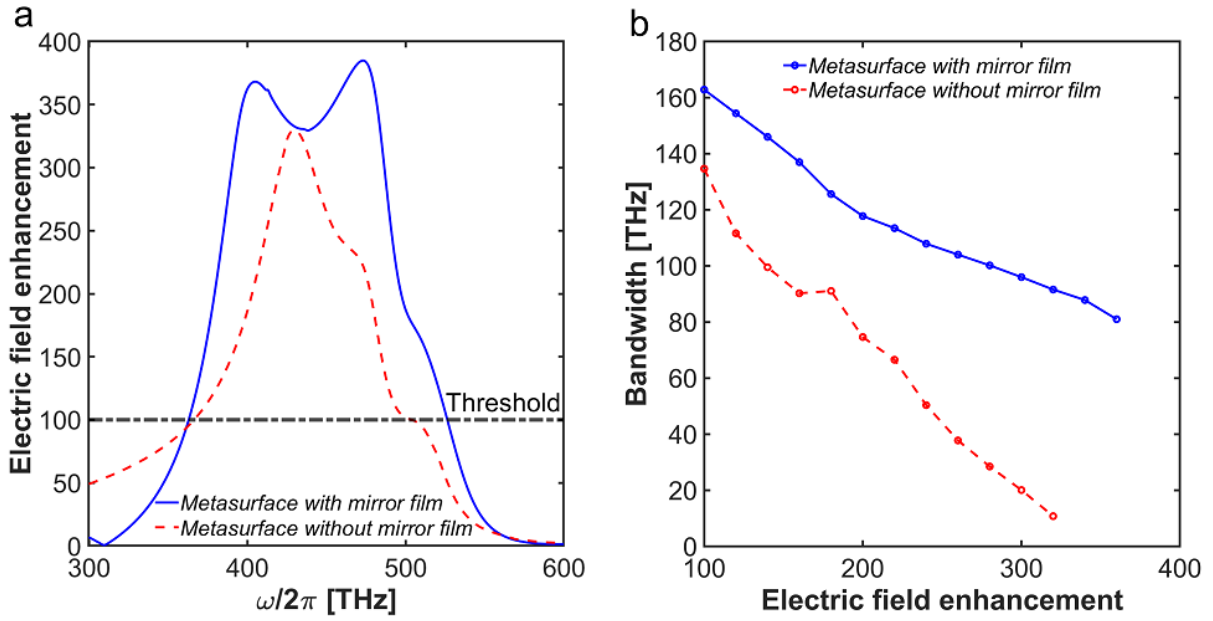


Figure S4: Comparison of (a) Electric Field Enhancement, and (b) Bandwidth in metasurface with and without mirror film.

electric circuit model is used to describe plasmon resonances in periodic structures, with each metal element characterized by an analogue resistance R , inductance L , and capacity C . As depicted in Fig. S5, $R_{1,2}$, $L_{1,2}$, and $C_{1,2}$ correspond to the two coupled nanodisks in the upper layer, while R_3 , L_3 , and C_3 pertain to the metal thin film in the lower layer. The parameter M describes the coupling of the nanodisks. The dielectric layer is defined by its electric permittivity ϵ , permeability μ , and thickness. The transmission line corresponding to the dielectric spacer links the periodic structure's upper and lower metal layers.

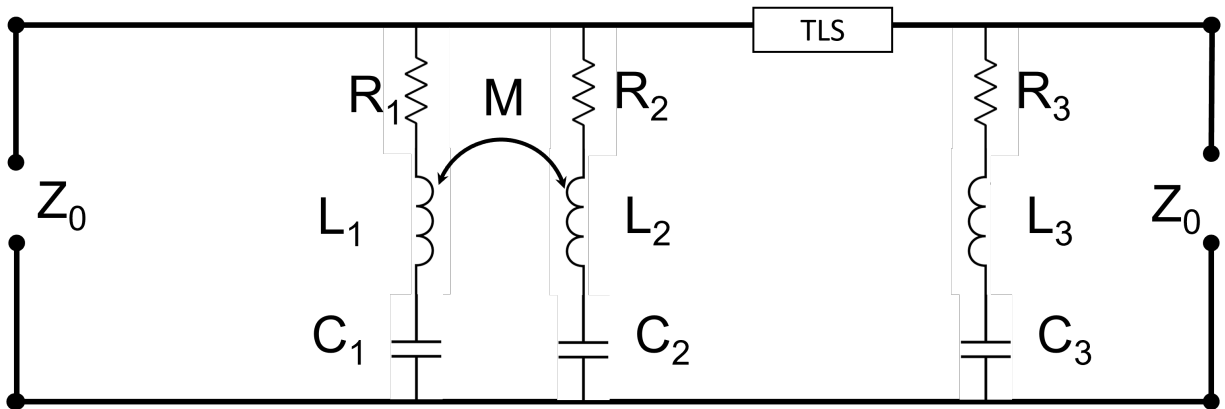


Figure S5: RLC circuit of two coupled resonators in GSPM system in vacuum

The scattering parameters of the metasurface are derived from the ABCD matrix^{12,13}. The ABCD matrix is calculated for each layer and then used to determine the S -parameter

matrix. The ABCD matrices of the coupled nanodisks layer, spacer layer, and thin film provide the ABCD matrix of the entire system as follows

$$\begin{bmatrix} A & B \\ C & D \end{bmatrix} = \underbrace{\begin{bmatrix} 1 & 0 \\ \frac{Z_1+Z_2-2M}{Z_1Z_2-M^2} & 1 \end{bmatrix}}_{\text{disks layer}} \underbrace{\begin{bmatrix} \cos(kd) & jZ_c \sin(kd) \\ \frac{j \sin(kd)}{Z_c} & \cos(kd) \end{bmatrix}}_{\text{dielectric spacer}} \underbrace{\begin{bmatrix} 1 & 0 \\ \frac{1}{Z_3} & 1 \end{bmatrix}}_{\text{metal film}} \quad (\text{S1})$$

Here, $Z_1 = \frac{1}{i\omega C_1} + R_1 + i\omega L_1$, $Z_2 = \frac{1}{i\omega C_2} + R_2 + i\omega L_2$, and $Z_3 = \frac{1}{i\omega C_3} + R_3 + i\omega L_3$, respectively, Z_0 is the intrinsic impedance of free space, and Z_c - of the dielectric spacer, k is the wave vector, and d is the spacer thickness.

The S -parameters matrix is¹⁴:

$$\begin{bmatrix} s_{11} & s_{12} \\ s_{21} & s_{22} \end{bmatrix} = \frac{1}{AZ_0 + B + (CZ_0 + D)Z_i} \times \begin{bmatrix} AZ_0 + B - (CZ_0 + D)Z_i & 2(AD - BC) \\ 2 & AZ_0 + B - (CZ_0 + D)Z_i \end{bmatrix} \quad (\text{S2})$$

$$A = \cos(kd) + j\frac{\sin(kd)}{Z_c}, \quad (\text{S3})$$

$$B = jZ_c \sin(kd), \quad (\text{S4})$$

$$C = \frac{Z_1 + Z_2 - 2M}{Z_1Z_2 - M^2} \cos(kd) + j\frac{\sin(kd)}{Z_c} + \frac{Z_1 + Z_2 - 2M}{Z_1Z_2 - M^2} j\frac{Z_c}{Z_3} \sin(kd) + \frac{\cos(kd)}{Z_3}, \quad (\text{S5})$$

$$D = \frac{Z_1 + Z_2 - 2M}{Z_1Z_2 - M^2} jZ_c \sin(kd) + \cos(kd) \quad (\text{S6})$$

The elements s_{11} and s_{22} of the matrix characterize the reflection coefficients of the metasurface, respectively, for illumination from the top or the bottom, while s_{12} and s_{21} describe the corresponding transition coefficients.

We fit the above analytical theory to reproduce the numerical simulation results obtained from the finite element method. The fit is performed using built-in Matlab procedures, as described in the Methods section of the main text. As shown in Fig. 1 of the main text, we obtain a very good agreement for the fit parameters in Table IV. An alternative, semi-analytical approach relying on the transmission line theory could generalize the treatment of Ref.¹⁵ to account for nanostructure dimers in the top metasurface layer.

Table IV: Fit parameters reproducing the numerically obtained spectra for the metasurface investigated in the main text.

RLC parameters									
C_1	C_2	C_3	L_1	L_2	L_3	R_1	R_2	R_3	M
[aF]	[aF]	[aF]	[pH]	[pH]	[pH]	[Ω]	[Ω]	[Ω]	[Ω]
0.2712	1.887	0.3965	0.5001	0.1248	0.2117	168.8	1.0	136.8	2.0

5 Field distribution of a pair of coupled dipoles

Here we demonstrate that the near-field distribution in the investigated metasurface corresponds in the relevant wavelength range to that of a pair of coupled electric dipoles. Fig.S6 shows the electric field distribution in the metasurface unit cell upon x -polarized plane wave illumination from the top. The frequency is fixed at $\omega/2\pi = 494$ THz. The figure is overlaid with a schematic of the field distribution for a pair of coupled dipoles, which is in very good qualitative agreement with the numerically obtained result. This confirms the coupled-dipole nature of the observed resonances. Since the width of the resonances is larger than their separation, we obtain a broad, plateaux-type response.

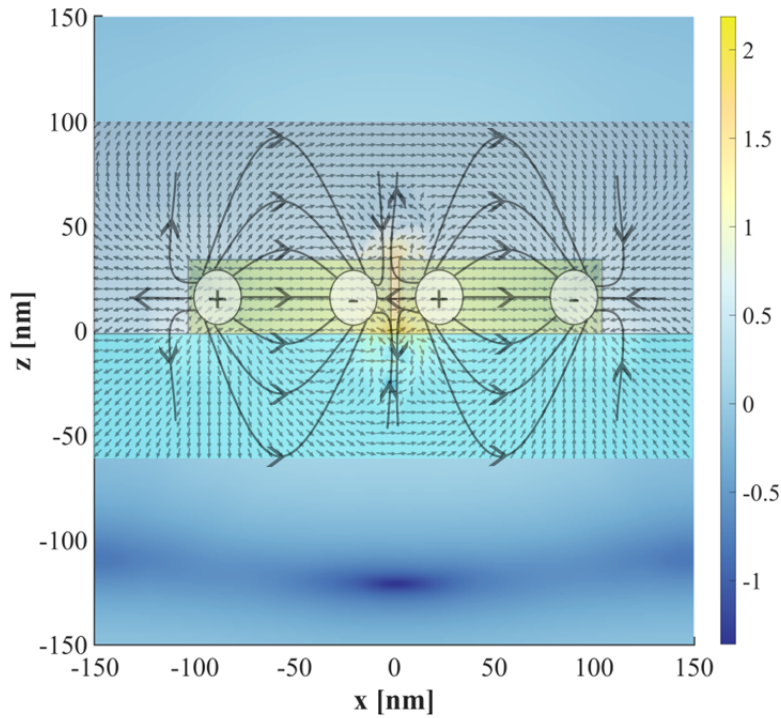


Figure S6: Electric field distribution (colors) and electric field displacement (arrows) of coupled two electric dipoles. The displacement distribution shown with arrows shows qualitative agreement with the basic scheme corresponding to a pair of coupled dipoles (overlaid sketch).

6 Expanding Applications of Broadband Metasurfaces

Based on the previous section, our metasurface with mirror film exhibits a remarkably broad resonance band, and high electric field enhancement which is applicable to enhance the probability of various quantum phenomena. One such phenomenon is surface-enhanced

Raman scattering (SERS), for which we define the signal enhancement factor (SEF) as³

$$SEF_{SERS} = \left| \frac{E_{x,MS}(\mathbf{r}_m, \omega_S)}{E_{x,0}(\omega_S)} \right|^2 \left| \frac{E_{x,MS}(\mathbf{r}_m, \omega_p)}{E_{x,0}(\omega_p)} \right|^2. \quad (S7)$$

Figure S7 demonstrates the substantial signal enhancement across a wide range of Raman shifts, spanning impressive eight orders of magnitude.

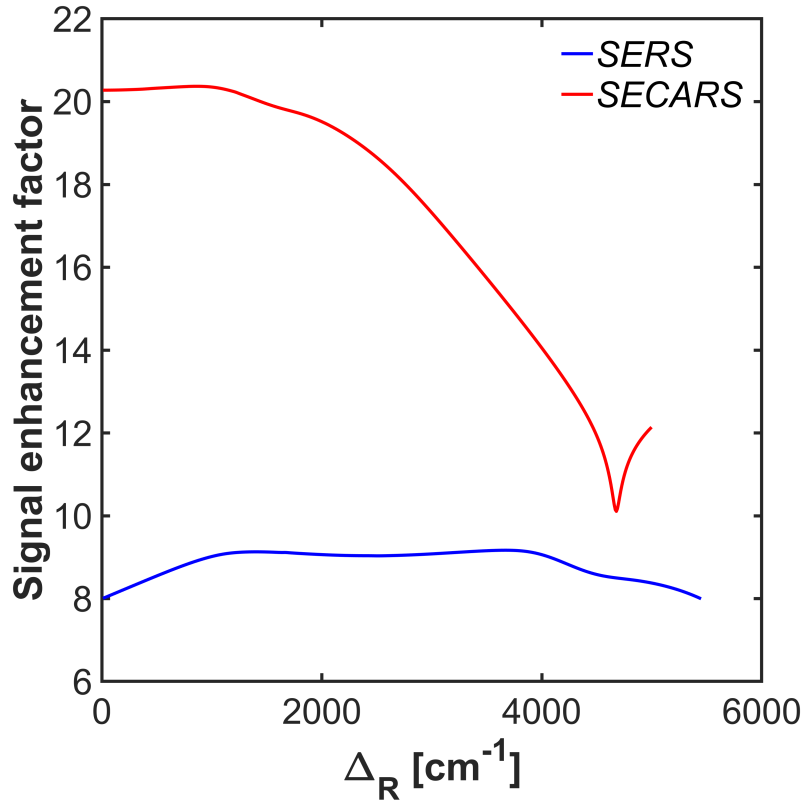


Figure S7: Comparison of SERS, and SECARS signal enhancement factors in the broadband metasurface.

References

- ¹ S. Abedin, K. Roy, X. Jin, H. Xia, S. Brueck, and E. O. Potma, “Surface-enhanced coherent anti-Stokes Raman scattering of molecules near metal–dielectric nanojunctions,” *The Journal of Physical Chemistry C*, vol. 126, no. 20, pp. 8760–8767, 2022.
- ² S. Abedin, Y. Li, A. A. Sifat, K. Roy, and E. O. Potma, “Enhancement of molecular coherent anti-stokes raman scattering with silicon nanoantennas,” *Nano Letters*, vol. 22, no. 16, pp. 6685–6691, 2022.

- ³ L. Ouyang, T. Meyer-Zedler, K.-M. See, W.-L. Chen, F.-C. Lin, D. Akimov, S. Ehtesabi, M. Richter, M. Schmitt, Y.-M. Chang, *et al.*, “Spatially resolving the enhancement effect in surface-enhanced coherent anti-Stokes Raman scattering by plasmonic Doppler gratings,” *ACS Nano*, vol. 15, no. 1, pp. 809–818, 2020.
- ⁴ C. Zong, R. Cheng, F. Chen, P. Lin, M. Zhang, Z. Chen, C. Li, C. Yang, and J.-X. Cheng, “Wide-field surface-enhanced coherent anti-Stokes Raman scattering microscopy,” *ACS Photonics*, vol. 9, no. 3, pp. 1042–1049, 2022.
- ⁵ A. D. Shutov, Z. Yi, J. Wang, A. M. Sinyukov, Z. He, C. Tang, J. Chen, E. J. Ocola, J. Laane, A. V. Sokolov, *et al.*, “Giant chemical surface enhancement of coherent Raman scattering on MoS₂,” *ACS Photonics*, vol. 5, no. 12, pp. 4960–4968, 2018.
- ⁶ Y. Feng, Y. Wang, F. Shao, L. Meng, and M. Sun, “Surface-enhanced coherent anti-Stokes Raman scattering based on coupled nanohole–slit arrays,” *Physical Chemistry Chemical Physics*, vol. 24, no. 22, pp. 13911–13921, 2022.
- ⁷ Y. Zhang, Y.-R. Zhen, O. Neumann, J. K. Day, P. Nordlander, and N. J. Halas, “Coherent anti-Stokes Raman scattering with single-molecule sensitivity using a plasmonic Fano resonance,” *Nature Communications*, vol. 5, no. 1, pp. 1–7, 2014.
- ⁸ C. Steuwe, C. F. Kaminski, J. J. Baumberg, and S. Mahajan, “Surface enhanced coherent anti-Stokes Raman scattering on nanostructured gold surfaces,” *Nano Letters*, vol. 11, no. 12, pp. 5339–5343, 2011.
- ⁹ H. Kim, D. K. Taggart, C. Xiang, R. M. Penner, and E. O. Potma, “Spatial control of coherent anti-Stokes emission with height-modulated gold zig-zag nanowires,” *Nano Letters*, vol. 8, no. 8, pp. 2373–2377, 2008.
- ¹⁰ S. Yampolsky, D. A. Fishman, S. Dey, E. Hulkko, M. Banik, E. O. Potma, and V. A. Apkarian, “Seeing a single molecule vibrate through time-resolved coherent anti-Stokes Raman scattering,” *Nature Photonics*, vol. 8, no. 8, pp. 650–656, 2014.
- ¹¹ Y. Singh, *Electro magnetic field theory*. Pearson Education India, 2011.
- ¹² L. Fu, H. Schweizer, H. Guo, N. Liu, and H. Giessen, “Synthesis of transmission line models for metamaterial slabs at optical frequencies,” *Physical Review B*, vol. 78, no. 11, p. 115110, 2008.
- ¹³ D. Pozar, *Microwave Engineering, 4th Edition*. John Wiley & Sons, 2011.
- ¹⁴ T. Itoh and C. Caloz, *Electromagnetic metamaterials: transmission line theory and microwave applications*. John Wiley & Sons, 2005.
- ¹⁵ X. Xu, Y. Li, B. Wang, and Z. Zhou, “Prediction of multiple resonance characteristics by an extended resistor–inductor–capacitor circuit model for plasmonic metamaterials absorbers in infrared,” *Optics Letters*, vol. 40, no. 19, pp. 4432–4435, 2015.



Hybrid graphene - silver nanoantenna to control THz emission from polar quantum systems

SAEID IZADSHENAS,^{*}  PIOTR GŁADYSZ,^{*}  AND KAROLINA SŁOWIK 

Institute of Physics, Faculty of Physics, Astronomy and Informatics, Nicolaus Copernicus University in Toruń, Grudziądzka 5/7, 87-100 Toruń, Poland

**.izadshenas@doktorant.umk.pl*

Abstract: Fluorescent light emission from atomic quantum systems routinely occurs at the illumination frequency. If the system is polar, an additional fluorescence peak appears at a much lower Rabi frequency, which scales with the illumination field amplitude. This opens the possibility of spectrally controlling the emission, promising tunable coherent radiation sources. However, typically the emission occurs in the MHz to GHz regimes, and its intensity from a single quantum system is relatively low. Here, we propose a hybrid nanoantenna combining noble-metal and graphene elements, exploited for an unusual goal: The silver elements spectrally tune the emission frequency of the molecule and shift it to the THz band, where novel sources of coherent radiation are still desired. Additionally, the graphene elements are used to plasmonically enhance the emission intensity. Their tunability allows for adjustment of the operational frequencies of the device to the illumination conditions and to counteract the fluctuations related to the field modulations in space. All these features are discussed based on the real-life example of a polar molecule of barium monofluoride (BaF).

Published by Optica Publishing Group under the terms of the [Creative Commons Attribution 4.0 License](https://creativecommons.org/licenses/by/4.0/). Further distribution of this work must maintain attribution to the author(s) and the published article's title, journal citation, and DOI.

1. Introduction

The unique optical properties of polar quantum systems have triggered a growing interest in investigating their response and exploiting them as radiation sources [1–12]. Specifically, when resonantly driven, these systems sustain a dipolar response at both the illumination frequency and at a frequency reduced by orders of magnitude. The latter corresponds to the interaction strength with the driving field, known as the Rabi frequency [1]. In the electric dipole approximation, it linearly depends on the amplitude of the driving field [1,6,13]. This observation gave rise to the concept of all-optically tunable, efficient, coherent radiation sources based on polar quantum systems. The ultimate goal is to tune the frequency of the emitted radiation to the THz regime [2,7,13], and to contribute to bridging the THz gap [14–17]. This approach has led to proposing laser-driven polar molecules or quantum dots for THz lasing [2,7,13] or generating squeezed states of radiation [6,8]. Arrays of quantum dots or molecular ensembles have been investigated, where coherent radiation of macroscopic powers has been predicted [10,13].

Another approach to enhancing the emission power involves plasmonic nanoantennas. Recent proposals exploit surface plasmons to modify the light interaction strength with polar molecules, particularly to influence the molecular optical rectification coefficient [18], or to boost the intensity of THz lasing [7]. In the current scheme, the emission frequency scales the driving field amplitude, hence, the tunability of plasmonic devices is required to support the emission efficiently. To address this requirement, we propose a tunable nanoantenna design that brings the radiation generated by polar molecules to the THz range. The proposed hybrid antenna is made of metallic and graphene components. The metallic elements support the molecular excitation with visible light, leading to Rabi oscillations. For electronic transitions in atoms and molecules, these

oscillations typically occur at the MHz to GHz rates. Here, the field amplitude enhancement by the silver nanoparticles blue-shifts the Rabi frequency to the THz regime. The tunable graphene components boost the emission within the THz band. The proposed scheme stands against the paradigmatic approach, where plasmonic nanoantennas are exploited as passive elements merely enhancing quantum transition rates. Here, the antenna actively impacts the spectral properties of the emitted light.

Below, we explain the concept in detail and introduce the proposed nanoantenna. We also engineer the antenna to operate with BaF molecules and demonstrate its tunability. Our proposed design shows promise for developing efficient and tunable radiation sources in the THz regime.

2. Concept

Below we describe the mechanisms of low-frequency radiation generation in polar systems and the impact of plasmonic nanoantennas on the emitted radiation intensity and spectral characteristics.

2.1. Radiation emission from polar quantum systems

The electric dipole moment operator of a two-level quantum system takes the form

$$\vec{d} = \frac{1}{2} (\vec{d}_{ee} - \vec{d}_{gg}) \sigma_z + \frac{1}{2} (\vec{d}_{ee} + \vec{d}_{gg}) I + \vec{d}_{eg} \sigma^+ + \vec{d}_{ge} \sigma^-, \quad (1)$$

where σ_z , σ^- and $\sigma^+ = (\sigma^-)^\dagger$ are Pauli inversion, lowering and raising operators. The dipole moment has off-diagonal, *induced* elements $\vec{d}_{ge} = \vec{d}_{eg}^*$ responsible for transitions between the excited $|e\rangle$ and ground $|g\rangle$ upon illumination with electromagnetic field and diagonal, *permanent* elements $\vec{d}_{ee}, \vec{d}_{gg}$ which are nonzero for polar systems, i.e. systems breaking the spatial inversion symmetry. The latter elements, referred to as "permanent dipole moments" (PDMs), are routinely neglected in light-matter interaction problems; however, they may give rise to interesting physics, including low-frequency radiation emission (Fig. 1). Below, for simplicity, we will assume real values of the dipole moment elements.

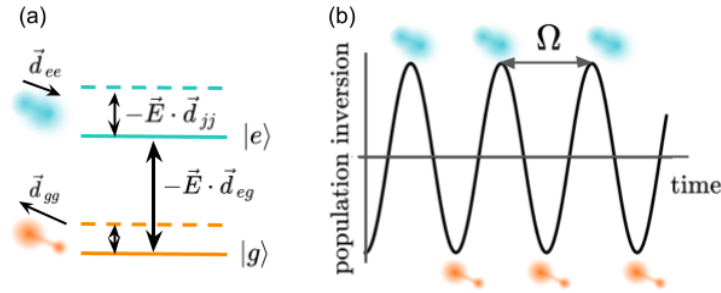


Fig. 1. Energy scheme (a) and dynamics (b) of a two-level polar system subject to illumination with a resonant driving field \vec{E} . The colour insets in (a) schematically depict charge distributions giving rise to the permanent dipole moments d_{jj} in the ground ($j = g$, orange) and excited ($j = e$, cyan) states $|g\rangle$, $|e\rangle$. Upon illumination, the population of the system oscillates between the eigenstates with the Rabi frequency Ω proportional to the field amplitude \vec{E}_0 and the transition dipole element \vec{d}_{eg} , as shown in (b) for the population inversion, or the difference between the excited and ground state population. The Rabi oscillation gives rise to an oscillating permanent dipole $\vec{d}_{ee} - \vec{d}_{gg}$, being the source of radiation at Rabi frequency.

Upon electromagnetic illumination with a monochromatic beam and in the electric dipole approximation, a polar two-level system is described by the time-dependent Hamiltonian given

below. It consists of terms that we refer to as "non-polar" since they are independent of PDMs and describe interactions of non-polar systems with light, and terms called "polar" since they require nonzero PDMs.

$$H = \underbrace{\frac{1}{2}\hbar\omega_0\sigma_z - \hbar\Omega(\sigma^+ + \sigma^-)\cos\omega t}_{\text{non-polar terms}} - \underbrace{\frac{1}{2}\vec{E}_0(\vec{d}_{ee} - \vec{d}_{gg})\sigma_z\cos\omega t}_{\text{polar terms}}. \quad (2)$$

Here, ω_0 is a transition frequency between the excited and ground states, $\Omega = \vec{E}_0 \cdot \vec{d}_{eg}/\hbar$ is the Rabi frequency, ω and \vec{E}_0 are the illumination frequency and amplitude. We dropped the term proportional to the identity operator I as it trivially shifts the energies of the eigenstates by relatively small values $|\frac{1}{2}\vec{E}_0 \cdot \vec{d}_{ij}| \ll \hbar\omega_0$. The electric dipole approximation intrinsically assumes the point-dipole character of the quantum system, and the electric field amplitude is evaluated at the position of the polar system. From now on, we assume all the dipole moments are parallel to the driving field. Hence, we can omit the vector notation in Eqs. (1) and (2).

We now make use of the unitary transformation [1]

$$U = e^{\frac{1}{2}i(\omega t - \kappa \sin\omega t)\sigma_z}, \quad (3)$$

where $\kappa = E_0(d_{ee} - d_{gg})/\hbar\omega$ is a dimensionless parameter connected to the PDMs difference. Note that $\kappa = 0$ for non-polar systems. By using the Jacoby-Augur identity $\exp(i\kappa \sin\omega t) = \sum_{n=-\infty}^{\infty} J_n(\kappa) \exp(in\omega t)$ with Bessel functions of the first kind $J_n(\kappa)$, and applying the rotating-wave approximation, we obtain the time-independent Hamiltonian in the interaction picture with corrections induced by the PDMs

$$H_{int} = -\frac{1}{2}\hbar\delta\sigma_z - \frac{1}{2}\hbar \underbrace{\frac{\Omega^2}{\kappa} J_1(\kappa)}_{\text{effective Rabi frequency}} (\sigma^+ + \sigma^-). \quad (4)$$

Here, $\delta = \omega - \omega_0$ is the laser detuning. The derived Hamiltonian can be interpreted in an effective picture in which the light-matter coupling strength quantified in terms of effective Rabi frequency is modified by the PDMs. In general, the frequency of population oscillations additionally depends on the detuning and damping in the system. Below, we focus on resonant illumination with $\delta = 0$, while the spontaneous emission rate γ of the two-level system near a plasmonic nanoantenna can be significant. Following the analytical derivation shown in Ref. [19], the generalised Rabi frequency of a polar system can be shown to take the form:

$$\Omega_{\text{polar}} = \sqrt{\left(\frac{\Omega^2}{\kappa} J_1(\kappa)\right)^2 - \left(\frac{\gamma}{4}\right)^2}. \quad (5)$$

Note that in the non-polar case and for $\gamma = 0$, as $\kappa \rightarrow 0$, the Bessel function $\frac{J_1(\kappa)}{\kappa} \rightarrow \frac{1}{2}$ and $\Omega_{\text{polar}} \rightarrow \Omega$. Despite the general character of the above expression, in our further investigation, κ always remains small and the influence of the PDMs on the Rabi frequency is negligible. However, they may significantly influence the emission properties of the system. For $|E(d_{ee} - d_{gg})| \ll \hbar\omega$, the expectation value for the dipole moment of a polar system is given by [1]

$$d(t) = \underbrace{-d_{eg} \sin(\omega t) \sin(\Omega_{\text{polar}} t)}_{\text{Mollow triplet component}} + \underbrace{\frac{1}{2}(d_{ee} - d_{gg}) \cos(\Omega_{\text{polar}} t)}_{\text{low-energy component}}, \quad (6)$$

where one can distinguish the components giving rise to the Mollow triplet in the emission spectrum [20] and a low-energy component at the generalised Rabi frequency. In this work, we focus on enhancing the low-frequency contribution with the use of plasmonic nanostructures.

2.2. Emission enhancement with plasmonic nanoantennas

Plasmons, which are collective oscillations of conduction electrons, can be excited in metallic materials. Near interfaces with dielectrics, they interact strongly with light giving rise to hybrid excitations called surface plasmon polaritons. Their electromagnetic component can be confined down to the nanoscale, which is associated with enormous optical field intensity enhancements. These remarkable properties have many applications, including optical sensing [21–25], modulation of optical signals [26,27], or light-matter interaction enhancement [28,29].

Metallic nanoparticles called plasmonic nanoantennas are routinely exploited in the latter context due to their ability to mediate between propagating radiation and locally confined fields [30]. A quantum system interacts with the electromagnetic field with a strength Ω proportional to its amplitude. In the confinement volume, the field amplitude and, hence, the interaction strength are enhanced to:

$$\Omega_{\text{NP}} = \Omega \frac{E_{\text{NP}}}{E_0}, \quad (7)$$

where $\vec{E}_{\text{NP}}(\vec{r}, \omega) = \vec{E}_{\text{scat}}(\vec{r}, \omega) + \vec{E}_0(\omega)$ is the electric field in the vicinity of the nanoantenna, including the illuminating \vec{E}_0 and the scattered contributions \vec{E}_{scat} , and E_{NP} is its component along the direction of molecular dipole moments. For polar systems, the field enhancement induces a spectral shift of the emitted radiation according to Eqs. (5), (6) with Ω replaced by Ω_{NP} .

Another consequence of the nanoantenna presence near a molecule is the Purcell effect – an enhancement of the spontaneous emission rate of the system

$$\gamma_{\text{NP}} = \gamma \frac{P_{\text{NP}}(\vec{r}_0, \omega_0)}{P_0(\omega_0)}. \quad (8)$$

For a dipolar transition, the enhancement factor is evaluated as a ratio of P_{NP} and P_0 , representing powers emitted by a dipole oscillating at the transition frequency and positioned near the nanoantenna or in free space, respectively [30,31]. This effect depends on the nanoantenna geometry and material, as well as the respective position of the source \vec{r}_0 . Hence, contrary to the coupling strength (7), the spontaneous emission rate is independent of the driving field. In order to achieve Rabi oscillations and the resulting low-frequency emission, the intensity of the driving field has to be large enough to compensate for the Purcell-enhanced losses: There is a threshold value of the driving electric field E_t for which squared Rabi frequency, now expressed as

$$\Omega_{\text{polar, NP}}^2 = \Omega_{\text{NP}}^2 - \left(\frac{\gamma_{\text{NP}}}{4}\right)^2, \quad (9)$$

becomes positive. We have assumed here the $\kappa \rightarrow 0$ limit, justified in all cases discussed further. Below that value, the system is overdamped and the low-frequency radiation is quenched.

2.3. Concept summary

This work is based on two observations:

1. Polar quantum systems driven at their transition frequency (typically near-infrared to visible), may emit radiation at the Rabi frequency (typically MHz to GHz).
2. Plasmonic nanostructures enhance interactions of light at resonance frequencies with quantum systems positioned in the field-enhancement volume.

We consider a nanoantenna with two operating modes: one in the near-infrared to visible range and one in the THz domain. The mode in the near-infrared to the visible domain tuned to resonance with the polar system's transition frequency ω_0 , is exploited to locally enhance the electric field at this frequency upon plane-wave illumination. In consequence, the Rabi oscillation

frequency of the polar system and hence, its emission frequency, are blue-shifted from GHz to THz, according to Eq. (7). The THz antenna mode is tuned to the blue-shifted Rabi frequency, enhancing the emission power of the corresponding molecular dipole. Graphene elements enable a significant degree of tunability for this mode, which allows one to adjust it, e.g., to the intensity of the incoming beam.

Below we characterize the performance of a specific, graphene-based nanoantenna tuned to support a selected example molecule.

3. Results

In this section, we introduce the parameters of the BaF molecule we have chosen for demonstration. Next, we present the design of the tunable bimodal nanoantenna and provide a broad range of numerically calculated characteristics of frequency-dependent enhancement. Finally, as proof of principle, we evaluate the resulting field and emission-power enhancements in the real-life case of the BaF molecule. However, we emphasize that the structure could be re-engineered for other polar systems.

3.1. Molecule

For a real-life example of a polar system, we consider a BaF molecule [32]. We approximate it as a two-level system with electronic states: ground $|g\rangle \sim X^2\Sigma^+$, and excited $|e\rangle \sim A^2\Pi_{1/2}$. The following quantities are given in SI units and atomic units a.u. ($\hbar = e = m_e = k_e = 1$). The transition energy between the eigenstates is $\omega_0 = 2\pi \cdot 348$ THz (1.44 eV or 860 nm; 0.053 a.u.) in the near-infrared regime [33], and the transition dipole moment element is $d_{eg} = d_{ge} = 5.54$ D (2.18 a.u.) [34]. The PDM of the ground state $d_{gg} = 3.17$ D (1.25 a.u.) has been obtained experimentally [35]. The PDM of the excited state has not yet been measured, however, the calculated value yields $d_{ee} = 3.4$ D (1.36 a.u.) [32]. The lifetime of the excited state is 57 ns [36], and hence, the spontaneous emission rate $\gamma = 110$ MHz ($2.66 \cdot 10^{-9}$ a.u.).

3.2. Nanoantenna geometry

Plasmonic nanoantennas are typically made of noble metals whose specific sizes and morphologies allow tailoring the spectral position of plasmonic resonances in the visible and infrared domains [31]. Recently, highly doped graphene has emerged as an alternative plasmonic material, sustaining resonances in the THz regime [37]. Compared to noble metals, graphene plasmons arise through a collective response of a small number of charge carriers, bringing within reach the ability to actively tune the plasmon resonance frequency via electric gating [38].

The combination of graphene and noble-metal elements allows us to design a tunable plasmonic device with two modes: The one operating in the near-infrared domain is fixed at the selected transition frequency of BaF. The other mode appears in the terahertz range, where we expect the blue-shifted Rabi frequency to occur. The corresponding resonance can be adjusted to the Rabi frequency by changing the chemical potential of the graphene elements.

The proposed nanoantenna is composed of a pair of silver nanorods with the length l , a circular cross-section of diameter $w = 2r$, located on top of two graphene micro-disks of radius R (Fig. 2). The gap between the graphene nanodisks or silver nanorods is denoted as s .

3.3. Nanoantenna performance

We now discuss the performance of the nanoantenna components, i.e. the pair of silver nanorods and the nanodisk dimer. We numerically model the optical response of the nanoantenna using the finite integration method in COMSOL Multiphysics. We employed the user-control mesh method to effectively adjust the mesh size according to the elements present in the simulated structure. Specifically, we increased the mesh size in smaller gaps to ensure accurate representation. By

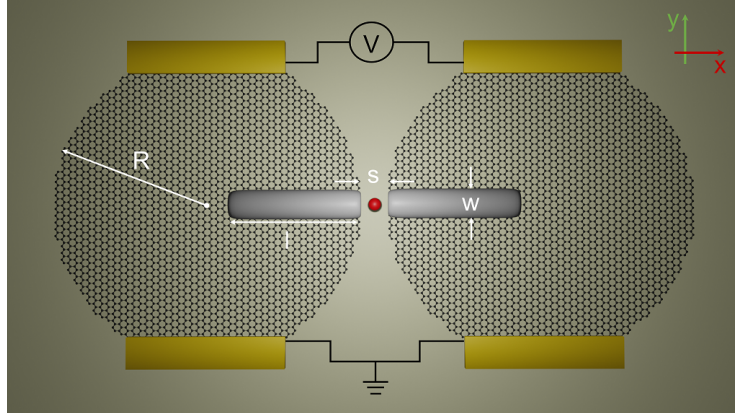


Fig. 2. Schematic of a nanoantenna combining graphene micro-disks and silver nanorods.

using a free tetrahedral mesh, we employed varying mesh sizes for different elements, with the highest mesh density implemented in the gap region. For the dipole illumination, we utilized a mesh size ranging from 1 nm/3 to 1 nm/15, while for the plane wave illumination, the mesh size was determined as radius/3 to radius/10 between the nanoparticles. To optimize the simulation process, we exploited the symmetries inherent in the structure. By limiting the simulation domain to a quarter of the structure and assigning perfect electric conductor properties to the yz plane, and perfect magnetic conductor properties to the xz plane, we were able to significantly reduce the simulation time and memory requirements. The optical properties of silver are based on the Johnson and Christy measurements [39]. We model graphene conductivity $\sigma(\omega)$ with the Kubo formula through its intra- and interband components [40]

$$\sigma(\omega) = \sigma_{\text{intra}}(\omega) + \sigma_{\text{inter}}(\omega), \quad (10)$$

with the Drude model describing the intraband contribution accounting for the plasmonic response [40]

$$\sigma_{\text{intra}}(\omega) = \frac{2ie^2T}{\pi\hbar(\omega + i\tau^{-1})} \ln \left[2 \cosh\left(\frac{\mu}{2T}\right) \right], \quad (11)$$

and the interband contribution described by [40]

$$\sigma_{\text{inter}}(\omega) = \frac{e^2}{4\hbar} \left[G(\omega/2) - \frac{4\omega}{i\pi} \int_0^\infty \frac{G(\epsilon) - G(\frac{\omega}{2})}{\omega^2 - 4\epsilon^2} d\epsilon \right]. \quad (12)$$

Here, i is the imaginary unit, e represents the elementary charge, T is the electron temperature, μ stands for the chemical potential tunable with gating voltage, $\tau = 1$ ps is carrier relaxation time in graphene, and

$$G(\epsilon) = \frac{\sinh(\frac{\epsilon}{T})}{\cosh(\frac{\mu}{T}) + \cosh(\frac{\epsilon}{T})}. \quad (13)$$

The dielectric function of graphene is evaluated as

$$\epsilon(\omega) = 1 + \frac{i\sigma(\omega)}{\epsilon_0\omega t_g} \quad (14)$$

with $t_g = 1$ nm being the graphene thickness.

The dimensions of graphene and silver antenna components differ by order of magnitude and the material properties sustain resonances at distinct spectral regimes. As we have verified

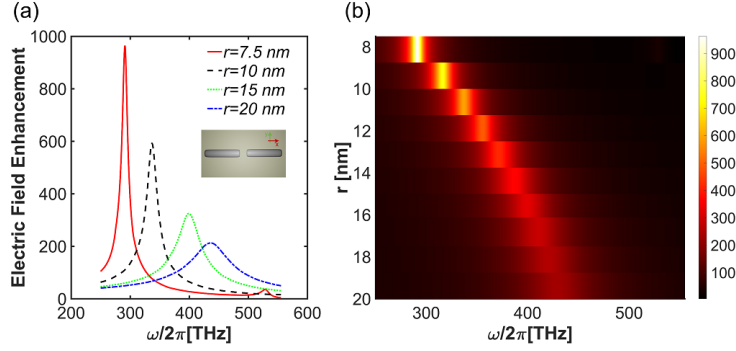


Fig. 3. Electric field enhancement spectra for different nanorod radii: (a) results for selected values of radii, (b) results for a greater number of radii demonstrate the scaling of resonance position with the nanorod radius.

numerically, by using a 4 nm TiO₂ layer as a spacer that is sandwiched between silver NPs and graphene disks, the graphene components have a negligible influence on the plasmonic peak in the visible domain, and, vice versa, the silver elements have no notable impact on the spectral position of the peak in the THz regime. However, silver absorption would suppress the radiated power ratio shown in Figs. 8-10 by about 2 orders of magnitude. The results have been obtained for separately modeled near-infrared to visible and THz problems, with identical, COMSOL-built-in scattering boundary conditions at a 250 μm-diameter sphere that prevents reflection back from infinite space, with an additional perfectly matched layer.

We use Poynting's theorem to calculate the power radiated from and absorbed by the nanoantenna [41,42]:

$$P_{\text{rad}}(\omega) = \oint \langle \vec{E}_{\text{sca}}(\vec{r}, \omega) \times \vec{H}_{\text{sca}}(\vec{r}, \omega) \rangle d\vec{A}, \quad (15)$$

$$P_{\text{abs}}(\omega) = \int \langle \vec{J}_{\text{ind}}(\vec{r}, \omega) \cdot \vec{E}_{\text{ind}}(\vec{r}, \omega) \rangle dV, \quad (16)$$

where similarly to $\vec{E}_{\text{sca}}(\vec{r}, \omega)$, the symbol $\vec{H}_{\text{sca}}(\vec{r}, \omega)$ denotes the scattered part of the magnetic field, and $\vec{J}_{\text{ind}}(\vec{r}, \omega)$ and $\vec{E}_{\text{ind}}(\vec{r}, \omega)$ represent the currents and electric field in the nanoantenna volume. The integrals are evaluated, respectively, at the spherical surface of the simulation volume and inside the volume of the nanoantenna elements.

3.3.1. Optical response of silver components

We first characterize the impact of the silver nanorod dimer on the electric field in the gap region. We assume the plane wave illumination scenario in the visible and infrared range, with the illuminating field polarization along the x axis in Fig. 2. As we are interested in the impact of the nanoantenna on the light-matter interaction strength, we quantify the nanoantenna optical response through the local field enhancement at the high-symmetry point \vec{r}_0 in the middle of the gap indicated by the red dot in Fig. 2. Figures 3, 4, 5 show the local field enhancement spectra $\frac{|\vec{E}_{\text{sca}}(\vec{r}_0, \omega)|}{|\vec{E}_0(\omega)|}$, with the plasmonic resonance positions shifted as the geometry parameters are varied. Unless otherwise stated, the nanorod length is $l = 115$ nm, radius $r = 10$ nm, and the gap is set to $s = 3$ nm. As expected, we find a redshift with the increasing nanorod length and gap size and a blueshift for the growing radius.

These investigations allow us to optimize the silver nanoantenna elements and tailor them to match the near-infrared to visible resonance of the nanoantenna with the transition frequency of

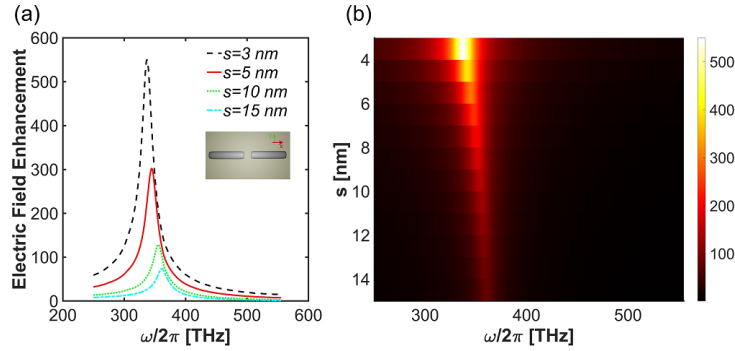


Fig. 4. Electric field enhancement spectra for different gap sizes between nanorods: (a) results for selected gap sizes, (b) results for a greater number of gap sizes demonstrate the strong influence of the gap size on the field enhancement factor.

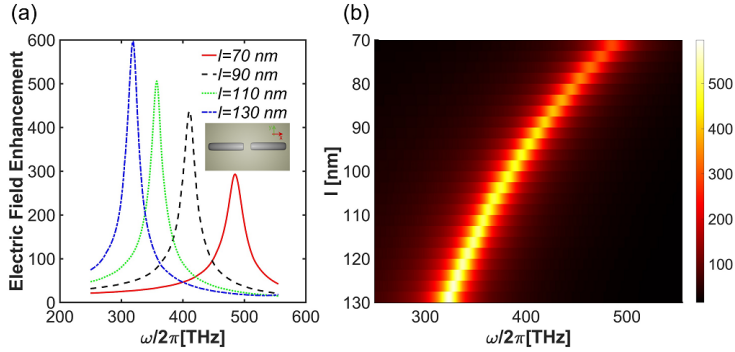


Fig. 5. Electric field enhancement spectra for different nanorod lengths: (a) results for selected values of the lengths, (b) results for a greater number of lengths demonstrate the scaling of the resonance position with the nanorod length.

the BaF molecule. Figure 6(a) demonstrates that with the optimized geometry, the resonance is indeed achieved at $\omega_0 = 2\pi \cdot 348$ THz with a high electric field enhancement factor of $\frac{|\vec{E}_{\text{scat}}(\vec{r}_0, \omega)|}{|\vec{E}_0(\omega)|} = 531$. Figure 6(b) illustrates the field enhancement distribution around the nanorods, highlighting the best performance in the middle of the gap. Note that, according to Eq. (7), this distribution corresponds to the blue-shifted Rabi frequency distribution as a function of the molecular position. Importantly, the nanorods were designed to have a much larger scattering cross-section than the absorption cross-section by carefully adjusting the shape and size of the nanoparticles to mitigate losses. As illustrated in Fig. 6(c), the cross-section ratio on resonance is found to be approximately 3.78.

Next, we investigate the impact of the Purcell enhancement of the spontaneous emission rate on the Rabi frequency Ω_{polar} . For all results shown in Fig. 7, we assume a resonance condition so that the drive and molecular transition frequencies coincide $\omega = \omega_0$. In other words, the frequency was modified for evaluation of both the field enhancement and the gamma rate. The Purcell-enhanced γ_{NP} rates, evaluated according to Eq. (8) are significant especially around the resonance frequency [Fig. 7(a)]. In Fig. 7(b), we plot the squared Rabi frequency as a function of the electric field E_0 , and drive frequency ω , calculated using Eq. (9). The blue regions correspond to negative values, i.e. overdamped conditions in which the Rabi oscillations and low-frequency emission are quenched. Increasing the incident field amplitude allows for achieving positive

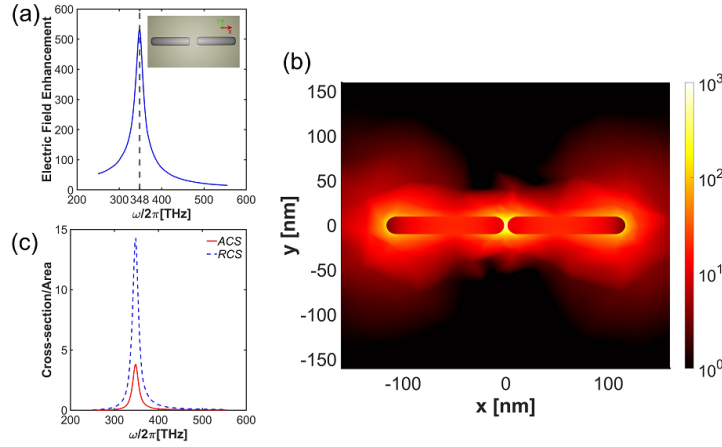


Fig. 6. (a) Electric field enhancement spectrum for the optimized nanorod dimer with $l = 115$ nm, $s = 3$ nm, $r = 10$ nm shows a resonant peak at the BaF transition frequency $\omega_0 = 2\pi \cdot 348$ THz. (b) Electric field enhancement factor distribution for plane-wave illumination at the resonant frequency. Note the enhancement is shown in logarithmic scale. (c) Scattering (RCS) and absorption (ACS) cross-sections of the nanorod dimer upon plane-wave illumination.

values and tuning the Rabi frequency. Figure 7(c) shows the squared Rabi frequency for three selected values of E_0 [dashed lines in Fig. 7(b)], from the highly damped regime where emission is suppressed by the presence of the nanorods (blue dashed line, $E_0 = 5.5$ kV/cm), through the region of two peaks with a local minimum at resonance (black dashed line $E_0 = 7.5$ kV/cm), and eventually in the most interesting regime of a single peak at resonance (red dashed line, $E_0 = 12.0$ kV/cm). The threshold field value can be read out from Fig. 7(d), which concludes the above observations by showing Rabi frequency for the molecular resonance $\omega_0 = 2\pi \cdot 348$ THz as a function of the driving field [solid line in Fig. 7(b)]. The red arrow points at the evaluated threshold $E_t \approx 7.5$ kV/cm for the electric field above which low-frequency radiation can be emitted by the system. For moderate field values, the achieved Rabi frequency depends nonlinearly on the illumination amplitude. Finally, for relatively strong drives, as the damping rate becomes negligible, the linear scaling of Rabi frequency on the illumination amplitude is restored.

The evaluated field enhancement factor of about 500 and characteristics from Fig. 7(d) allow us to estimate the range of Rabi frequencies that can be reached with a moderately strong electric field amplitude of $E_0 = 8.27$ kV/cm ($1.61 \cdot 10^{-6}$ a.u.) by the use of the Eq. (5):

$$\Omega_{\text{polar}} = 2\pi \cdot 5 \text{ THz} = 2\pi \cdot 7.6 \cdot 10^{-4} \text{ a.u.} \quad (17)$$

This suggests that emission at Rabi frequencies in the range of $2\pi \cdot 1$ up to $2\pi \cdot 10$ THz can be achieved in this manner. Without the field enhancement, the Rabi frequency for the given above field amplitude would be $\Omega_{\text{polar}} = 2\pi \cdot 10$ GHz. In this way, the plasmonic field enhancement sustained by the silver nanorods leads to a spectral shift of the emission frequency. This unique effect can be achieved by the integration of nanoantennas with polar molecules.

The threshold amplitude of $E_t \approx 7.5$ kV/cm corresponds to the beam intensity of 750 W/mm^2 . Estimating the size of the nanorod to be $20 \text{ nm} \times 100 \text{ nm}$, the fluence applied becomes roughly $1.5 \mu\text{J/s}$, which is well below the threshold of 20 mJ/s , related to material melting, e.g., in gold nanoantennas [43,44].

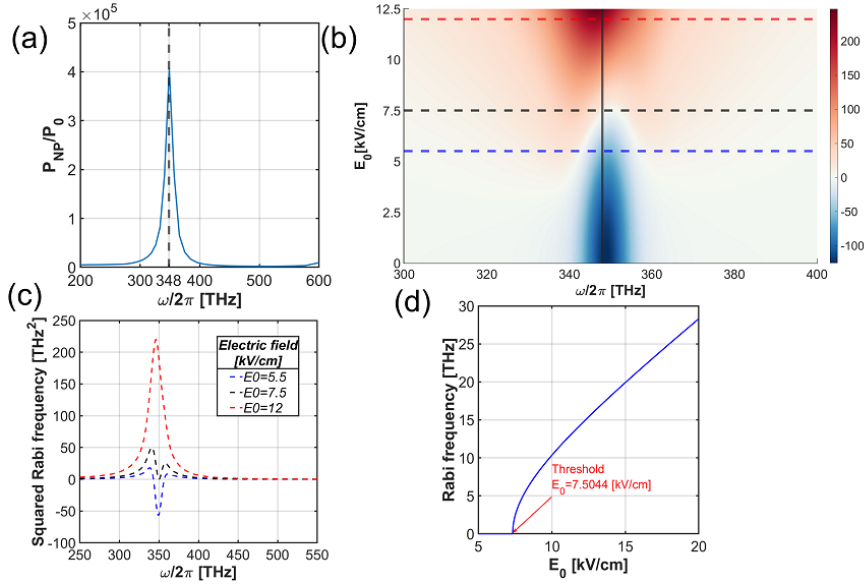


Fig. 7. (a) Purcell enhanced emission rate as a function of the molecular frequency ω_0 . (b) Squared Rabi frequency [Eq. (9)] as a function of the incident electric field amplitude E_0 and frequency ω . For this calculation, both the illumination frequency and the molecular transition frequency are varied but always assumed on resonance $\omega = \omega_0$. Dashed lines for particular values of E_0 correspond to the curves plotted in panel (c) and represent several regimes for the Rabi frequency – overdamped (blue), nonlinear (black), and linear (red). (d) Rabi frequency of the system in the vicinity of the nanorods as a function of the incident field E_0 for $\omega = 2\pi \cdot 348$ THz corresponding to BaF molecules and marked with the vertical black solid line in (b). The marked threshold value indicates a minimal required field to observe low-frequency radiation for a given geometry.

With this information at hand, we tune the graphene disk dimer to enhance the THz emission power.

3.3.2. Optical response of graphene disk dimer

We perform the simulations using the dipolar illumination scheme, with the source positioned in the gap between the graphene micro-disks, as indicated by the red dot in Fig. 2 and oriented along the x axis. The radiated power spectra for varied graphene disk radii are illustrated in Fig. 8 and show an impressive enhancement in comparison with the free space values. We find the resonance frequency to approximately scale inversely with the graphene disk radii $\omega_{\text{res}} \propto \sqrt{\frac{1}{r}}$ (blue dashed line in Fig. 8). This result has been derived analytically in the quasistatic approximation for a single disk in Ref. [45]. For larger disks, we find improved radiated and suppressed absorbed powers [Fig. 9(a,b)]. This implies that the efficiency of the graphene micro-disks is enhanced with larger radii.

According to Eq. (5), the Rabi frequency of the emitted radiation can be modulated with the intensity of the laser field illuminating the molecule. Figure 6(b) reveals the resulting Rabi frequency's sensitivity to the position of the molecule with respect to the antenna. One of the most significant advantages of graphene is its tunability, which enables adjustment of the resonance frequency of the antenna and its fine-tuning to match the achieved Rabi frequency by changing the chemical potential. As we vary the chemical potential in the range of 0.2 eV

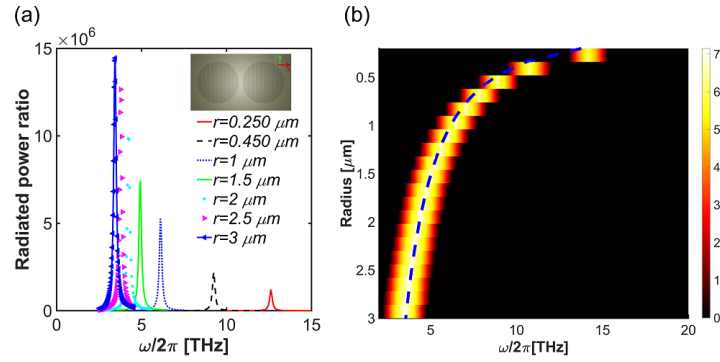


Fig. 8. Radiated power ratio with respect to the free space values (a) for selected radii of graphene micro-disks, (b) for more values of radii in a logarithmic scale. The blue dashed line follows the relation $\omega_{\max} = \frac{2\pi a}{\sqrt{r}}$, where $\omega_{\max}/2\pi$ is the resonance frequency and $a = 6.159\text{THz}\sqrt{\text{nm}}$.

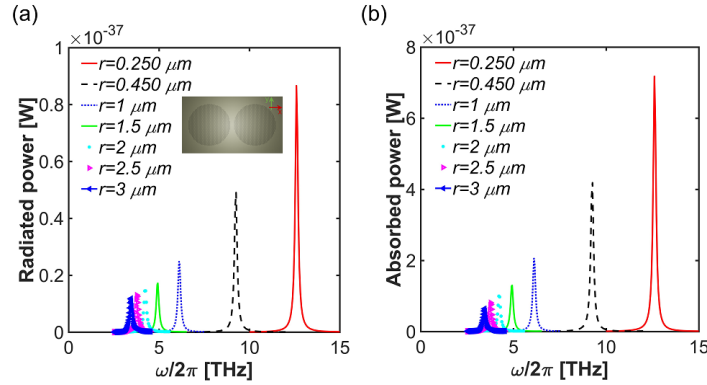


Fig. 9. Radiated (a) and absorbed (b) power spectra for varying radii of graphene micro-disks.

to 1.2 eV, we observe a blueshift of the resonance from 3 THz to 11 THz and a decrease in the radiated power ratio with respect to the free space (Fig. 10). In the quasistatic approximation, the predicted scaling of the plasmonic resonance is $\omega \propto \sqrt{\mu_c}$ [45] and applies here to a very good approximation, as demonstrated by the blue dashed line in Fig. 10.

We have thus confirmed that the graphene-based nanoantenna component can be designed to achieve a plasmonic resonance in the desired frequency range of several THz, promising emission power enhancement by up to 8 orders of magnitude. The spectral position of the resonance can be fine-tuned with the chemical potential to adjust to the Rabi frequency variations.

3.4. Discussion

As shown in the Concept section, upon resonant near-infrared illumination, the polar molecule of BaF becomes a source of radiation at the Rabi frequency. The nanoantenna characterized above was designed to influence the emission properties of the molecule. Its impact is two-fold:

1. The nanoantenna shifts the emission frequency to the THz range. This occurs as the Rabi frequency increases proportionally to the enhancement of the electric field at the driving, near-infrared frequency. In our example, the field in the middle of the gap is enhanced by

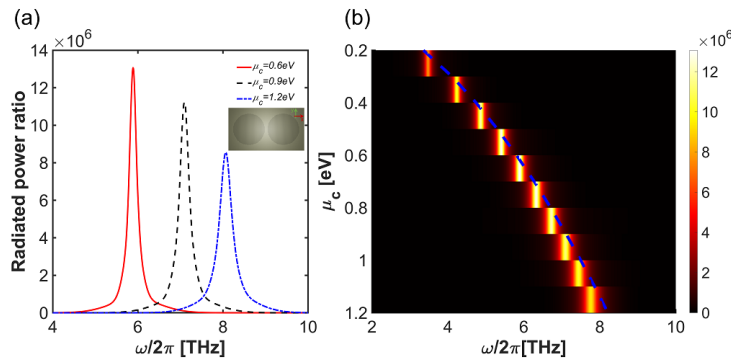


Fig. 10. Radiated power spectra (a) for selected values of the chemical potential of graphene micro-disks, (b) for more values of the potential. The blue dashed line follows the relation $\omega_{\max} = 2\pi a \sqrt{\mu_c}$, where $\omega_{\max}/2\pi$ is the resonance frequency and $a = 7.498 \frac{\text{THz}}{\sqrt{\text{eV}}}$.

more than two orders of magnitude, shifting the Rabi frequency from the GHz to the THz range. The field enhancement is achieved with the silver components of the antenna.

2. The nanoantenna increases the power of the signal. This is achieved through an enhanced emission power at the THz frequency using the graphene components of the antenna. Note that the emission frequency depends on the applied illumination amplitude of the near-infrared field. The tunability of the graphene disks with the chemical potential enables matching the THz resonance to that amplitude. On the other hand, the tunability can also be exploited to counteract the effect of spatial field fluctuations in the close vicinity of the nanoantenna.

4. Conclusion

We have proposed a hybrid noble-metal – graphene nanoantenna with a bimodal optical response to tune radiation from polar quantum systems into the THz range and improve their emission power. The silver components sustain resonance in the near-infrared to the visible regime, which is used to improve the light-matter coupling strength quantified in terms of Rabi frequency. The enhanced Rabi frequency, at which the polar system emits, is thus blue-shifted to the THz regime. The graphene components are exploited to support the emission from the polar system in the THz range. Graphene tunability plays a crucial role for the proposed antenna since it allows us to adjust its operational frequencies to counteract imperfections in molecule positioning, to adjust to temporal changes in laser intensity, or to modulate the signal on purpose.

We have thoroughly investigated the antenna's optical response as a function of its geometry parameters to eventually engineer a nanostructure adjusted to the specific target molecule of BaF. Similar scenarios could be realized with alternative polar systems, including molecules, quantum dots, or solid-state defects.

Funding. National Science Centre, Poland (2018/31/D/ST3/01487).

Disclosures. The authors declare no conflicts of interest.

Data availability. Data underlying the results presented in this paper are not publicly available at this time but may be obtained from the authors upon reasonable request.

References

1. O. Kibis, G. Y. Slepyan, S. Maksimenko, and A. Hoffmann, "Matter coupling to strong electromagnetic fields in two-level quantum systems with broken inversion symmetry," *Phys. Rev. Lett.* **102**(2), 023601 (2009).

2. H. Avetissian, B. Avchyan, and G. Mkrtchian, "Coherent radiation by two-level quantum systems with permanent dipole moments under multiphoton resonant laser excitation," *J. Phys. B: At., Mol. Opt. Phys.* **45**(2), 025402 (2012).
3. I. Savenko, O. Kibis, and I. A. Shelykh, "Asymmetric quantum dot in a microcavity as a nonlinear optical element," *Phys. Rev. A* **85**(5), 053818 (2012).
4. E. Paspalakis, J. Boviatsis, and S. Baskoutas, "Effects of probe field intensity in nonlinear optical processes in asymmetric semiconductor quantum dots," *J. Appl. Phys.* **114**(15), 153107 (2013).
5. M. Macovei, M. Mishra, and C. H. Keitel, "Population inversion in two-level systems possessing permanent dipoles," *Phys. Rev. A* **92**(1), 013846 (2015).
6. M. Koppenhöfer and M. Marthaler, "Creation of a squeezed photon distribution using artificial atoms with broken inversion symmetry," *Phys. Rev. A* **93**(2), 023831 (2016).
7. M. Marthaler, M. Koppenhöfer, K. Slowik, and C. Rockstuhl, "Lasing at arbitrary frequencies with atoms with broken inversion symmetry and an engineered electromagnetic environment," *arXiv*, arXiv:1601.01511 (2016).
8. M. Antón, S. Maede-Razavi, F. Carre no, I. Thanopoulos, and E. Paspalakis, "Optical and microwave control of resonance fluorescence and squeezing spectra in a polar molecule," *Phys. Rev. A* **96**(6), 063812 (2017).
9. G. Y. Kryuchyan, V. Shahnazaryan, O. V. Kibis, and I. Shelykh, "Resonance fluorescence from an asymmetric quantum dot dressed by a bichromatic electromagnetic field," *Phys. Rev. A* **95**(1), 013834 (2017).
10. P. Gładysz, P. Wcisło, and K. Slowik, "Propagation of optically tunable coherent radiation in a gas of polar molecules," *Sci. Rep.* **10**(1), 17615 (2020).
11. G. Scala, F. V. Pepe, P. Facchi, S. Pascazio, and K. Słowik, "Light interaction with extended quantum systems in dispersive media," *New J. Phys.* **22**(12), 123047 (2020).
12. G. Scala, K. Słowik, P. Facchi, S. Pascazio, and F. V. Pepe, "Beyond the rabi model: Light interactions with polar atomic systems in a cavity," *Phys. Rev. A* **104**(1), 013722 (2021).
13. I. Y. Chestnov, V. A. Shahnazaryan, A. P. Alodjants, and I. A. Shelykh, "Terahertz lasing in ensemble of asymmetric quantum dots," *ACS Photonics* **4**(11), 2726–2737 (2017).
14. A. Borak, "Toward bridging the terahertz gap with silicon-based lasers," *Science* **308**(5722), 638–639 (2005).
15. R. Won, "Bridging the terahertz gap," *Nat. Photonics* **4**(10), 673–674 (2010).
16. Y.-M. Bahk, G. Ramakrishnan, J. Choi, H. Song, G. Choi, Y. H. Kim, K. J. Ahn, D.-S. Kim, and P. C. Planken, "Plasmon enhanced terahertz emission from single layer graphene," *ACS Nano* **8**(9), 9089–9096 (2014).
17. R. A. Lewis, "A review of terahertz sources," *J. Phys. D: Appl. Phys.* **47**(37), 374001 (2014).
18. N. Domenikou, I. Thanopoulos, V. Yannopoulos, and E. Paspalakis, "Nonlinear optical rectification in an inversion-symmetry-broken molecule near a metallic nanoparticle," *Nanomaterials* **12**(6), 1020 (2022).
19. R. Loudon, *The Quantum Theory of Light*, Oxford science publications (Clarendon Press, 1983).
20. D. A. Steck, *Quantum and atom optics* (2007).
21. N. Liu, M. Mesch, T. Weiss, M. Hentschel, and H. Giessen, "Infrared perfect absorber and its application as plasmonic sensor," *Nano Lett.* **10**(7), 2342–2348 (2010).
22. S. Izadshenas, A. Zakery, and Z. Vafapour, "Tunable slow light in graphene metamaterial in a broad terahertz range," *Plasmonics* **13**(1), 63–70 (2018).
23. C. Caucheteur, J. Villatoro, F. Liu, M. Loyez, T. Guo, and J. Albert, "Mode-division and spatial-division optical fiber sensors," *Adv. Opt. Photonics* **14**(1), 1–86 (2022).
24. C. Lee, B. Lawrie, R. Pooser, K.-G. Lee, C. Rockstuhl, and M. Tame, "Quantum plasmonic sensors," *Chem. Rev.* **121**(8), 4743–4804 (2021).
25. R. Singh, Z. Wang, C. Marques, R. Min, B. Zhang, and S. Kumar, "Alanine aminotransferase detection using TIT assisted four tapered fiber structure-based LSPR sensor: From healthcare to marine life," *Biosens. Bioelectron.* **236**, 115424 (2023).
26. Z. Sun, A. Martinez, and F. Wang, "Optical modulators with 2D layered materials," *Nat. Photonics* **10**(4), 227–238 (2016).
27. Y. Xu, C. Zhang, W. Li, R. Li, J. Liu, Z. Liu, and Z. Wu, "High sensitivity ultraviolet graphene-metamaterial integrated electro-optic modulator enhanced by superlubricity," *Nanophotonics* **11**(16), 3547–3557 (2022).
28. K. Koshelev, S. Kruk, E. Melik-Gaykazyan, J.-H. Choi, A. Bogdanov, H.-G. Park, and Y. Kivshar, "Subwavelength dielectric resonators for nonlinear nanophotonics," *Science* **367**(6475), 288–292 (2020).
29. S. Izadshenas, P. Masłowski, T. Herr, and K. Słowik, "Multiresonant metasurface for raman spectroscopy beyond single molecule detection level," *EPJ Appl. Metamat.* **9**, 11 (2022).
30. L. Novotny and N. Van Hulst, "Antennas for light," *Nat. Photonics* **5**(2), 83–90 (2011).
31. P. Biagioni, J.-S. Huang, and B. Hecht, "Nanoantennas for visible and infrared radiation," *Rep. Prog. Phys.* **75**(2), 024402 (2012).
32. S. N. Tohme and M. Korek, "Theoretical study of the electronic structure with dipole moment calculations of barium monofluoride," *J. Quant. Spectrosc. Radiat. Transfer* **167**, 82–96 (2015).
33. T. Chen, W. Bu, and B. Yan, "Structure, branching ratios, and a laser-cooling scheme for the BaF 138 molecule," *Phys. Rev. A* **94**(6), 063415 (2016).
34. A.-R. Allouche, G. Wannous, and M. Aubert-Frécon, "A ligand-field approach for the low-lying states of Ca, Sr and Ba monohalides," *Chem. Phys.* **170**(1), 11–22 (1993).
35. W. Ernst, J. Kändler, and T. Törring, "Hyperfine structure and electric dipole moment of BaF X 2 σ^+ ," *J. Chem. Phys.* **84**(9), 4769–4773 (1986).

36. P. Aggarwal, V. Marshall, H. Bethlem, A. Boeschoten, A. Borschevsky, M. Denis, K. Esajas, Y. Hao, S. Hoekstra, K. Jungmann, and T. Meijknecht, "Lifetime measurements of the $A\ 2\ \pi\ 1/2$ and $A\ 2\ \pi\ 3/2$ states in BaF," *Phys. Rev. A* **100**(5), 052503 (2019).
37. Q. Bao and K. P. Loh, "Graphene photonics, plasmonics, and broadband optoelectronic devices," *ACS Nano* **6**(5), 3677–3694 (2012).
38. Z. Fei, A. Rodin, G. O. Andreev, W. Bao, A. McLeod, M. Wagner, L. Zhang, Z. Zhao, M. Thiemens, G. Dominguez, and M. Fogler, "Gate-tuning of graphene plasmons revealed by infrared nano-imaging," *Nature* **487**(7405), 82–85 (2012).
39. P. B. Johnson and R.-W. Christy, "Optical constants of the noble metals," *Phys. Rev. B* **6**(12), 4370–4379 (1972).
40. L. A. Falkovsky, "Optical properties of graphene," in *Journal of Physics: conference series*, vol. 129 (IOP Publishing, 2008), p. 012004.
41. J. D. Jackson, *Classical electrodynamics* (John Wiley & Sons, 2021).
42. J. Straubel, R. Filter, C. Rockstuhl, and K. Słowik, "Plasmonic nanoantenna based triggered single-photon source," *Phys. Rev. B* **93**(19), 195412 (2016).
43. A. Plech, V. Kotaidis, M. Lorenc, and J. Boneberg, "Femtosecond laser near-field ablation from gold nanoparticles," *Nat. Phys.* **2**(1), 44–47 (2006).
44. J. Chen and J. Beraun, "Modelling of ultrashort laser ablation of gold films in vacuum," *J. Opt. A: Pure Appl. Opt.* **5**(3), 168–173 (2003).
45. R. Yu, J. D. Cox, J. Saavedra, and F. J. García de Abajo, "Analytical modeling of graphene plasmons," *ACS Photonics* **4**(12), 3106–3114 (2017).

Multiresonant metasurface for Raman spectroscopy beyond single molecule detection level

Saeid Izadshenas^{1,*}, Piotr Masłowski¹, Tobias Herr^{2,3}, and Karolina Słowik¹

¹ Institute of Physics, Faculty of Physics, Astronomy and Informatics, Nicolaus Copernicus University in Torun, ul. Grudziądzka 5, 87–100 Torun, Poland

² Deutsches Elektronen-Synchrotron DESY, Notkestr. 85, 22607 Hamburg, Germany

³ Physics Department, Universität Hamburg UHH, Luruper Chaussee 149, 22761 Hamburg, Germany

Received: 22 November 2021 / Accepted: 7 March 2022

Abstract. A metasurface in the metal-insulator-grating configuration is designed and optimised to support enhancement of coherent Raman signal of selected molecules orders of magnitude above the single-molecule detection threshold. The tunability is demonstrated by adjusting the structure to match selected Raman peaks of rhodamine, however, its spectral response is broad enough to cover a range of Raman shifts. Finally, the grating allows switching between distinct values of Raman shift with a single metasurface illuminated at different angles.

Keywords: metasurface / coherent anti-stokes Raman scattering / surface plasmon / plasmonic grating / molecular spectroscopy

1 Introduction

Raman spectroscopy allows detection and identification of different molecular species even in complex samples with relatively simple experimental setups. Raman techniques can be used on various types of samples, and the spectra can be acquired in short times and from small, even microscopic volumes [1]. However, the major drawback of the technique is the typically weak signal, that makes the approach inefficient especially for low concentration, for example in bio-medical diagnostics. Enhancement of the Raman signal at nanostructured metallic surfaces [2,3] allowed lowering the detection threshold to extremely low concentrations, making sensing at the level of single molecules possible [4–6]. However, operation at such low concentrations remains challenging and requires tip-enhanced spectroscopy techniques [5,7–9] or novel dedicated microscope designs [10]. Further improvement of sensitivity is still needed, on the one hand, to relax these requirements. On the other hand, greater sensitivity would allow extending the range of detected molecular species, or would even enable identification of single unknown molecules. A potential to achieve these ambitious goals is offered by the coherent anti-Stokes Raman scattering (CARS) technique, that exploits a nonlinear four-wave mixing process [11–13]: Two beams, referred to as pump and Stokes beams of frequencies ω_p and ω_s coherently

interact and, as a result, give rise to a coherent signal at the anti-Stokes frequency ω_a under the resonance condition that corresponds to the energy conservation requirement

$$\omega_p - \omega_s = \omega_a - \omega_p = \Delta, \quad (1)$$

where the Raman shift Δ is a characteristic feature of a given molecule related to its vibronic profile (Fig. 1). Surface enhanced CARS (SECARS) additionally exploits signal intensity enhancement related to occurrence of plasmonic excitations at the surface of metallic nanoparticles: these nanoparticles can be tailored in order to locally enhance electromagnetic fields of desired optical to near-infrared frequencies [14]. Still, engineering particles that would simultaneously enhance electric fields at multiple desired frequencies is in general a challenging task. The SECARS technique can be significantly more sensitive than the standard surface-enhanced Raman spectroscopy [15]. In order to achieve single-molecule sensitivity, huge signal enhancement is required of at least 10–11 orders of magnitude [4]. With exactly this performance level, exploiting two broad plasmonic modes resonant with the Stokes and anti-Stokes field, the technique has already been demonstrated to enable molecular detection at the single-molecule level [16,17]. Plasmonic nanostructures with even stronger predicted enhancement have been engineered such as gold trimers [18] or silver metal-insulator-metal configurations [19].

Here, we make a contribution towards exploring the potential of plasmonic enhancement of CARS in greater depth, and propose a metal-insulator-grating metasurface that

* e-mail: s.izadshenas@doktorant.umk.pl

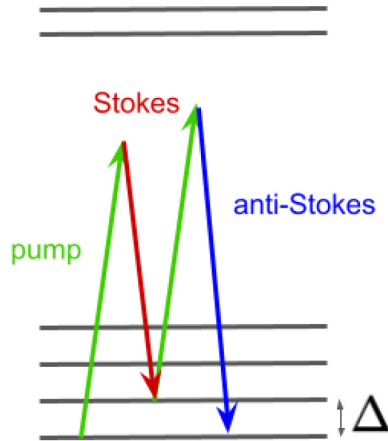


Fig. 1. Scheme of the coherent anti-Stokes Raman scattering event: an absorption of two photons of the probe beam along with a stimulated emission of a photon in the Stokes beam results in a coherent emission of a photon at the anti-Stokes frequency. Black lines represent molecular energy levels, e.g., associated with its vibrational structure. Note that the sample is illuminated with two, pump and Stokes fields, while the anti-Stokes radiation is generated through the nonlinear process.

supports multiple, tunable resonance peaks. Similar structures have been investigated before in the context of tunable multi-resonant optical response [20,21]. We base the design on gold elements, which is generally more stable in experimental conditions than silver that performs better in theory leading to stronger enhancement predictions. The structure unit cell combines a nanodisk dimer and a grating: three elements which, when coupled, support three resonance modes in the near-infrared regime of interest. In particular, each of the disks supports a peak corresponding to its fundamental resonance. Their coupling leads to the resonance splitting in a pair. This pair will give rise to the Stokes and anti-Stokes peaks, however, influenced by the presence of grating. That allows us to shift the pair in the spectral domain and achieve tunability by modification of the incidence angle of illuminating beams. Additionally, the grating sharpens the Stokes and anti-Stokes pair and gives rise to a third resonance that will play the role of the pump peak. To demonstrate the potential to tailor the metasurface by design to match the Raman profiles of various molecules, we adjust the geometry parameters to selected peaks in the Raman spectrum of rhodamine 6G. Finally, we demonstrate how the same structure could be tuned post fabrication to match other values of Raman shift.

2 Metasurface geometry CARS signal enhancement of rhodamine

A unit cell of the metasurface under consideration is schematically depicted in Figure 2a (side view) and Figure 2b (top view). We exploit the metal-insulator-grating (MIG) arrangement. In the top layer, each unit cell contains two coupled gold nanodisks of the same radius R and height h_d , separated by a gap of size d . A gold grating with each slab of width w_g and height h_g extended in the y direction makes the bottom layer. The slabs are separated by gaps of size g . A glass (SiO_2) insulator spacer slab of height h_s is sandwiched in

between as the middle layer. In the xy plane, the unit cell has a square shape of side length P . The surrounding medium is air. The structure could be fabricated in a bottom up scenario, where subsequent layers could be structured by electron beam lithography.

This choice of a metasurface offers a rich multi-resonant optical spectrum with three peaks in the near-infrared regime that can be tuned by design to match the Raman profile of a molecule of choice (see example spectra in Fig. 3 and below for a detailed discussion). Each of the nanodisks plays the role of an electric dipole, and their coupling gives rise to a pair of resonances. The third peak results from coupling the nanodisks with the grating. Naturally, in the miniaturized structure, all geometry parameters affect the spectral positions of each of these resonances. However, to the first approximation, we can spectrally tune the side peaks modifying the disks while changing the grating pattern mostly affects the middle resonance (see Appendix A).

The geometry parameters of the unit cell are engineered to match prominent Raman peaks of rhodamine 6G at $\Delta_1 = 1314 \text{ cm}^{-1}$, $\Delta_2 = 1363 \text{ cm}^{-1}$ and $\Delta_3 = 1512 \text{ cm}^{-1}$ [22,23]. Optimisation of the structure for each value of the Raman shift corresponds in general to a whole new design, where modification of the geometry parameters allows for tuning the three peak positions of the spectral response to match the CARS resonance condition (1) for a given Δ_j . The design is performed numerically, by solving full-vectorial Maxwell's equations in the frequency domain with the finite integration technique, using the commercial solver CST Studio Suite.

Periodic boundary conditions in x and y directions are used to extend the unit cell of the metasurface. For the SiO_2 insulator, we have set the refractive index $n = 1.45$ [24], and Palik's data were used to model the dielectric permittivity of gold [25] in the two nanodisks and the grating. The metasurface is illuminated with a plane wave incident in the z direction from the top (disk) side with electric and magnetic fields polarised in the x and y directions, respectively. Default surface-based tetrahedral meshing was chosen in the numerical study. The number of mesh cells was 230638, with the cell per max model box edge was 10. The length of the shortest and longest edge was 2.5 nm and 255.399 nm, respectively. The minimum and maximum of all mesh cell quality values were 0.071 and 0.998, respectively. Matching the metasurface with a given value of the Raman shift Δ_j is based on variation of metasurface geometry parameters, and here, adjustment of the gaps d between the disks and g between the grating slabs plays the key role. With fixed thicknesses of all elements: $h_d = 35 \text{ nm}$, $h_s = 250 \text{ nm}$, $h_g = 30 \text{ nm}$, fixed disk radius $R = 90 \text{ nm}$, grating width $w_g = 20 \text{ nm}$ and unit cell size $P = 600 \text{ nm}$, the gap sizes can be adjusted to match any of the three rhodamine Raman shifts given above. The resonant values are collected in the 3rd and 4th columns of Table 1.

We now investigate in greater detail the optical response of the metasurface for the set of geometry parameters corresponding to the Raman shift $\Delta_1 = 1314 \text{ cm}^{-1}$. The setup sustains the required multi-resonant character, as evident from the reflection $R(\lambda)$, transmission $T(\lambda)$ and absorption $A(\lambda) = 1 - R(\lambda) - T(\lambda)$ spectra in Figure 3, where λ stands for the free-space wavelength. The three peak positions in the near-infrared are given in Table 1 in terms of the

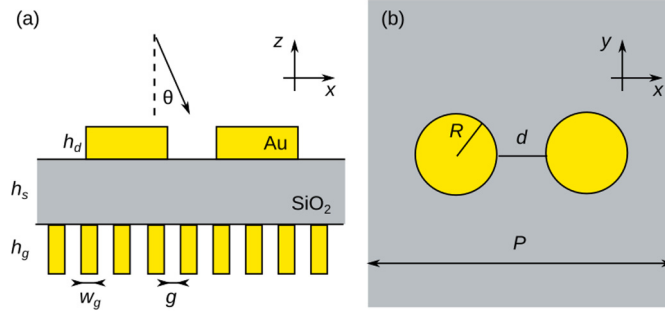


Fig. 2. Unit cell of the proposed metasurface: side (a) and top (b) views.

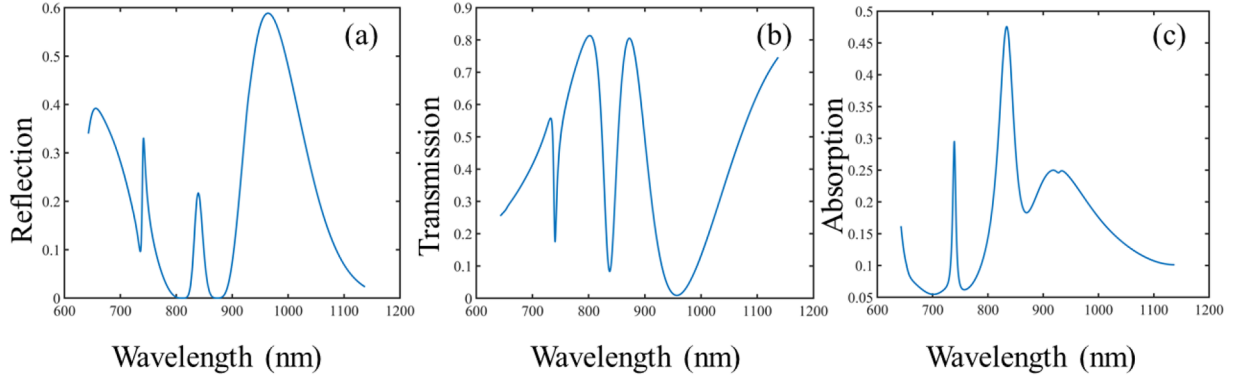


Fig. 3. Spectra of the MIG metasurface with geometry arrangements matching the rhodamine 6G Raman shift $\Delta_1=1314 \text{ cm}^{-1}$: (a) reflection, (b) transmission and (c) absorption.

Table 1. Geometry parameters (d, g) for which the spectral response of the investigated metasurface adjusts to different rhodamine 6G Raman shifts Δ_j , resonance positions of the resulting peaks in the metasurface spectral response $\lambda_{s,p,a}^j$, maximum value of the corresponding local scattered field enhancement factors at peak wavelengths $FE(\lambda_{s,p,a}^j) \equiv FE(\vec{r}_{max}, \lambda_{s,p,a}^j)$, and the maximum value of the local SECARS enhancement factor $G_{SECARS}^{\Delta_j}$. Maximization is here performed over positions within the unit cell.

$\Delta_j [\text{cm}^{-1}]$	Geometry		Stokes		Pump		Anti-Stokes		G^{Δ_j}
	d [nm]	g [nm]	λ_s^j [nm]	$FE(\lambda_s^j)$	λ_p^j [nm]	$FE(\lambda_p^j)$	λ_a^j [nm]	$FE(\lambda_a^j)$	
$j = 1$	1314	7.4	920	81	821	71	741	28	1.3×10^{14}
$j = 2$	1363	7.5	930	79	825	69	742	25	1.1×10^{14}
$j = 3$	1512	10.0	939	82	822	55	731	18	0.2×10^{14}

corresponding peak wavelengths $\lambda_{s,p,a} = 2\pi c/\omega_{s,p,a}$, where c is the vacuum speed of light and we refer to the lowest-, mid- and highest-energy resonances respectively as the Stokes, pump and anti-Stokes. The peak wavelengths fulfill the CARS resonance condition (1).

The spectra in Figure 3 are related to the local electric field enhancement factors

$$FE(r, \lambda) = \frac{|\vec{E}(\vec{r}, \lambda)|}{|\vec{E}_0|}, \quad (2)$$

where $\vec{E}(\vec{r}, \lambda)$ corresponds to the scattered electric field at position \vec{r} in the unit cell for illumination at the wavelength λ with a plane wave of amplitude $|\vec{E}_0|$. In general, the field

enhancement factor depends on polarisation of the illuminating beam, which we here set parallel to the x direction as indicated above. Please note that frequency conversion effects in gold nanostructures are relatively inefficient and the corresponding signal would not be expected to spectrally overlap with the Raman signal.

The near-field distributions for resonant illumination at the Stokes, pump and anti-stokes wavelengths are presented in Figure 4, where the absolute value of the electric field amplitude normalized to the input field is shown in the xy plane directly above the nanodisks. Regions of strong electric field enhancement for different illumination wavelengths overlap, promising high local SECARS enhancement. Also, the points of maximum electric field enhancement \vec{r}_{max} occur in the gap region between the

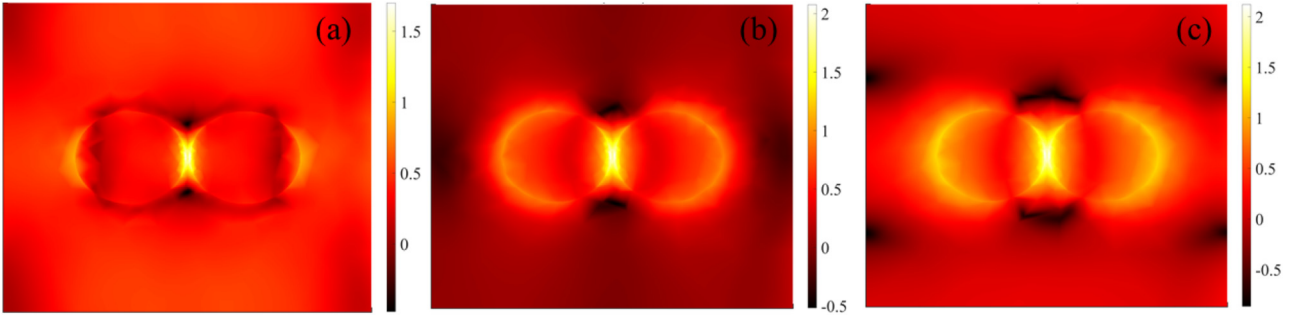


Fig. 4. The near field amplitude enhancement distributions $\log_{10}[FE(\vec{r}, \lambda_{a,p,s}^1)]$ across the unit cell, in the plane directly above the nanodisks at the wavelengths corresponding to the (a) anti-stokes (741 nm), (b) pump (821 nm), and (c) stokes (920 nm) peaks.

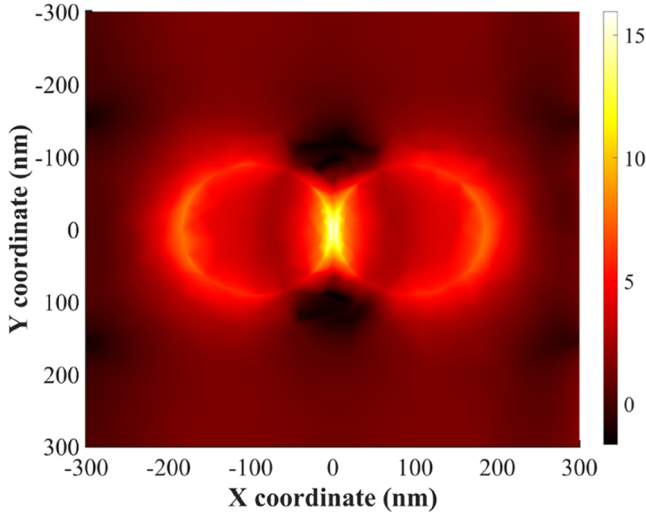


Fig. 5. Distribution of the SECARS enhancement factor $\log_{10}G^{\Delta_1}(\vec{r}, \lambda_s^1, \lambda_p^1, \lambda_a^1)$ across the unit cell directly above the nanodisk top surface.

disks for all three wavelengths. This means that a rhodamine molecule positioned in a hotspot generated in the nanodisk gap would be subject to a significantly enhanced field that would give rise to a strong CARS signal.

In quantitative terms, local SECARS enhancement factor is evaluated as a product of the field enhancement factors in accordance with the nonlinear four wave mixing scheme depicted in Figure 1

$$G(r, \lambda_s, \vec{\lambda}_p, \lambda_a) = FE(\vec{r}, \lambda_s)^2 FE(\vec{r}, \lambda_p)^4 FE(\vec{r}, \lambda_a)^2. \quad (3)$$

Below we will denote as $G^{\Delta_1}(\vec{r}, \lambda_s, \lambda_p, \lambda_a)$ the value of the enhancement provided by the metasurface optimised to match the Raman shift Δ_1 in accordance with Table 1. The metasurface under consideration gives rise to the local SECARS enhancement factor of maximum value $G^{\Delta_1}(\vec{r}_{\max}, \lambda_s^1, \lambda_p^1, \lambda_a^1) \approx 1.3 \times 10^{14}$. Geometries optimised for other selected Raman shifts Δ_2, Δ_3 result in similar values with 13–14 orders of magnitude CARS signal

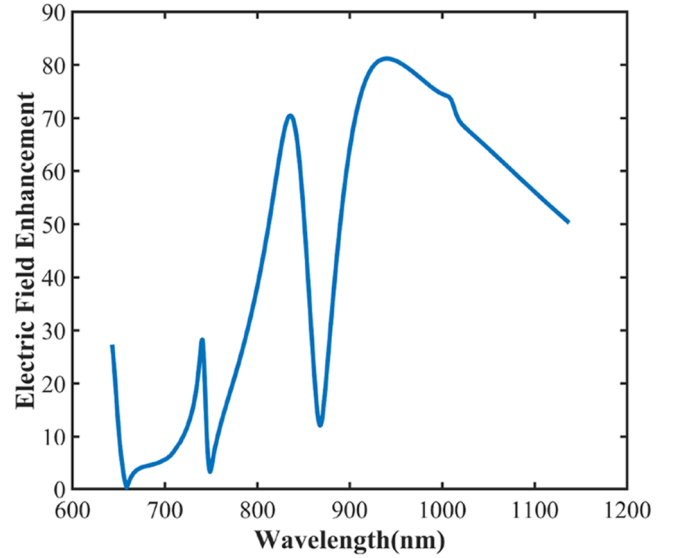


Fig. 6. Electric field enhancement factor $FE(\vec{r}_{\max}, \lambda)$ at the position of strongest enhancement \vec{r}_{\max} in the nanodisk gap as a function of the free space illumination wavelength λ .

enhancement, as can be read out from Table 1. These values exceed the single-molecule detection threshold [4] by 3 orders of magnitude.

The values given above reflect local CARS signal enhancement at the most favourable point \vec{r}_{\max} . The spatial distribution of the enhancement factor of the Raman peak at 1314 cm^{-1} $G^{\Delta_1}(\vec{r}, \lambda_s^1, \lambda_p^1, \lambda_a^1)$ across the optimised unit cell in the xy plane directly above the nanodisks is depicted in Figure 5. Following the field enhancement profiles, SECARS signal enhancement exceeding the threshold value of 10 orders of magnitude can be achieved in the yellow regions in the gap between the nanodisks of approximate volume of $5 \times 10^4 \text{ nm}^3$. This volume can hold a rhodamine molecule of approximately 1 nm in size, as well as other, potentially larger molecules.

Figure 6 depicts the field enhancement factor $FE(\vec{r}_{\max}, \lambda)$ for the same metasurface geometry arrangement at the fixed position of maximum field enhancement, but depending on the illumination wavelength. The peak values can be read out from Table 1. The near-field spectrum in Figure 6

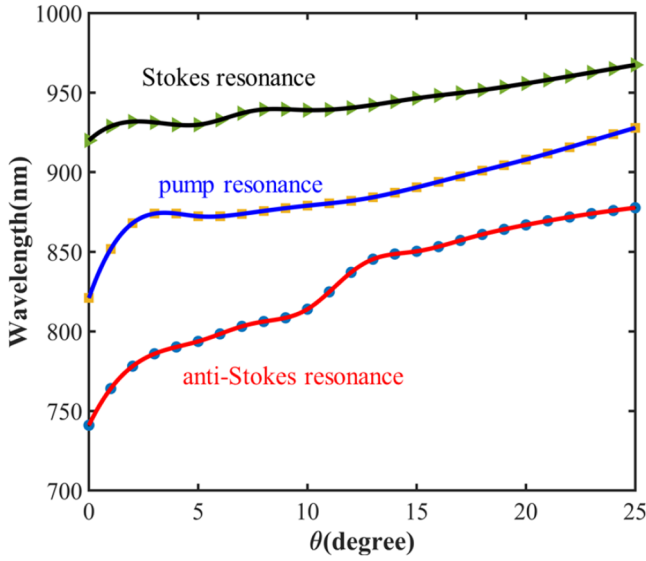


Fig. 7. Resonance wavelengths dependence on the incidence angle for the three resonance peaks of the investigated metasurface.

demonstrates the broad character of the resonance peaks, in particular, of the pump and Stokes resonances. This suggests that although the metasurface geometry is now optimised for the Raman shift at $\Delta_1 = 1314 \text{ cm}^{-1}$, it would still provide significant CARS signal enhancement corresponding to other prominent Raman shifts at Δ_2 or Δ_3 . Indeed, the value of the CARS enhancement factor corresponding to the shift of Δ_2 sustained by the metasurface optimised for Δ_1 reaches $G^{\Delta_1}(\vec{r}_{\max}, \lambda_s^2, \lambda_p^2, \lambda_a^2) \approx 9 \times 10^{13}$. The value corresponding to the third investigated Raman shift $\Delta_3 = 1512 \text{ cm}^{-1}$ provided by the same nanostructure geometry is an order of magnitude smaller due to the slight mismatch with the relatively narrow anti-Stokes peak. In consequence, the structure could support Raman signal enhancement from rhodamine molecules in a broad range of a few hundred inverse centimetres around the Δ_1 shift, bringing it even 2–3 orders of magnitude above the single-molecule threshold. Similarly, the signal from other molecules could be improved with the same metasurface structure, e.g., CO_2 with the most prominent peak at 1385 cm^{-1} [26], the 1360 cm^{-1} peak of glucose [27], and many others.

Finally, please note that the investigated structure is tailored for the detection of molecules at extremely low concentrations, in particular, at the single-molecule level. The presence of molecules at such low concentrations has little influence on the refractive index of the nanoparticles' surroundings. Therefore, we expect the metasurface's optical response would hardly be modified by their presence. The molecules are rather detected with Raman techniques due to the generation of the anti-Stokes signal, absent without the molecules, therefore delivering background-free detection possibility.

3 Post-fabrication tunability

In the previous section we have demonstrated the structure's capability to improve the Raman signal in the range around

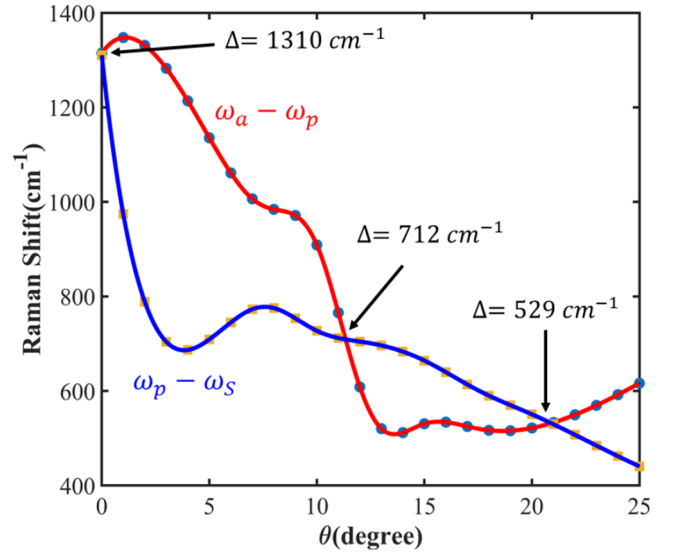


Fig. 8. Differences of resonance frequencies in function of the incidence angle. The crossing points correspond to fulfilling the Raman resonance condition (1) for different Raman shifts indicated in the figure.

1310 cm^{-1} , with the enhancement peaks fulfilling the resonance condition (1) under normal incidence. In the MIG configuration, integration of the grating in the metasurface design provides an additional degree of freedom and a tuning knob, related to the illumination incidence angle on which the optical response of the metasurface strongly depends. The angle is denoted as θ in Figure 2. Below we demonstrate how this tunability knob can be exploited to switch between different Raman shift ranges.

Moreover, in a practical fabrication process the nano-scaled shapes, sizes and even the varying material quality are sources of imperfections that will in general degrade the achieved signal enhancement. This is typically overcome by preparing multiple samples with increasingly modified geometry parameters [28]. Here, an alternative strategy by adjustment of the illumination angle could be used instead.

We analyse the effect for the metasurface designed to match the Raman shift Δ_1 at normal incidence. As the incident angle is modified in the range from 0 to 25 deg, the resonances redshift (Fig. 7), in general breaking the CARS resonance condition (1). The differences between pairs of resonance frequencies $\omega_p - \omega_s$ and $\omega_a - \omega_p$ are shown in Figure 8, where each of the crossing points fulfills the CARS condition with a different Raman shift, in this case $\Delta = 712 \text{ cm}^{-1}$ for $\theta = 13^\circ$ and $\Delta = 529 \text{ cm}^{-1}$ for $\theta = 21^\circ$. This means that by changing the incident angle the resonance wavelengths can be switched from one to another Raman shift, making one metasurface operational with different molecular species.

4 Conclusions

We have discussed a MIG metasurface suitable to enhance the CARS signal, in particular from rhodamine G6, exceeding the single-particle detection threshold by up to 3 orders of magnitude.

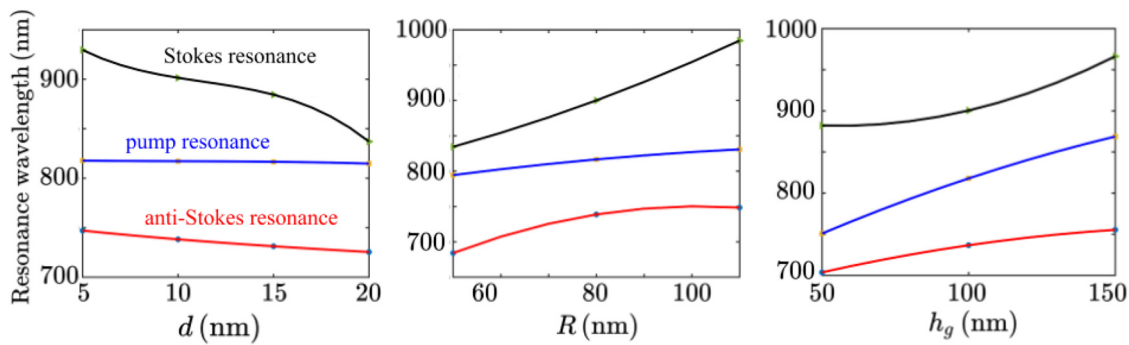


Fig. A1. Spectral position of the three investigated resonance peaks as functions of the disk geometry parameters (left: distance between nanodisks, middle: nanodisk radius) and grating height (right).

Despite the high sensitivity of the setup's spectral response with respect to its geometry parameters, especially the gap sizes, due to the broad character of the resonances the value of the SECARS enhancement factor is not crucially dependent on the very small size variation. In fact, one geometric setup arrangement can actually cover many resonances and adjust to several molecular species. Moreover, integration of the grating in the metasurface geometry makes switching between distinct ranges of Raman shifts possible by adjusting the angle at which the structure is illuminated.

We acknowledge the support from the National Science Centre, Poland (project No. 2016/23/G/ST3/04045) and Helmholtz Young Investigators Group (VH-NG-1404).

Appendix A: Spectral tuning

Figure A1 presents the spectral shift of the three resonance peaks as geometry parameters of the top layer (disks) and the grating are modified. The figure corresponds to $h_d = 65$ nm, $h_s = 200$ nm, $w_g = 20$ nm, $P = 600$ nm and, unless specified differently in the figure, $R = 80$ nm, $d = 10$ nm, $h_g = 100$ nm. The figure illustrates that the positions of the two side (Stokes and anti-Stokes) resonances are sensitive to the disk parameters, while the middle pump resonance is rather robust with respect to disk geometry tuning. This is expected since the side peaks arise due to the hybridisation of the disk resonances and are absent as the disks are removed. Contrary, all three resonances red-shift as the grating height is increased, with the slightly more sensitive response of the middle peak found in the investigated range of parameters. All resonances are relatively robust to modulations of the disk height: They shift by approximately 10 nm as the disk height is scanned between 30 to 100 nm (not shown). Similarly, the spacer height being varied between 150 and 250 nm results in linear shifts of all resonances with a similar slope, weakly affecting the Raman effect.

References

1. E. Smith, G. Dent, *Modern Raman Spectroscopy: A Practical Approach* (John Wiley & Sons, 2019)
2. P.L. Stiles, J.A. Dieringer, N.C. Shah, R.P. Van Duyne, Surface-enhanced Raman spectroscopy, *Annu. Rev. Anal. Chem.* **1**, 601 (2008)
3. J.B. Jackson, N.J. Halas, Surface-enhanced Raman scattering on tunable plasmonic nanoparticle substrates, *Proc. Natl. Acad. Sci.* **101**, 17930 (2004)
4. E.J. Blackie, E.C. Le Ru, P.G. Etchegoin, Single-molecule surface-enhanced Raman spectroscopy of nonresonant molecules, *J. Am. Chem. Soc.* **131**, 14466 (2009)
5. R. Zhang et al., Chemical mapping of a single molecule by plasmon-enhanced Raman scattering, *Nature* **498**, 82 (2013)
6. E.C. Le Ru, P.G. Etchegoin, Single-molecule surface-enhanced Raman spectroscopy, *Annu. Rev. Phys. Chem.* **63**, 65 (2012)
7. C. Chen, N. Hayazawa, S. Kawata, A 1.7 nm resolution chemical analysis of carbon nanotubes by tip-enhanced Raman imaging in the ambient, *Nat. Commun.* **5**, 1 (2014)
8. S. Jiang et al., Distinguishing adjacent molecules on a surface using plasmon-enhanced Raman scattering, *Nat. Nanotechnol.* **10**, 865 (2015)
9. F. Benz et al., Single-molecule optomechanics in 'picocavities,' *Science* **354**, 726 (2016)
10. C. Zong et al., Plasmon-enhanced stimulated Raman scattering microscopy with single-molecule detection sensitivity, *Nat. Commun.* **10**, 5318 (2019)
11. R. Begley, A. Harvey, R.L. Byer, Coherent anti-Stokes Raman spectroscopy, *Appl. Phys. Lett.* **25**, 387 (1974)
12. M.D. Duncan, J. Reintjes, T. Manuccia, Scanning coherent anti-Stokes Raman microscope, *Opt. Lett.* **7**, 350 (1982)
13. A. Zumbusch, G.R. Holtom, X.S. Xie, Three-dimensional vibrational imaging by coherent anti-Stokes Raman scattering, *Phys. Rev. Lett.* **82**, 4142 (1999)
14. S. Lal, N.K. Grady, J. Kundu, C.S. Levin, J.B. Lassiter, N.J. Halas, Tailoring plasmonic substrates for surface enhanced spectroscopies, *Chem. Soc. Rev.* **37**, 898 (2008)
15. C. Steuwe, C.F. Kaminski, J.J. Baumberg, S. Mahajan, Surface enhanced coherent anti-Stokes Raman scattering on nanostructured gold surfaces, *Nano Lett.* **11**, 5339 (2011)
16. Y. Zhang, Y.-R. Zhen, O. Neumann, J.K. Day, P. Nordlander, N.J. Halas, Coherent anti-Stokes Raman scattering with single-molecule sensitivity using a plasmonic Fano resonance, *Nat. Commun.* **5**, 4424 (2014)
17. S. Yampolsky et al., Seeing a single molecule vibrate through time-resolved coherent anti-Stokes Raman scattering, *Nat. Photonics* **8**, 650 (2014)

18. J. He, C. Fan, P. Ding, S. Zhu, E. Liang, Near-field engineering of Fano resonances in a plasmonic assembly for maximizing CARS enhancements, *Sci. Rep.* **6**, 20777 (2016)
19. J. Wang et al., Theoretical investigation of a multi-resonance plasmonic substrate for enhanced coherent anti-Stokes Raman scattering, *Opt. Express* **25**, 497 (2017)
20. D.M. Nguyen, D. Lee, J. Rho, Control of light absorbance using plasmonic grating based perfect absorber at visible and near-infrared wavelengths, *Sci. Rep.* **7**, 2611 (2017)
21. S. Zhang, Y. Wang, S. Wang, W. Zheng, Wavelength-tunable perfect absorber based on guided-mode resonances, *Appl. Opt.* **55**, 3176 (2016)
22. E. Kirubha, P. Palanisamy, Green synthesis, characterization of Au–Ag core–shell nanoparticles using gripe water and their applications in nonlinear optics and surface enhanced Raman studies, *Adv. Nat. Sci. Nanosci. Nanotechnol.* **5**, 045006 (2014)
23. S. Shim, C.M. Stuart, R.A. Mathies, Resonance Raman cross-sections and vibronic analysis of Rhodamine 6G from broadband stimulated Raman spectroscopy, *ChemPhysChem* **9**, 697 (2008)
24. C. Tan, Determination of refractive index of silica glass for infrared wavelengths by IR spectroscopy, *J. Non-Cryst. Solids* **223**, 158 (1998)
25. D.P. Edward, I. Palik, *Handbook of Optical Constants of Solids* (Academic Press, New York, 1985)
26. G. Tejada, B. Maté, S. Montero, Overtone Raman spectrum and molecular polarizability surface of CO₂, *J. Chem. Phys.* **103**, 568 (1995)
27. O. Lyandres, J.M. Yuen, N.C. Shah, R.P. VanDuyne, J.T. Walsh Jr, M.R. Glucksberg, Progress toward an in vivo surface-enhanced Raman spectroscopy glucose sensor, *Diabetes Technol. Ther.* **10**, 257 (2008)
28. M. Asano et al., Distillation of photon entanglement using a plasmonic metamaterial, *Sci. Rep.* **5**, 18313 (2015)

Cite this article as: Saeid Izadshenas, Piotr Masłowski, Tobias Herr, Karolina Słowik, Multiresonant metasurface for Raman spectroscopy beyond single molecule detection level, *EPJ Appl. Metamat.* **9**, 11 (2022)

To be published in Optics Letters:

Title: Multi-Photon Absorption Enhancement by Graphene-Gold Nanostructure

Authors: Saeid Izadshenas Jahromi, Karolina Slowik

Accepted: 27 June 24

Posted 28 June 24

DOI: <https://doi.org/10.1364/OL.531669>

Published by Optica Publishing Group under the terms of the [Creative Commons Attribution 4.0 License](#). Further distribution of this work must maintain attribution to the author(s) and the published article's title, journal citation, and DOI.

OPTICA
PUBLISHING GROUP

Multiphoton absorption enhancement by graphene-gold nanostructure

SAEID IZADSHENAS JAHROMI^{1,*} AND KAROLINA SŁOWIK¹

¹Institute of Physics, Faculty of Physics, Astronomy and Informatics, Nicolaus Copernicus University in Toruń, 87-100 Toruń, Poland

*s.izadshenas@doktorant.umk.pl

Compiled June 27, 2024

We present a hybrid graphene-gold nanoantenna designed to enhance multiphoton absorption signals in molecules. The enhancement process involves two key steps: Firstly, the graphene component of the antenna supports molecular absorption in the mid-infrared and terahertz bands. By applying gate voltage, one can adjust the spectral positions of its resonances and select the desired absorption order, determining the number of photons absorbed in a single transition event. Secondly, gold nanorods with carefully tailored geometrical parameters enhance fluorescent single-photon emission. As a proof of concept, we adjust the geometry parameters of the hybrid antenna to the ATTO 700 dye molecule, taking into account its spectrally-resolved emission characteristics. We predict a significant local enhancement of the fluorescence signal indicating the highly nonlinear process of N -photon absorption to exceed 5 orders of magnitude for $N = 2$ and 13 orders of magnitude for higher nonlinearity orders. Our proposed nanoantenna offers a promising platform for the tunable enhancement of highly nonlinear light-matter interactions.

<http://dx.doi.org/10.1364/ao.XX.XXXXXX>

Nonlinear light-matter interactions, such as multiphoton absorption, are essential in scientific and technological applications, including 3D microscopy imaging [1], optical data storage [2], and photodynamic therapy [3]. These interactions offer unique advantages in fields spanning life sciences [4] to materials sciences [5] due to their ability to probe deeper into samples [6], encode information densely [7], and selectively activate biological processes [8]. Despite their potential, the observation of nonlinear light-matter interactions at low levels of light or low matter densities faces challenges primarily due to the inherently low cross-sections associated with these processes [9–11]. Overcoming these limitations is crucial for advancing the practical utilization of multiphoton phenomena in diverse applications.

To address the issue of low cross-sections, plasmonic nanoparticles have emerged as promising candidates [12]. They exploit surface plasmon resonances to concentrate electromagnetic fields, thereby enhancing the interaction between light and matter. Several applications have been proposed or realised, including Raman signal enhancement [13, 14], frequency up-

conversion [15], or two-photon absorption [16–18].

In this work, we propose a hybrid nanoantenna combining graphene and noble-metal elements. Graphene sustains a strong plasmonic response when subject to external gate voltage that enables spectral tuning of the plasmonic resonances [19, 20], and has already been proposed as a platform mediating light-matter interactions [21, 22]. Here, this feature is exploited to adjust the spectral response of the antenna for a plasmonic enhancement of multiphoton absorption in adjacent molecules: Voltage modulations tune the plasmonic peak not only to match the specific transition of a specific molecule, but also to realize an N -photon resonance with the target transition where the number of photons N can be varied. The gold antenna elements support the conversion of the absorbed energy into a fluorescent signal, being a background-free manifestation of the nonlinear interaction. We elaborate on the details of this concept below. The antenna scheme and optical properties are investigated next. Based on these properties, we predict significant enhancements of multiphoton processes and the resulting fluorescent signal with respect to free-space realizations.

We consider a molecule with the ground $|g\rangle$ and excited $|e\rangle$ states, respectively with energies $\hbar\omega_g$ and $\hbar\omega_e$, and multiple states in between of energies $\hbar\omega_i$, i being the state index. N -photon absorption may occur upon illumination at the frequency ω considerably lower than the molecular transition frequency $\omega_{eg} = \omega_e - \omega_g$, which however adheres approximately to the resonance condition $N\omega \approx \omega_{eg}$. The absorption is expected to be followed by a single-photon fluorescence, being a background-free indication of the nonlinear light-matter interaction. See the schematical depiction of this scenario in Fig. 1(a).

To boost both the absorption and fluorescence rates, we employ a hybrid graphene-gold nanostructure [Fig. 1(b,c)]. It consists of a graphene disk sustaining plasmonic resonances tunable in the terahertz to mid-infrared range with gate voltage, and four gold nanobars with a resonance at the molecular transition frequency. The structure's symmetry ensures that all optical responses are polarization-independent. The graphene element can be tuned to support N -photon absorption, in principle, for a wide range of $N = 2, 3, 4, \dots$. However, we focus on even values of N , for which the generation of harmonics is suppressed in graphene that might otherwise overshadow the molecular signal. The gold elements enhance the molecular fluorescence in a broad range of frequencies according to the bandwidth of plasmonic resonances in gold. The graphene and gold elements are

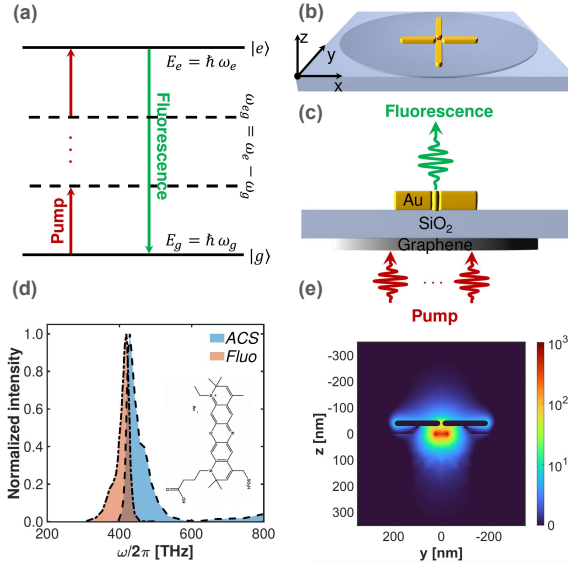


Fig. 1. (a) Energy scheme of the illuminated molecule. (b) Proposed nanoantenna geometry. (c) Side-view of the nanoantenna geometry with pump beams and fluorescent emission depicted. (d) Normalized scattering cross-section and fluorescence spectra. (e) Electric field enhancement distribution for plane-wave illumination at a resonant frequency.

separated by a glass spacer. In consequence, the enhancement factor of the fluorescence signal arising through N -photon absorption and subsequent single-photon emission can be written as (see *Supplement Sec. 1* for a derivation):

$$I^{(N)}(\mathbf{r}, \mu_c) = \frac{|\mathbf{E}(\mathbf{r}, \omega_{\text{abs}}, \mu_c)|^{2N}}{|\mathbf{E}_0(\omega_{\text{abs}})|^{2N}} \times \frac{1}{\mathcal{F}(N\omega_{\text{abs}})} \int_0^{N\omega_{\text{abs}}} d\omega_{\text{flu}} \frac{P(\mathbf{r}, \omega_{\text{flu}})}{P_0(\omega_{\text{flu}})} f(\omega_{\text{flu}}), \quad (1)$$

where \mathbf{r} is the molecular position, ω_{abs} and ω_{flu} represent the frequencies at which the illumination (absorption) and fluorescence occur. Note that the fluorescence emission frequency has an upper limit of $N\omega_{\text{abs}}$ and can, in general, be smaller than this limit due to nonradiative energy dissipation in the excited electronic state. The symbol $f(\omega_{\text{flu}})$ stands for the fluorescence emission spectrum. The symbol $|\mathbf{E}_0(\omega_{\text{abs}})|$ stands for the illuminating field amplitude which we assume constant in space for the plane wave illumination, and $|\mathbf{E}(\mathbf{r}, \omega_{\text{abs}}, \mu_c)|$ is the nanoantenna-enhanced amplitude of the field frequency component at ω_{abs} . The field enhancement is a function of the chemical potential μ_c in graphene, tunable with gate voltage. The fluorescence emission spectrum $f(\omega)$ is depicted in Fig. 1(d) together with the single-photon absorption cross-section $C_{\text{abs}}^{(1)}(\omega)$. The latter does not impact the enhancement factor in the case of monochromatic illumination. As shown in *Methods*, it does influence the emission signal enhancement for a more complicated illumination scheme. Finally, $P_0(\omega_{\text{flu}})$ and $P(\mathbf{r}, \omega_{\text{flu}})$ are the dipole emission powers in free space and at position \mathbf{r} near the antenna. The dipole source represents here a molecular transition at the ω_{flu} frequency, whose intensity is enhanced in the presence of the nanoantenna through the well-known Purcell effect [23].

Our goal in this work is to find the impact of the proposed

hybrid nanoantenna on the intensity of fluorescence signal occurring due to the preceding N -photon absorption. This impact is characterized by the enhancement given by Eq. (1), and is determined by the antenna geometry and chemical potential in graphene. We analyse these below.

Below, we describe the optical response of individual nanoantenna components: the graphene disk in the mid-infrared and terahertz regimes, and the gold nanorods in the visible and infrared domains. The optical properties of graphene, gold and glass are modelled as described in the *Supplement Sec. 2*.

For the graphene disk, we assume the plane wave illumination scenario with the illuminating field propagating from the bottom to the top and polarized along the x -axis in Fig. 1(b,c). An example field distribution for a resonant illumination at the frequency $\omega = 54.5$ THz is shown in Fig. 1(e). The highest field enhancement is achieved near the graphene disk. Thus, we first investigate the electric field enhancement spectra $|\mathbf{E}(\mathbf{r}, \omega, \mu_c)|/|\mathbf{E}_0(\omega)|$ for \mathbf{r} corresponding to the position 1 nm below the centre of the disk. The spectra are shown as functions of the two key parameters decisive for the plasmonic resonance position: the disk radius and the chemical potential [Fig. 2(a) and (b), respectively]. In Fig. 2(a), the chemical potential is fixed at $\mu_c = 0.7$ eV and we sweep the graphene radius from 10 nm to 100 nm. The figure illustrates the redshift and suppression of the plasmonic resonance with increasing disk radius. In Fig. 2(b), the radius of the graphene disk is fixed at $R = 25$ nm, and the chemical potential varies from 0.1 eV to 1.2 eV by step of 0.025 eV. The figure highlights the tunability of the resonance position, which can be adjusted by a proper choice of gate voltage to support N -photon absorption in a molecule.

Calculating signal enhancement, we assume the molecule is located at the middle of the gap among the nanorods, at a point $z = 40$ nm above the graphene disk, indicated with the red dot in Fig. 1. At that point, the field enhancement spectra shown in Fig. 2(c,d) sustain resonances at the same frequencies as in the position just above the graphene disk (Fig. 2(a,b)). Yet, due to the plasmonic confinement, at the distance of 40 nm the field enhancement drops with decreased radii. Regardless of the position, a higher chemical potential leads to a stronger resonance [Figs. 2b and 2d] due to a larger charge density that contributes to the plasmonic response.

The strong field confinement achieved for small graphene radii is correlated with relatively low nanoantenna efficiency η defined as the ratio of scattering RCS and extinction (scattering+absorption, ACS) cross sections $\eta = \frac{\text{RCS}}{\text{RCS} + \text{ACS}}$. The efficiency of the graphene disks is shown as a function of radius and chemical potential in Fig. 3. For graphene radii smaller than $R = 85.5$ nm, owing to the confined electric field near the graphene disk, the nanoantenna's efficiency drops below 50%, as depicted in Fig. 3(a). Larger disk radii correspond to less confinement and suppress field absorption in graphene.

The nanostructure's efficiency can be enhanced through the modification of the chemical potential. For a graphene disk radius of $R = 100$ nm, the scattering cross-section surpasses the absorption cross-section when the potential exceeds $\mu_c = 0.57$ eV, as shown in Fig. 3(b). Note the linear scaling of the antenna efficiency with the chemical potential.

We model the optical characteristics of the gold nanorods using the dipolar illumination scheme to mimic the molecular dipolar transition as a source. The dipole is positioned in the middle of the gap between the gold nanorods, as indicated by the red dot in Fig. 1(b), and oriented along the x -axis. The quantity of

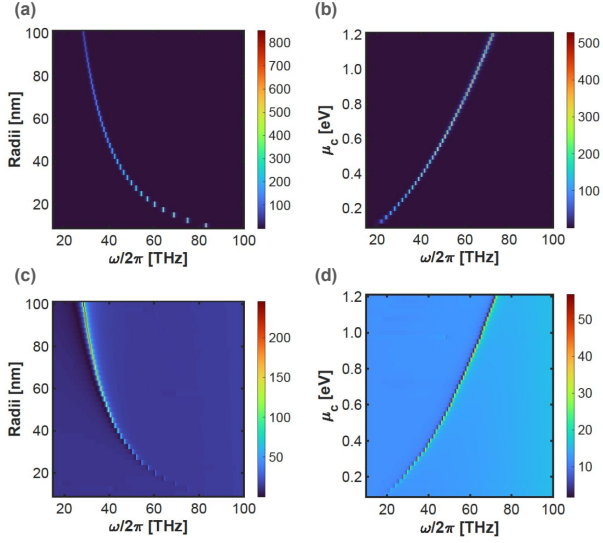


Fig. 2. Electric field enhancement spectra at $z = 1$ nm above the graphene disk as functions of (a) disk radius with a fixed chemical potential $\mu_c = 0.7$ eV, (b) chemical potential for a fixed radius $R = 25$ nm, (c,d) as (a,b) but for $z = 40$ nm.

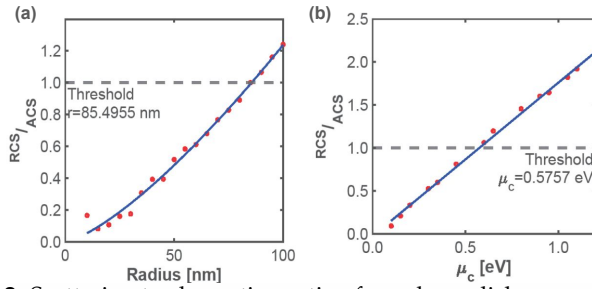


Fig. 3. Scattering to absorption ratio of graphene disk as a function of (a) radius, (b) chemical potential. The black dashed line indicates the efficiency of the nanostructure equal to $\eta = 0.5$. The red dots represent simulation outcomes, while the blue line is a fit.

interest is the radiated power spectrum normalized by the free space results $P(\mathbf{r}, \omega)/P_0(\omega)$, which we calculate as functions of geometry parameters of the rods. The resulting spectra are illustrated in Fig.4(a,b) for varied gold nanorods' lengths which is the main tuning knob for the resonance position. For larger nanorods, there is a significant increase in radiated powers that are enhanced by up to 5 orders of magnitude in the presence of the nanoantenna, which is the consequence of the improved efficiency of gold elements of greater lengths.

The gap size is one of the most important parameters that significantly impacts the achievable values of the radiated power enhancement. For nanorods of fixed lengths of $l = 190$ nm and radii $r = 10$ nm, we sweep the gap size from 10 nm to 100 nm with a step of 2.5 nm. The resulting radiated power spectra for varied nanorods' gaps are shown in Fig.4(c,d). As expected, the radiated power is increased for smaller gap sizes. Compared to the free space values, the power enhancement exceeds 4 orders of magnitude for gaps below 20 nm.

Finally, we investigate the influence of gold nanorods' radii on the radiated power spectra. For a fixed gap of $g = 30$ nm and nanorod lengths $l = 190$ nm, we sweep the radii from 5

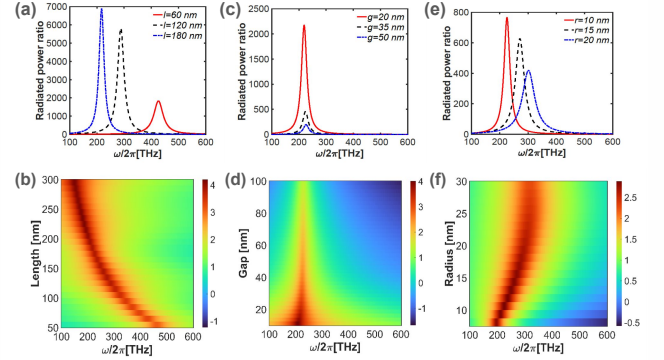


Fig. 4. Radiated power ratio to the free space values for gold nanorods: (a,b) with fixed radius $r = 10$ nm and gap $g = 10$ nm, and varied length l ; (c,d) for fixed $r = 10$ nm and $l = 190$ nm and varied g ; (e,f) for $l = 190$ nm, $g = 30$ nm and varied r . Note the logarithmic scale in (b,d,f).

to 30 nm with the step of 1.25 nm. Fig.4(e,f) demonstrates that enlarging the radii of the nanorods leads to a reduction in the radiated power ratio and a shift of the resonance towards a higher frequency, being an additional knob for resonance frequency tuning.

We now analyse the enhancement factors in Eq. (1) for varied illumination and nanoantenna characteristics. Each of the investigated factors corresponds to a fixed number N of absorbed photons and a following single-photon fluorescence. Their comparative performance depends on the nanoantenna characteristics: For a fixed chemical potential, the nanoantenna may be tuned to efficiently support one of those processes for a specific N . Modification of the potential allows us to alter the supported process, e.g., shift the antenna resonance frequency from a $\omega_{eg}/2$ corresponding to the two- to $\omega_{eg}/4$ supporting the four-photon absorption, etc. The following calculations are made for a model ATTO 700 dye molecule positioned in the selected point near the graphene-gold nanostructure, because of its relatively high optical cross-sections. The normalized absorption $C^{(1)}(\omega)$ and fluorescence $f(\omega)$ profiles of ATTO 700 are available in the database in Ref. [24] and displayed in Fig.1(d), indicating fluorescence and absorption peaks at 418 THz and 428 THz, respectively. The signal enhancement factors, evaluated according to Eq.(1), are plotted in Fig. 5 for $N = 2, 4, \dots, 10$. The frequencies ω_{gr}^{res} on the vertical axis denote the spectral position of the nanoantenna resonance in the infrared range, originating at the graphene disk. Different points along this axis correspond to different values of the chemical potential which serves as the knob for resonance frequency tuning. The graphene radius has been fixed at 12.5 nm. Similarly, the horizontal axis shows the spectral position ω_{Au}^{res} of the visible resonance supporting molecular fluorescence. Different points along the axis correspond to different nanorod lengths for the fixed rod radius of 10 nm, and the gap of 10 nm. The location of the signal-enhancement peaks is determined by the spectral positions and widths of plasmonic resonances: The narrow peak along the vertical axis achieved for $N = 4, \dots, 10$ in Fig. 5(b-e) results from the narrowband graphene plasmon. On the contrary, the resonance in gold rods is broad, and so is the signal enhancement factor along the horizontal axis. We find that the enhancement factor increases with the nonlinearity order (i.e., increasing N) roughly by 4 orders of magnitude as $N \rightarrow N + 2$ [Fig. 5(b-e)]. The predicted fluorescence enhancement for $N = 2$ in Fig. 5(a) has a different character because, for

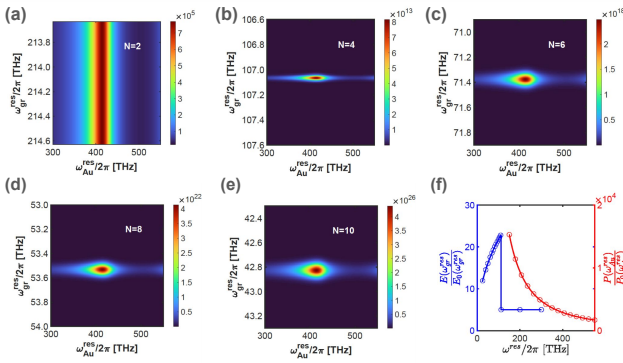


Fig. 5. Fluorescence enhancement factor in N -photon absorption with (a) $N = 2$, (b) $N = 4$, (c) $N = 6$, (d) $N = 8$, (e) $N = 10$, and (f) as a function of spectral positions of the plasmonic resonances of the graphene disk $\omega_{\text{gr}}^{\text{res}}$ and the gold nanorods $\omega_{\text{Au}}^{\text{res}}$.

frequencies exceeding 110.8 THz, graphene is no more metallic but becomes a dielectric, with the electric field enhancement factor of about 5 in a relatively broad spectral range. On the contrary, the emission power enhancement still has a resonant character and reaches the factor of $\sim 3 \times 10^3$, leading to an overall 5 orders-of-magnitude enhancement of the fluorescence signal. This is confirmed in Fig. 5(f). The blue line shows the field enhancement for resonant illumination, as the frequency ω_{res} is modified with the gate voltage. Note that there is threshold frequency around 110.8 THz for the graphene radius of 12.5 nm, above which the graphene response is flat and does not sustain a resonant character. The red line in the same panel shows the radiated power enhancement on resonance due to the presence of the gold nanoantenna elements, whose resonant frequency is tuned with the nanorod length. This explains the qualitatively different result obtained for the case of two-photon absorption in panel (a). Note that the enhancement factors defined in Eq. (1) are independent of the pump-field amplitude as the nanoantenna's optical response is assumed linear in our calculations. A potential limitation of this assumption might arise due to the Kerr effect, which could modify the scattered field amplitude at the illumination frequency. Nonetheless, linear response has been verified in graphene nanoribbons with widths similar to the size scales in our study, up to illumination amplitudes of approximately 10^5 V/m [25]. For gold, Kerr nonlinearity arises in ultrathin films due to quantum size effects and drastically drops with the size [26].

We have proposed a hybrid graphene-gold nanoantenna for molecular multiphoton absorption signal enhancement. The enhancement is achieved by combining the graphene and gold elements, operating respectively in the terahertz and visible regimes. The optical properties of the nanoantenna have been thoroughly characterised, with emphasis on the tunability offered by graphene: Through gate voltage manipulation one can adjust the nanoantenna to support nonlinear light interaction with molecules at the desired nonlinearity order, in this case, absorption of a predefined number of photons. We have analyzed two- to ten-photon absorption by the ATTO 700 dye molecule supported by the proposed nanoantenna, and found that the enhancement factor can exceed 5 orders of magnitude for two-photon absorption, capitalising on the resonant character of the gold nanoantenna elements. For a higher number of absorbed photons at frequencies up to 108 THz, the process is additionally

supported by the occurrence of graphene resonances, leading to the predicted signal enhancement above 13 orders of magnitude.

Our work provides a promising solution for nonlinear light-matter interaction applications, as the tunable character of the operation makes the device adjustable for various types of molecules, which opens the perspectives for applications for molecular detection and identification. Furthermore, the conversion from the terahertz and mid-infrared regimes to the visible spectrum makes the device versatile for different applications such as enhancement of multiphoton fluorescence and selective excitation of molecular vibrational modes. This design holds significant implications for the field of nonlinear optics and could advance the study of molecular interactions at the nanoscale.

Acknowledgments. The authors acknowledge the support of the National Centre for Research and Development (QUANTERA II project no. QUANTERAII/1/21/E2TPA/2023).

Disclosures. The authors declare no conflicts of interest.

Data availability. No data were generated or analyzed in the presented research.

Supplemental document. See Supplement for supporting content.

REFERENCES

- W. Denk, J. H. Strickler, and W. W. Webb, *Science* **248**, 73 (1990).
- Y. Kawata, H. Ishitobi, and S. Kawata, *Opt. Lett.* **23**, 756 (1998).
- A. Kachynski, A. Pliss, A. Kuzmin, *et al.*, *Nat. Photonics* **8**, 455 (2014).
- S. Zhang, L. Liu, S. Ren, *et al.*, *Opto-Electronic Adv.* **3**, 200003 (2020).
- B. Gu, C. Zhao, A. Baev, *et al.*, *Adv. Opt. Photonics* **8**, 328 (2016).
- E. E. Hoover and J. A. Squier, *Nat. photonics* **7**, 93 (2013).
- F. Walter, G. Li, C. Meier, *et al.*, *Nano letters* **17**, 3171 (2017).
- W. D. de Boer, J. J. Hirtz, A. Capretti, *et al.*, *Light. Sci. & Appl.* **7**, 100 (2018).
- G. Remppe, *Science* **345**, 871 (2014).
- M. G. Raymer, T. Landes, and A. H. Marcus, *The J. Chem. Phys.* **155**, 081501 (2021).
- D. Tabakaev, M. Montagnese, G. Haack, *et al.*, *Phys. Rev. A* **103**, 033701 (2021).
- H. Yu, Y. Peng, Y. Yang, and Z.-Y. Li, *npj Comput. Mater.* **5**, 45 (2019).
- S. Nie and S. R. Emory, *science* **275**, 1102 (1997).
- S. Izadshenas and K. Słowik, *APL Mater.* **11**, 081120 (2023).
- J. Park, K. Kim, E.-J. Jo, *et al.*, *Nanoscale* **11**, 22813 (2019).
- J. D. Cox, M. R. Singh, M. A. Anton, and F. Carreno, *J. Physics: Condens. Matter* **25**, 385302 (2013).
- J. Olesiak-Banska, M. Waszkielewicz, P. Obstarczyk, and M. Samoc, *Chem. society reviews* **48**, 4087 (2019).
- X. Lu, D. Punj, and M. Orrit, *Nano Lett.* **22**, 4215 (2022).
- F. J. Garcia de Abajo, *Acs Photonics* **1**, 135 (2014).
- T. Guo and C. Argyropoulos, *Adv. Photonics Res.* **2**, 2000168 (2021).
- F. H. Koppens, D. E. Chang, and F. J. Garcia de Abajo, *Nano letters* **11**, 3370 (2011).
- P. Gonçalves, N. Stenger, J. D. Cox, *et al.*, *Adv. Opt. Mater.* **8**, 1901473 (2020).
- L. Novotny and N. Van Hulst, *Nat. photonics* **5**, 83 (2011).
- I. AAT Bioquest, "Spectrum [atto 700]," https://www.aatbio.com/fluorescence-excitation-emission-spectrum-graph-viewer/atto_700 (2024). Accessed: 2024-02-06.
- T. Christensen, W. Yan, A.-P. Jauho, *et al.*, *Phys. Rev. B* **92**, 121407 (2015).
- H. Qian, Y. Xiao, and Z. Liu, *Nat. Commun.* **7**, 13153 (2016).

FULL REFERENCES

- 320
321 1. W. Denk, J. H. Strickler, and W. W. Webb, "Two-photon laser scanning
322 fluorescence microscopy," *Science* **248**, 73–76 (1990).
- 323 2. Y. Kawata, H. Ishitobi, and S. Kawata, "Use of two-photon absorption
324 in a photorefractive crystal for three-dimensional optical memory," *Opt.*
325 *Lett.* **23**, 756–758 (1998).
- 326 3. A. Kachynski, A. Pliss, A. Kuzmin, *et al.*, "Photodynamic therapy by in
327 situ nonlinear photon conversion," *Nat. Photonics* **8**, 455 – 461 (2014).
- 328 4. S. Zhang, L. Liu, S. Ren, *et al.*, "Recent advances in nonlinear optics
329 for bio-imaging applications," *Opto-Electronic Adv.* **3**, 200003 (2020).
- 330 5. B. Gu, C. Zhao, A. Baev, *et al.*, "Molecular nonlinear optics: recent
331 advances and applications," *Adv. Opt. Photonics* **8**, 328–369 (2016).
- 332 6. E. E. Hoover and J. A. Squier, "Advances in multiphoton microscopy
333 technology," *Nat. photonics* **7**, 93–101 (2013).
- 334 7. F. Walter, G. Li, C. Meier, *et al.*, "Ultrathin nonlinear metasurface for
335 optical image encoding," *Nano letters* **17**, 3171–3175 (2017).
- 336 8. W. D. de Boer, J. J. Hirtz, A. Capretti, *et al.*, "Neuronal photoactivation
337 through second-harmonic near-infrared absorption by gold nanoparti-
338 cles," *Light. Sci. & Appl.* **7**, 100 (2018).
- 339 9. G. Rempe, "A photon steers a photon with an atom," *Science* **345**,
340 871–871 (2014).
- 341 10. M. G. Raymer, T. Landes, and A. H. Marcus, "Entangled two-photon
342 absorption by atoms and molecules: A quantum optics tutorial," *The J.*
343 *Chem. Phys.* **155**, 081501 (2021).
- 344 11. D. Tabakaev, M. Montagnese, G. Haack, *et al.*, "Energy-time-entangled
345 two-photon molecular absorption," *Phys. Rev. A* **103**, 033701 (2021).
- 346 12. H. Yu, Y. Peng, Y. Yang, and Z.-Y. Li, "Plasmon-enhanced light-matter
347 interactions and applications," *npj Comput. Mater.* **5**, 45 (2019).
- 348 13. S. Nie and S. R. Emory, "Probing single molecules and single nanopar-
349 ticles by surface-enhanced raman scattering," *science* **275**, 1102–1106
350 (1997).
- 351 14. S. Izadshenas and K. Słowik, "Metasurface for broadband coherent ra-
352 man signal enhancement beyond the single-molecule detection thresh-
353 old," *APL Mater.* **11**, 081120 (2023).
- 354 15. J. Park, K. Kim, E.-J. Jo, *et al.*, "Plasmon enhanced up-conversion
355 nanoparticles in perovskite solar cells for effective utilization of near
356 infrared light," *Nanoscale* **11**, 22813–22819 (2019).
- 357 16. J. D. Cox, M. R. Singh, M. A. Anton, and F. Carreno, "Plasmonic control
358 of nonlinear two-photon absorption in graphene nanocomposites," *J.*
359 *Physics: Condens. Matter* **25**, 385302 (2013).
- 360 17. J. Olesiak-Banska, M. Waszkielewicz, P. Obstarczyk, and M. Samoc,
361 "Two-photon absorption and photoluminescence of colloidal gold
362 nanoparticles and nanoclusters," *Chem. society reviews* **48**, 4087–
363 4117 (2019).
- 364 18. X. Lu, D. Punj, and M. Orrit, "Two-photon-excited single-molecule
365 fluorescence enhanced by gold nanorod dimers," *Nano Lett.* **22**, 4215–
366 4222 (2022).
- 367 19. F. J. Garcia de Abajo, "Graphene plasmonics: challenges and opportu-
368 nities," *Acs Photonics* **1**, 135–152 (2014).
- 369 20. T. Guo and C. Argyropoulos, "Recent advances in terahertz photonic
370 technologies based on graphene and their applications," *Adv. Photonics*
371 *Res.* **2**, 2000168 (2021).
- 372 21. F. H. Koppens, D. E. Chang, and F. J. García de Abajo, "Graphene
373 plasmonics: a platform for strong light-matter interactions," *Nano letters*
374 **11**, 3370–3377 (2011).
- 375 22. P. Gonçalves, N. Stenger, J. D. Cox, *et al.*, "Strong light-matter inter-
376 actions enabled by polaritons in atomically thin materials," *Adv. Opt.*
377 *Mater.* **8**, 1901473 (2020).
- 378 23. L. Novotny and N. Van Hulst, "Antennas for light," *Nat. photonics* **5**,
379 83–90 (2011).
- 380 24. I. AAT Bioquest, "Spectrum [atto 700]," [https://www.aatbio.com/](https://www.aatbio.com/fluorescence-excitation-emission-spectrum-graph-viewer/atto_700)
381 [fluorescence-excitation-emission-spectrum-graph-viewer/atto_700](https://www.aatbio.com/fluorescence-excitation-emission-spectrum-graph-viewer/atto_700)
382 (2024). Accessed: 2024-02-06.
- 383 25. T. Christensen, W. Yan, A.-P. Jauho, *et al.*, "Kerr nonlinearity and plas-
384 monic bistability in graphene nanoribbons," *Phys. Rev. B* **92**, 121407
385 (2015).
- 386 26. H. Qian, Y. Xiao, and Z. Liu, "Giant kerr response of ultrathin gold films
387 from quantum size effect," *Nat. Commun.* **7**, 13153 (2016).

Supplemental document accompanying submission to *Optics Letters*

Title: Multi-Photon Absorption Enhancement by Graphene-Gold Nanostructure

Authors: Saeid Izadshenas Jahromi, Karolina Slowik

Submitted: 5/30/2024 9:47:57 AM

OPTICA
PUBLISHING GROUP

Supplementary Material for
Multi-Photon Absorption Enhancement by Graphene-Gold
Nanostructure

Saeid Izadshenas Jahromi* and Karolina Słowik

Institute of Physics, Faculty of Physics, Astronomy and Informatics,
Nicolaus Copernicus University in Toruń, 87-100 Toruń, Poland

1 Derivation of Eq. (1)

According to Fermi's golden rule, a molecular transition rate from a lower- $|g\rangle$ to a higher-energy state $|e\rangle$ that occurs through the absorption of N photons of predefined frequencies ω_j , $j = 1, \dots, N$ is given by

$$\Gamma_{g \rightarrow e} = \frac{2\pi}{\hbar} \int_0^\infty |\langle e|V(\omega_{eg})|g\rangle|^2 \text{DOS}(\omega_{eg}) d\omega_{eg}, \quad (\text{S1})$$

where $\text{DOS}(\omega)$ stands for the density of molecular states which takes into account the broadening of levels, e.g., due to molecular vibrations. The transition element $\langle e|V(\omega_{eg})|g\rangle = \sum_{i_1, i_2, \dots, i_{N-1}} \langle e|\mathbf{E}(\omega_1) \cdot \hat{\mathbf{d}}|i_1\rangle \langle i_1|\mathbf{E}(\omega_2) \cdot \hat{\mathbf{d}}|i_2\rangle \dots \langle i_{N-1}|\mathbf{E}(\omega_N) \cdot \hat{\mathbf{d}}|g\rangle$ can be represented as a product of transitions involving intermediate states $|i_k\rangle$, $k = 1, \dots, N - 1$, $\hat{\mathbf{d}}$ is the molecular dipole moment operator, and on N -photon resonance $\omega_{eg} = \sum_{j=1}^N \omega_j$. The transition rate can be rewritten as

$$\Gamma_{g \rightarrow e} = \int_0^\infty \Pi_{j=1}^N |\mathbf{E}(\omega_j)|^2 C^{(N)}(\omega_{eg}) d\omega_{eg}, \quad (\text{S2})$$

where $C^{(N)}(\omega_{eg}) = \frac{2\pi}{\hbar} d_{ei_1}^\parallel d_{i_1 i_2}^\parallel \dots d_{i_{N-1} g}^\parallel \text{DOS}(\omega_{eg})$ represents the N -photon absorption cross-section, and d_{mn}^\parallel is the component of the transition dipole moment $\hat{\mathbf{d}}_{mn} = \langle m|\hat{\mathbf{d}}|n\rangle$, parallel to the electric field at the corresponding frequency.

*Corresponding author: s.izadshenas@doktorant.umk.pl

We assume that the illuminating field is spectrally narrow sufficiently to set $\omega_j \approx \frac{\omega_{eg}}{N}$. In this regime, the absorption rate becomes

$$\Gamma_{g \rightarrow e} = \int_0^\infty \left| \mathbf{E}\left(\frac{\omega_{eg}}{N}\right) \right|^{2N} C^{(N)}(\omega_{eg}) d\omega_{eg}. \quad (\text{S3})$$

The absorption rate enhancement by a nanoantenna can thus be written as

$$I_{\text{abs}} = \frac{\int_0^\infty \left| \mathbf{E}\left(\frac{\omega_{eg}}{N}\right) \right|^{2N} C^{(N)}(\omega_{eg}) d\omega_{eg}}{\int_0^\infty \left| \mathbf{E}_0\left(\frac{\omega_{eg}}{N}\right) \right|^{2N} C^{(N)}(\omega_{eg}) d\omega_{eg}} \quad (\text{S4})$$

where $\mathbf{E}\left(\frac{\omega_{eg}}{N}\right)$ represents the field near the nanoantenna and $\mathbf{E}_0\left(\frac{\omega_{eg}}{N}\right)$ is the illuminating field in free-space. Note that the fields could depend on the molecular position or the chemical potential of graphene, but we omit these arguments as inessential for the discussion in this section. The absorption enhancement factor simplifies for specific illumination regimes. For example, for monochromatic illumination at the frequency ω_l the spectral field distribution $|\mathbf{E}(\omega)|^{2N} = |\mathbf{E}(\omega_l)|^{2N} \delta(\omega - \omega_l)$ and the absorption enhancement becomes independent of the cross-section $C^{(N)}(\omega)$

$$I_{\text{abs}} = \frac{|\mathbf{E}(\omega_l)|^{2N}}{|\mathbf{E}_0(\omega_l)|^{2N}}. \quad (\text{S5})$$

With the molecular emission spectrum $f(\omega_{\text{flu}})$, the emission rate in free space upon N -photon absorption at frequency ω_{abs} is $\int_0^{N\omega_{\text{abs}}} f(\omega_{\text{flu}}) d\omega_{\text{flu}}$. The integral accounts for the nonelastic character of fluorescence where energy can be partially dissipated nonradiatively, and the upper integration limit indicates that emission cannot occur at energies higher than the excitation energy. Near the nanoantenna, the spectral profile of fluorescence can be altered, since emission through the frequency contribution ω_{flu} is enhanced by the factor $\frac{P(\omega_{\text{flu}})}{P_0(\omega_{\text{flu}})}$. Thus, the emission enhancement factor becomes

$$I_{\text{em}} = \frac{1}{\mathcal{F}(N\omega_{\text{abs}})} \int_0^{N\omega_{\text{abs}}} \frac{P(\omega_{\text{flu}})}{P_0(\omega_{\text{flu}})} f(\omega_{\text{flu}}) d\omega_{\text{flu}}, \quad (\text{S6})$$

with $\mathcal{F}(N\omega_{\text{abs}}) = \int_0^{N\omega_{\text{abs}}} f(\omega_{\text{flu}}) d\omega_{\text{flu}}$. Normalization of the emission spectrum is chosen so that $\lim_{\omega \rightarrow \infty} \mathcal{F}(\omega) = 1$.

2 Classical electromagnetic simulations

We numerically model the optical responses of the MIG nanostructure using the finite integration method in COMSOL Multiphysics. We employed the user-control

mesh method to effectively adjust the mesh size according to the element present in the simulated structure. To optimize the simulation process, we exploited the symmetries inherent in the structure. By limiting the simulation domain to a quarter of the structure and assigning perfect electric conductor properties to the yz plane and perfect magnetic conductor properties to the xz plane, we were able to reduce the simulation time and memory requirements significantly. In our calculations, we model gold using Drude-model fits to the dielectric functions based on two different sets of experimental data: the data from Johnson and Christy [1] in the visible and near-infrared regimes (wavelengths from 188 nm to 2 μm) and the data from Olmon et al. [2] in the IR regime (wavelengths above 2 μm). The refractive index of silica is $n = 1.45$ [3]. We model graphene conductivity $\sigma(\omega)$ with the Kubo formula through its intra- and interband components[4].

$$\sigma(\omega) = \sigma_{intra}(\omega) + \sigma_{inter}(\omega), \quad (\text{S7})$$

with the Drude model describing the intraband contribution accounting for the plasmonic responses:

$$\sigma_{intra}(\omega) = \frac{2ie^2T}{\pi\hbar(\omega + i\tau^{-1})} \ln[2\cosh(\frac{\mu}{2T})] \quad (\text{S8})$$

and the interband contribution described by:

$$\sigma_{inter}(\omega) = \frac{e^2}{4\hbar} [G(\frac{\omega}{2}) - \frac{4\omega}{i\pi} \int_0^\infty \frac{G(\epsilon) - G(\frac{\omega}{2})}{\omega^2 - 4\epsilon^2} d\epsilon]. \quad (\text{S9})$$

Here, i is the imaginary unit, e represents the elementary charge, T is the electron temperature, μ stands for the chemical potential tunable with gating voltage, $\tau = 1$ ps is carrier relaxation time in graphene, and

$$G(\epsilon) = \frac{\sinh(\frac{\epsilon}{T})}{\cosh(\frac{\mu}{T}) + \cosh(\frac{\epsilon}{T})}. \quad (\text{S10})$$

The dielectric function of graphene is evaluated as

$$\epsilon(\omega) = 1 + \frac{i\sigma(\omega)}{\epsilon_0\omega t_g} \quad (\text{S11})$$

with $t_g = 1$ nm being the graphene thickness.

By employing silica spacer between gold nanorods and graphene disk, the graphene component has a negligible influence on the plasmonic peak in the visible-infrared domain, and vice versa, the gold components have no notable impact on the spectra position of the peak in the mid-infrared and terahertz regime.

The results have been obtained for separately modeled infrared to visible and mid-infrared to terahertz problems, with identical, COMSOL-built-in scattering boundary conditions at a 5 μm -diameter sphere that prevents reflection back from infinite space, with an additional perfectly matched layer.

We use Poynting's theorem to calculate the power radiated from and absorbed by the nanoantenna [5, 6, 7]:

$$P_{\text{rad}}(\omega) = \oint \langle \vec{E}_{\text{sca}}(\vec{r}, \omega) \times \vec{H}_{\text{sca}}(\vec{r}, \omega) \rangle d\vec{A}, \quad (\text{S12})$$

$$P_{\text{abs}}(\omega) = \int \langle \vec{J}_{\text{ind}}(\vec{r}, \omega) \cdot \vec{E}_{\text{ind}}(\vec{r}, \omega) \rangle dV \quad (\text{S13})$$

where similarly to $\vec{E}_{\text{sca}}(\vec{r}, \omega)$, the symbol $\vec{H}_{\text{sca}}(\vec{r}, \omega)$ denotes the scattered part of the magnetic field, and $\vec{J}_{\text{ind}}(\vec{r}, \omega)$ and $\vec{E}_{\text{ind}}(\vec{r}, \omega)$ represent the currents and electric field in the nanoantenna volume. The integrals are evaluated, respectively, at the spherical surface of the simulation volume and inside the volume of the nanoantenna elements.

References

- [1] P. B. Johnson and R.-W. Christy, "Optical constants of the noble metals," *Physical Review B*, vol. 6, no. 12, p. 4370, 1972.
- [2] R. L. Olmon, B. Slovick, T. W. Johnson, D. Shelton, S.-H. Oh, G. D. Boreman, and M. B. Raschke, "Optical dielectric function of gold," *Physical Review B*, vol. 86, no. 23, p. 235147, 2012.
- [3] I. H. Malitson, "Interspecimen comparison of the refractive index of fused silica," *Josa*, vol. 55, no. 10, pp. 1205–1209, 1965.
- [4] L. A. Falkovsky, "Optical properties of graphene," in *Journal of Physics: conference series*, vol. 129, p. 012004, IOP Publishing, 2008.
- [5] J. D. Jackson, *Classical electrodynamics*. John Wiley & Sons, 2021.
- [6] S. Izadshenas, P. Gładysz, and K. Słowik, "Hybrid graphene-silver nanoantenna to control thz emission from polar quantum systems," *Optics Express*, vol. 31, no. 18, pp. 29037–29050, 2023.
- [7] S. Izadshenas and K. Słowik, "Metasurface for broadband coherent raman signal enhancement beyond the single-molecule detection threshold," *APL Materials*, vol. 11, no. 8, p. 081120, 2023.

Molecular saturation determines distinct plasmonic enhancement scenarios for two-photon absorption signal

Saeid Izadshenas* and Karolina Słowik

Institute of Physics, Faculty of Physics, Astronomy and Informatics, Nicolaus Copernicus University in Toruń, Gagarina 11, 87-100 Toruń, Poland

E-mail: s.izadshenas@doktorant.umk.pl

Abstract

Two-photon absorption in molecules, of significance for high-resolution imaging applications, is typically characterised with low cross sections. To enhance the TPA signal, one effective approach exploits plasmonic enhancement. For this method to be efficient, it must meet several criteria, including broadband operational capability and a high fluorescence rate to ensure effective signal detection. In this context, we introduce a novel plus-shaped silver nanostructure designed to exploit the coupling of bright and dark plasmonic modes. This configuration considerably improves both the absorption and fluorescence of molecules across near-infrared and visible spectra. By fine-tuning the geometrical parameters of the nanostructure, we align the plasmonic resonances with the optical properties of specific TPA-active dyes, i.e., ATTO 700, Rhodamine 6G, and ATTO 610.

The expected TPA signal enhancement is evaluated using classical estimations based on the assumption of independent enhancement of absorption and fluorescence. These results are then compared with outcomes obtained in a quantum-mechanical

approach to evaluate the stationary photon emission rate. Our findings reveal the important role of molecular saturation determining the regimes where either absorption or fluorescence enhancement leads to an improved TPA signal intensity, considerably below the classical predictions.

The proposed nanostructure design not only addresses these findings, but also might serve for their experimental verification, allowing for active polarization tuning of the plasmonic response targeting the absorption, fluorescence, or both. The insight into quantum-mechanical mechanisms of plasmonic signal enhancement provided in our work is a step forward in the more effective control of light-matter interactions at the nanoscale.

Introduction

Two-photon absorption (TPA) is a nonlinear optical phenomenon in which two photons from a pump laser, typically within the near-infrared (NIR) range, excite a molecule from its ground to an excited state, subsequently producing visible fluorescence. The key advantages of this nonlinear process include spatial precision due to high absorption probability¹ with minimized photodamage,² and deeper penetration.³ However, the TPA process typically requires a high-intensity illumination to overcome its low cross-sections.³

To enhance the TPA signal, several methods can be employed, including material engineering with plasmonic and dielectric nanostructures,^{4,5} molecular selection⁶ and light source optimization.⁷⁻⁹ These approaches focus on improving the interaction between light and matter at the molecular level to maximize TPA efficiency.

Plasmonic nanostructures can be used to enhance TPA due to their ability to concentrate electromagnetic fields at the nanoscale. This enhancement arises from localized surface plasmon resonances (LSPRs), which occur when the free electrons in the metal collectively oscillate in response to an external light source.^{10,11} This phenomenon results in a dramatic increase in the local electric field intensity, thereby boosting the efficiency of TPA by

molecules subject to enhanced field.¹²

To enhance both the absorption and fluorescence of molecules in TPA, nanostructures may be engineered supporting plasmonic resonances both around the absorption and the fluorescence wavelengths. One approach to achieving two distinct plasmon resonances is through plasmon-induced transparency. This method involves spatial symmetry breaking,^{13,14} altering incident angle,¹⁵ and polarization¹⁶ to couple bright and dark modes and produce two split resonances. Plasmonic modes are effective in enhancing light absorption in molecules due to their strong coupling with incident light that allows to achieve high electromagnetic field intensity at the location of the molecules.¹⁷ On the other hand, they can enhance fluorescence and radiate the signal towards predefined directions in the far field, facilitating its detection. Bimodal nanostructures can simultaneously support both absorption and fluorescence. This dual-mode approach exploits the strengths of each mode to maximize overall TPA efficiency, offering a powerful strategy for optimizing light-matter interactions at the nanoscale.

In this article, we propose a plasmonic nanostructure capable of selective enhancement of absorption and fluorescence of molecules. We demonstrate the tuning capabilities of the nanostructure that can be adjusted by design to match the optical properties of several TPA active dyes, e.g., ATTO 700, Rhodamine 6G, and ATTO 610. We estimate the signal enhancement for TPA using the classical approach, commonly applied in the community, and compare it with the quantum-mechanical predictions. We identify molecular saturation as the key factor that determines the regimes in which either the absorption- or fluorescence-enhancement efficiently occurs, and which, in consequence, limits the overall enhancement.

Semiclassical description of TPA

A TPA process involves a simultaneous absorption of two pump photons whose combined energy is equivalent to the transition energy necessary to excite the dye molecule from its

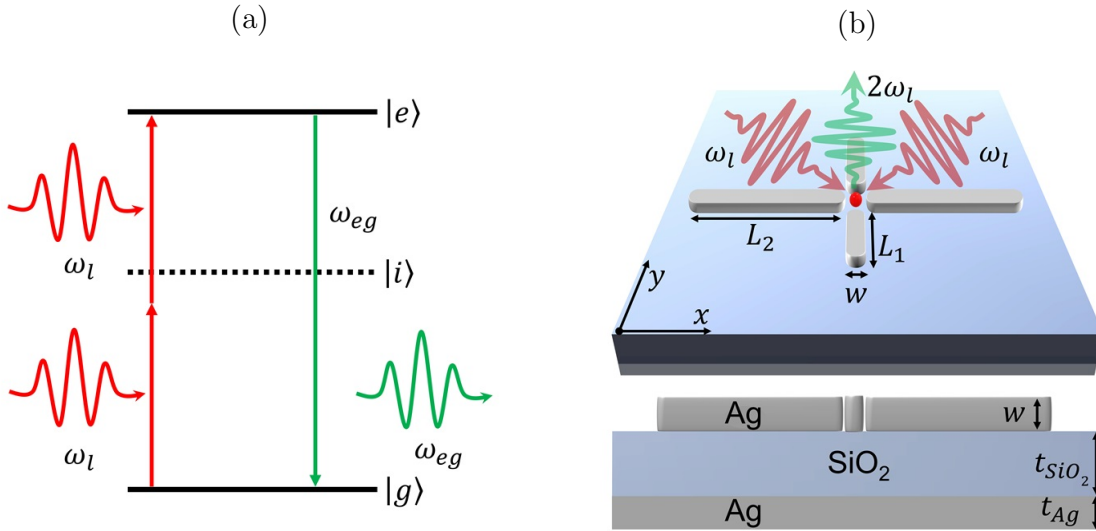


Figure 1: Diagram (a) illustrates the TPA process where two NIR photons, absorbed by a fluorescent molecule, excite it to the excited state $|e\rangle$. This is followed by the emission of visible fluorescence as the molecule relaxes back to its ground state. (b) Illustration of a plus-shaped silver nanostructure on a SiO_2 substrate, with a red point in the gap representing a molecule. Two NIR photons (red arrows) excite the molecule, and a single fluorescence photon is emitted (green arrow).

ground to excited state. As a result, the molecule may emit a fluorescent photon, as depicted in Fig. 1(a). Since the absorption occurs through a virtual state, the probability of TPA is maximized when two photons simultaneously interact with the molecule. One technique to improve the likelihood of their simultaneous arrival at the molecular position is exploiting entangled pairs.^{7,18} Another, that we investigate here, involves plasmonic nanostructures to localize light in space rather than time.⁹ We begin with a consideration of a semiclassical model of a molecule positioned near a nanostructure subject to classical laser light, and indicate the field-enhancement and Purcell emission-enhancement mechanisms through which the plasmonic nanostructure can influence its stationary state.

We consider a two-level model of the molecule, with the ground and excited states $|g\rangle$ and $|e\rangle$, respectively with energies ω_g and ω_e . The intermediate states, denoted as $|i\rangle$ in the scheme in Fig. 1(a), can be integrated out as derived in *Supplementary Material: Effective two-level description*. We allow the molecule to be positioned near the nanostructure [Fig. 1(b)] that scatters the incoming plane wave of amplitude $\mathbf{E}_0(\omega_l)$, and gives rise to the

field distribution $\mathbf{E}(\omega_l, \mathbf{r})$. The resulting Hamiltonian of the molecule near the nanostructure subject to a classical continuous-wave illumination at frequency ω_l , can be written in the form

$$H = \frac{1}{2}\hbar\omega_{eg}\sigma_z + \hbar \left(\Omega_{\text{NP}}^{(2)}e^{-2i\omega_l t}\sigma_+ + \Omega_{\text{NP}}^{(2)*}e^{2i\omega_l t}\sigma_- \right), \quad (1)$$

where $\sigma_- = |e\rangle\langle g|$ and $\sigma_+ = \sigma_-^\dagger$ are Pauli flip operators describing molecular transitions between the ground and excited states, $\sigma_z = |e\rangle\langle e| - |g\rangle\langle g|$ is the population inversion operator, $\omega_{eg} = \omega_e - \omega_g$ is the transition frequency from the ground state to excited state, and $\Omega_{\text{NP}}^{(2)}$ is the two-photon coupling strength with the molecule in presence of the nanostructure. In *Supplementary Material: Effective two-level description*, this quantity is derived in the form

$$\Omega_{\text{NP}}^{(2)} = \sum_i \underbrace{\frac{E(\omega_l, \mathbf{r}_m)}{E_0(\omega_l)} \frac{E(\omega_l, \mathbf{r}_m)}{E_0(\omega_l)}}_{\text{field enhancement factors}} \Omega_i^{(2)} \quad (2)$$

being a sum of contributions arising in the presence of virtual states $|i\rangle$ of energy $\hbar\omega_i$ being considerably detuned from single-photon resonances: $|2\omega_l - \omega_{eg}| \ll |\omega_l - \omega_{ig}|, |\omega_l - \omega_{ei}| \ll \omega_l$. Each contribution is a product of the field enhancement factors and the free-space effective two-photon coupling $\Omega_i^{(2)}$. The field enhancement factors are ratios of the electric field of amplitude $E(\omega_l, \mathbf{r}) = |\mathbf{E}(\omega_l, \mathbf{r}_m)|$ evaluated at the molecular position \mathbf{r}_m , and the plane wave amplitude $E_0(\omega_l) = |\mathbf{E}_0(\omega_l)|$. The effective two-photon coupling takes the form $\Omega_i^{(2)} = \frac{\Omega_{ig}^{(1)}\Omega_{ei}^{(1)}}{\omega_l - \omega_{ig}}$. In this expression, $\Omega_{ei}^{(1)}, \Omega_{ig}^{(1)}$ are the coupling strengths of single-photon molecular transitions involving the virtual states, $\omega_l - \omega_{ig}$ is the detuning between the laser frequency and the transition frequency between the ground and virtual intermediate levels $\omega_{ig} = \omega_i - \omega_g$. Deriving Eq. (2), we have assumed all relevant molecular transition dipole moment elements to be co-oriented.

Once the TPA excites the molecule from $|g\rangle$ to $|e\rangle$, two main scenarios can be considered for its return to the ground state: a two-photon transition through the σ_- Hamiltonian term (1), or an emission of a single fluorescent photon. In this section, we assume that fluorescence occurs at ω_{eg} , as depicted in Fig. 1(a) with the green arrow. In practice, fluorescence serves as

a background-free evidence of TPA in experimental scenarios.¹⁸ To account for fluorescence, we turn to a density matrix description of the molecular state. Its stationary form can be found from the Gorini - Kossakowski - Lindblad - Sudarshan equation, written here for the steady state ρ ^{19,20}

$$\frac{i}{\hbar} [H, \rho] - \mathcal{L}_\gamma(\rho) = 0. \quad (3)$$

where $\mathcal{L}_\gamma(\rho) = \gamma (\sigma_- \rho \sigma_+ - \frac{1}{2} \{ \sigma_+ \sigma_-, \rho \})$ is the Lindblad operator describing spontaneous emission from $|e\rangle$ to $|g\rangle$ with the rate γ . Near the nanostructure, this rate can be enhanced *via* the Purcell effect²¹

$$\gamma = \frac{P(\omega_{eg}, \mathbf{r}_m)}{P_0(\omega_{eg})} \gamma_0, \quad (4)$$

where γ_0 is the free-space emission rate given by the Weisskopf-Wigner formula.²² The ratio $\frac{P(\omega, \mathbf{r})}{P_0(\omega)}$ is the Purcell enhancement factor of the total (radiated and absorbed) emission power $P(\omega, \mathbf{r})$ of an electric dipole oscillating at the frequency ω , positioned at \mathbf{r} near the nanostructure, over the emission power $P(\omega)$ of a dipole oscillating at the same frequency in free space. In Eq. (4), the dipole is located at the molecular position \mathbf{r}_m and has the frequency ω_{eg} so that it models a dipolar transition $|e\rangle \leftrightarrow |g\rangle$.

Before we continue to discuss the plasmonic impact on the TPA in this semiclassical framework, we introduce the nanostructure engineered to support the sequence of TPA and fluorescent emission.

Plasmonic nanostructure

Figure. 1(b) illustrates a plus-shaped silver nanostructure composed of four nanobars separated by a gap, situated on an SiO_2 substrate. The silver film located on the bottom of the nanostructure reflects all incident light and enhances optical response of the nanobars. The red point represents a dye molecule located in the gap between the nanobars. The incident electric field is polarized in the xy plane, while light propagates in the z direction.

The nanostructure geometry is designed to obtain two split resonances in near-infrared and visible regimes: Different nanobar lengths are chosen along the x and y directions, respectively $L_2 = 135$ nm and $L_1 = 60$ nm. All nanobars have the same widths and heights $w = 25$ nm. The glass spacer thickness is $t_{SiO_2} = 50$ nm. The overall response of the nanostructure weakly depends on the bottom silver film thickness. A perfectly matched layer is assumed as domain around the plasmonic nanostructure. The metal film's length and width are $P_x = 400$ nm and $P_y = 400$ nm, and the thickness is $t_{Ag} = 60$ nm.

Using nanobars of different lengths gives rise to a pair of plasmonic resonances, which we refer to as NIR and visible modes due to their spectral characteristics. The NIR mode is spectrally tuned to enhance absorption, while the visible one boosts fluorescence. The polarization angle ϕ and illumination frequency of the incident light allow us to selectively address these resonances. To characterize them, we investigate three different polarizations of the incident beam: x -polarization at $\phi = 0^\circ$, y -polarization at $\phi = 90^\circ$, and xy -polarization at $\phi = 45^\circ$, being the superposition of the x and y . The NIR resonance occurs under x -polarized illumination, and the visible resonance is excited for the y -oriented polarization. By setting xy -polarization, we couple both NIR and visible resonances. The NIR resonance, visible resonance, and the coupled bright-dark mode in xy -polarization are characterized in Fig. 2. When x -polarized light is applied, a single plasmonic NIR resonance at 246.1 THz is observed in the electric field enhancement spectrum $E(\omega, \mathbf{r}_m)/E_0(\omega)$ [Fig. 2(a)]. On NIR resonance, the nanostructure's scattering is dominated by longer nanobars, as it may be concluded from the bright response seen in the field enhancement distribution shown in Fig. 2(b). In Fig. 2(c), we also show the field distribution for x -polarized input beam at 420.6 THz, where the visible mode is located, but it turns out to be dark for this illumination scenario. When the polarization is aligned with the y axis, a single resonance appears at 420.6 THz, i.e., in the visible regime [Fig. 2(d)], with a lower resonant electric field enhancement. The resonance at 246.1 THz is dark under y -polarized illumination [Fig.2(e)], while the one at 420.6 THz becomes bright [Fig. 2(f)] mainly due to the interaction with the shorter y -oriented nanobars.

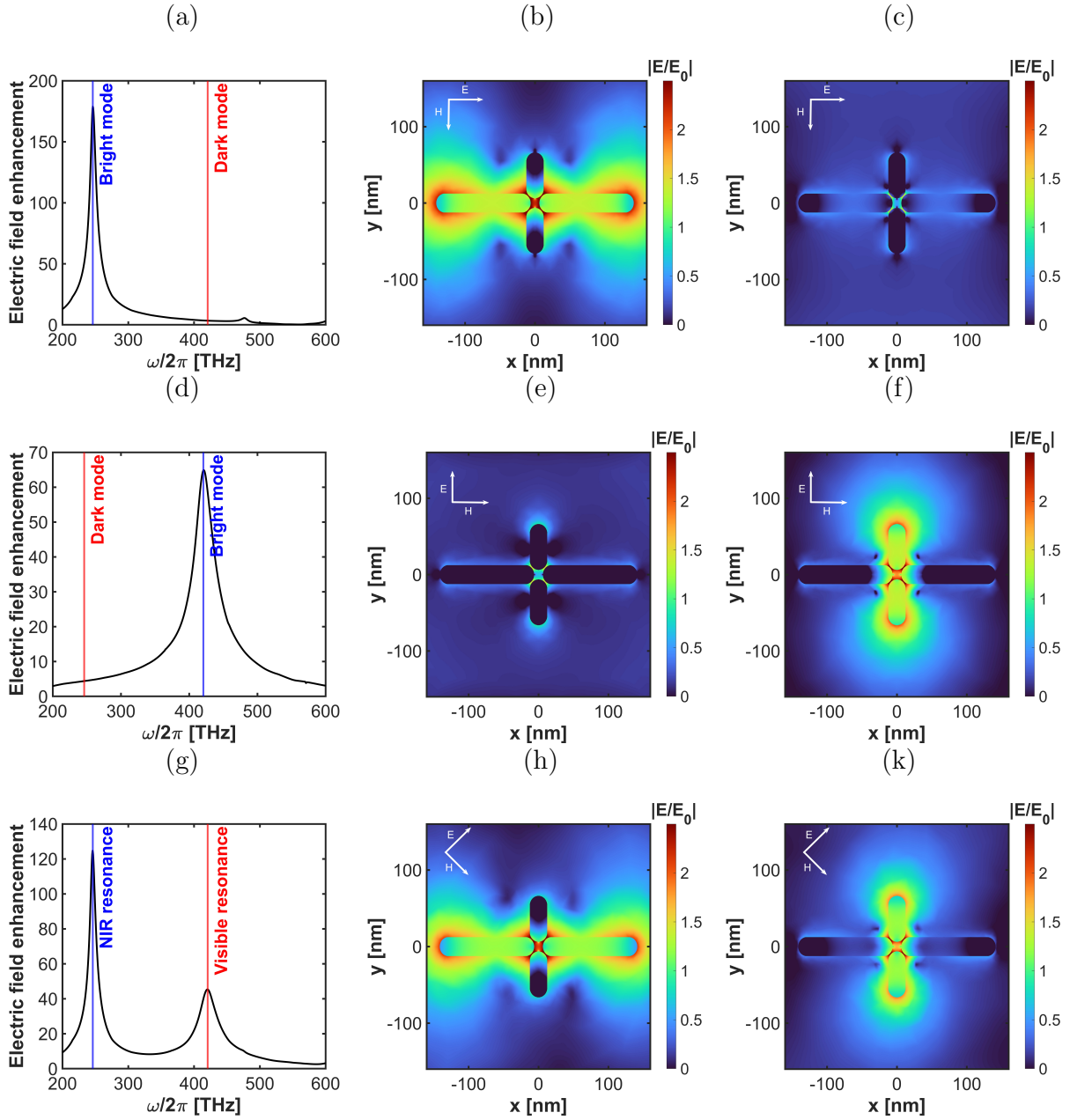


Figure 2: Illustration of the electric field enhancement spectrum and electric field distribution for various conditions: (a) x-polarization at $\phi = 0^\circ$, (b) bright mode map at $\omega/2\pi = 246.1$ THz, (c) dark mode map at $\omega/2\pi = 420.6$ THz, (d) y-polarization at $\phi = 90^\circ$, (e) bright mode map at $\omega/2\pi = 246.1$ THz, (f) dark mode map at $\omega/2\pi = 420.6$ THz, (g) xy-polarization at $\phi = 45^\circ$, (h) bright mode map at $\omega/2\pi = 246.1$ THz, and (k) dark mode map at $\omega/2\pi = 420.6$ THz

When the polarization is oriented at $\phi = 45^\circ$, both visible and near-infrared resonances are excited, resulting in a coupling of the NIR and visible modes, as illustrated in the field

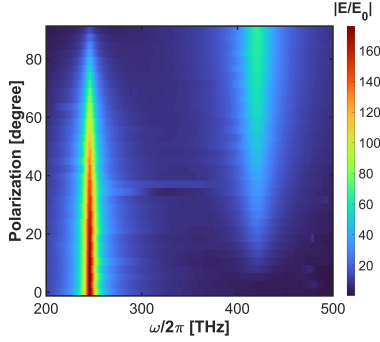


Figure 3: Electric field enhancement spectrum varying by polarization.

enhancement spectrum in Fig. 2(g) and field distributions in Fig. 2(h,u), respectively for illumination frequencies of 246.1 and 420.6 THz. Thus, by adjusting the polarization, we switch the character of the plasmonic mode from dark to bright. By sweeping the polarization angle $\phi = 0^\circ$ to $\phi = 90^\circ$, we observe a smooth transition between the above-discussed cases (Fig.3).

Having characterized the resonances in the plasmonic response, we aim to match the nanostructure's geometry to the absorption and fluorescence profile of the molecule. This can be done as the resonances can be controlled independently by two parameters: The length of the longer nanobars affects the resonance position and the electric field enhancement $\frac{E(\omega_l, \mathbf{r}_m)}{E_0(\omega_l)}$ in the near-infrared regime, leading to the light-matter interaction strength enhancement according to Eq. (2). The length of the shorter nanobars influences the resonance position and radiated power enhancement in the visible regime, boosting the Purcell enhancement $\frac{P(\omega_{eg}, \mathbf{r}_m)}{P_0(\omega_{eg})}$ of the fluorescence rate, as stated in Eq. (4). This independent control allows optimizing the performance of plasmonic nanostructure in the nonlinear process of TPA. Below, we investigate the nanostructure tunability with these key parameters in detail, focusing on the field enhancement at the highest symmetry point indicated by the red dot in Fig. 1(b) for the NIR resonance, and at the power enhancement with the dipolar source positioned at the same point for the visible resonance.

As shown in Fig. 4(a,b), increasing the size of the shorter nanobars results in a red-shift of the resonance frequency and an increase in the radiated power within the visible regime.

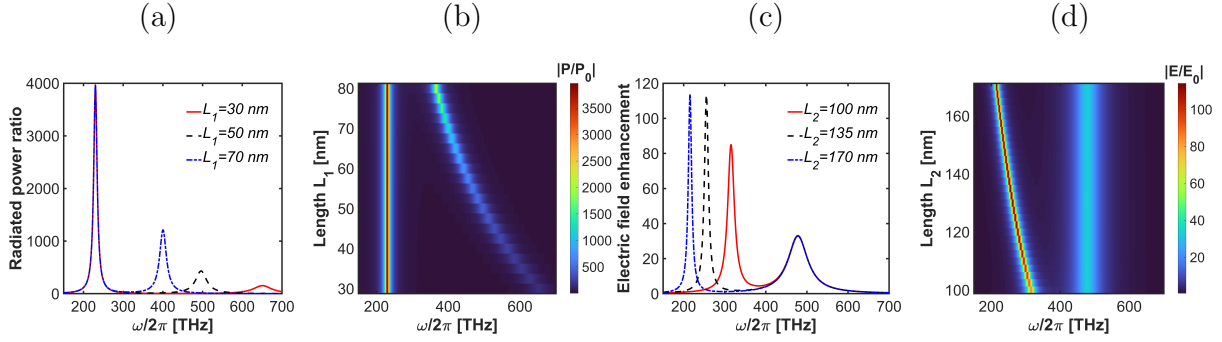


Figure 4: (a) Radiated power, and (b) radiated power map by varying L_1 with mirror film. (c) Electric field enhancement, and (d) electric field enhancement map by varying L_2 with mirror film.

Conversely, by keeping the dimensions of the shorter nanobars fixed and varying the size of the longer nanobars, we shift the NIR resonance while maintaining the visible resonance at a fixed spectral position, as depicted in Fig. 4(c,d). Increasing the size of the longer nanobars not only leads to a red-shift in the nanostructure's optical response but also significantly enhances the electric field amplitude. For a comparison, we provide similar results without the bottom mirror film in *Supplementary Material: Plasmonic nanostructure without mirror film*. We now investigate the role of the mirror in a greater detail.

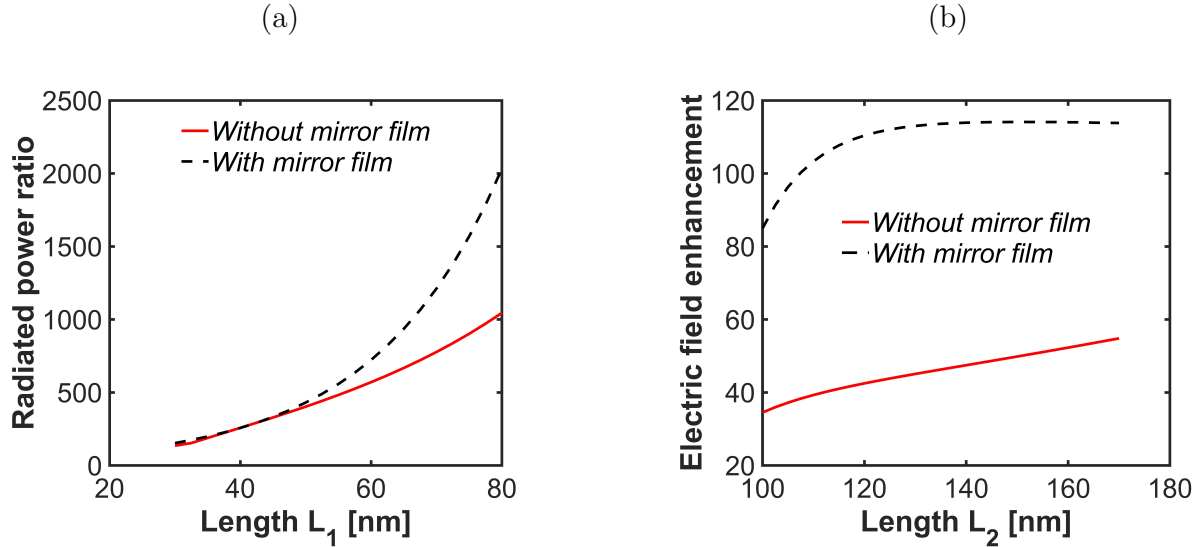


Figure 5: (a) Radiated power ratio, (b) electric field enhancement with and without mirror film

By integrating a metal mirror film on the bottom of the nanostructure, we can enhance both the radiated power and the electric field intensity without altering the geometry size of the nanostructure. This substantial enhancement results from the constructive interference of the electromagnetic fields between the metal layers. As shown in Fig. 5(a), the amplitude of the radiated power increases up to two times in the investigated range of lengths compared to the configuration without the mirror film. However, in the case of smaller nanobars, the mirror film does not significantly enhance the radiated power. This is due to the limited field confinement and weaker constructive interference in these configurations. The electric field enhancement is even larger with the mirror film, as demonstrated in Fig. 5(b).

The other parameters that influence the nanostructure’s optical response are the width and gap between the nanobars. In the considered plus-shaped silver nanobar configuration, the width is set as twice the gap, and for the simulation we varied $w = 2g$ from 10 nm to 40 nm. As shown in Fig. 6(a,b) and (c,d), increasing the values of w and g results in a reduction of the amplitude of the radiated power and electric field enhancement, accompanied by a blue-shift in the resonance spectrum. Additionally, as shown in Fig. 6(d), increasing the width and gap also broadens the resonance, indicating higher losses. This will be important in our later considerations in *section: Quantum simulations of two-photon absorption*. Before we are ready to comment on this issue in a greater depth, we estimate the signal enhancement for specific molecules in a fully classical approach and compare it with the semiclassical one taking into account the saturation effects.

TPA signal enhancement in molecules: classical approach

We now consider three different dye molecules: ATTO 700,²³ ATTO 610,²⁴ and Rho 6G.²⁵ Their single-photon absorption $C_{\text{abs}}^{(1)}$ and fluorescence F_{flu} cross-sections are shown in Fig. 7(a-c). Assuming independent absorption and emission processes, the signal intensity component arising from subsequent absorption of a pair of photons at the illumination frequency

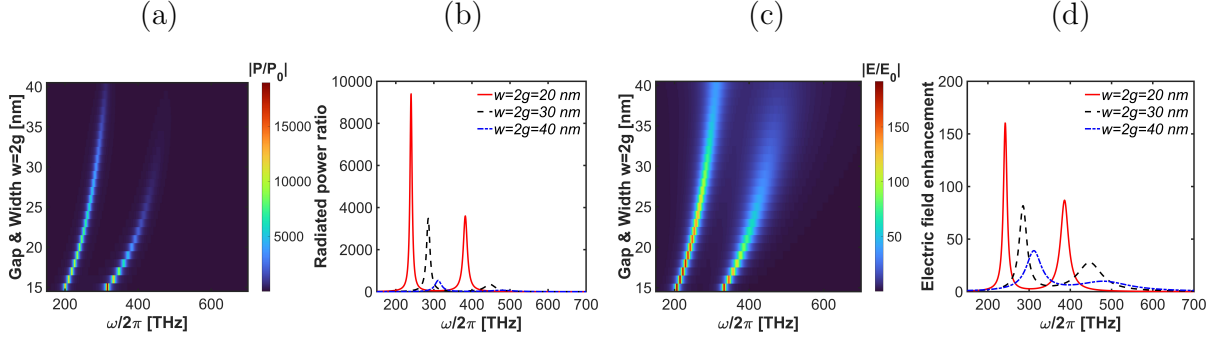


Figure 6: (a) Radiated power ratio, (b) radiated power ratio map by varying gap and width with mirror film. (c) Electric field enhancement, and (d) electric field enhancement map by varying gap and width in mirror film.

ω_l and single-photon fluorescence at the frequency ω [Fig. 1(a)] is proportional to

$$I(\mathbf{r}_m, \omega_l, \omega) \propto |E(\mathbf{r}_m, \omega_l)|^4 C_{abs}^{(2)}(\omega_l) P(\mathbf{r}_m, \omega) F_{flu}^{(1)}(\omega) \theta(2\omega_l - \omega), \quad (5)$$

and, in general, depends on the molecular position with respect to the nanostructure. Here, $\theta(\cdot)$ is the Heaviside function that accounts for the assumption that the fluorescent photon cannot have energy larger than the absorbed pair. The total signal upon illumination with a monochromatic beam is thus²⁶

$$I(\mathbf{r}_m, \omega_l) \propto |E(\mathbf{r}_m, \omega_l)|^4 C_{abs}^{(2)}(\omega_l) \int_0^{\omega_l} d\omega P(\mathbf{r}_m, \omega) F_{flu}^{(1)}(\omega). \quad (6)$$

In both cases, in free space E and P should be replaced by E_0 and P_0 . Below, we evaluate frequency-resolved signal enhancement defined in the domain $2\omega_l \geq \omega$ as a ratio of expressions in Eq. (5) near the nanostructure and in free space

$$I_{se}(\omega_l, \omega) = \left| \frac{E(\mathbf{r}_m, \omega_l)}{E_0(\omega_l)} \right|^4 \frac{P(\mathbf{r}_m, \omega)}{P_0(\omega)} \quad (7)$$

Note that this definition is based on assumption that the excitation and emission processes are independent, hence, the overall enhancement can be evaluated as a product of enhancements of the two contributing processes. This approach is common in literature when consid-

ering plasmonic enhancement.²⁷ The validity of formula (7) and the underlying assumption in the context of TPA signal enhancement is verified in *section: Quantum simulations of two-photon absorption*.

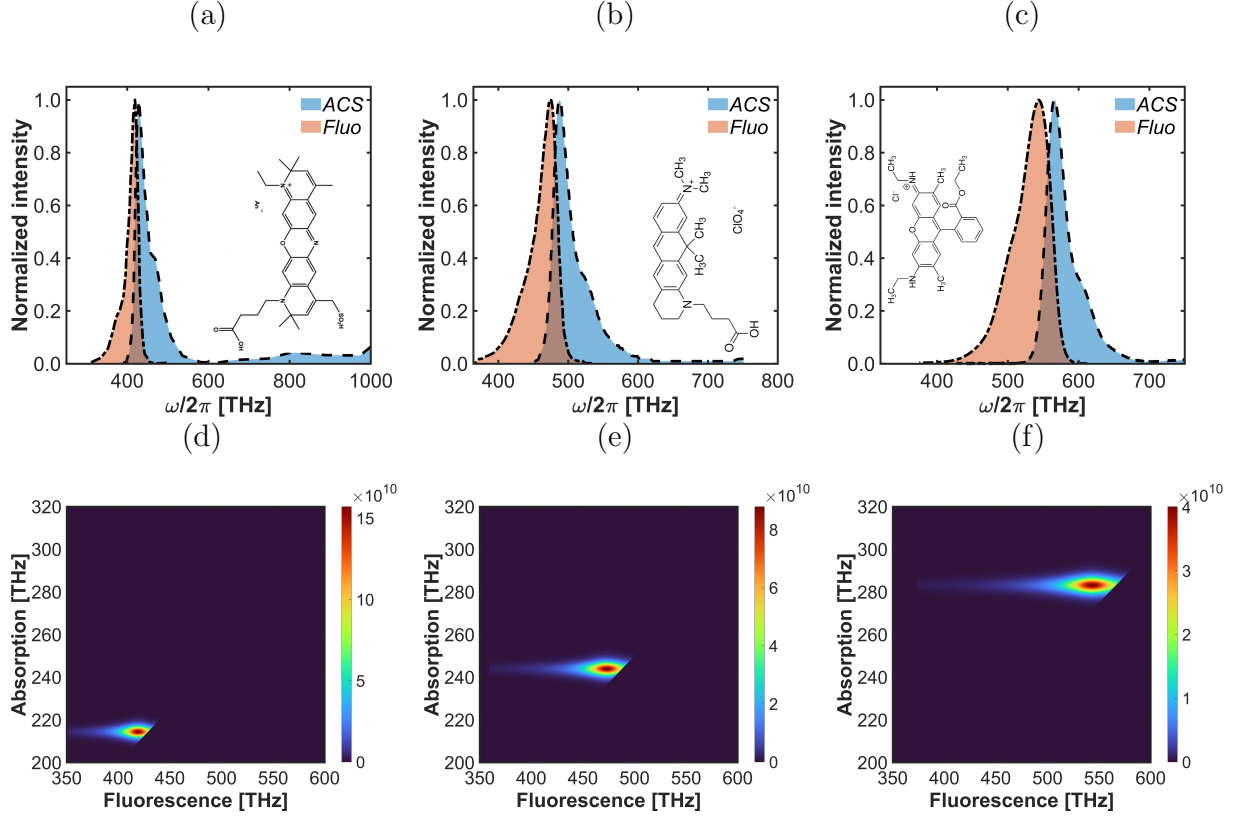


Figure 7: Normalized intensity of fluorescence and absorption of (a) ATTO 700, (b) ATTO 610, and (c) Rho 6G. Signal enhancement map based on absorption and fluorescence of (d) ATTO 700, (b) ATTO 610, and (c) Rho 6G.

To demonstrate the nanostructure’s tunability by design, we adjust the plasmonic nanostructure to each molecule separately. For the ATTO 700 dye molecule, the bar lengths were set to $L_1 = 65.2$ nm and $L_2 = 171.0$ nm. For the ATTO 610 dye molecule, $L_1 = 54.0$ nm and $L_2 = 144.0$ nm. For the Rho 6G dye molecule, $L_1 = 42.7$ nm and $L_2 = 116.3$ nm. The remaining parameters remain as given in the previous section. We match the plasmonic resonances with the two-photon absorption and fluorescence maxima of each dye molecule. For the two-photon absorption, we assume $C_{abs}^{(2)}(\omega) = C_{abs}^{(1)}(2\omega)$ following experimental data²⁸, which means that the NIR resonance is set at half the single-photon-absorption peak, and

the visible resonance at the fluorescence peak. For different frequencies of the pump laser ω_l and the detection signal frequency ω , we calculate the signal enhancement for each molecule according to Eq. (7). The results are illustrated in Fig. 7(d-f), where we identify a resonant behaviour both in the absorption and fluorescence frequencies. The fluorescence resonance is broader due to the broader character of resonances at higher frequencies on the one hand, and to the 4th power with which the field enhancement is weighted on the other. Due to the high nonlinearity order, the overall frequency-resolved enhancement factor is predicted at large peak values of 10 to 11 orders of magnitude, and is slightly larger for molecules with fluorescence in lower frequency range. This greater enhancement is due to the plasmon frequency of silver providing more effective electric field confinement at lower frequencies. This result suggests that significant signal enhancement can be achieved for a molecules with the two-photon transition frequencies in a broad range within the visible regime.

So high predictions for the enhancements raise the question of the role of saturation, which is not accounted for in the above calculations. Below, we address this point by turning to the quantum description of molecular TPA in *section: Semiclassical description of TPA*.

Quantum simulations of two-photon absorption

In this section, we apply the quantum-mechanical description to evaluate the TPA signal enhancement and verify the assumption of independent enhancement of the excitation and the emission processes being the basis of Eq. (7).

We consider a molecular model system with a single intermediate level detuned from the resonance with the illuminating beam, as shown in Fig.1(a). In this case, the sum in Eq. (2) is replaced by a single term. The calculations are performed with the Quantum Toolbox in Python package QuTiP.²⁹ For this section, we assume that the fluorescent light is emitted at doubled absorption frequency and the system is illuminated resonantly, i.e. $\omega = \omega_{eg} = 2\omega_l$. We detune the spectral position of the virtual state ω_{ig} by $\delta_{ig} = \omega_{ig} - \omega_l = 0.1\omega_{eg}$.

The quantity of interest is the stationary signal enhancement, defined as the ratio of the number of photons emitted by the molecule in presence of the nanostructure and in free space.

$$I_{\text{qm}} = \frac{\rho_{ee}^{\text{NP}} \gamma}{\rho_{ee}^0 \gamma_0}. \quad (8)$$

The subscript "qm" stands for *quantum mechanical*, "NP" denotes the case with the nanostructure and "0" - the free space scenario. The number of emitted photons is calculated as the product of the excited-state population ρ_{ee} and the fluorescence rate γ , which may be Purcell-enhanced near the nanostructure. Note that the enhancement calculated in this way accounts for the photons emitted by the molecule, but not for what happens with them afterwards: A photon could be radiated in the far field, where it can be detected to contribute to the signal, or absorbed by the metal forming the nanostructure. Thus, when estimating the signal one should rescale the above quantity by the nanostructure efficiency. In this section, however, we focus on mechanisms of photonic emission by the molecule and, hence, assume perfect efficiency for the moment.

The classical expression (7) is based on the assumption of the excitation and emission processes occurring at rates that can be independently enhanced. To verify this assumption in the TPA process, we compare I_{se} and I_{qm} in three cases: when two-photon absorption is enhanced by the nanostructure, but the fluorescent emission occurs at the free-space rate [Fig. 8(a,d,g)], when the absorption occurs at the free-space rate, but fluorescence is Purcell-enhanced [Fig. 8(b,e,h)], and when both contributions are plasmon-enhanced [Fig. 8(c,f,i)].

We first analyze the case of enhanced excitation followed by nonenhanced emission occurring at the free-space rate [Fig. 8(a,d,g)]. This happens if the nanostructure's NIR resonance is tuned around the TPA absorption resonance of the molecule, while the VIS resonance is far detuned and the Purcell enhancement factor can be approximated as 1. For the nanostructure field enhancement spectral profile, We assume a Lorentzian resonance centred at $\omega_{\text{NIR}} = \Delta_{\text{NIR}} + \omega_{eg}/2$ with the width of $2\pi \times 9.74$ THz, and present results as functions of the nanostructure NIR resonance detuning Δ_{NIR} . We consider the process for three different

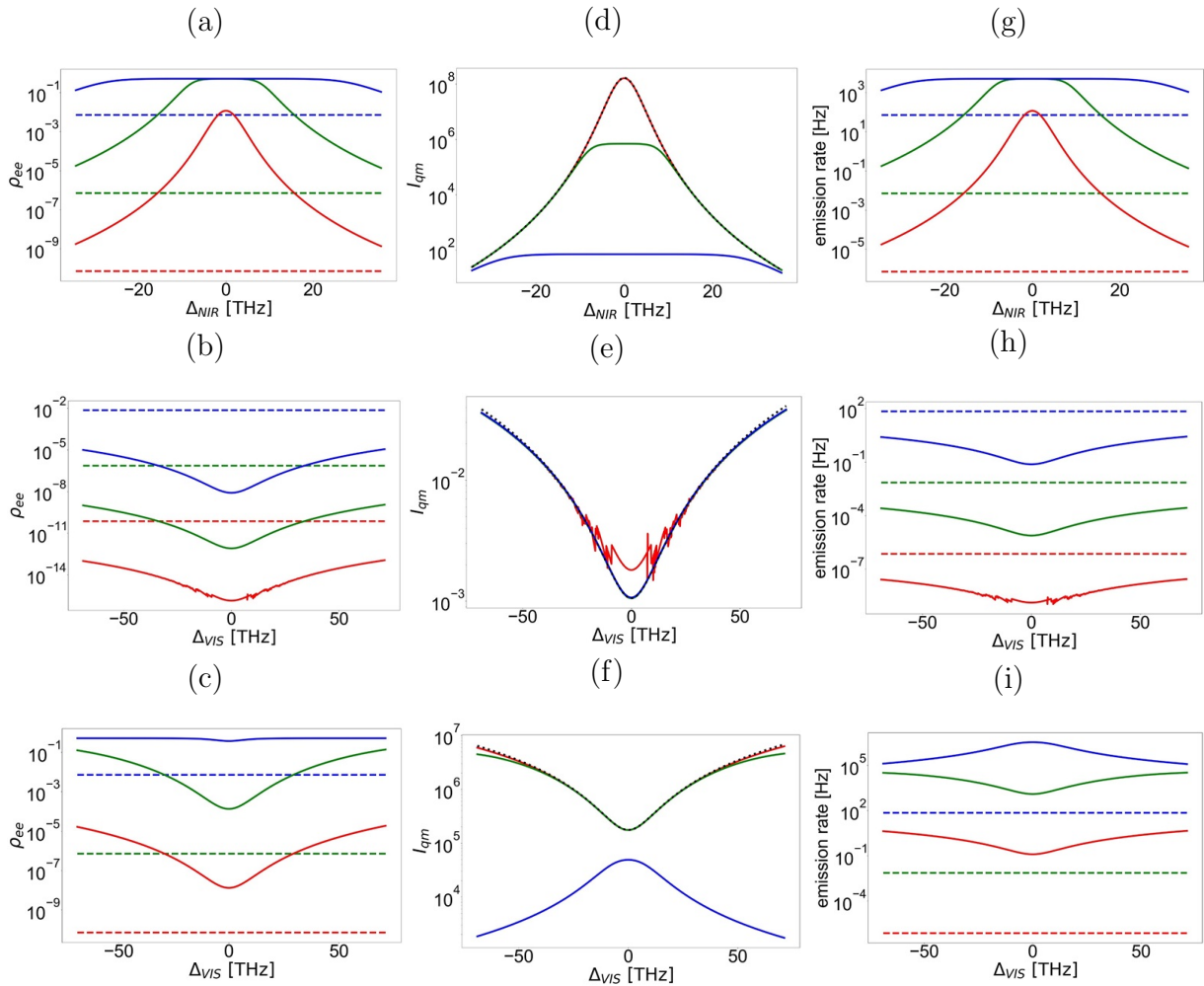


Figure 8: Excited state population (a,b,c), TPA signal enhancement (d,e,f), and photon emission rate (g,h,i) in three scenarios. Panels (a,d,g) corresponds to the case of plasmonic NIR resonance tuned around the two-photon absorption resonance with the detuning Δ_{NIR} from $\omega_{eg}/2$. Here, the visible resonance is assumed far-detuned and the Purcell fluorescence enhancement factor is 1. In (b,e,h), the NIR resonance is far detuned, with the local field enhancement factor being 1, while the fluorescence is enhanced, as shown in function of the visible nanostructure resonance detuning Δ_{VIS} from ω_{eg} . In (c,f,i), both effects are simultaneously considered: the electric field is resonantly enhanced by the factor of 113.5, while the position of the visible resonance is modified according to the detuning Δ_{VIS} . In (a-c) and (g-i), solid lines correspond to the case of the molecule positioned near the nanostructure, while dashed lines - to the free-space case. In (d-f), solid lines are enhancement factors calculated quantum-mechanically, while black dotted lines denote the phenomenological enhancement factors: the fourth power of the field enhancement factor E^4/E_0^4 in (d), the inverse Purcell factor $1/F$ in (e), the inverse Purcell factor multiplied by the fourth power of the field enhancement factor $1/F \times E^4/E_0^4$ in (f). In all panels, red lines are plotted for the illuminating beam amplitude leading to the single-photon interaction strength with the molecule of $g_0 = 1$ MHz, green lines - to $g_0 = 10$ MHz, and blue lines - to $g_0 = 100$ MHz.

amplitudes of the electric field of the illumination beam: $g_0 = 1$ MHz (red lines in all panels), 10 MHz (green) and 100 MHz (blue). In (a), stationary excited-state populations ρ_{ee} due to TPA are shown with dashed lines in the free-space scenario. Naturally, in this case the population does not depend on the nanostructure detuning. The excited population grows with the illuminating-beam amplitude and, below the saturation level, scales with its fourth power. The results obtained for the nanostructure vicinity are shown with solid lines. For the weakest of considered illumination strengths, the enhanced population is still below the saturation level and its spectral profile in (a) reflects the Lorentzian profile of the enhanced field. Thus, the enhancement factor I_{qm} evaluated according to Eq. (8) shows perfect agreement with the classically evaluated enhancement I_{se} shown with the black dashed line in (d). The photon emission profile reflects the same shape in (g). As the illumination strength is increased, a resonant nanostructure drives the molecular excited-state population at the saturation limit, as seen in a narrower range around the resonance for $g_0 = 10$ MHz (panel a, green), and a broader range for $g_0 = 100$ MHz (blue). As the saturation is reached, the enhancement factor drops (d) and spectral profile is modified with respect to the classical prediction. As a result, the photon emission rate reaches the saturation level in (g). We conclude that the classical prediction for signal enhancement due to the plasmonically-enhanced field amplitude is valid below the saturation level.

We turn to the analysis of the impact of Purcell enhancement of the spontaneous emission. In all calculations, the free-space emission rate is assumed at the level of $\gamma_0 = 10$ kHz, corresponding to a relatively low single-particle transition dipole moment, as it might be realistic for molecules supporting two-photon absorption. Again, free-space population and photon emission rate levels are indicated with dashed lines in panels (b) and (h), respectively. For the Purcell-enhanced case, we assume the NIR resonance to be far-detuned so that the electric field enhancement factor is 1, while the visible resonance position is swept according to the detuning Δ_{VIS} of the resonance modeled with a Lorentzian lineshape with the width of $2\pi \times 23.1$ THz. We find that the Purcell-enhanced emission rate leads to a suppression of the

excited-state population in (b). Below saturation, the impact of the Purcell enhancement has the same profile for all considered illumination amplitudes (red,green,blue). Thus, the Purcell effect *decreases* the signal, as shown in panel (e). In the same panel, we also demonstrate that this result is reflected by the *inverse* of the classical prediction: the black dotted line is the inverse $1/F$ of the Purcell enhancement factor evaluated as $F = P(\omega)/P_0(\omega)$. This result can be understood as follows: A large Purcell enhancement leads to emission of photons shortly after the excitation of the molecule. However, as the molecular excitation rate in TPA is small, further Purcell enhancement leads to an even faster photon emission each time a molecule gets excited, but the overall number of excitation events remains low. On the contrary, Purcell effect suppresses the excited-state probability and, as a result, the number of photons emitted per unit time.

Finally, we allow both the local electric field and the Purcell emission enhancements by both NIR and visible resonances in panels (c,f,i). We assume the NIR nanostructure resonance to be tuned exactly at half the molecular transition so that $\Delta_{NIR} = 0$. The visible resonance is tuned with the Lorentzian profile as before. This time, due to the strong absorption enhancement, saturation is reached in the excited-state population in the case of strongest illumination beam (blue) in panel (c). Below the saturation limit, the red and green lines indicate excited-state population strongly increased with respect to the free-space level. As before, Purcell enhancement of spontaneous emission rate leads to a resonant dip in the stationary excited population. However, when the saturation level is reached, the Purcell enhancement may not be able to efficiently suppress the excited-state population as its impact is balanced by the enhanced field increasing the two-photon absorption level. As a result, we find the population steadily at the saturation limit as shown by the solid blue line in panel (c). This qualitatively different behavior below and within the saturation limit is reflected in the signal enhancement factors in panel (f): the unsaturated results have the same profile as in panel (e), however, at a higher level due to the impact of the field enhancement. This result is overlapped with the black dotted line given by the product

of the classical enhancement factor $(E/E_0)^4$ and the *inverse* P_0/P of the Purcell factor. However, in the saturation regime, the Purcell enhancement actually improves the signal. This time, the enhanced field drives the two-photon absorption so that the excitation rate keep up with the emission rate and, in consequence, the act of emitting a photon does not lead to a drop in the excited population level. Therefore, in the saturation regime a peak in the enhancement factor I_{qm} reappears: The blue solid line overlaps with the Purcell enhancement curve rescaled by the excited population ratio $\frac{P}{P_0} \frac{\rho_{ee}}{\rho_{ee}^0}$. The resulting photon emission rate is presented in panel (i) and again, shows qualitatively different profiles in the unsaturated (red, green lines) and saturated regimes (blue line).

In summary, analysing plasmonic TPA signal enhancement in the quantum-mechanical approach, we were not able to identify a case for which the molecular excitation and fluorescent emission could be described as independent - the assumption justifying Eq. (7). On the contrary, we identify qualitatively different mechanisms for plasmonic signal enhancement to be efficient below and above the saturation limit. Below the saturation level, TPA signal can be enhanced through increasing the stationary probability for the molecule to be in the excited state. This can be achieved through electric field enhancement, fully in line with the classical predictions. Enhancing the fluorescent emission rate through the Purcell mechanism turns out inefficient, because it suppresses the probability of molecular excitation, and in consequence, the number of emitted photons. In other words, in the unsaturated case Purcell enhancement increases the rate at which a photon is emitted from an excited molecule, but does not increase the number of emitted photons. This is due to the excitation rate being too small in the unsaturated regime to keep up with the emission rate. In the saturation regime, on the other hand, field enhancement targeting the excitation stage is inefficient - the molecule is already saturated. In this case, excitation rate exceeds the emission rate and signal enhancement can be achieved by improving the latter. Hence, Purcell fluorescence enhancement does not lead to suppressing the excited-state population and becomes an efficient factor increasing the signal. These findings are summarized in Table 1.

Table 1: Summary of findings in Section *Quantum simulations of two-photon absorption*. Saturation limit determines two distinct regimes where different enhancement scenarios should be targeted.

	field enhancement	fluorescence enhancement	phenomenological signal enhancement formula
below saturation	efficient	counterproductive	$\frac{E^4}{E_0^4} \times \frac{1}{P/P_0}$
saturation regime	limited efficiency	efficient	$\frac{P}{P_0} \times \frac{\rho_{ee}}{\rho_{ee}^0}$

The nanostructure design proposed in *Section: Plasmonic nanostructure* could be used for verification of the above findings. The illuminating beam amplitude provides a control knob for reaching the saturation level, while its polarization can be a factor orienting the molecule in a selected direction for which one can target the two-photon absorption enhancement through local field confinement in the NIR mode, or fluorescence enhancement in the Purcell mechanism for the visible mode.

Conclusions

The quantum-mechanical analysis of plasmonic TPA signal enhancement indicates that molecular excitation and fluorescent emission are not independent processes. We identified distinct mechanisms for signal enhancement below and above the saturation limit. Below saturation, TPA signal enhancement is driven by increasing the stationary probability of the molecule being in the excited state, primarily through electric field enhancement. However, Purcell fluorescence enhancement is ineffective in this regime because it suppresses the excitation probability. Above saturation, where the molecule is already saturated, enhancing the emission rate becomes the key to increasing signal strength through Purcell enhancement.

The proposed plus-shaped silver nanostructure design may offer a way to verify these findings. The plasmonic design has been fine-tuned to match the optical characteristics of specific TPA-active dyes. The molecular absorption and fluorescence across near-infrared and visible spectra can be selectively addressed by illuminating beam polarization. Independent tuning of each plasmonic mode was achieved by adjusting nanobar lengths, which

effectively controlled the resonance spectral characteristics. The integration of the metal mirror film further amplified the radiated power and electric field intensity through constructive interference.

Supplementary materials

Effective two-level description

Here, we derive the free-space form of the two-photon coupling strength in Eq. (2).

We consider a model molecule composed of ground and excited levels $|g\rangle, |e\rangle$ and a group of virtual levels $\{|i\rangle\}$ of energies $\omega_{g,e,\{i\}}$, respectively, and we assume $\omega_g < \omega_i < \omega_e$. The Bohr frequencies are $\omega_{mn} = \omega_m - \omega_n$ with $m, n \in \{g, e, \{i\}\}$. The free Hamiltonian is

$$H_0 = \hbar \sum_{j=g,e,\{i\}} \omega_j |j\rangle \langle j|, \quad (9)$$

where the set labeled with $\{i\}$ includes all virtual states.

The system is subject to a monochromatic illumination with a frequency $\omega_l \approx \frac{1}{2}\omega_{eg}$ near the two-photon resonance. The interaction Hamiltonian is

$$H_{\text{int}} = \sum_i \hbar \left[\left(\Omega_{ig}^{(1)} |g\rangle \langle i| e^{i\omega_l t} + \Omega_{ig}^{(1)*} |i\rangle \langle g| e^{-i\omega_l t} \right) + \left(\Omega_{ei}^{(1)} |i\rangle \langle e| e^{i\omega_l t} + \Omega_{ei}^{(1)*} |e\rangle \langle i| e^{-i\omega_l t} \right) \right], \quad (10)$$

where $\hbar\Omega_{pq}^{(1)} = \mathbf{E}_0(\omega_l, \mathbf{r}_m) \cdot \mathbf{d}_{pq}$ is the coupling strength of the free-space field with the amplitude $\mathbf{E}_0(\omega_l)$ evaluated at the molecular position with the molecular transition described with the dipole moment \mathbf{d}_{pq} . We have applied the electric-dipole and the rotating-wave approximations.

The intermediate levels are not, in general, spectrally positioned in the middle of the energy gap between the ground and excited states so that the single-photon resonance condition is generally not met. Here, we assume that the single-photon detuning between the

field and the single-photon transitions $|g\rangle \leftrightarrow |i\rangle$, $|i\rangle \leftrightarrow |e\rangle$, is much larger than the two-photon detuning, but much smaller than the transition frequency scales:

$$|2\omega_l - \omega_{eg}| \ll |\omega_l - \omega_{ig}|, |\omega_l - \omega_{ei}| \ll \omega_l.$$

In this case, the population of the middle state is typically small, and the state can be adiabatically eliminated from the dynamics. Below, we perform the elimination to find the relation between the single-photon and two-photon transition rates.

In the Schrodinger picture, the molecular state is a superposition $|\psi(t)\rangle = c_g(t)|g\rangle + c_e(t)|e\rangle + \sum_i c_i(t)|i\rangle$ with $c_g(0) = 1$ and $|c_g(t)|^2 + |c_e(t)|^2 + \sum_i |c_i(t)|^2 = 1$. The Schrödinger equation yields the following set of equations for the amplitudes:

$$\begin{aligned} i\dot{d}_g &= \sum_i \Omega_{ig}^{(1)} d_i \\ i\dot{d}_e &= (\omega_{eg} - 2\omega_l)d_e + \sum_i \Omega_{ei}^{(1)*} d_i \\ i\dot{d}_i &= (\omega_{ig} - \omega_l)d_i + \Omega_{ig}^{(1)*} d_g + \Omega_{ei}^{(1)} d_e, \end{aligned} \tag{11}$$

where we have set $\omega_g = 0$ and substituted $c_e = d_e e^{-2i\omega_l t}$, $c_i = d_i e^{-i\omega_l t}$, $c_g \equiv d_g$ to approximately separate the free evolution.

Near the two-photon resonance, the virtual-level amplitudes are relatively small $|c_i(t)| \ll |c_g(t)|, |c_e(t)|$ and these states can be adiabatically eliminated from the dynamics

$$d_i = \frac{\Omega_{ig}^{(1)*} d_g + \Omega_{ei}^{(1)} d_e}{\omega_l - \omega_{ig}}, \tag{12}$$

which we plug back into the first pair of equations (11). We find an effective two-level system

description

$$i\dot{d}_g = \sum_i \frac{|\Omega_{ig}^{(1)}|^2}{\omega_l - \omega_{ig}} d_g + \sum_i \frac{\Omega_{ig}^{(1)} \Omega_{ei}^{(1)}}{\omega_l - \omega_{ig}} d_e, \quad (13)$$

$$i\dot{d}_e = \left(\omega_{eg} - 2\omega_l + \sum_i \frac{|\Omega_{ei}^{(1)}|^2}{\omega_l - \omega_{ig}} \right) d_e + \sum_i \frac{\Omega_{ei}^{(1)*} \Omega_{ig}^{(1)*}}{\omega_l - \omega_{ig}} d_g. \quad (14)$$

In the above equations, we identify frequency shifts $\Delta\omega_j = \sum_i \frac{|\Omega_{ij}|^2}{\omega_l - |\omega_{ij}|}$, $j \in \{e, g\}$ and the effective coupling constant between the ground and excited states

$$\Omega^{(2)} = \sum_i \frac{\Omega_{ig}^{(1)} \Omega_{ei}^{(1)}}{\omega_l - \omega_{ig}}. \quad (15)$$

The effective Hamiltonian takes the form given in Eq. (1). This result justifies the two-level model assumed in *section: Semiclassical description of TPA*.

To account for the presence of the plasmonic nanostructure, each of the contributions of the effective coupling strength (15) arising due to the presence of the intermediate states is rescaled by factors related to the plasmonic enhancement of the field component parallel to the corresponding electric dipole moment elements \mathbf{d}_{ig} and \mathbf{d}_{ei} of the transitions involving the virtual states:

$$\Omega_{\text{NP}}^{(2)} = \sum_i \underbrace{\frac{\mathbf{E}(\omega_l, \mathbf{r}_m) \cdot \mathbf{d}_{ei}}{\mathbf{E}_0(\omega_l) \cdot \mathbf{d}_{ei}} \frac{\mathbf{E}(\omega_l, \mathbf{r}_m) \cdot \mathbf{d}_{ig}}{\mathbf{E}_0(\omega_l) \cdot \mathbf{d}_{ig}}}_{\text{enhancement factors}} \underbrace{\frac{\Omega_{ig}^{(1)} \Omega_{ei}^{(1)}}{\omega_l - \omega_{ig}}}_{\text{free-space two-photon coupling}}.$$

Assuming all transition dipoles to be co-oriented, the two-photon-transition coupling strength with the external field becomes rescaled by the field enhancement factors, as given in Eq. (2).

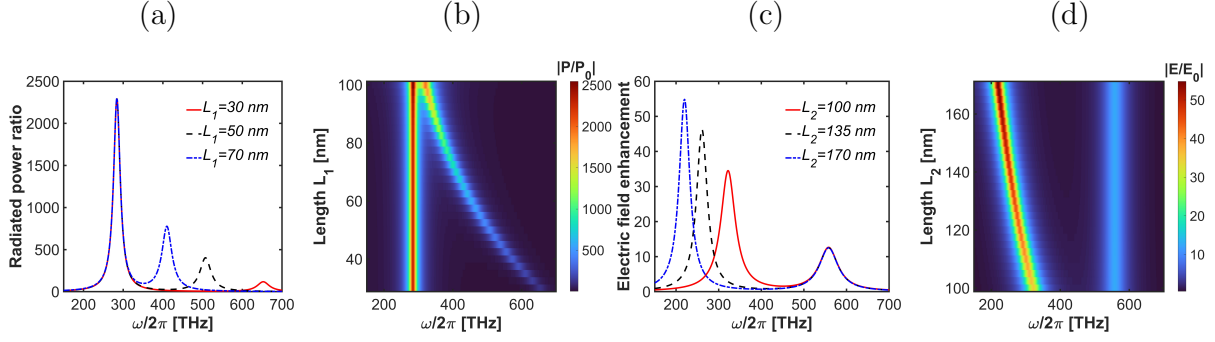


Figure 9: (a) Radiated power for selected lengths, and (b) radiated power spectrum by varying L_1 (c) Electric field enhancement, and (d) electric field enhancement spectrum by varying L_2 .

Plasmonic nanostructure without mirror film

Methods

Classical electromagnetic simulations

We numerically model the optical response of the nanostructure using the finite integration method in COMSOL Multiphysics. We employed the user-control mesh method to effectively adjust the mesh size according to the element present in the simulated structure. The silver nanostructures model with the Drude model fits to dielectric permittivity based on experimental data of Johnson and Christy.³⁰ The refractive index of silica is $n = 1.45$.³¹

The results have been obtained for separately modeled infrared to visible problems, with identical, COMSOL-built-in scattering boundary conditions at a $1 \mu\text{m}$ -diameter sphere that prevents reflection back from infinite space, with an additional perfectly matched layer.

We use Poynting's theorem to calculate the power radiated from and absorbed by the nanostructure:^{32–34}

$$P_{\text{rad}}(\omega) = \oint \langle \vec{E}_{\text{sca}}(\vec{r}, \omega) \times \vec{H}_{\text{sca}}(\vec{r}, \omega) \rangle d\vec{A}, \quad (16)$$

$$P_{\text{abs}}(\omega) = \int \langle \vec{J}_{\text{ind}}(\vec{r}, \omega) \cdot \vec{E}_{\text{ind}}(\vec{r}, \omega) \rangle dV, \quad (17)$$

where similarly to $\vec{E}_{\text{sca}}(\vec{r}, \omega)$, the symbol $\vec{H}_{\text{sca}}(\vec{r}, \omega)$ denotes the scattered part of the magnetic field, and $\vec{J}_{\text{ind}}(\vec{r}, \omega)$ and $\vec{E}_{\text{ind}}(\vec{r}, \omega)$ represent the currents and electric field in the nanostructure volume. The integrals are evaluated, respectively, at the spherical surface of the simulation volume and inside the volume of the nanostructure elements.

Two-photon absorption calculations

For our quantum calculations, we used the QuTiP package in Python with the following details: The longer nanobars have a length of $L_2 = 171$ nm, with a frequency resonance at 214.42 THz and an electric field enhancement of 113.49. The smaller nanobars are $L_1 = 65.3$ nm in length, with a frequency resonance at 418.98 THz and a radiated power ratio of 948. The Rabi frequency of the molecule without the nanostructure is $2\pi \times 10^{10}$ [Hz].

Acknowledgement

The authors acknowledge the funding by the National Centre for Research and Development, Poland, within the QUANTERA II Programme under Project QUANTERAII/1/21/E2TPA/2023.

Supporting Information Available

Derivation of effective two-level description. Simulations of optical response of the plasmonic nanostructure without the mirror film.

References

- (1) Garcia-Lechuga, M.; Fuentes, L. M.; Grützmacher, K.; Pérez, C.; Rosa, M. I. D. L. Calculation of the spatial resolution in two-photon absorption spectroscopy applied to plasma diagnosis. *Journal of Applied Physics* **2014**, *116*, 133103.

- (2) Yi, M.; Yang, S.; Peng, Z.; Liu, C.; Li, J.; Zhong, W.; Yang, R.; Tan, W. Two-photon graphene oxide/aptamer nanosensing conjugate for in vitro or in vivo molecular probing. *Analytical chemistry* **2014**, *86* 7, 3548–54.
- (3) Pascal, S.; David, S.; Andraud, C.; Maury, O. Near-infrared dyes for two-photon absorption in the short-wavelength infrared: strategies towards optical power limiting. *Chemical Society reviews* **2021**, *50* 11, 6613–6658.
- (4) Ojambati, O.; Chikkaraddy, R.; Deacon, W. M.; Huang, J.; Wright, D.; Baumberg, J. Efficient Generation of Two-Photon Excited Phosphorescence from Molecules in Plasmonic Nanocavities. *Nano Letters* **2020**, *20*, 4653 – 4658.
- (5) Yang, Y.; Wang, W.; Boulesbaa, A.; Kravchenko, I. I.; Briggs, D. P.; Puretzky, A.; Geoghegan, D.; Valentine, J. Nonlinear Fano-resonant dielectric metasurfaces. *Nano letters* **2015**, *15*, 7388–7393.
- (6) Lee, W.; Lee, H.; Kim, J.-A.; Choi, J. H.; Cho, M.; Jeon, S.; Cho, B. R. Two-photon absorption and nonlinear optical properties of octupolar molecules. *Journal of the American Chemical Society* **2001**, *123* 43, 10658–67.
- (7) Giri, S.; Schatz, G. Manipulating Two-Photon Absorption of Molecules through Efficient Optimization of Entangled Light. *The journal of physical chemistry letters* **2022**, 10140–10146.
- (8) Dayan, B.; Pe'er, A.; Friesem, A.; Silberberg, Y. Two photon absorption and coherent control with broadband down-converted light. *Physical review letters* **2004**, *93* 2, 023005.
- (9) Lu, X.; Punj, D.; Orrit, M. Two-Photon-Excited Single-Molecule Fluorescence Enhanced by Gold Nanorod Dimers. *Nano Letters* **2022**, *22*, 4215–4222.

- (10) Giannini, V.; Fernández-Domínguez, A.; Heck, S.; Maier, S. Plasmonic nanoantennas: fundamentals and their use in controlling the radiative properties of nanoemitters. *Chemical reviews* **2011**, *111* 6, 3888–912.
- (11) Akselrod, G. M.; Argyropoulos, C.; Hoang, T. B.; Ciraci, C.; Fang, C.; Huang, J.; Smith, D. R.; Mikkelsen, M. H. Probing the mechanisms of large Purcell enhancement in plasmonic nanoantennas. *Nature Photonics* **2014**, *8*, 835–840.
- (12) Feng, A.; You, M.; Tian, L.; Singamaneni, S.; Liu, M.; Duan, Z.; Lu, T.; Xu, F.; Lin, M. Distance-Dependent Plasmon-Enhanced Fluorescence of Upconversion Nanoparticles using Polyelectrolyte Multilayers as Tunable Spacers. *Scientific Reports* **2015**, *5*.
- (13) Chen, J.; Li, Z.; Yue, S.; Xiao, J.; Gong, Q. Plasmon-induced transparency in asymmetric T-shape single slit. *Nano letters* **2012**, *12*, 2494–2498.
- (14) Izadshenas, S.; Zakery, A.; Vafapour, Z. Tunable slow light in graphene metamaterial in a broad terahertz range. *Plasmonics* **2018**, *13*, 63–70.
- (15) Song, J.; Liu, J.; Li, K.; Song, Y.; Wei, X.; Song, G. Dynamically tunable plasmon-induced transparency in planar metamaterials. *IEEE Photonics Technology Letters* **2014**, *26*, 1104–1107.
- (16) Luo, P.; Wei, W.; Lan, G.; Wei, X.; Meng, L.; Liu, Y.; Yi, J.; Han, G. Dynamical manipulation of a dual-polarization plasmon-induced transparency employing an anisotropic graphene-black phosphorus heterostructure. *Optics express* **2021**, *29*, 29690–29703.
- (17) Chu, M.; Myroshnychenko, V.; Chen, C.-H.; Deng, J.; Mou, C.; de Abajo, F. G. Probing bright and dark surface-plasmon modes in individual and coupled noble metal nanoparticles using an electron beam. *Nano letters* **2009**, *9* 1, 399–404.
- (18) Tabakaev, D.; Montagnese, M.; Haack, G.; Bonacina, L.; Wolf, J.-P.; Zbinden, H.;

- Thew, R. Energy-time-entangled two-photon molecular absorption. *Physical Review A* **2021**, *103*, 033701.
- (19) Gorini, V.; Kossakowski, A.; Sudarshan, E. C. G. Completely positive dynamical semigroups of N-level systems. *Journal of Mathematical Physics* **1976**, *17*, 821–825.
- (20) Lindblad, G. On the generators of quantum dynamical semigroups. *Communications in mathematical physics* **1976**, *48*, 119–130.
- (21) Novotny, L.; Van Hulst, N. Antennas for light. *Nature photonics* **2011**, *5*, 83–90.
- (22) Scully, M.; Zubairy, M. *Quantum Optics*; Quantum Optics; Cambridge University Press, 1997.
- (23) AAT Bioquest, I. Spectrum [Atto 700]. https://www.aatbio.com/fluorescence-excitation-emission-spectrum-graph-viewer/atto_700, 2024; Accessed: 2024-05-31.
- (24) AAT Bioquest, I. Spectrum [Atto 610]. https://www.aatbio.com/fluorescence-excitation-emission-spectrum-graph-viewer/atto_610, 2024; Accessed: 2024-05-24.
- (25) AAT Bioquest, I. Spectrum [Atto Rho6G]. https://www.aatbio.com/fluorescence-excitation-emission-spectrum-graph-viewer/atto_rho6g, 2024; Accessed: 2024-05-26.
- (26) Izadshenas Jahromi, S.; Słowik, K. Multiphoton absorption enhancement by graphene–gold nanostructure. *Optics Letters* **2024**, *49*, 3914–3917.
- (27) Bharadwaj, P.; Deutsch, B.; Novotny, L. Optical antennas. *Advances in Optics and Photonics* **2009**, *1*, 438–483.
- (28) Drobizhev, M.; Makarov, N. S.; Tillo, S. E.; Hughes, T. E.; Rebane, A. Two-photon absorption properties of fluorescent proteins. *Nature methods* **2011**, *8*, 393–399.

- (29) Johansson, J. R.; Nation, P. D.; Nori, F. QuTiP: An open-source Python framework for the dynamics of open quantum systems. *Computer Physics Communications* **2012**, *183*, 1760–1772.
- (30) Johnson, P. B.; Christy, R.-W. Optical constants of the noble metals. *Physical Review B* **1972**, *6*, 4370.
- (31) Malitson, I. H. Interspecimen comparison of the refractive index of fused silica. *Josa* **1965**, *55*, 1205–1209.
- (32) Jackson, J. D. *Classical electrodynamics*; John Wiley & Sons, 2021.
- (33) Izadshenas, S.; Gładysz, P.; Słowik, K. Hybrid graphene-silver nanoantenna to control THz emission from polar quantum systems. *Optics Express* **2023**, *31*, 29037–29050.
- (34) Izadshenas, S.; Słowik, K. Metasurface for broadband coherent Raman signal enhancement beyond the single-molecule detection threshold. *APL Materials* **2023**, *11*, 081120.